



EXTREME ENVIRONMENTS:  
FROM SUPERMASSIVE BLACK HOLES  
TO SUPERNOVAE

FELICIA KRAUSS

EXTREME ENVIRONMENTS: FROM  
SUPERMASSIVE BLACK HOLES TO SUPERNOVAE

---

EXTREME BEDINGUNGEN IM UNIVERSUM:  
VON SUPERMASSIVEN SCHWARZEN LÖCHERN  
UND SUPERNOVAE

DER NATURWISSENSCHAFTLICHEN FAKULTÄT  
DER FRIEDRICH-ALEXANDER-UNIVERSITÄT  
ERLANGEN-NÜRNBERG

ZUR  
ERLANGUNG DES DOKTORGRADES DR. RER. NAT.

VORGELEGT VON  
**FELICIA KRAUSS**  
AUS NÜRNBERG



Als Dissertation genehmigt  
von der Naturwissenschaftlichen Fakultät  
der Friedrich-Alexander-Universität Erlangen-Nürnberg

Tag der mündlichen Prüfung: 15.06.2016

Vorsitzender der Promotionsorgans: Prof. Dr. Jörn Wilms

Gutacher: Prof. Dr. Jörn Wilms & Prof. Dr. Matthias Kadler  
Prof. Dr. Eduardo Ros



The cover picture shows a composite image of Centaurus A including optical data collected by an amateur astronomer (red, green, and blue), X-ray data from NASA's Chandra X-ray Observatory (pink) and infrared data from the Spitzer Space Telescope (red). Centaurus A is the closest active galactic nuclei which likely harbors a supermassive black hole. Perpendicular to the galaxy, it produces a relativistic outflow of matter, called jets. These jets form lobes when they interact with the surrounding medium, which is seen in the south-eastern lobe of Cen A. The shell surrounding the galaxy is likely due to an earlier merger with a smaller galaxy.

©X-ray: NASA/CXC/SAO; Optical: Rolf Olsen; Infrared: NASA/JPL-Caltech



# Zusammenfassung

In dieser Arbeit verwende ich Beobachtungen im Röntgenbereich um zwischen zwei Modellen für Supernovae des Typs Ia zu unterscheiden. Außerdem untersuche ich relativistische Jets, dies sind kollimierte Materieausstöße von aktiven Galaxienkernen (AGN).

Supernovae des Typs Ia sind thermonukleare “runaways”, Explosionen, deren Ursprung entweder im Verschmelzen zweier weißer Zwerge liegt oder in einem akkretierenden weißen Zwerg. Im Falle des akkretierenden weißen Zwergs befindet sich dieser in einem Doppelsternsystem, wobei das zweite Objekt ein massiver Stern ist, welcher Materie auf den weißen Zwerg überträgt. Der weiße Zwerg explodiert in einer Supernova, wenn er durch Akkretion die Chandrasekhar Masse erreicht. Beim Verschmelzen zweier weißer Zwerge im zweiten Modell jedoch wäre die addierte Masse der beiden Sterne von Supernova zu Supernova verschieden, was zu unterschiedlichen Leuchtkräften führen würde. Damit würden Supernovae des Typs Ia nicht mehr als Standardkerzen fungieren, da die unterschiedlichen Leuchtkräfte zu einer Verzerrung der Entfernungsmessung führen. Es ist deshalb wichtig für Supernovae des Typs Ia den Entstehungsmechanismus bestimmen zu können. Das Akkretionsmodell sagt eine höhere Menge  $^{55}\text{Co}$  voraus, welche 3.5-fach mehr radioaktives  $^{55}\text{Fe}$  produziert. Das resultierende Liniendublett entsteht bei 5.888 keV und bei 5.899 keV. Ich verwende derzeitige und zukünftige Röntgenmissionen um herauszufinden ob man diese Linienemission verwenden kann um zwischen beiden Modellen zu unterscheiden. Meine Simulationen zeigen, dass man mit dem *Chandra* Satellit beide Modelle bis zu einer Entfernung von 2 Mpc unterscheiden kann, also Supernovae innerhalb der lokalen Gruppe. Der geplante Athena Satellit ist vielversprechend für die Detektion der Linienemission, welche im Akkretionsmodell bis zu einer Entfernung von 5 Mpc nachgewiesen werden kann. Die Supernova SN2014J im Januar 2014 war die nächste Supernova der letzten vier Jahrzehnte mit einer Entfernung von 3.5 Mpc. Zum Zeitpunkt des höchsten erwarteten Linienflusses konnte die Supernova weder mit *XMM-Newton* noch mit *Chandra* beobachtet werden.

In der verbleibenden Arbeit untersuche ich Jets von Aktiven Galaxienkernen (AGN) mit Multiwellenlängendaten vom Radiobereich bis hin zum Hochenergiebereich. Jets sind energiereiche, beständige und leuchtkräftige Phänomene, die noch nicht komplett verstanden sind, besonders wie ein Jet gestartet wird und wie er kollimiert bleibt. Weiterhin ist die Teilchenbeschleunigung nicht verstanden. Blazare sind eine Unterklasse der AGN, bei denen der Jet unter einem kleinen Winkel sichtbar ist, wodurch es möglich ist die Emissionsmechanismen direkt zu untersuchen. Dies sind sehr variable Quellen, was eine kontinuierliche Überwachung und zeitnahe Daten in vielen Wellenlängegebieten erfordert.

Das TANAMI Programm ist ein Multiwellenlängen Projekt, welches Jets der südliche Hemisphäre studiert und eine Auswahl von  $\sim 100$  Quellen regelmäßig mit VLBI Methoden beobachtet. Ich verwende weiterhin Daten des *Fermi* Satelliten, dessen Instrumente kontinuierlich den Himmel beobachten. Mit einem Bayesschen Block Algorithmus können die Zeitbereich eingegrenzt werden in denen der *Fermi*/LAT Quellfluss statistisch konstant ist. Aus diesen Zeitbereichen wähle ich diejenigen aus in welchen genügend Multiwellenlängendaten vorhanden sind um ein Breitbandspektrum (*engl.* Broadband spectral energy distribution; SED) zu erstellen. Ich verwende die VLBI Daten des TANAMI Programm in Kombination mit quasi-simultanen Daten im Optischen/UV, Röntgen und  $\gamma$ -Bereich von den folgenden Instrumenten: *Swift*/UVOT, SMARTS, *Swift*/XRT und *Fermi*/LAT. Ich erhalte damit 81 SEDs der 22 TANAMI Quellen 22, die in *Fermi*/LAT am hellsten

sind.

Blazar SEDs zeigen typischerweise zwei nicht-thermische “Höcker” in ihrer SED und FSRQs haben oft ein zusätzlichen thermischen Exzess im Optischen/UV. Ich modelliere diese Daten mit einem empirischen Modell, welches aus zwei logarithmischen Parabeln besteht. Die Blazar-Sequenz sagt aus, dass die beiden Maxima (“Peaks”) der Parabeln mit steigender Leuchtkraft bei niedrigeren Frequenzen liegen. Obwohl die Blazar-Sequenz umstritten ist und auch modifiziert wurde, stimmen meine Ergebnisse mit ihr überein. Ich kann die 81 SEDs durch die kontinuierlichen *Fermi*/LAT Beobachtungen unterteilen in niedrige, mittlere und hohe Flusszustände, basierend auf ihrem gemittelten LAT Fluss. Im niedrigen und mittleren Zustand stimmen die Ergebnisse gut mit der Blazar-Sequenz überein. Im hohen Zustand gibt es eine große Streuung der Datenpunkte. Es deutet darauf hin das im hohen, aber nicht im niedrigen oder mittleren Flusszustand, eine Änderung im Jet stattfindet. Es werden keine Quellen im hohen Flusszustand gefunden, deren Peak bei einer hohen Frequenz liegt. Dies könnte dadurch zustande kommen, dass keine kontinuierlichen Beobachtung im Optischen, Röntgen oder VHE-Bereich vorhanden sind, aber es ist interessant, dass diese Quellen keine großen Ausbrüche im *Fermi*/LAT Bereich zeigen. Das beobachtete Muster der Blazar-Sequenz ist konsistent mit dem “härter-wenn-heller” Trend, der aus den Röntgenspektren von Blazaren bekannt ist. Des weiteren stimmt die Compton-Dominanz (die eine Rotverschiebungs-unabhängige Untersuchung der Sequenz erlaubt), mit der Blazar-Sequenz in meinen Daten überein. Die Fermi Blazar Teilung (engl. Fermi’s blazar divide) zeigt einen Mangel an Quellen deren Peak zwischen  $10^{14}$  und  $10^{16}$  Hz liegt. Ich zeige, dass diese Teilung vermutlich wegen Absorption und Extinktionseffekten in diesem Energieband entsteht und nicht durch einen quell-intrinsischen Effekt. Ich untersuche den thermischen Exzess in optischen/UV Spektren von Blazaren, der meist der Große Blaue Höcker (“Big Blue Bump”; BBB) genannt wird. Die Temperatur des BBB in BL Lac Objekten liegt typischerweise bei  $\sim 6000$  K, was bedeutet, dass dies die Emission der Wirtsgalaxie ist, die nicht von dem nicht-thermischen Kontinuum überstrahlt wird. In Quasaren liegt die Temperatur höher, zwischen 10000 K und 40000 K, deutlich niedriger als die erwarteten 760000 K für eine Akkretionsscheibe um ein supermassives schwarzes Loch mit einer Masse von  $\sim 10^9 M_{\odot}$ . Dieser Unterschied lässt sich dadurch erklären, dass die BBB Emission von Gaswolken nahe der Broad Line Region zu niedrigeren Temperaturen reprozessiert wird. In meinen Spektren können alle 22 Quellen besser mit einem Schwarzkörper mit einer einzelnen Temperatur erklärt werden als mit einer Überlagerung von Schwarzkörpern bei unterschiedlichen Temperaturen. In einer Akkretionsscheibe erwarten wir eine große Breite an Temperaturen, nach außen hin abnehmend. Dieses Spektrum würde durch Gravitation und die Geschwindigkeit der Scheibe weiter verbreitert werden. Eine weitere Möglichkeit den BBB zu erklären wäre frei-frei Emission in einer heißen Korona um das Schwarze Loch, aber eine ausführlichere Studie der BBBs ist notwendig um endgültige Schlüsse ziehen zu können. Ich hab weiterhin die fundamentale Ebene der Schwarzen Löcher draufhin untersucht, ob sie verwendet werden kann um die Schwarzslochmasse in Blazaren vorherzusagen. Die fundamentale Ebene findet eine Ebene in einem 3D Raum aus Schwarzslochmasse, Röntgenleuchtkraft und Radioleuchtkraft. Verschiedene Arbeiten in der Literatur finden unterschiedliche Parameter dieser Ebene, abhängig von der Quellpopulation welche zur Bestimmung verwendet worden ist. Mithilfe der neueren Werke, der Röntgen- und der Radioleuchtkraft habe ich die Schwarzslochmasse mittels der Fundamentalebene abgeschätzt. Die Parameter von Bonchi et al. (2013) liegen nahe an den gemessenen Schwarzslochmassen. Allerdings gibt es zwei Quellen bei denen die Abschätzungen mit allen Ebenen einige Größenordnungen unterhalb der gemessenen Werte liegen. Es ist möglich, dass die Schwarzslochmessungen von Boostingeffekten betroffen sind, allerdings würde dies bedeuten dass die Schwarzslochmassen für einige Quellen deutlich geringer sind als bisher angenommen,

oder sogar in den Bereich der Schwarzen Löcher mit mittlere Masse fallen.

Des weiteren habe ich mich mit den IceCube Ergebnissen beschäftigt. Detaillierte physikalische Modelle sind meist nicht in der Lage zwischen hadronischen und leptonische Prozessen zu unterscheiden. Existierende und geplante Neutrinoexperimente erlauben eine mögliche Assoziation von Neutrinos mit Blazaren. Dies wäre ein eindeutiger Beweis für hadronische Prozesse in AGN und ihre Beteiligung an der kosmischen Strahlung. Der IceCube Detektor am Südpol hat in den letzten Jahren Hochenergieneutrinos über 1 PeV detektiert. Da der atmosphärische Hintergrund mit steigender Energie stark fällt, sind diese höchstwahrscheinlich extraterrestrisch. Wegen der isotropen Verteilung aller IceCube Neutrinos, ist ein extragalaktischer Ursprung wahrscheinlich. Aus dem integrierten Fluss des zweiten "Höckers", bei höheren Energien, (der hadronischen Ursprungs sein könnte), berechne ich den maximalen Neutrinofluss. Ich verwende die TANAMI Quellen deren Position konsistent ist mit den ersten zwei detektieren PeV events. Die maximale Anzahl an Neutrinos die von den TANAMI Quellen produziert und in IceCube detektiert hätte werden können ist  $1.9 \pm 0.4$ . Dies ist noch kein Hinweise auf eine Assoziation mit Blazaren, aber zeigt das die Klasse der Blazare energetisch in der Lage ist die beobachteten Neutrinos zu produzieren. Das dritte Neutrino, welches wahrscheinlich extraterrestrisch ist, wurde mit 2 PeV detektiert und war zeitgleich mit einem Blazar der einen starken Ausbruch zeigte. Bei einem höheren elektromagnetischen Fluss bei hohen Energien (im Röntgen und Gammabereich) erwarten wir auch einen höheren Neutrinofluss. Dies deutet eine Verbindung zwischen dem Neutrino und der Quelle an, aber eine 5% Wahrscheinlichkeit für eine Zufallsassoziation bleibt bestehen.



# Abstract

In this work I study X-ray observations as a tool of distinguishing between models of supernovae type Ia and relativistic jets – collimated outflows of matter from active galactic nuclei (AGN).

Supernovae type Ia are thermonuclear runaways that are expected to originate from either a merger of two white dwarfs or from an accreting white dwarf in a binary system with a massive star. The first model challenges supernovae type Ia as standard candles for distance measurements. In an accreting system, the white dwarf is expected to undergo the thermonuclear runaway when reaching the Chandrasekhar mass. In a merger of two white dwarves the final mass would differ from supernova to supernova, leading to varying luminosities and subsequent errors in the distance calculations. The accretion model predicts a higher amount of  $^{55}\text{Co}$ , which synthesizes 3.5 times more radioactive  $^{55}\text{Fe}$ . The resulting line doublet is emitted at 5.888 keV and 5.899 keV. I study current and future X-ray missions as a tool for distinguishing between both models by measuring the line flux. My simulations show that with the current satellite *Chandra*, the models can be distinguished up to a distance of 2 Mpc, within the local group. The proposed Athena mission holds promise for a detection of the 5.9 keV line for the accretion model of distances up to 5 Mpc. The recent supernova SN2014J in January 2014 was the closest supernova in four decades with a distance of  $\sim 3.5$  Mpc. At the highest expected  $^{55}\text{Fe}$  line flux it could not be observed by either *XMM-Newton* or *Chandra*.

In the remaining work I study jets from active galactic nuclei (AGN) using broadband observations from the radio band to high-energy  $\gamma$ -rays. Jets are powerful, persistent, and luminous phenomena and are not fully understood, especially their jet launching, confinement and particle acceleration. Blazars are a subclass of AGN, with the jet pointed at a small angle to the line of sight, which allows to directly study the emission mechanisms in jets. They are very variable sources, requiring monitoring and quasi-simultaneous spectral data.

The TANAMI program is a multiwavelength project studying southern jets and monitoring a sample of 100 sources with high cadence with VLBI methods. In addition, *Fermi*/LAT is continuously monitoring the sky. I apply a Bayesian Blocks algorithm to the LAT data in order to find the time ranges where the source flux is statistically consistent with being constant. From these time ranges I choose the time ranges with sufficient multiwavelength data for constructing broadband SEDs. I use VLBI data from the TANAMI program in combination with quasi-simultaneous data at optical/UV, X-ray and gamma-ray energies from *Swift*/UVOT, SMART, *Swift*/XRT, and *Fermi*/LAT to construct broadband spectral energy distributions (SEDs) for the 22 *Fermi*/LAT brightest TANAMI blazars, resulting in 81 SEDs.

Blazar SEDs typically show two non-thermal humps, and FSRQs often have an additional thermal excess in the optical/UV. I fit the data with an empirical log parabolic model. The blazar sequence states that peaks of sources with high luminosities are found at lower frequencies. While this blazar sequence has been challenged and modified, my results generally agree with it. I am able to separate the 81 SEDs into states of low, intermediate, and high fluxes, based on their LAT flux in respect to the average LAT flux. The blazar sequence for SEDs in the low and in the intermediate state agree well with the sequence. In the high state a large scatter is present, and the sequence is not visible. It suggests that during an outburst a change in the jet occurs, which is not present in the intermediate state. No high-peaked sources are found in a high state. This is possibly due to a lack of flux information in the optical, X-ray or VHE regime, but it is interesting

to note that these sources do not show large outbursts in the *Fermi*/LAT. The observed pattern in the high state is consistent with the 'harder- when-brighter' trend often found in the X-ray spectra of flaring blazars. I further find that the Compton dominance (which is redshift independent) agrees well with the blazar sequence. I find that the Fermi's blazar divide, which seems to indicate a lack of sources peaking between  $\sim 10^{14}$  Hz and  $\sim 10^{16}$  Hz is likely due to absorption/extinction in this energy band, and is not source-intrinsic. I study the thermal excess found in the optical/UV spectra of blazars, often called the "Big Blue Bump"(BBB). The temperature of the BBB in BL Lac objects is usually  $\sim 6000$  K, which suggest that the BBB is emission from the host galaxy, which is not completely outshone by the non-thermal continuum. In quasars the temperatures of the BBB lie between 10000 K and 40000 K, much lower than the expected 76000 K for an accretion disk temperature of a supermassive black hole with a mass of  $\sim 10^9 M_{\odot}$ . It is possible that this is due to reprocessing of the emission by clouds near the broad line region. It is interesting to note however, that the BBB of the 22 sources can be better described by a single temperature black body than a multi-temperature black body. For an accretion disk we would expect a very large range in temperatures, possibly further broadened by gravity and the velocity of disk. Another possible explanation is free-free emission in a hot corona surrounding the black hole, though a more detailed investigation is necessary to draw firm conclusions about the BBB in blazars. I have studied the fundamental plane of black holes as a tool for estimating the black hole mass. The fundamental plane of black holes finds one plane in a black hole mass, X-ray luminosity, and radio luminosity three-dimensional space. Separate works in the literature find various parameters for this plane, depending on the source population used for determining the parameters. I have tested most of the recent works and used the X-ray and radio luminosity from the SEDs to estimate the black hole mass. This estimate has been compared to measured black hole masses. I find that the parameters by Bonchi et al. (2013) match the observed values closely, although I find two sources, which are consistently lower by a few orders of magnitude than their measured values. It is possible that these measurements are affected by boosting effects, although that would imply much lower black hole masses for some sources than expected, possibly falling into the range of intermediate mass black holes.

While detailed physical modeling of SEDs is often not able to distinguish between hadronic and leptonic models for blazars jets, current and future neutrino observatories offer the exciting possibility of an association of neutrinos with a blazar. This would provide unambiguous evidence of hadronic processes in AGN and their contribution to the cosmic ray spectrum. The IceCube detector at the South Pole has recently seen high-energy neutrino events above 1 PeV. Due to the steeply falling atmospheric background spectrum, these are most likely of extraterrestrial origin. Due to the isotropic distribution of all neutrinos, they are likely extragalactic. From the integrated flux of the high-energy hump (which is possibly of hadronic origin), I calculate the maximum possible neutrino flux. I used the six TANAMI sources in positional agreement with the first two PeV events and calculated the maximum-possible event number detectable by IceCube to be  $1.9 \pm 0.4$ . This is not directly indicative of a physical association, but shows that blazars as a class are energetically capable of producing the observed neutrinos. For the third PeV neutrino, which was detected with a reconstructed energy of  $\sim 2$  PeV, we found that one individual blazar in the error circle dominated the expected neutrino output. This blazar was undergoing a huge outburst at the time of arrival of the neutrino event. For a higher electromagnetic flux we expect to detect more neutrinos. This is indicative of a physical association, but a 5% possibility of a chance coincidence remains.

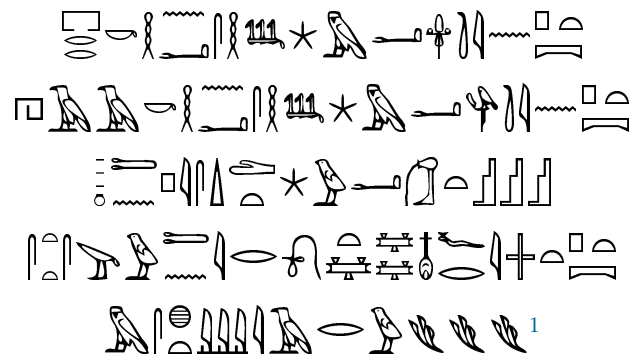
# Contents

1	Astronomy	1
1.1	From galactic to extragalactic astronomy	1
1.2	From multiwavelength to multimessenger astronomy	2
1.3	Plan of thesis	4
2	The death of a star	7
2.1	Stars and supernovae	7
2.1.1	Low-mass stars and type Ia supernovae	8
2.2	Production and decay of $^{55}\text{Fe}$	9
2.2.1	Simulations and results	9
2.3	The closest SN type Ia in four decades	13
2.4	High-mass stars and supernovae	17
3	Active galactic nuclei	19
3.1	From stellar mass to supermassive black holes: a historical view	19
3.2	Fundamental plane of black hole existence	20
3.3	Building an active galactic nucleus (AGN)	20
3.3.1	Black Holes	20
3.3.2	Intermediate mass and supermassive black holes	21
3.3.3	Accretion processes and accretion disks	22
3.3.4	The broad and narrow line regions and the dusty torus	22
3.3.5	Jets	23
3.3.6	Unification of observational picture	27
3.4	Blazars	27
3.4.1	Broadband spectra of blazars	28
3.4.2	Variability of blazars	29
3.4.3	The big blue bump	30
4	Observational data and analysis	31
4.1	Observational data	31
4.2	TANAMI	32
4.3	X-ray astronomy	33
4.3.1	Introduction	33
4.3.2	Wolter telescopes	33
4.3.3	X-ray charge-coupled devices (CCD)	34
4.4	<i>Swift Gamma-Ray Burst mission</i>	36
4.4.1	The X-Ray Telescope, reduction and analysis	36
4.4.2	The Burst Alert Telescope	38
4.5	The X-ray Multi-Mirror Mission	38

4.6	INTEGRAL . . . . .	39
4.7	Gamma-ray astronomy . . . . .	39
4.7.1	<i>The Fermi Gamma-ray Space Telescope</i> . . . . .	39
4.7.2	Large Area Telescope (LAT) . . . . .	39
4.7.3	<i>Fermi</i> /LAT data extraction . . . . .	40
4.8	Optical astronomy . . . . .	42
4.8.1	The UltraViolet and Optical Telescope (UVOT) and the Optical Monitor (OM) . . . . .	42
4.9	Radio astronomy . . . . .	42
4.10	Very Large Baseline Interferometry (VLBI) . . . . .	43
4.11	Additional data . . . . .	45
4.11.1	<i>Fermi</i> /LAT 3FGL . . . . .	45
4.11.2	SMARTS . . . . .	45
4.11.3	REM . . . . .	45
4.11.4	<i>WISE</i> . . . . .	45
4.11.5	2MASS . . . . .	45
4.11.6	<i>Planck</i> . . . . .	46
5	Constructing a broadband spectrum . . . . .	47
5.1	Calculating fluxes . . . . .	47
5.1.1	Systematic uncertainties . . . . .	50
5.2	Absorption and extinction . . . . .	51
5.2.1	Unabsorbed fluxes . . . . .	53
5.3	VLBI, small arrays and single dish . . . . .	54
5.4	The big blue bump . . . . .	54
5.5	Fitting the broadband spectrum . . . . .	54
5.5.1	Caveats . . . . .	56
6	A southern hemisphere blazar catalog . . . . .	57
6.1	<i>Fermi</i> /LAT light curve analysis . . . . .	57
6.1.1	The sample . . . . .	57
6.1.2	Bayesian Blocks . . . . .	59
6.1.3	Quasi-simultaneous time periods . . . . .	61
6.2	Fitting strategy . . . . .	62
6.2.1	Correlation of parameters . . . . .	62
6.3	The peak positions . . . . .	63
6.3.1	Blazar sequence . . . . .	63
6.3.2	Spectral index and peak position . . . . .	66
6.3.3	Compton dominance and the blazar sequence . . . . .	68
6.4	The <i>Fermi</i> blazar’s divide . . . . .	68
6.5	The big blue bump . . . . .	69
6.6	The black hole mass, $M_{\text{BH}}$ . . . . .	72
6.7	The strange SED of 2005–489 . . . . .	73
7	Neutrinos from blazar jets . . . . .	75
7.1	Broadband transmission of Ernie and Bert . . . . .	75
7.1.1	TANAMI sources in the two PeV-neutrino fields . . . . .	77
7.1.2	VLBI images . . . . .	77
7.1.3	Broadband spectra . . . . .	78

7.1.4	Possible other AGN sources of the IceCube events . . . . .	78
7.1.5	Expected neutrino rate from pion photoproduction . . . . .	81
7.2	The story of Big Bird . . . . .	82
7.2.1	Introduction . . . . .	82
7.2.2	2LAC blazars in the error field of IC 35 . . . . .	83
7.2.3	Contribution from unresolved blazars . . . . .	84
7.2.4	The empirical and theoretical scaling factor . . . . .	84
7.2.5	PKS B1424–418 in outburst . . . . .	86
7.2.6	The non-detection of other outbursts . . . . .	87
7.3	Summary . . . . .	89
8	Conclusion and Outlook	91
	References	95
	Appendix	107
A.1	<i>Fermi</i> /LAT light curves . . . . .	107
A.2	TANAMI Broadband spectra . . . . .	111
A.3	Fit result of the Broadband SEDs . . . . .	119
	Acknowledgments	123





You rise with Orion in the eastern sky,  
 you descend with Orion in the wesern sky,  
 your third is Sirius, she is the pure one who  
 guides you on the beautiful pathes in the sky,  
 through the marshes of reed.

---

<sup>1</sup>Kurt Sethe, Die Altaegyptischen Pyramidentexte nach den Papierabdrucken und Photographien des Berliner Museums Leipzig, J. C. Hinrichs'sche Buchhandlung, 1908



Astronomy? Impossible to understand and madness to investigate.

Sophocles, c. 420 BCE

# Chapter

# 1

# Astronomy

## From galactic to extragalactic astronomy

Contrary to the quote above, a large number of astronomers from varying cultures have observed and investigated the night sky and contributed to understanding the heavens above. From antiquity to recent times, the night sky has always fascinated humankind. In previous times religious or spiritual meaning was often attributed to celestial phenomena.

The oldest recorded observations from Babylonians date back to 2000 BC. They were the first to apply mathematics and observe periodicities in celestial bodies (Aaboe, 1992). Centuries of observations were recorded in the *Enûma Anu-Enlil*, including observations of Venus (Koch-Westenholz, 1995, Evans, 1998).

Egyptian astronomy dates back to prehistoric times, as shown by the stone circles at Nabta Playa (5th millennium BC; Wendorf & Malville, 2001, McK Mahille et al., 2007). The constellations and stars were important in religious ceremonies, such as the rising of Sirius (Sopdet). However, for the Egyptians (and other cultures) the observation of the night sky and its constellations did not only have a religious meaning, rather it was necessary for daily life. Annual Nile flooding could be determined by observations of the night sky, leading to accurate calendars (Parker, 1950, Clagett, 1989, Spalinger, 2002). Recent research has also shown that the Great Pyramids of Giza were aligned towards the pole star (Thuban, also know as  $\alpha$  Draconis) at the time. Further, the two shafts connecting the King's chamber to the outside were directly aligned with Thuban (north), and one of the stars of Orion's belt (south). Their purpose was likely to allow the "Ba" (𓆎; personality/soul) of the Pharaoh to travel to the stars in the afterlife (Ruggles, 2005).

Chinese astronomers were very accurate observers, but their observations were used for divination and astrology. Supernovae were named 'guest stars' (客星), as they could only be seen for a short time, with the oldest recorded supernova during 185 AD. They were often seen as the bringers of doom and considered a bad omen for a ruler (Xu et al., 2000, Zhao et al., 2006).

In Europe, astronomy has also played a significant role, as shown by archaeological finds, such as the Nebra sky disk. It probably shows the Pleiades specifying the times for sowing and harvest. It possibly also shows the angle between the sun rise at the equinoxes (Meller et al., 2004).

Astronomy and night sky observations have been an integral part of our past cultures and influenced daily life with time keeping, necessary for agriculture, religion as well as navigation

during past and present times. Currently point sources at large distances (such as quasars), are used for navigation systems, such as the Global Positioning System (GPS)<sup>1</sup>.

Astronomical observations by ancient cultures are an important aspect in archaeology, however, they are still relevant today. Some of the remnants of the supernovae recorded by Chinese and European astronomers since 185 AD have been found and studied in detail, such as Tycho's supernova (SN 1572; Brahe, 1573). Knowing the date of the explosion greatly improves our knowledge of the long-term evolution of supernova remnants and the velocities of the expanding shells.

The first five 'extended stars' were recorded by Ptolemy in the second century (Toomer, 1984). Abd al-Rahman al-Sufi recognized the Andromeda galaxy as a 'little cloud' (Kunitzsch, 1987), and so the first extragalactic object was found, although the distance was only measured in the 20th century. In the 18th and 19th century many catalogs of nebulae were compiled (e.g. in the Messier catalog; Messier, 1781), including Galactic nebulae, but also many objects that we now know are other galaxies. These catalogs were expanded (e.g., by Herschel, 1786, and Dreyer, 1888), the latter of which became known as the New General Catalogue (NGC). Some of the so called nebulae were indeed planetary or emission nebulae located in our Galaxy. Some of the 'nebulae' showed emission lines at unusual wavelengths (Huggins & Miller, 1864), leading to the identification of 'nebulium' as a proposed new element (Huggins, 1898). Only ~25 years later was it realized that these emission lines were forbidden transitions that only occur in very low density media, in this case a forbidden line of doubly ionized oxygen (written as: [O III]; Bowen, 1927). In the beginning of the 19th century, before the extragalactic nature of the galaxies had been established, an unusual phenomenon was found:

*A curious straight ray lies in a gap in the nebulosity in p.a. 20°, apparently connected with the nucleus by a thin line of matter. They ray is brightest at its inner end, which is 11" from the nucleus.*

— Curtis (1918).

This was the first jet – a relativistic outflow of matter from the central supermassive black hole – that was observed. It took nearly 10 years to realize that many nebulae are extragalactic sources (Hubble, 1926). Today, almost 100 years after the discovery of the first jet, many questions about these *active galaxies* still remain unanswered.

## From multiwavelength to multimessenger astronomy

For the majority of human history the night sky has only been observed in the optical wavelengths that are visible to the human eye. That the electromagnetic spectrum extends beyond the optical waveband was discovered in the early 19th century, with the discovery of infrared light by Herschel (1800) and that of ultraviolet radiation only three years later (Ritter, 1803). The Maxwell equations provided the first theoretical framework of electromagnetic waves (Maxwell, 1865). Electromagnetic waves at lower frequencies were discovered by Hertz (1888, 1889) who used a dipole. Although radio waves are now widely used in, e.g., communication, Hertz believed his discovery only proved the Maxwell equations, but was of no practical use (Norton, 2000). In the same year X-rays were discovered through studies of the fluorescence phenomenon (Röntgen, 1898a,b). Gamma-rays were detected shortly after through radioactivity by Becquerel (1896), while M. Curie found that only certain elements are radioactive (Pasachoff, 1997). While the electromagnetic spectrum was known at the beginning of the 20th century, observations at

---

<sup>1</sup><http://www.nasa-usa.de/centers/goddard/news/topstory/2009/icrf2.html>

different wavelengths only started much later. It was speculated that astronomical sources emit radio waves, but many observations failed (Wilsing & Scheiner, 1896). Karl Jansky detected radio emission from the Milky Way at radio wavelengths (Jansky, 1932, Jansky, 1933). Long wavelengths were of particular interest during the world wars as means of communication and the invention of radar. It took until the 1960s that radio observations were commonly used, and the sky first mapped in the Second and Third Cambridge Catalogue of radio sources (Shakeshaft et al., 1955, Edge et al., 1959). The 1950 – 60s were also the decades of the first astronomical X-ray experiments (Giacconi, 2003). These were the first catalogs that contained many active galaxies. Due to large uncertainties of the radio positions (several arcminutes) Cyril Hazard used the method of lunar occultations to find precise positions of some of the 3C sources, including 3C 273 (Hazard, 1961, 1962, Hazard et al., 1963). Surprisingly, 3C 273 showed a two component structure, separated by 20 arcseconds. It is now known that this structure corresponds to the radio lobes of an active galaxy, the areas where the jets interact with the surrounding medium, producing radio emission. Gamma-ray emission was expected from astronomical sources since the 1940s (Feenberg & Primakoff, 1948, Hayakawa, 1952, Morrison, 1958). Morrison predicted a  $\gamma$ -ray flux from astronomical sources of  $10^2$ – $10^4$  times of the flux predicted by Hayakawa. His high flux values motivated the first balloon experiments, although Hayakawa's prediction about the flux of  $\gamma$ -rays proved to be true. The first  $\gamma$ -ray missions include *Explorer 11* (launched in 1961; Kraushaar et al., 1965), *OSO-3* (1967; Kraushaar et al., 1972), *OSO-7* (1971; Clark et al., 1973, Datlowe et al., 1974, Markert et al., 1977), and the *Solar Maximum Mission* (1980; Forrest et al., 1980). These were used to study the Sun in  $\gamma$ -rays, although *OSO-3* detected  $\gamma$  rays from our Galaxy. *SAS-2* (1972; Fichtel et al., 1973) and *COS-B* (1975; Bignami et al., 1975) provided a first  $\gamma$ -ray sky map, but with low resolution. In the 70s NASA started its High Energy Astronomy Observatory Program, with the launches of *HEAO-1* (Matteson, 1978), *HEAO-2* (also called *The Einstein Observatory*; Giacconi et al., 1979), and *HEAO-3* (Binns et al., 1981). Launched in 1991 the Compton Gamma-Ray Observatory (CGRO) was the first  $\gamma$ -ray satellite with large angular and temporal resolution, which detected many active galaxies (Ulmer et al., 1995, Mukherjee et al., 1997). It was succeeded in 2008 June by the *Fermi* satellite, which provides the best view of the  $\gamma$ -ray sky.  $\gamma$  rays are thought to be tracers of the sources of cosmic rays.

In the late 19th century, cosmic rays ("atmospheric electricity") were attributed to the radiation from the ground. Theodor Wulf built an electrometer to measure the intensity of (secondary) cosmic rays (Wulf, 1909a). First results seemed to indicate that the intensity decreases with lower air pressure, and it was concluded that it originates from radioactive elements in the ground (Wulf, 1909b). In a further experiment, Wulf took an electrometer to the top of the Eiffel tower. The findings did not confirm the previous theory. While the intensity was lower than at the ground, it was not gone, as would have been expected (Wulf, 1910, Hörandel, 2013). In 1911 and 1912 two independent studies were carried out. Domenico Pacini found that when immersing an electrometer into the sea it disagreed with radioactivity from the crust (Pacini, 1912). This was confirmed by Victor Hess in 1912 in a balloon experiment. Above a height of 150 m, the intensity of radiation increases steadily (Hess, 1912). Cosmic rays mainly consist of protons originating from outside our Solar System, with energies between  $10^9$  and  $10^{21}$  eV (Blasi, 2014). Cosmic rays are of practical interest as they can inflict damage on microelectronics, especially in satellites, but also in airplanes, and on the ground (Pickel & Blandford, 1980). Further, they are dangerous for space travel, as cosmic rays can damage DNA and generate reactive oxygen species (Atri & Melott, 2014). From an astronomical point of view finding the sources responsible for the cosmic rays is a priority, as these are capable of accelerating particles to extremely high energies, and one goal is to understand these powerful acceleration mechanisms. Active galaxies are thought

to be prime candidates, as the jets consist of electrons, but these sources might also be able to accelerate protons. As protons (which constitute the majority of cosmic rays) are charged particles it is impossible to derive their point of origin, as they are deflected by magnetic fields both inside, and outside our Galaxy. Neutrinos provide the missing window, they are neutral, but very weakly interacting, resulting only in small numbers of detected events. Astrophysical sources that can accelerated protons to these high-energies interact with ambient light, e.g., from stars. These photon seed fields are large enough to produce pion-photoproduction. The photons interact with the ultra-high energy protons, creating neutral and charged pions:  $\pi^0$  and  $\pi^\pm$ . These decay into  $\gamma$ -rays and produce neutrinos amongst others. Currently the only extraterrestrial neutrino sources that have been confirmed are the Sun (Davis et al., 1968) and supernova SN1987A (Burrows & Lattimer, 1987, Alexeyev et al., 1988). The first underwater neutrino telescopes were the Deep Underwater Muon and Neutrino Detector (DUMAND; Spiering, 2012), the Baikal Neutrino Telescope, and AMANDA (Katz & Spiering, 2012). These experiments were succeeded by Super-Kamiokande, ANTARES, and IceCube (Fukuda et al., 2003, Ageron et al., 2011, Anton & ANTARES Collaboration, 2012, Halzen, 2006). ANTARES will be discontinued at the end of 2016 and succeeded by KM3Net, which is planned with a volume of five cubic kilometers (Adrián-Martínez et al., 2016). Recent results from the IceCube detector has shown a neutrino signal in excess of the expected atmospheric contribution, and is likely partly of extraterrestrial origin. Neutrino events, even those that are fully contained, still have large angular uncertainties of  $\sim 15^\circ$ . This challenges a direct association of neutrino events with astrophysical counterparts.

A further multimessenger approach is the detection of gravitational waves. These are ripples in space-time that propagate like waves. As massive objects move in space-time the curvature of the latter changes. These change can generate gravitational waves. One would expect a strong gravitational wave signal from a merger of two black holes, neutron stars, or inspiralling white dwarfs. Several detectors such as the Laser Interferometer Gravitational-Wave Observatory (LIGO), LISA/eLISA, and VIRGO are planned or have been built (Abbott et al., 2004, Accadia et al., 2012, Amaro-Seoane et al., 2012). Only in 2015 has such a signal been detected from the merger of two black holes (Abbott et al., 2016). This offers a promising tool of further investigating compact objects.

I show in this thesis that combining multiwavelength and multimessenger information from neutrino observations is a promising tool for understanding the underlying physics of active galaxies and black holes.

## Plan of thesis

In this thesis I start with Galactic astronomy, supernovae, and then move to extragalactic astronomy and AGN, which were the focus of this thesis. In Chapter I discuss supernovae type Ia and their explosion mechanisms. The main two scenarios involve white dwarfs, either one accreting material from a large companion star, or two white dwarfs merging. In both cases the Chandrasekhar limit is reached, and the object explodes in a thermonuclear runaway. Supernovae were generally thought to explode in the first of the two scenarios, reaching the limit of  $1.4 M_\odot$  via accretion. This would mean a nearly constant mass of all explosions. This, of course, is not given in a merger scenario, where two white dwarfs with arbitrary masses explode. In the accretion model, equivalent luminosities would be reached in all explosions, making them ideal tracers of distance for nearby galaxies. In the merging model, without similar luminosities, this would not be possible. It is therefore crucial to distinguish between both models. I discuss the possibility of distinguishing them with X-ray observations. The amount of iron predicted for both scenarios

differ, which subsequently leads to a higher X-ray iron emission lines flux for the accretion model. I calculate necessary exposure times for existing and planned X-ray mission for SNe for a range of distances.

In supernova explosions of massive stars (core-collapse supernovae) the core is much more massive than a white dwarf. If the star was very massive, it collapses to a black hole. In the center of galaxies supermassive black holes (million to billion solar masses) are thought to exist. It is not yet clear how they form, whether a small black hole accretes matter or if they form in black hole mergers. The central black hole of our Galaxy, Sgr A\* is well studied. We observe some galaxies ('active galaxies') with particular emission lines in the optical and emission over many decades of the electromagnetic spectrum. A subclass of these exhibit 'jets', outflows of matter, often extending well beyond the galaxy. These galaxies, and especially jets are not well understood. In galaxies, where this jet is pointed at a very small angle to our line of sight (called 'blazars'), the emission is relativistically boosted and the emission processes can be studied directly. They emit across the whole of the electromagnetic spectrum and show rapid variability (which is thought to be related to the relativistic boosting). In the third Chapter I introduce AGN and blazars and I talk about the observational methods used in the observations of blazars. I then explain how the broadband SEDs are compiled and what problems arise and how they are solved. In Chapter 6 I introduce a catalog of blazar SEDs from the TANAMI project. TANAMI monitors a sample of blazars on the Southern Hemisphere, studying radio morphology, kinematics and multiwavelength spectral and temporal evolution. In the following Chapter I talk about the study of IceCube neutrinos in relation to the TANAMI and 3LAC blazars. IceCube is a neutrino experiment located at the South Pole. Downwards-going neutrinos at very high energies (PeV) are likely of extraterrestrial origin. We study whether blazars and particular sources can explain the observed signal. This would not only be an unambiguous detection of hadronic processes in AGN jets, it would also show evidence for the role AGN play in the observed cosmic ray spectrum. In the last Chapter I conclude and present an outlook of possible ways to improve and extend this work.

*The time will come when diligent research over long periods will bring to light things that now lie hidden. A single life time, even though entirely devoted to research, would not be enough for the investigation of so vast a subject. . . And so this knowledge will be unfolded through long successive ages. There will come a time when our descendants will be amazed that we we did not know things that are so plain to them. . . Many discoveries are reserved for ages still to come, when memory of us will have been effaced. Our universe is a sorry little affair unless it has in it something for every age to investigate. . . Nature does not reveal her mysteries once and for all.*

— Seneca, Natural Questions Book 7, c. first century (Seneca, Hine, H. M. , 2010).



When I had satisfied myself that no star of that kind had ever shone forth before, I was led into such perplexity by the unbelievability of the thing that I began to doubt the faith of my own eyes.

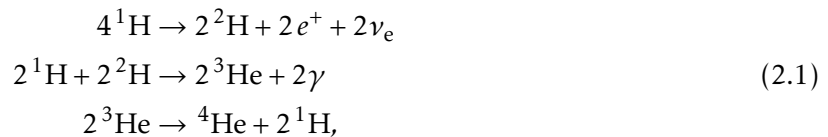
---

Tycho Brahe, 1610, *Astronomiae instauratae progymnasmata*, on SN 1572

## Stars and supernovae

Stars are easily visible to the human eye in the night sky, as they produce photons in the infrared to ultraviolet wavebands. The Sun is the closest star to Earth and its light is crucial for life on Earth. In this Chapter I introduce the life cycle of a star and how X-ray observations can help us learn more about the supernova explosions of stars at the end of their life time, following Clayton (1984), Murdin & Murdin (1985), Petschek (1990), Chandrasekhar (1994), Ryan & Norton (2010).

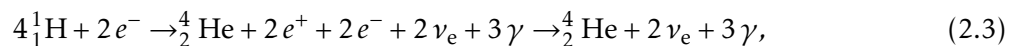
After a star is born within a molecular cloud it spends most of its lifetime on the main sequence in the Hertzsprung-Russell diagram, burning its hydrogen fuel, fusing it to helium. One of the main processes responsible for this (e.g., a process that happens in our Sun) is the proton-proton chain, in which protons fuse to produce deuterium first, then a light helium isotope, which then produce helium:



which results in a total production of 26.7 MeV and can be written as



Helium can also be produced in the carbon-nitrogen-oxygen cycle (CNO cycle), which is the main reaction path for stars above a mass of  $\sim 1.3M_{\odot}$ :



also producing 26.7 MeV. Carbon, nitrogen and oxygen are used as catalysts (Girardi et al., 2000).

A star is a very massive object with high gravity, balanced by its gas pressure. Towards the end of its life, when the star runs out of hydrogen to burn via either the cycle or the reaction chain, gravity starts to dominate and the star shrinks, increasing the density and temperature. At a core temperature of  $10^8$  K helium can be burned via the triple-alpha (and the alpha) process, which produces carbon from three helium nuclei. Carbon burning (for  $T \gtrsim 10^9$  K) and subsequent burning of heavier elements (neon, and oxygen) up to silicon produces elements up to  $^{56}\text{Fe}$ , as

no energy is released in the production of heavier elements. However, a small amount of heavier elements can be produced at high densities and temperatures. This is not true for low mass stars ( $M < 0.2 M_{\odot}$ ), which do not have a red giant phase (Laughlin et al., 1997). The burning phases can only start if the initial mass of the star was high enough, which subsequently allows the star to reach high densities and temperatures towards the end of its lifetime. Carbon burning is found in stars with  $M \gtrsim 8 M_{\odot}$  and burning of heavier elements in stars with  $M \gtrsim 10 M_{\odot}$  (Burbidge et al., 1957).

### Low-mass stars and type Ia supernovae

This section explains the explosion of low-mass stars type Ia supernovae (SN Ia) and follows Hillebrandt & Niemeyer (2000), Mazzali et al. (2007), and Hillebrandt et al. (2013). If a star does not reach the required temperature for carbon burning, carbon and oxygen accumulates in its center. After expelling its outer layers due to radiation pressure, the remnant is called a ‘white dwarf’ (or CO white dwarf). Between a progenitor mass of 8 to  $10.5 M_{\odot}$  carbon burning may take place, forming an oxygen-neon-magnesium white dwarf (Weidemann & Koester, 1983, Weidemann, 1990). The white dwarf cannot fuse elements anymore and therefore has no source of energy available. The collapse is balanced by electron degeneracy pressure. It can explode in a supernova type Ia if it reaches the ignition temperature for carbon fusion. If the white dwarf reaches the Chandrasekhar limit of  $\sim 1.4 M_{\odot}$  (Anderson, 1930) the electron degeneracy pressure is not sufficient and the white dwarf can explode in a supernova via thermonuclear runaway. In order to reach the Chandrasekhar limit, the white dwarf has to be in a binary (or triple,...) system.

There are two main models that describe how a white dwarf can reach the limit. In the first model (‘single-degenerate’), the white dwarf is accreting material from its companion star, reaching the Chandrasekhar mass and commencing carbon fusion. This is the ignition of a thermonuclear flame near the center of the CO white dwarf. It starts as subsonic deflagration, travels outwards and undergoes deflagration-to-detonation transition. This produces a shock-driven supersonic detonation wave (called ‘delayed detonation’; Mazzali et al., 2007). In an alternative scenario of this first model the white dwarf has a helium shell, accreted from its companion. Turbulent motions in the envelope can lead to a detonation of this shell and subsequently trigger the detonation of the core (‘double detonation’). This detonation can occur below the Chandrasekhar mass (Woosley & Weaver, 1994, Kromer et al., 2010, Shen et al., 2010).

In the second ‘double-degenerate’ model, two white dwarfs are in a binary system, losing angular momentum due to the emission of gravitational waves, merging, and thus reaching the limit. Only recently, Abbott et al. (2016) found direct evidence of gravitational waves, although from a merger of two black holes. White dwarf supernovae (classified as type Ia) are particularly interesting, because if (as in the first model) the same amounts of  $^{56}\text{Ni}$  are produced, the expected light curves and luminosities are very similar, if not identical. This would mean that observing a type Ia supernova in a distant galaxy would immediately allow for a determination of the distance to that galaxy, independent of the redshift. This makes these supernovae an important step in the distance ladder and they can be used for cosmological studies (Schmidt et al., 1998, Riess et al., 1998, Perlmutter et al., 1999).

Besides the application of supernovae to cosmological studies, supernovae are important in star formation and galaxy dynamics, heating cold interstellar gas (Scannapieco et al., 2008). Additionally, the nucleosynthesis in supernovae of all types contributes to the chemical evolution in a galaxy (Burbidge et al., 1957, Kobayashi & Nomoto, 2009). However, recent studies suggest that a significant fraction of type Ia supernovae explode via the second model, in which two white

dwarfs merge. These mergers might have a large distribution in combined masses that must not be close to the Chandrasekhar limit. It is therefore crucial to find a method to differentiate between both models. Both models can currently reproduce the observed light curve and spectra. Alternative approaches include simulating both scenarios and comparing the results to the observed data (e.g., Röpke et al., 2012). Another method is the study of the light curve. The ejecta of the supernova with the companion star could be seen in the light curve hours to days after the explosion (Kasen, 2010, Bloom et al., 2012, Brown et al., 2012). Spectroscopic observations are able in some cases to study the circumstellar material of previous outflows and absorption therein (Sternberg et al., 2011, Dilday et al., 2012). Patat et al. (2007) found that in one supernova the observed sodium lines rule out a double-degenerate model. It is further possible to study the  $\gamma$ -ray line and continuum emission for close supernovae (Sim & Mazzali, 2008, Maeda et al., 2012, Summa et al., 2013). This will be discussed further in Sect. 2.3. X-rays can theoretically be produced in SNe Ia via Bremsstrahlung of recoil Compton electrons, Compton down-scattering of  $\gamma$  rays, collisional ionization, electron capture decay and photoelectric absorption lines (Burrows & The, 1990, Clayton & The, 1991, The et al., 1994). It has been shown that observation in the hard X-ray band by *INTEGRAL* or *NuSTAR* could possibly distinguish between explosion models (The & Burrows, 2014). The possibility of detecting emission lines from the electron capture of radionuclides such as  $^{55}\text{Fe}$  has been suggested by Leising (2001, 2006). We studied methods of distinguishing between both models with X-ray observations of the  $^{55}\text{Fe}$  emission line (see Sect. 2.2). Crucial for this is the evolution of manganese (Seitenzahl et al., 2013a). See Hillebrandt et al. (2013) for a review of type Ia supernovae and the current status of theory and observations.

## Production and decay of $^{55}\text{Fe}$

This section is based on Seitenzahl et al. (2015), and some of the parts have been taken from there in verbatim. I have contributed to this publication with my simulations of X-ray spectra of SN type Ia for the merger and the delayed detonation model as a study of the detectability of the iron emission lines with current and future X-ray satellites, as well as to the text. The radioactive decay of  $^{55}\text{Fe}$  produces  $^{55}\text{Mn}$  via electron capture. An inner K-shell electron interacts with a proton and produces a neutron and an electron neutrino. This produces a line doublet with energies of 5.888 keV (8.2%) and 5.899 keV (16.2%; Junde, 2008). The half-life is 2.74 years. Using three-dimensional hydrodynamical simulations and subsequent radiative transfer calculations, we determine the respective line fluxes for two explosion models – a violent merger of two WDs with a sub-Chandrasekhar mass primary, and a delayed detonation in a near-Chandrasekhar mass WD. For the latter, we use the N100 model from Seitenzahl et al. (2013b). For the violent merger of two WDs (1.1 and 0.9  $M_{\odot}$ ), we use the model published in Pakmor et al. (2012). These two explosion models have been shown to reproduce many of the observable characteristics of “normal” SNe type Ia (Röpke et al., 2012, Sim et al., 2013) and are representatives of the single degenerate and double degenerate evolutionary channels, respectively. Both models employ a fully three-dimensional treatment of the explosion hydrodynamics, which compared to lower dimensional models, establishes a more realistic description of the distribution of the radioactive isotopes in the ejecta and enables radiative transfer calculations for different lines of sight.

### Simulations and results

The results from the simulations are shown in Fig. 2.1. The left panel shows the integrated photon flux for the emission line in both models. The predicted flux is much larger for the delayed detonation (single-degenerate model) than for the merger model due to the greater mass

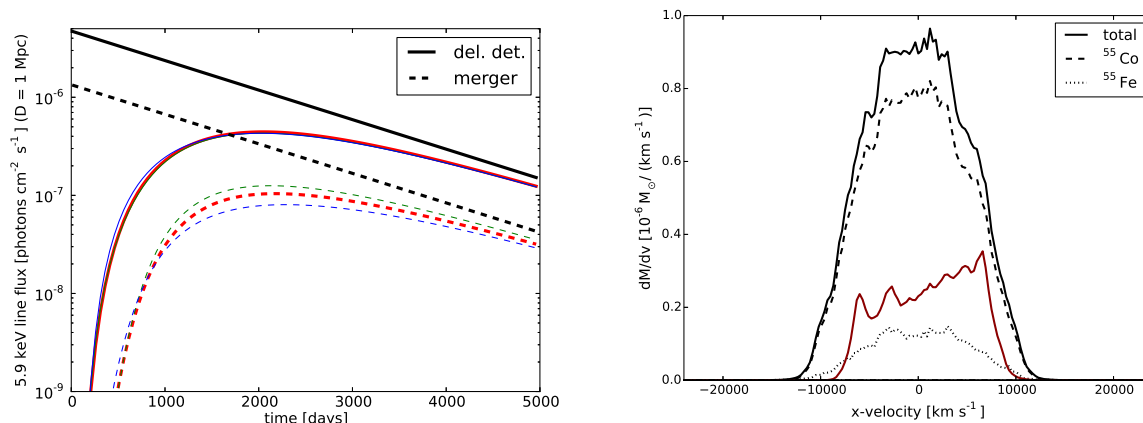


Figure 2.1.: *Left*: X-ray line flux at 5.9 keV at different times after the explosion for the two different explosion models at a distance of 1 Mpc. The solid (dashed) lines show the delayed-detonation (merger) model. The three different colors indicate three orthogonal lines of sight. Black lines indicate the optically thin limit (no absorption). *Right*: Solid lines are the distribution of the combined mass of <sup>55</sup>Co and <sup>55</sup>Fe in velocity space projected along a line of sight (simulation X-axis); the delayed-detonation model in black and the merger model in red. For the delayed-detonation model, <sup>55</sup>Co (black dashed) and <sup>55</sup>Fe (black dotted) are also shown separately. Both figures including the captions have been taken from Seitzzahl et al. (2015).

of synthesized <sup>55</sup>Co. The explosive burning at higher density in the delayed detonation model synthesizes 3.5 times more radioactive <sup>55</sup>Fe; the predicted line flux for N100 (delayed-detonation) model then exceeds the merger model flux by a factor of  $\sim 4.5$ . Due to the long half-life of the iron isotope the maximum emission is at  $\sim 2100$  days, which would be the ideal time frame for X-ray observations. From these photon fluxes it is possible to estimate the exposure times that are necessary with current instruments to significantly detect the line flux (and in the best case to distinguish between the two explosion channels). If the line flux can be measured with a high signal-to-noise ratio, a single measurement of a supernova at X-ray energies would then be sufficient to determine the explosion channel if the model holds. I therefore estimate the detectability of the 5.9 keV emission line, which we assume to be monochromatic for this simple estimate. The detection significance  $S/\sigma_s$  is given by

$$\frac{S}{\sigma_s} = r_s \frac{\sqrt{\delta t}}{\sqrt{r_s + 2r_b}} \quad (2.4)$$

with the source count rate  $r_s$ , the background count rate  $r_b$ , and the exposure time  $\delta t$  (Bradt, 2004). The background count rate includes instrumental background and continuum count rates. In order to calculate the count rates for various instruments it is necessary to take into account the effective areas of the various satellites. Figure 2.2 shows the results for the *Astro-H/SXS*, the *NuSTAR*, the *XMM-Newton/pn*, the *eROSITA*, the *Chandra/ACIS* and the *Athena/X-IFU* missions. Out of these, *NuSTAR*, *XMM-Newton*, and *Chandra* are active missions, *Astro-H* has been launched successfully in the beginning of 2016, and the others are planned missions. The two main factors in this estimate is the difference in effective area and the background count rate. *XMM-Newton* has the largest area of the current missions, and is therefore the best choice in the non background-dominated case (for higher fluxes than  $\sim 10^{-7}$  ph s<sup>-1</sup> cm<sup>-2</sup>). The *Chandra*

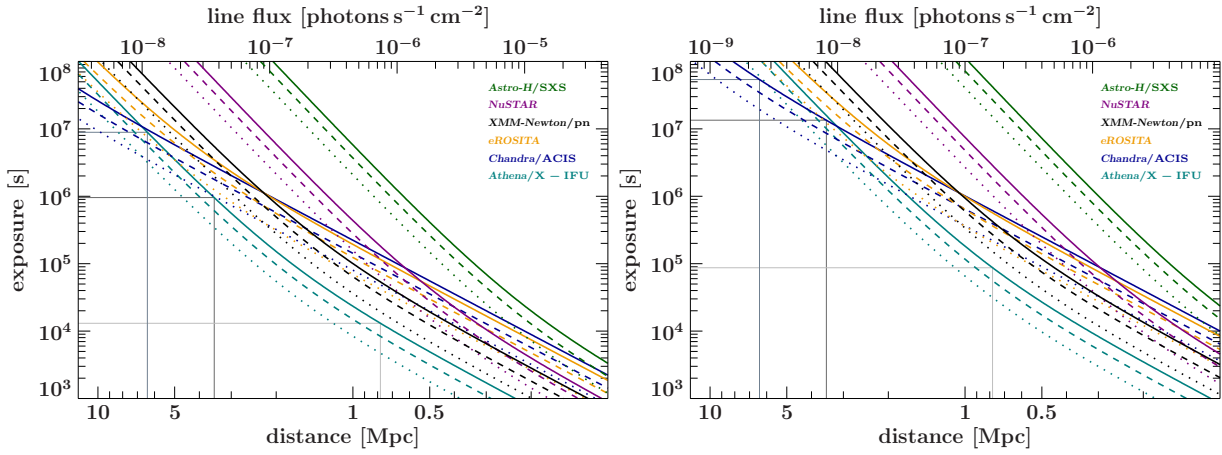


Figure 2.2.: Exposure times required for the detection of the 5.9 keV line with different X-ray instruments as a function of photon flux (upper X-axis) for the delayed-detonation model. The left panel shows the estimate for the delayed detonation model, and the right panel shows the estimate for the merger model. The line style (dotted, dashed, solid) encodes the significance of the line detection (3, 4, and 5 $\sigma$  respectively). For the maximum X-ray line flux predicted by the model at  $\sim 2100$  d after explosion, the lower X-axis shows the corresponding distances to the SN explosion. For a distance of 6.4 Mpc (distance to SN 2011fe), 3.5 Mpc (distance to SN 2014J), and 0.78 Mpc (distance to M31), the thin vertical lines mark the required exposure times for a 5 $\sigma$  detection of the 5.9 keV line with respect to the most sensitive instrument in each case.

satellite has a very low background count rate and is thus a good choice for low fluxes. Figure 2.2 also shows that currently very large exposures are necessary for a significant line detection at distances larger than  $\sim 1$  Mpc (especially for the merger model). With a very long exposure time (1 Msec) *Chandra* can distinguish between both models up to distance of  $\sim 2$  Mpc, as a non-detection would hint at the merger model. This is only an estimate based on monochromatic lines. Therefore I have used the line profile that has been determined from the simulation (Fig. 2.1) as input for a detailed detector simulation.

The radiative transfer calculations take the Doppler broadening arising from the velocity distributions of  $^{55}\text{Co}$  and  $^{55}\text{Fe}$  along the line of sight into account. I can therefore simulate line detection with *Athena/X-IFU* and *XMM-Newton/pn* in greater detail, including the broadening and shape for a fully resolved line. Figure 2.3 compares simulated *Athena/X-IFU* data of a Gaussian model to the model obtained from the hydrodynamical simulations, showing the Doppler broadening. The right panel compares the spectrum for different viewing angles to the source, showing a significant difference in the merger model. The fluxes however, can still be differentiated. For a detailed simulation of the expected spectral shape I assume a distance of 0.78 Mpc (distance to the Andromeda Galaxy M31) and an exposure time of 500 ks. For such an exposure time, the delayed-detonation model could be detected up to a distance of  $\sim 2.9$  Mpc and the merger model up to a distance of  $\sim 1.4$  Mpc by *Athena/X-IFU* at the 5 $\sigma$  level and a clear distinction of the two models is possible. For the distance of 3.5 Mpc to M82, which is the host galaxy of the recently discovered SN 2014J (Fossey et al., 2014, Cao et al., 2014), line detection for our models is within reach (see Sect. 2.3). Figure 2.4 shows a simulated spectrum for a 500 ks observations with *Athena/X-IFU* in detector space for the  $y$ , and the  $z$  direction.  $y$  and  $z$  are at

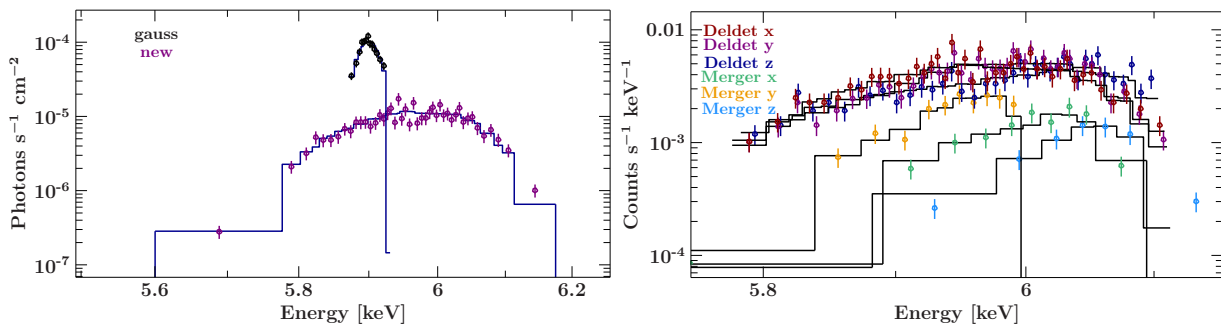


Figure 2.3.: *Left*: Comparison of a Gaussian with the given line flux to the Doppler broadened line flux given by the simulation of *Athena*/X-IFU data. *Right*: Comparison of the spectrum at different inclination angles to the explosion.

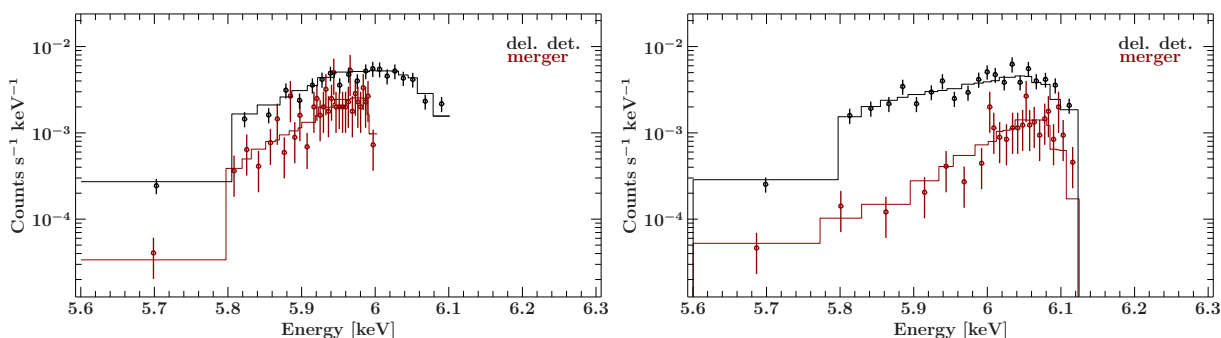


Figure 2.4.: Simulated 500ks *Athena*/X-IFU background-subtracted spectra of the 5.9 keV emission line in the *y* (left) and *z* (right) direction at a distance of 0.78 Mpc for the delayed-detonation (black) and the violent-merger model (red). The symbols show the simulated data and the solid lines show the best fit of the input model to the data. The continuum count rate (emission measure of  $10^{51} \text{ cm}^{-3}$ ) is below the instrumental background.

different angles to the explosion, since we see asymmetries in the explosion. The quantitative statements about the detectability of SNe Ia are model dependent. In particular, the assumed metallicity of the zero-age main sequence (ZAMS) progenitor has a direct effect on the production of the slightly neutron rich radionuclides  $^{55}\text{Co}$  and  $^{55}\text{Fe}$ . The metallicity dependent yields for the N100 model are taken from Seitzzahl et al. (2013b), who approximately take the effect of ZAMS metallicity into account by making the simplifying assumption that all metals in the ZAMS progenitor are locked up in CNO, which is efficiently converted to  $^{14}\text{N}$  during H-burning and then to  $^{22}\text{Ne}$  during core He-burning. For the merger case, we use the yields from the  $1.1 + 0.9 M_{\odot}$  model from Pakmor et al. (2012), which treated ZAMS metallicity in the same way.

We have shown that the 5.9 keV X-ray line provides a distinguishing feature between the observable signatures of two leading explosion scenarios of SNe Ia: a near-Chandrasekhar mass delayed detonation and a violent merger of two WDs. By performing detector simulations of several current and future X-ray instruments, I quantified the prospects for detecting the 5.9 keV line and find that, due to very low background, *Chandra*/ACIS is currently the most suitable instrument for SNe at distances greater than  $\sim 2$  Mpc. Of the existing instruments, *XMM-Newton*/pn is preferable for distances below  $\sim 2$  Mpc because of the larger effective area. For delayed-detonation SNe Ia at distances  $\lesssim 5$  Mpc, the proposed *Athena* mission holds promise for

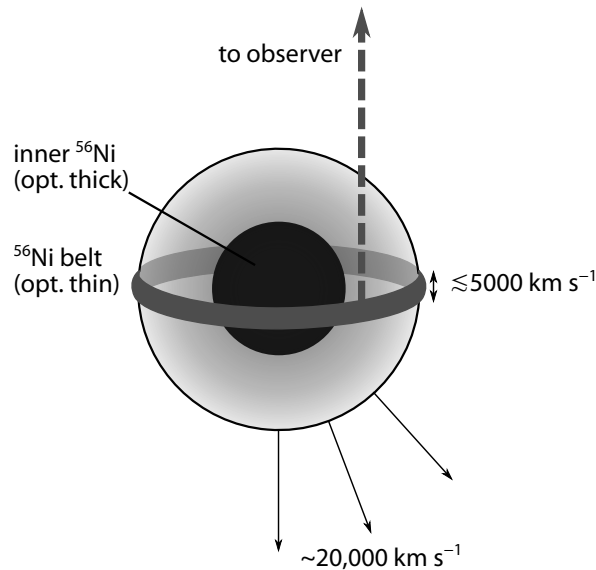


Figure 2.5.: The ring geometry suggested by the *INTEGRAL*  $\gamma$ -ray line data (Diehl et al., 2014).

a detection of the 5.9 keV line. Thus, observations of the 5.9 keV line provide an independent diagnostic tool that can be used together with measurements at UV, optical, and IR wavelengths to address the open questions of SN Ia explosion scenarios and progenitor channels.

### The closest SN type Ia in four decades

Supernova 2014J in M82 was discovered 2014 January 21 (Fossey et al., 2014). With a distance of  $\sim 3.5$  Mpc, it is the closest SNe type Ia in four decades. It provides a unique opportunity to study a close by supernova. In particular, the proximity of SN2014J means that its detection has been possible with *INTEGRAL*, leading to the first ever successful  $\gamma$ -ray detection of a normal SN Ia (Diehl et al., 2014, Churazov et al., 2014). Since SNe Ia are powered by the decay of radioactive isotopes produced in the explosion, by directly probing the  $\gamma$ -ray emission lines formed during radioactive decay, the *INTEGRAL* data provide a key window on the physics at work. However, the *INTEGRAL* data taken for SN2014J have led to some startling conclusions that seem to contradict most of the established models for SNe Ia. In particular, 17–19 days post explosion, *INTEGRAL* detected emission that Diehl et al. (2014) attribute to radioactive decay of  $^{56}\text{Ni}$  to  $^{56}\text{Co}$ . At such an early epoch, the  $\sim 1.4 M_{\odot}$  ejecta of a SN Ia are expected to be mostly optically thick to  $\gamma$ -rays. The detection therefore implies that a significant amount of radioactive Ni must be located in the outer ejecta. However, the  $\gamma$ -lines are narrow ( $\lesssim 2000 \text{ km s}^{-1}$ ) and not significantly Doppler shifted from their rest energies. The kinematics/line profiles of the gamma-ray data require the surface  $^{56}\text{Ni}$  to be confined to a narrow equatorial belt (Fig. 2.5). Together, these statements are inconsistent with any of the established models for SNe Ia: in many models, there should be little or no surface radioactivity and – more importantly – in all models, the outer ejecta should be expanding rapidly, and therefore would give rise to broad lines at all aspect angles. The most plausible explanation of the  $\gamma$ -ray data favors a double detonation scenario where surface  $^{56}\text{Ni}$  resulted from an initial detonation in a He layer on top of a CO white dwarf (WD), which then triggered the secondary SN Ia explosion. The explosion process is thus more complicated than generally assumed. The only direct way to test the picture suggested by the *INTEGRAL* data is via X-ray observations: specifically,  $^{56}\text{Ni} \rightarrow ^{56}\text{Co}$  decay must be followed by  $^{56}\text{Co} \rightarrow ^{56}\text{Fe}$  decay, which

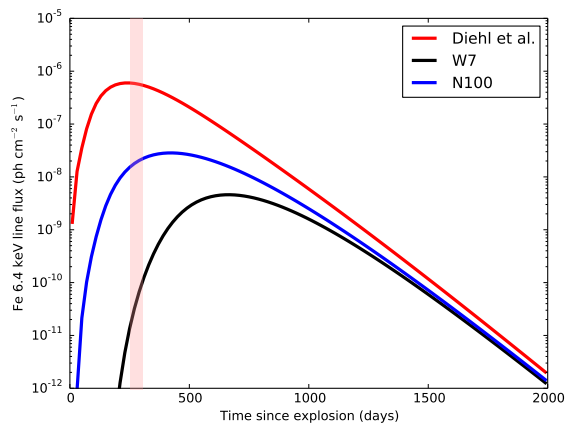


Figure 2.6.: Fe  $K\alpha$  X-ray line flux time evolution adopting a distance of 3.5 Mpc. The red area marks the time 250–300 d after the outburst, i.e., 2014 Sept. 25 until 2014 Nov. 18. The red line is the line flux from a model explaining the *INTEGRAL* measurements. The blue and black lines are for two standard SN Ia models, which, however, do not predict the  $^{56}\text{Ni}$  lines at epochs as early as observed.

produces Fe  $K\alpha$  photons with a yield of  $\sim 0.2$ . The decay timescale of this process is 113 d. Since X-ray opacities are comparatively high, the optimum window for observing the Fe  $K\alpha$  emission from the surface material is much later than for the equivalent  $\gamma$ -rays: The predicted Fe  $K\alpha$  light curve for models explaining the *INTEGRAL* data peaked in September/October 2014 ( $\sim 250$  days after explosion), with an expected line flux of  $\sim 6 \times 10^{-7} \text{ ph cm}^{-2} \text{ s}^{-1}$ . A successful detection of  $K\alpha$  emission with line energy showing little or no Doppler shift would give independent confirmation of the  $\gamma$ -ray data and its radical implications for SN type Ia theory. Conversely, a robust non-detection would exclude the interpretation proposed by (Diehl et al., 2014), place further strong constraints on theoretical models for SNe type Ia, and thus force reconsideration of the  $\gamma$ -ray data, possibly implying a non-radioactive origin for the detected features. I have therefore performed simulations of the expected line shape and flux for *XMM-Newton*, *Chandra* and *Athena/X-IFU*. Figure 2.6 shows the flux in the Fe  $K\alpha$  line for several different assumptions: (i) the model for 2014J proposed by Diehl et al. (2014, hereafter Diehl2014), (ii) W7, a widely used, standard model for SNe Ia (Nomoto et al., 1984), and (iii) N100, a 3D delayed-detonation model which is an example of a modern hydrodynamic explosion model (Seitenzahl et al., 2013b, Sim et al., 2013). It is important to note, however, that the latter two models do not account for the  $^{56}\text{Ni}$  emission seen so early in the  $\gamma$ -ray light curve of SN 2014J. While the Fe  $K\alpha$  flux can already constrain the explosion mechanism, the Fe  $K\alpha$  profile, i.e., the energy and width of the line, can place further constraints on the kinematics. This is illustrated in Fig. 2.7, which shows the predicted Fe  $K\alpha$  profile for the Diehl2014 scenario. The geometry of this model leads to a very specific line profile shape. Even if a model with turbulent mixing, such as N100, could be modified to account for the observed early onset of  $\gamma$ -ray line emission, such a model predicts broad and strongly blueshifted line profiles (as the  $^{56}\text{Ni}$  is brought relatively close to the surface in a quasi-spherical distribution). Our favored geometry, however, predicts Fe  $K\alpha$  profiles that are narrow and only weakly shifted. An Fe  $K\alpha$  line detection would be inconsistent with most hydrodynamical models for SNe Ia and require a substantial revision of the model picture. A non-detection would immediately rule out the proposed explosion scenario for SN 2014J, but still provide the strongest observational constraint on the production of radioactive surface nickel in

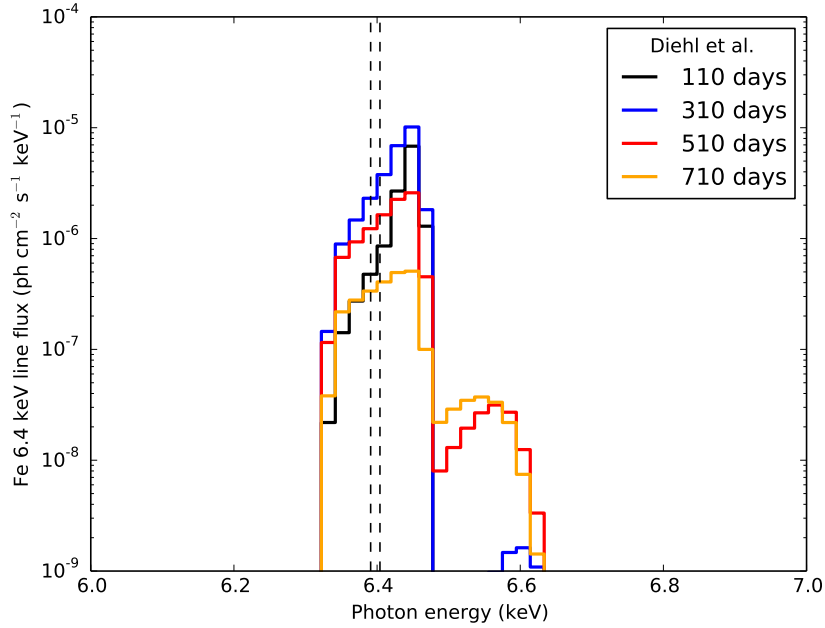


Figure 2.7.: Fe  $K\alpha$  X-ray line profile in the Diehl2014 model of SN 2014J. The dashed vertical lines indicate the rest energies of Fe  $K\alpha_{1,2}$ . The line consists of a narrow component at the rest energy coming from the surface  $^{56}\text{Ni}$  and a weaker blueshifted component coming from  $^{56}\text{Ni}$  deep in the ejecta. The latter is close to lines from canonical detonation models, which yield blueshifted lines which are broader (S. Sim, priv. comm.).

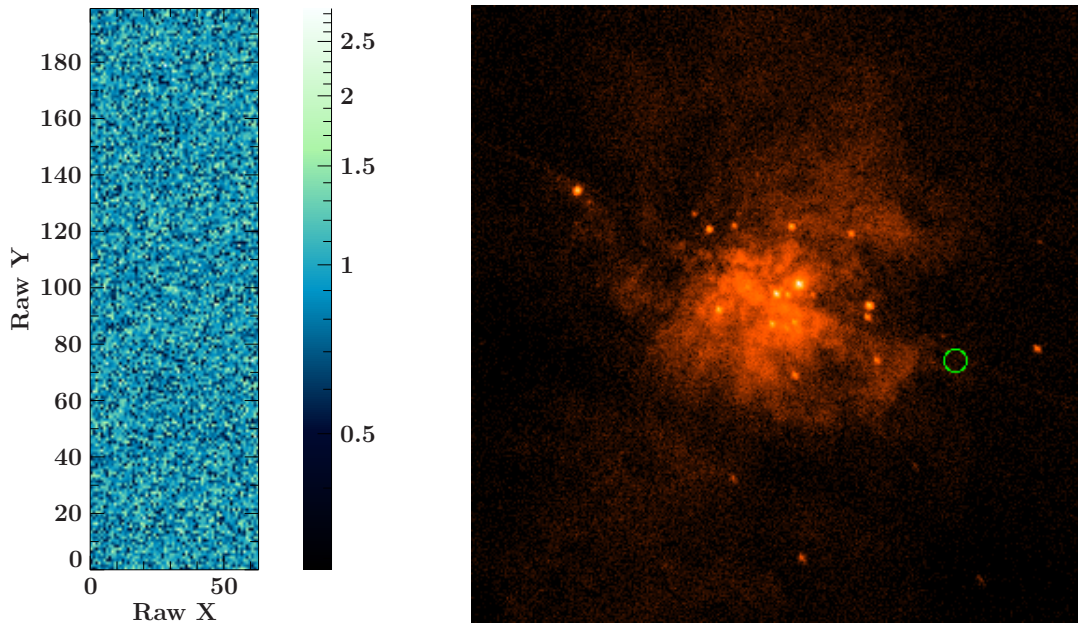


Figure 2.8.: *Left*: Simulated image of a 300 ksec *XMM-Newton* observation. Only one of the EPIC/pn chips has been used for the simulation, the supernova is located in the center of the picture (T. Brand, priv. comm.). *Right*: *Chandra*/ACIS image (observation ID 10542, 120 ksec) of the region showing the location of the supernova, used for the extraction of the background region for the simulation of the *Chandra* data (C. Gräfe, priv. comm.).

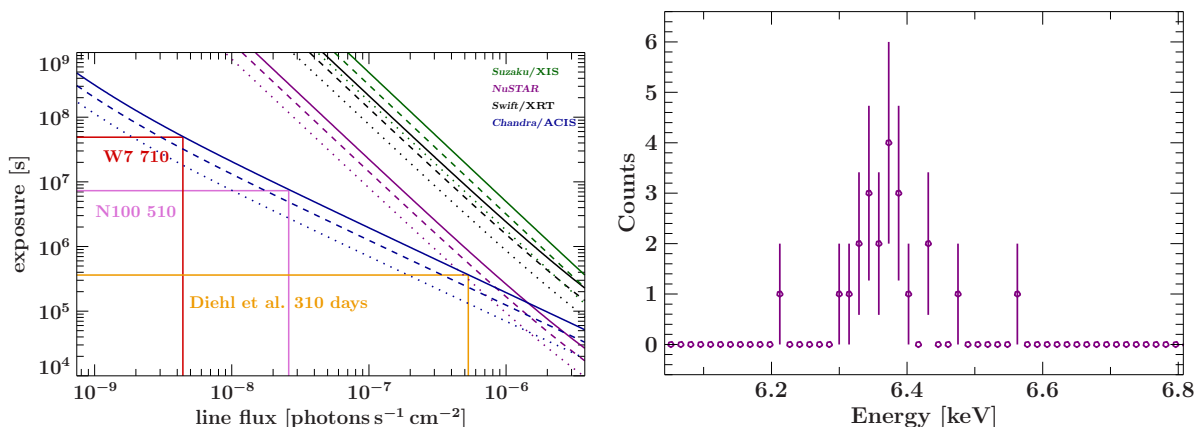


Figure 2.9.: *Left*: Estimate of the necessary exposure times for various satellites, including the proposed model by Diehl et al. (yellow, 310 days after the explosion), as well as the N100 model 510 days after the explosion, and the W7 model (710 d after the explosion). *Right*: 300 ksec *Chandra*/ACIS-I simulation for a line with the Diehl et al. line shape, showing the significant detection of the line. The line width can be clearly seen.

SNe Ia to date. Figure 2.8 shows an image simulation in SIXTE<sup>1</sup> of a 300 ksec observation with *XMM-Newton*. *XMM-Newton* would be a slightly better choice than *Chandra* due to the higher effective area. Unfortunately, the supernova is in the Earth exclusion zone for *XMM-Newton* and will only become observable again with this satellite several years from now. I therefore estimated the necessary exposures for *Swift*/XRT, *Suzaku*/XIS, *NuSTAR*, and *Chandra* (see Fig. 2.9) for the peak flux of the three models. The estimates are based on Poisson statistics and typical backgrounds. To refine our estimate, we perform simulations where we use the line flux from Fig. 2.6 and the line shape from Fig. 2.7 and perform simulations with the software package ISIS for the conservative case of 310 days after the explosion. Because of the low absorbing column towards the supernova ( $N_{\text{H}} = 5.06 \times 10^{20} \text{ cm}^{-2}$ ; Kalberla et al., 2005a) the line flux is not affected by foreground absorption. As the supernova is still optically thick, no significant continuum emission is expected at this epoch (see Clayton & The, 1991). The background at the location of SN 2014J is dominated by diffuse emission from its host galaxy (M82 is a starburst galaxy). I have used the longest archival *Chandra* observations of M82 (ObsIDs 10542 [120 ksec], 10543 [120 ksec], and 10545 [96 ksec]) to measure the background flux in a  $3''$  circle at the position of the supernova (Fig. 2.8, right panel). I find  $1.67 \times 10^{-6} \text{ counts s}^{-1}$  in the 6.3–6.8 keV band relevant for the line detection. This shows that background will be negligible for the detection of the line.

Figure 2.9 (right panel) shows an example spectrum at the native resolution of the ACIS-I. This simulated observation detected 21 source counts and 0 background counts yielding a detection at a  $4.5\sigma$  level (Li & Ma, 1983). The mean photon energy is 6.55 keV and the standard deviation of the photon energy is 0.14 keV. Because of the low number of counts expected, we study the distribution of individual realizations of the line spectrum and background in a series of Monte Carlo simulations (see Fig. 2.10). For the line flux of 310 days after the explosion the expected number of counts is expected to lie between 12 and 20 counts, while the background is between 0 and 2 counts. Most simulations yield detections above  $3\sigma$ , confirming our exposure time estimate of 300 ks. Unfortunately it was not possible to observe SN 2014J with *Chandra*, as 300 ks would

<sup>1</sup><http://www.sternwarte.uni-erlangen.de/research/sixte/>

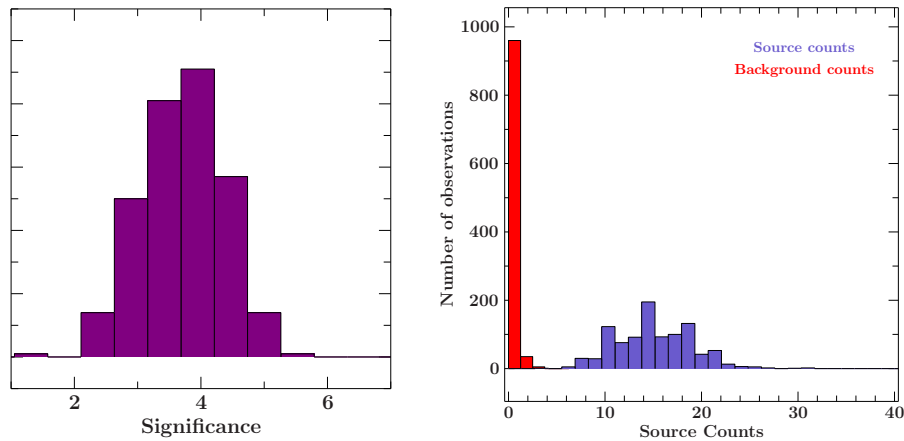


Figure 2.10.: Distribution of line detection significances for individual Monte Carlo realizations using observations of 300 ks (right) and distribution of background and source counts in the Fe K $\alpha$  band.

have been a significant fraction of the total Director's Discretionary Time (DDT) available (700 ks) during one year.

## High-mass stars and supernovae

In stars that are large enough to reach the temperatures for silicon burning, it continues until the iron core reaches the  $1.4 M_{\odot}$  limit and can no longer balance the gravity; it collapses. Inverse beta decay and photo-disintegration collapses the core, which produces neutrons, neutrinos and  $\gamma$ -rays.

The outer shells are in free fall and are only halted when they hit the already very dense core that will become the neutron star or black hole. The shock wave of this collapse travels outwards halted by the photo-disintegration. Neutrinos produced in the core heat the material and accelerated the shock blasting the material outwards in the so-called 'core-collapse' supernova. Most of the mass of the star is shedded in this explosion, leaving only the core of the star, which can be (depending on the initial mass of the star) a neutron star (sometimes seen as a pulsar), or a black hole. In order to form a black hole the mass has to be so large that a complete collapse is inevitable (Hillebrandt et al., 1984). In the next Chapter I talk about supermassive black holes in detail.



# Chapter 3

## Active galactic nuclei

Observing quasars is like observing the exhaust fumes of a car from a great distance and then trying to figure out what is going on under the hood.

---

Carole Mundell, *Scientific American* magazine, June 1998

Active galaxies harbor a supermassive black hole in their center with masses between  $\sim 10^6 M_{\odot}$  and  $\sim 10^{10} M_{\odot}$ . Every black hole is a large mass collapsed to a singularity, an infinitely dense point mass. Nothing can escape the gravity once it crosses the event horizon. Observational evidence of black holes include persistent non-thermal emission, compactness, and highly relativistic bulk motion ( $\Gamma \sim 20$  in extragalactic supermassive black holes). In this Chapter I give a brief summary of the history of black hole and AGN research, and the physics of supermassive black holes in active galaxies. This chapter is based on Meier (2012).

### From stellar mass to supermassive black holes: a historical view

The concept of a black hole dates back to the 18th century, where “dark stars” were first proposed by Michell (1783), and a few years later by Laplace (1796), but their results were largely ignored until the 20th century and Einstein’s General Theory of Relativity, which suggested that light could be bent by massive objects (Einstein, 1915a,b). Light bending was proven only four years later using a total solar eclipse (Eddington, 1919a,b). Schwarzschild (1916a,b) found a solution to the Einstein field equations, which suggested that above a certain mass a star at the end of its life would collapse, forming a singularity. This was believed to be a mathematical concept, but Oppenheimer & Snyder (1939) suggested that this indeed happens to stars. In 1969 it was proposed that matter in the ergosphere can extract rotational energy from the black hole, as the matter inside the ergosphere can still escape to infinity. The ergosphere is affected by frame-dragging, i.e., distorting the space-time metric in the direction of the black hole’s rotation. One possibility of extracting rotational energy from a black hole is the Penrose process (Penrose, 1969). Only two years after the theoretical framework for black holes was established, a black hole candidate was found, Cyg X-1 (Oda et al., 1971). Many detections of stellar mass black holes that originate from the collapse of stars have been found since then. In the same year it was first suggested that the Milky Way contains a supermassive black hole with a mass of  $\sim 10^8 M_{\odot}$  (Lynden-Bell & Rees, 1971), which is now called Sagittarius A\*. It is now believed that all galaxies harbor a supermassive black hole at their center (Kormendy & Richstone, 1995, King, 2003).

It is curious to note that other galaxies harboring supermassive black holes were found much earlier, although their significance was not understood until much later. In 1909 Edward A. Fath found emission lines in the spectrum of NGC 1068, similar to the spectra of planetary nebulae

(Fath, 1909). A decade later Heber D. Curtis noted that „M87 exhibits a curious straight ray [...] apparently connected with the nucleus by a thin line of matter“ (Curtis, 1918). This was the first detection of a “jet” – an outflow of matter, often detected from radio to X-ray energies. Carl Seyfert studied spiral galaxies with high-excitation emission lines, now called Seyfert galaxies (Seyfert, 1943). Woltjer (1959) discovered that the central region of galaxies need to have large masses for normal mass-to-light ratios, but it was not clear that this is due to a central supermassive black hole. All these various types of peculiar galaxies are now thought to be active galaxies.

Black holes have been found since the 70s. They can be found by searching for massive, compact sources with a high energy output. Some of these show a relativistic outflows in the radio. Most of the black holes show a power law spectrum at X-rays energies associated with the inner part of an accretion flow. While all galaxies are thought to harbor a supermassive black hole, not all show non-thermal emission from radio to X-ray energies. In the 1990s it was realized that many of the different ‘peculiar’ galaxies are indeed part of one single phenomenon, an active galactic nuclei. Until today it is not clear how similar and how different stellar mass and supermassive black holes are and how they evolve.

## Fundamental plane of black hole existence

The fundamental plane of black holes is one attempt at comparing the properties of stellar mass to supermassive black holes. Many similarities between both populations exist, and indeed by studying one population it is possible to apply that knowledge to the other. In 2003 it was found that while the relation between X-ray and radio luminosity scatters for black holes, it can be improved by introducing the black hole mass as a third parameter

$$\log L_R = (0.60^{+0.11}_{-0.11}) \log L_X + (0.78^{+0.11}_{-0.09}) \log M + 7.33^{+4.05}_{-4.07}, \quad (3.1)$$

with the radio luminosity  $L_R$ , the X-ray luminosity  $L_X$ , and the black hole mass  $M$  (Merloni et al., 2003). This plane of black hole activity has been established for black hole binaries and a few AGN initially. Black hole binaries are easily visible in X-rays, as the black holes are in a binary system with a massive companion star. The black hole accretes material from the star and produces an accretion disk and jets. It was found that this fundamental plane of black holes agrees with supermassive black holes as well, and the relation was updated for varying source populations (Merloni et al., 2003, Gallo et al., 2003, Falcke et al., 2004, Körding et al., 2006, Gültekin et al., 2009, Plotkin et al., 2012, Bonchi et al., 2013, Gültekin et al., 2014, Saikia et al., 2015, Nisbet & Best, 2016, and references therein). It suggest a fundamental connection of accretion flow and jet activity. It has further been found that the spectral properties in the radio and in X-rays, as well as the jet morphologies are similar in stellar mass and supermassive black holes (McHardy et al., 2006, McHardy, 2010). Intermediate mass black holes are still missing, and it is unclear if they exist.

## Building an active galactic nucleus (AGN)

### Black Holes

The mass of a black hole can span a wide range, between several solar masses to several billion solar masses. All black holes are thought to be very similar objects. A single black hole is very hard to find. It is only possible through gravitational lensing, light bending around the black hole. If matter approaches a black hole and is gravitationally drawn to it, the interaction can be directly

observed. In dense environments these effects are also seen. The ‘black holes have no hair’ theorem states that no information can leave the black hole and the black hole is characterized by only two parameters: its mass and its spin (Misner et al., 1973). The black hole has an illusory horizon, the redshifting surface of the collapsed star, which is the observational boundary, and where Hawking radiation is expected to originate from. The information paradox states that in the horizon one of the quantum field theory (QFT) tenets must break down: Locality (causality) or Unitarity (Hawking, 1975). Locality (which is the one to likely break down) states that information cannot travel faster than light (spacelike separated field operators commute, enforcing causality) and unitarity states that information is conserved (quantum mechanics is deterministic and lossless).

The center of an active galaxy is expected to harbor a supermassive black hole, although it is unclear how they form. Observational evidence of supermassive black holes include their variability, ultra-relativistic outflows, compactness, and luminosity. The event horizon telescope (EHT) aims at resolving the event horizon of Sgr A\*, which would provide direct evidence of a supermassive black hole at the heart of our Galaxy (Falcke et al., 2000, Fish et al., 2016).

### Intermediate mass and supermassive black holes

They are the most energetic and powerful machines that are persistent over long time spans – supermassive black holes (SMBH). Only a small fraction of galaxies are active galaxies though all galaxies are thought to harbor a SMBH. Many stellar mass black holes (in binary systems), and supermassive black holes (in active galaxies) are well studied and it is relatively certain that these are indeed black holes. Surprisingly, only a few candidates for intermediate mass black holes (IMBH;  $100 M_{\odot} - 10^5 M_{\odot}$ ) are known, although active searches have been ongoing for many years. Candidates for IMBHs include NGC 4395 (Peterson et al., 2005), HLX-1 in ESO 243–49 (Farrell et al., 2009, 2012), and CO-0.40-0.22 (Oka et al., 2016). IMBHs are of particular interest for the formation of supermassive black holes, whose origin is still unknown (Djorgovski et al., 2008, Yajima & Khochfar, 2016). While SMBHs are expected to grow through either accretion and/or mergers, it is unclear how they start. The general assumption is that massive black holes with  $\sim 10^5 M_{\odot}$  form in haloes. Assuming that they formed in the first galaxies and accreted gas at the Eddington rate, the first supermassive black holes would have existed at  $z \sim 6$ , too late for the oldest quasars that are known (Yajima & Khochfar, 2016). The assumptions in this scenario are further unlikely, as the mass gain in these objects is negligible and likely does not lead to SMBHs (Alvarez et al., 2009). Another theory involves a direct gravitational collapse of a large mass, such as a dense star cluster, or a supermassive star (SMS) with a mass of  $\sim 10^5 M_{\odot}$ , possible in the early universe due to suppression of star formation by UV fields (Bromm & Loeb, 2003). Alternatively, a direct gravitational collapse to a SMBH of a dense protogalactic core, or a primordial BH remnant from the big bang could explain the earliest SMBHs (Djorgovski et al., 2008). Merger of galaxies are a favored theory for forming and/or growing SMBHs, as it does not require high accretion rates (Duschl & Strittmatter, 2011). Mayer et al. (2010) suggest that mergers of massive protogalaxies are able to reproduce the observed SMBH masses without the need to suppress star formation. The merger leads to inflows of gas which produce a massive nuclear gas disk, which collapses to a massive black hole and can accrete material from the surrounding disk, whose mass grows forming a SMBH. If SMBHs do grow from mergers or accretion, IMBHs should still be present in the Universe.

### Accretion processes and accretion disks

It is widely accepted that active galaxies are fuelled by accretion of matter onto the SMBH (Salpeter, 1964, Zel'dovich, 1964). The Eddington limit gives an approximation for the maximum accretion rate, balancing the radiation pressure and the accretion material gives the maximum Eddington luminosity

$$L_{\text{Edd}} = \frac{4\pi GMc}{\kappa} \quad (3.2)$$

with the opacity of ionized matter  $\kappa = \sigma_{\text{T}}/m_{\text{p}}$ , with the Thomson scattering cross-section  $\sigma_{\text{T}}$  and the proton mass  $m_{\text{p}}$ . It assumes spherically symmetric accretion of hydrogen gas, an assumption which is likely not the case, as accretion is expected to produce an accretion disk surrounding the black hole due to the conservation of angular momentum of infalling material. Assuming a simple thin disk, it is expected to emit multi-temperature blackbody radiation. The characteristic temperature is given by

$$T = 95000 \text{ K} \cdot L_E^{1/4} M_9^{-1/4} R_5^{-1/2} \quad (3.3)$$

with the luminosity in units of the Eddington luminosity  $L_E$ , the black hole mass  $M_9$  in units of  $10^9 M_{\odot}$ , and the radius  $R_5$  in units of 5 Schwarzschild radii  $R_S$ . For a supermassive black hole (e.g., 3C 273) with a mass of  $8.87 \times 10^8 M_{\odot}$ , and  $L_E = 0.356$  the temperature at  $5 R_S$  is expected to be  $T \sim 76000 \text{ K}$  (Lawrence, 2012).

Some jetted AGN show radiatively efficient thin-disks down to the innermost circular stable orbit (ISCO) and the spin is not the only factor in determining radio-loudness of source, though it is unclear what determines it. Some disk models and simulations predict optically thick geometrically thin radiatively-efficient disks, which is different from Galactic black hole disks. While the black hole mass has implications for the observed luminosities, we also observe low luminosity AGN. These are associated with radiatively inefficient accretion flows.

### The broad and narrow line regions and the dusty torus

Broad emission lines are observed from AGN in the optical and UV band. They are a signature of dense material surrounding the black hole and have been extensively studied for more than 50 years. It is clear that the material is close to the accretion disk and surrounds the central engine (Done & Krolik, 1996). The origin and formation of the broad line region remains unknown, but might be due to in- and outflowing material from the accretion disk or torus (Czerny & Hryniewicz, 2011). It is expected to be broadened by the velocity of the clouds.

The narrow line region is further outside, producing narrow forbidden emission lines in a low-density medium. It is expected to be highly ionized. This region also occurs in biconical shapes, which are called "ionization cones". The origin and formation of the narrow line region is still unclear (Cracco et al., 2011). The velocities are expected to be low.

A dusty torus surrounds the broad line region, obscuring the view onto the central engine when the galaxy is viewed edge-on. These tori have been found to be clumpy (Krolik & Begelman, 1988, Nenkova et al., 2008, Markowitz et al., 2014, Beuchert et al., 2015). It is possible that they form due to radiative pressure from the accretion disk (Liu & Zhang, 2011). This is in agreement with a previous model, which suggest that the torus consists of expelled shells of gas, and only the outer edge is dusty (Lawrence, 1991).

## Jets

### Jet formation

Relativistic outflows of matter are observed from radio-loud AGN. These jets can be launched above the accretion disk and form in objects which accrete matter. A jet powered by extracting angular momentum from the black hole is called a Blandford-Znajek jet (Blandford & Znajek, 1977). In the Blandford-Znajek jet, the magnetic field lines are confined by the accretion disc. Frame-dragging in the ergosphere of a rotating black hole twists the magnetic field lines, possibly helically, collimating the outflow of material. The model for magneto-centrifugal launching of the jet, i.e., removing momentum magnetically, is called the Blandford-Payne process (Blandford & Payne, 1982). Jet launching may be possible in several ways: angular momentum can be transferred to a disk which drives a wind; a transient wind in the ergosphere; a relativistic outflow from the radial magnetosphere, or a strong Poynting outflow. It is possible that one black hole launches a jet differently at one point in time or during varying accretion flows. It is thought that this strongly influences the flux level seen from jets (Meier, 2012). Observations of the well-known Seyfert galaxy MCG-6-30-15 indicate that while no jet is visible, its Fe K $\alpha$  line is very broad and it shows strong reflection features. This might suggest that rotational energy is extracted and dissipated (Wilms et al., 2001). Numerous simulations of jet launching, collimation, and propagation have been performed (e.g., Gaibler et al., 2009, Tchekhovskoy et al., 2011, McKinney et al., 2012). Lately, the explanation of short and extreme variability in jets has been challenging theoretical models and simulations (Sikora et al., 2005). While the properties of the jet can be reproduced with various models at small scales, it is unknown how a jet can stay collimated over several kpc. The acceleration of particles in the jet is also unclear, although it is generally believed that shock acceleration is able to explain the observed velocities (Blandford & Königl, 1979).

### Jet structure

High-resolution VLBI methods can be used to resolve jet structures on parsec or sub-parsec scales (Müller et al., 2011), and some evidence of limb brightening suggesting a helical magnetic field or a spine-sheath structure of the jet has been found (Reid et al., 1989, Nagai et al., 2014). A spine-sheath jet has a fast spine and an outer, slower sheath (Sol et al., 1989, Tavecchio & Ghisellini, 2008). This model is able to explain the “Doppler factor crisis”, where different Doppler factors are observed from radio observations and from high-energy and very high-energy  $\gamma$ -ray data (Lyutikov & Lister, 2010). Evidence of recollimation shocks and star-jet interaction in VLBI data exist as well (Perucho, 2013, Müller et al., 2014b). Depending on the injection rate of new particles into the jet, the observed flux can vary. AGN jets have been observed to be variable on time scales of minutes to decades. It is unclear where this variability is originating. Variability on short time scales is assumed to originate close to the base of the jet, and while propagating outwards, moving to longer wavelengths (Marscher et al., 2008).

### The leptonic jet

We can not see the particles in the jet or trace their propagation. It is likely that the accreted gas injects electrons and protons into the jet, although it is unclear whether protons can be accelerated to ultrarelativistic energies due to their higher rest mass. Therefore, the jet composition is unknown. It is further not known whether “radio-quiet” AGN produce a jet that simply does not radiate.

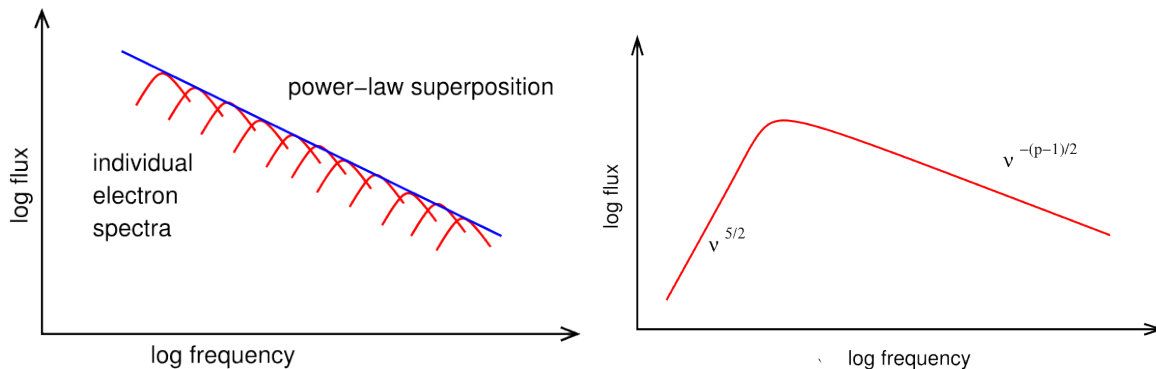


Figure 3.1.: *Left*: Emitted synchrotron spectrum (Figure: Wilms after Shu, 1991, Fig. 18.4), *Right*: Synchrotron self-absorption at low frequencies (Figure: Wilms after Shu, 1991, Fig. 18.6)

Electrons and positrons in a radio-loud AGN jet produce synchrotron radiation, which is observed from radio to X-ray energies (Schwinger, 1949, Alfvén & Herlofson, 1950). Synchrotron radiation is produced by accelerating relativistic, charged particles in a magnetic field (Ginzburg & Syrovatskii, 1965, Blumenthal & Gould, 1970, Rybicki & Lightman, 1979, Reynolds, 1982). In jets the electrons (and possibly protons) are gyrating in the magnetic field. This is also found in pulsar wind nebulae (Fleishman & Bietenholz, 2007) and supernova remnants (e.g., Auchettl et al., 2014). A relativistic particle with charge  $q$  and velocity  $v$  in a magnetic field  $B$  is described by

$$\gamma m \dot{\mathbf{v}} = \frac{q}{c} (\mathbf{v} \times \mathbf{B}). \quad (3.4)$$

This synchrotron emission has a dipole characteristic in the electron rest frame. When the jet is viewed at a small angle this dipole is observed to be Doppler boosted. The energy loss of the electron is

$$\left( \frac{dE}{dt} \right) = - \frac{e^4 B^2}{6\pi\epsilon_0 c m_e^2} \frac{v^2}{c^2} \gamma^2 \sin^2 \alpha. \quad (3.5)$$

In AGN, synchrotron radiation is mainly emitted by electrons with energies that follow a power law distribution

$$n(\lambda) d\lambda = n_0 \gamma^{-p} d\lambda, \quad (3.6)$$

which produces an electromagnetic power law spectrum through the superposition of the individual spectra with the spectral index  $\alpha = -(p-1)/2$  (see left panel of Fig 3.1). Synchrotron radiation at low energies is self-absorbed, resulting in a cut-off in the spectrum. Self-absorption is a process where electrons emitting synchrotron photons absorb the photons they produced (see right panel of Fig 3.1).

While the low-energy emission of jets is relatively well understood, the origin of the high-energy emission is unclear. The broadband spectrum shows a double humped structure in the  $\nu F_\nu$  (flux) representation, where the lower ‘‘bump’’ originates from synchrotron emission. The two possibilities for the origin of the high-energy peak are leptonic and hadronic models. While both leptonic and hadronic processes likely contribute to the emission, their relative contributions remain a deeply interesting open question (Abdo et al., 2011, Böttcher et al., 2013, Mannheim & Biermann, 1992, Finke et al., 2008, Sikora et al., 2009, Baloković et al., 2015, Weidinger & Spanier, 2015). Currently, hadronic and leptonic model can describe the observed broadband spectra equally well (Böttcher et al., 2013). In the leptonic scenario the relativistic electrons that

produce the synchrotron emission are assumed to up-scatter the photons to high energies. This process is called Synchrotron-Self Compton (SSC; Ghisellini et al., 1985, Maraschi et al., 1992, Bloom & Marscher, 1993, Ghisellini & Madau, 1996, Celotti et al., 1997). One-zone or two-zone SSC models can explain blazar spectra very well, although the emission is unlikely to stem from one single zone (e.g., Finke et al., 2008). Seed photons from the ambient medium, e.g. from the disk, broad line region/torus or the background light, can also contribute by being upscattered to gamma-ray energies (Sikora et al., 1994), this constitutes the External Compton (EC) contribution. It is further possible that the  $\gamma$ -ray emission is produced within the BLR, where broad line region photons are the seeds for the Inverse Compton scattering. This could explain the observed fast variability (Ghisellini & Tavecchio, 2010). Taking into account the anisotropies of the emission of the torus, the accretion disk, and the BLR, the ‘‘Compton rocket effect’’ is a further possibility which includes deceleration and acceleration along the jet, leading to variability that is produced further along the jet (Vuillaume et al., 2015).

### The hadronic jet and particle acceleration

In the hadronic scenario, protons and electrons are accelerated in the jet (e.g., Mannheim, 1993, Rachen & Mészáros, 1998, Atoyan & Dermer, 2001, 2003, Mücke & Protheroe, 2001, Mücke et al., 2003, Kelner & Aharonian, 2008, Dimitrakoudis et al., 2012, 2014, Böttcher et al., 2013). Proton acceleration occurs in blazar jets moving with bulk Lorentz factor  $\Gamma$ , thus avoiding pair attenuation above 511 keV. It is unclear how protons are accelerated, due to their higher rest mass, however shock acceleration processes are able to explain the observed energies (Fermi, 1949). In this processes a relativistic particle interacts with a turbulent magnetized plasma travelling in the opposite direction. If after multiple elastic scatterings it travels parallel to the cloud it gains the energy

$$\frac{E_1 - E_0}{E_0} = \gamma_{\text{cloud}}^2 (1 + \beta_{\text{cloud}})^2 - 1 \quad (3.7)$$

with

$$\beta_{\text{cloud}} = \frac{v_{\text{cloud}}}{c} \quad (3.8)$$

and

$$\gamma_{\text{cloud}} = (1 - \beta_{\text{cloud}}^2)^{-1/2} \equiv \eta \quad (3.9)$$

(Stanev, 2004). This is the second-order Fermi acceleration. In the more efficient first-order Fermi acceleration particles interact with a non-relativistic shock. If a relativistic particle crosses the shock front it gains energy, where  $\eta \propto \beta_{\text{shock}}$  (Longair, 2011). Another possibility for the acceleration of particles in jets is magnetic reconnection. Large amounts of energy are present in the magnetic fields close to the black hole. This energy can be dissipated and heats the plasma. Along the jet these lines can reconnect (Zenitani & Hoshino, 2001, de Gouveia Dal Pino et al., 2010, Sironi et al., 2015). It is possible that magnetic reconnection is able to explain ultra-high-energy cosmic rays (UHECRs), including the acceleration of heavy nuclei (Giannios, 2010).

If protons are accelerated, they are thought to interact with either other protons or photons, producing pions, which produces a hadronic cascade. If the pions are neutral they decay into two high-energy  $\gamma$ -rays

$$p + \gamma \longrightarrow \pi^0 + p \longrightarrow \gamma + \gamma + p \quad , \quad (3.10)$$

explaining the high-energy emission seen from jets (Mannheim & Biermann, 1989, 1992, Mannheim, 1993, Dermer & Schlickeiser, 1993, see Fig. 3.2). If a  $\pi^+$  or  $\pi^-$  is produced, it produces muons, positrons and neutrinos in a cascade via

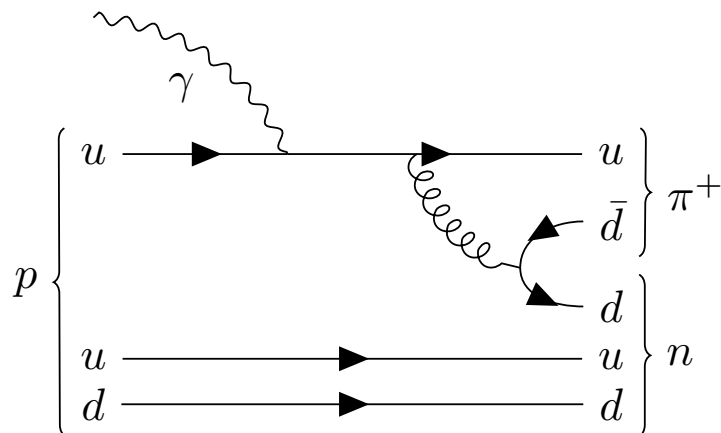


Figure 3.2.: Exemplary Feynman diagram of the interaction of a proton and a photon, producing a neutron and a  $\pi^+$ .

$$p + \gamma \longrightarrow \pi^+ + n + (\pi^- + \pi^+) \quad (3.11)$$

$$\pi^{+/-} \longrightarrow \mu^{+/-} + \bar{\nu}_\mu \quad (3.12)$$

$$\mu^+ \longrightarrow e^+ + \nu_e + \bar{\nu}_\mu \quad (3.13)$$

This effect is called pion photoproduction. The expected neutrinos would be an unambiguous tracer of hadronic processes in the jet. Associating a neutrino with an AGN would provide the required evidence and would further prove that AGN jets contribute to the flux of cosmic rays (Hillas, 1984). A further possibility is Bethe-Heitler pair production, where photon-proton interactions produce an electron-positron pair (Petropoulou & Mastichiadis, 2015). This process is expected to dominate at very high energies (Boettcher et al., 2012). Hadronic models have been updated to include time-dependence (Dimitrakoudis et al., 2012) and photon quenching (Petropoulou & Mastichiadis, 2012). Possible origins of the photon seed fields include UV photons from the accretion disk, torus, or BLR (Bednarek & Protheroe, 1999, Atoyan & Dermer, 2003, Fukugita & Suzuki, 2013). Another possibility that is often used to explain sources with weak jet and external radiation fields are the internal models, using the UV photons provided by the synchrotron emission. These models suggest a high contribution to the broadband SED from proton synchrotron processes (Mücke & Protheroe, 2001, Mücke et al., 2003). Neutrinos are assumed to be produced close to the jet base. As this would also be the site of high-energy  $\gamma$ -ray production, this poses the opacity problem. High-energy  $\gamma$  rays pair-produce in a dense environment. Such an environment is expected to be presented in the inner jet, and would not allow  $\gamma$ -rays to escape (Cavallo & Rees, 1978). This quenching of neutrinos has further implications for the observed variability at TeV energies. If the variability would have to be produced further down the jet, this would be in disagreement with the light-crossing distance  $c t_{\text{cross}}$  and suggests very high bulk Lorentz factors (Begelman et al., 2008).

In pion photoproduction the neutrino flux is expected to be related to the bolometric high-energy electromagnetic flux. In the following an electromagnetic flux has the symbol  $F$ , while particle flux has the symbol  $S$ . For the illustrative case of isospin symmetry (equal numbers of  $\pi^+$ ,  $\pi^-$ , and  $\pi^0$ ), it is possible to obtain an estimate of the neutrino flux. For the three neutrinos among the four light final-state leptons in charged pion decays  $S_\nu = 2/3 \cdot 3/4 \cdot S_\pi = 1/2 \cdot S_\pi$ , and the  $\gamma$ -ray flux after accounting for the conversion of electrons and positrons into  $\gamma$  rays by cascading,

Table 3.1.: The different types of AGN, sorted by radio-loudness and orientation

Radio property	Orientation	
	face-on	edge-on
radio-quiet	Seyfert I QSO	Seyfert II
radio-loud	Blazar BL Lac FSRQ/OVV BLRG	Radio galaxy FR I FR II NLRG

$F_\gamma = 1/3 \cdot S_\pi + 1/4 \cdot 2/3 \cdot S_\pi = 1/2 \cdot S_\pi$  giving  $S_\nu = F_\gamma$ . Monte-Carlo simulations confirm this simple estimate (Mücke et al., 2000). Neutrino oscillations establish full-flavor mixing across extragalactic distance scales, and therefore  $S_{b,\nu_e} = S_{b,\nu}/3 = F_{b,\gamma}/3$ . Electromagnetic cascades emerge from X-ray to  $\gamma$ -ray energies. In the jet's comoving frame (marked with primed quantities), the UV photons from the disk are redshifted ( $\epsilon' = \epsilon/\Gamma$ ) if they originate at the base of the jet, or blueshifted if they come from the outer parts of the disk or are scattered photons. Photoproduction of pions starts above the threshold energy  $E'_{p,th} = 2(\epsilon'/30 \text{ eV})^{-1}$  PeV. The neutrinos carry away  $\sim 5\%$  of the proton energy, implying a neutrino energy of  $E_\nu \sim 0.1\Gamma(\epsilon'/30 \text{ eV})^{-1}$  PeV in the observer's frame. For generic values  $\epsilon = 30 \text{ eV}$  and  $\Gamma = 10$ , the neutrino spectrum covers the energy range from 100 TeV to 10 PeV. Details of the spectrum, however, are subject to model assumptions.

### Unification of observational picture

Active galactic nuclei (AGN) are thought to be powered by supermassive black holes at their center, but how they are observed depends on their radio-loudness, and the inclination angle to the source. Fig. 3.3 shows the unification model after Urry & Padovani (1995). AGN can be separated into 2 types, according to their optical spectra. Type 1 AGN have broad and narrow optical emission lines, they are seen at a large angle to the plane of the accretion disk. Type 2 AGN lack the broad emission lines, and are seen at a small angle to the accretion disk (Peterson, 1997). Type 1 AGN allow for a direct view onto the black hole and the accretion disk, whereas type 2's view of the center is obscured by a dust torus. These dust torii are thought to be clumpy (Netzer, 2015, see Sect. 3.3.4). The unified model shows that Seyfert galaxies, QSO's, quasars and blazars are all the same type of galaxy, observed under different viewing angles (Urry & Padovani, 1995). I summarize the different types of AGN in Table 3.1. This thesis focuses on radio-loud AGN, and blazars in particular.

### Blazars

A subset of AGN, the radio-loud AGN, exhibit jets which are outflows of matter, perpendicular to the accretion disk. Objects where the angle between the line of sight and the jet is small, are called blazars, and are of particular interest in this work. Blazars in general are characterised by their high luminosity which originates in Doppler boosting, as well as a nonthermal spectrum showing rapid variability. Variability can occur on time scales between minutes to several months or even decades. The word Blazar was coined by E. Spiegel in 1978 as a joke, combining the words quasar and 'blazing', emphasizing the strong and rapid variability.

Blazars can be further subdivided into flat-spectrum radio quasars (FSRQs) and BL Lacertae

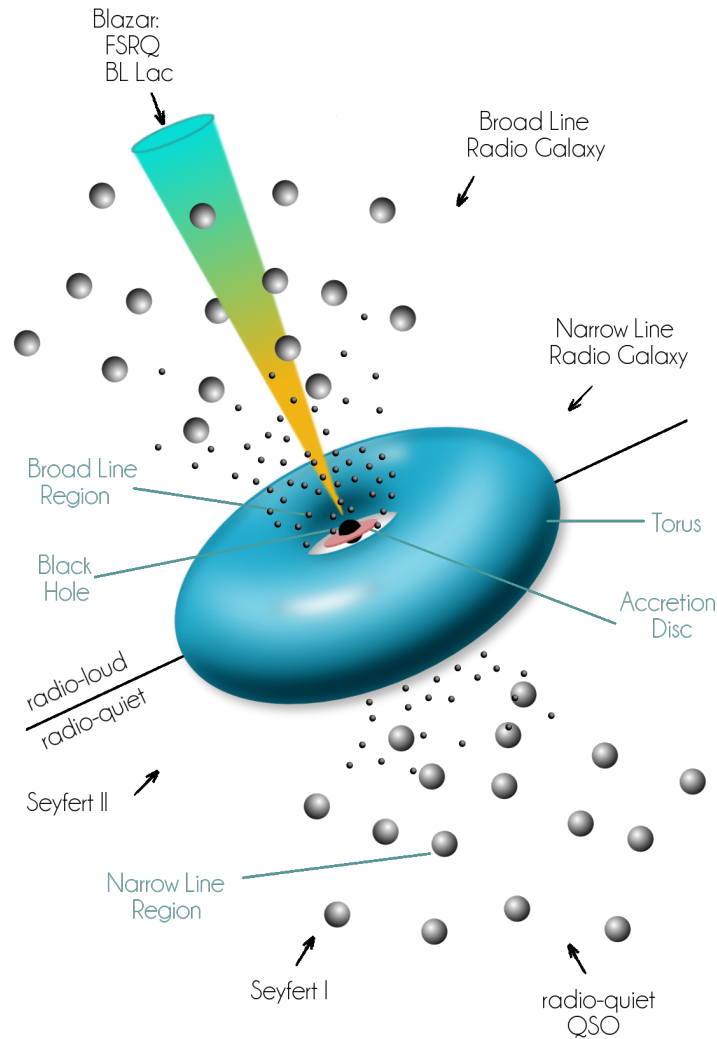


Figure 3.3.: Unified model showing the radio-loud (top) and radio-quiet (bottom) case. The center consists of a supermassive black hole with an accretion disk. This center is surrounded by a torus, a broad line region, and a narrow line region. Figure after Urry & Padovani (1995).

(BL Lac) objects. BL Lacerta was likely the first blazar that was discovered (Hoffmeister, 1929). FSRQs show broad emission lines in the optical waveband (rest-frame equivalent width  $> 5\text{\AA}$ ), while BL Lacs typically show none or only a few. Well known exceptions include OJ 287 (Sitko & Junkkarinen, 1985) and BL Lac (Vermeulen et al., 1995). Blazars can also be categorized by their synchrotron peak frequency in the  $\nu F_\nu$  representation into low, intermediate and high synchrotron peaked blazars (LSP, ISP, HSP; Padovani & Giommi, 1995, Abdo et al., 2010a), with the ISP blazar peak between  $10^{14}$  Hz and  $10^{15}$  Hz.

### Broadband spectra of blazars

The study of the broadband spectral energy distributions (SEDs) of blazars allows a direct view into the jet and its emission mechanisms. The nonthermal continua of blazars are generally power

laws with their photon flux

$$F_\nu = C \cdot \nu^{-\alpha} \quad (3.14)$$

with the normalization  $C$  and the spectral index  $\alpha$ . The photon index is  $\Gamma = \alpha + 1$ ,

$$F_\nu = \nu^{-\Gamma+1} \quad (3.15)$$

and

$$\nu F_\nu = \nu^{-\Gamma+2}. \quad (3.16)$$

The  $\nu F_\nu$  flux spectrum (in units of erg/s/cm<sup>2</sup>) is therefore roughly constant, which suggests that the same amount of energy is emitted per frequency decade. The spectra are not perfect power laws and show two humps in a  $\log \nu$  vs.  $\log \nu F_\nu$  representation of the spectrum. The left hump is due to synchrotron emission, produced by electrons that are accelerated in the jet. It typically spans from radio to X-ray frequencies. While both leptonic and hadronic processes likely contribute to the high-energy peak, their relative contributions remain an open question (Abdo et al., 2011, Böttcher et al., 2013, Mannheim & Biermann, 1992, Finke et al., 2008, Sikora et al., 2009, Baloković et al., 2015, Weidinger & Spanier, 2015). For details of emission processes in jets see Sect. 3.3.5.

AGN jets carry a fraction of the total gravitational energy released during the accretion of matter onto supermassive black holes. If observed at a small angle to the line of sight, the emission becomes relativistically boosted, so the source is classified as a blazar. While the spin might have an influence on jet formation, i.e., rapid spin may be necessary but not sufficient. Doppler boosting is described by the relativistic aberration

$$\cos \Theta_0 = \frac{\cos \Theta_s - \frac{v}{c}}{1 - \frac{v}{c} \cos \Theta_s}$$

with a source moving with velocity  $v$  at angle  $\Theta_s$  in the observer's frame of reference. This relativistic Doppler effect describes the change in observed brightness due to these effects. The intrinsic luminosity  $L_s$  is boosted and for a power law the observed luminosity becomes

$$L_0 = L_s \cdot \delta^{3-\alpha},$$

with the Doppler factor  $\delta$  and the spectral index  $\alpha$ . The Doppler factor is given by  $\delta = (\Gamma(1 - \beta \cos \Theta))^{-1}$ . The relativistic aberration contributes a  $\delta^2$  factor, while the time dilation contributes a  $\delta$ , and the Doppler effect a  $1/\delta^\alpha$ .

### Variability of blazars

AGN, and especially blazars, are variable in flux at all wavelengths. Due to their compact nature (a few parsecs) a variation time scale can be estimated by the light crossing time

$$r_{\max} = c \cdot \Delta t \quad (3.17)$$

with the variation time  $\Delta t$ . Surprisingly, in a few objects at high angles between the jet and the line of sight, variation has been seen on time scales that are equivalent to a region much smaller than the event horizon (Aleksić et al., 2014a). Variability in AGN can possibly be explained by comparing them to Galactic black holes and the transitions observed in these objects. Disk instabilities could lead to a growth of the central disk part which could lead to an injection of matter into the jet (observed in the radio). Then the disk would be refilled and the cycle continues. Some quasi-period oscillations have been observed in blazars (Ackermann et al., 2015a). This variability requires quasi-simultaneous data in order to study the broadband behavior of these sources in detail.

### The big blue bump

FSRQs usually have an additional thermal excess in the optical-UV range with a temperature of  $\sim 30000$  K (Sanders et al., 1989, Elvis et al., 1994). This is called the “big blue bump” (BBB), and is described as a broad peak, as expected from an accretion disk with a wide range of temperatures (Shields, 1978, Malkan & Sargent, 1982). The BBB is therefore often assumed to be thermal emission from the accretion disk. This is an appealing theory, as FSRQs are the more luminous objects, which are expected to have a higher accretion rate, and a stronger thermal emission from the accretion disk. The origin of the BBB is disputed (Antonucci, 2002). Some authors argue for it to stem from the accretion disk (Shields, 1978, Malkan & Sargent, 1982), alternatively, free-free emission has been proposed (Barvainis, 1993). The observed temperature of the feature, however, is lower than what is expected from an accretion disk (Zheng et al., 1997, Telfer et al., 2002, Binette et al., 2005). The origin of the BBB could be reprocessed accretion disk emission from clouds in the broad line region (BLR; Lawrence, 2012).

# Observational data and analysis

Many astronomers believe that CCDs are complicated, almost magical devices that are beyond their comprehension.

---

Mackay (1986): *Charge-coupled devices in astronomy*

## Observational data

In the previous chapters I have shown that AGN jets emit across the electromagnetic spectrum, from the radio band to the very high energies. To understand the processes concerning the jet- from the jet launching to its acceleration and confinement, it is necessary to study the multiwavelength and the multimessenger picture. The electromagnetic spectrum covers many orders of magnitude. The opacity of Earth's atmosphere is not constant across the spectrum. While optical light reaches the surface of the Earth and allows us to see sunlight during the day, and starlight at night, high energy photons at X-ray and  $\gamma$ -ray energies are absorbed in the atmosphere. High-energy astronomy therefore requires instruments above the atmosphere. An exception to this are Cherenkov telescopes (e.g., the H.E.S.S., MAGIC, and VERITAS telescopes, and the planned Cherenkov Telescope Array; CTA), which detect photons at very high energies indirectly. These photons (above  $\sim 100$  GeV) produce cascades in the atmosphere, and traveling faster than the speed of light in the medium, emit optical Cherenkov light. However, many other instruments must be placed above the atmosphere. The active galaxies that we study emit across the whole electromagnetic spectrum, and observing them therefore requires a multitude of instruments on the ground and above the atmosphere.

One difficulty is immediately obvious, due to the variable nature of AGN. The observations should be performed simultaneously in time. This is often not feasible as satellites are constrained in their possible targets; e.g., by the proximity of the source to the Sun, Moon or Earth while ground-based telescopes (e.g., optical) can only observe during cloudless nights on Earth. This constraint is not true for radio telescopes, which can observe during the day. Coordinating not only two, but more than four or five instruments is required and inherently challenging. Data of this quality is non-existent for the majority of all sources. Only for a small number of sources (e.g., Mrk 501, Mrk 421, 3C273, and 3C279) have extensive simultaneous multiwavelength campaigns been organized (Lichti et al., 1995, von Montigny et al., 1997, Kataoka et al., 1999, Tagliaferri et al., 2008, Abdo et al., 2011, Aleksić et al., 2013, Dutka et al., 2013, Aleksić et al., 2015), and Hayashida et al. (2015).

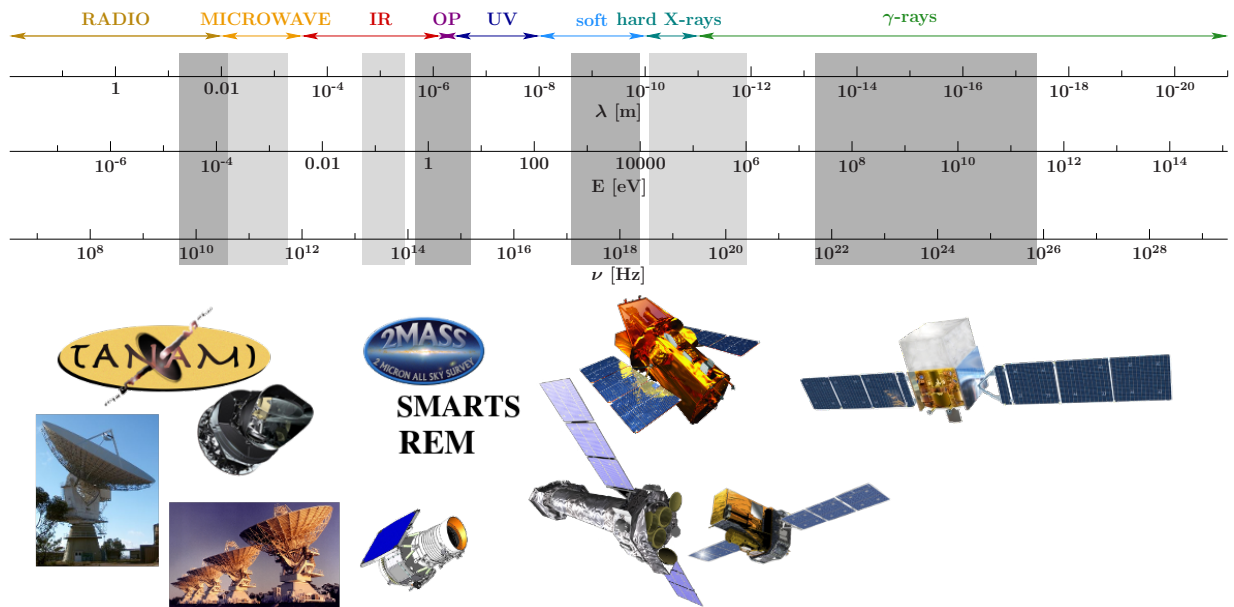


Figure 4.1.: *Top*: Electromagnetic spectrum showing the energy, wavelength, and frequency range from radio to  $\gamma$ -ray energies, as well as spectral coverage (dark gray) and additional non-simultaneous archival data (light gray). *Bottom*: Instruments corresponding to the shaded areas in the top panel; image credit: ATCA (CSIRO), Ceduna (<http://www.phys.utas.edu.au/physics/Ceduna.html>), *Planck* (ESA/NASA/JPL-Caltech), *WISE* (NASA/JPL), 2MASS (2MASS/UMass/IPAC-Caltech/NASA/NSF), *Swift* (Aurore Simonnet, NASA E/PO, Sonoma State University), *XMM* (ESA), *INTEGRAL* (ESA), *Fermi* (Aurore Simonnet, NASA E/PO, Sonoma State University).

## TANAMI

Tracking Active Galactic Nuclei with Austral Milliarcsecond Interferometry (TANAMI<sup>1</sup>) is a multiwavelength program monitoring a sample of extragalactic jets on the southern hemisphere (below  $-30^\circ$  declination) since 2007, complementary to the MOJAVE project on the northern hemisphere (Lister & Homan, 2005). The initial sample of 43 sources (Ojha et al., 2010) has been expanded to more than 90 sources since the launch of *Fermi* in 2008 (Kadler et al., 2015b). This sample, which consists of radio and  $\gamma$ -ray selected sources, is monitored at VLBI frequencies every  $\sim 4$  months at 8.4 and 22.3 GHz. Additional monitoring is performed by the Australian Telescope Compact Array (ATCA) at frequencies between 4.8 and 40 GHz. This is complemented by single-dish observations by the Ceduna telescope. At higher energies several successful proposals ensure good data coverage: a REM proposal (optical), two *Swift* fill-in programs (optical/UV, and X-rays), as well as a guest observer program with *Fermi*-LAT. TANAMI is also working together closely with the ANTARES collaboration in order to understand the origin of high-energy cosmic rays. For details on the collaboration and the first project see Müller (2014). A second project is discussed in Chapter 7.

Figure 4.1 shows the coverage of the electromagnetic spectrum that is used in this thesis. Simultaneous data are shown in dark gray, while additional archival data are marked in light gray. The corresponding instruments are shown below the spectrum. We use radio data from VLBI observations (see Sect. 4.10), ATCA, and Ceduna telescopes. Infrared to ultraviolet data

<sup>1</sup><http://pulsar.sternwarte.uni-erlangen.de/tanami/>

are taken from the SMARTS monitoring program, REM data that has been obtained with a TANAMI proposal, and the *Swift* and *XMM* satellites (see Sect. 4.4, and 4.5), which both have optical, UV, and X-ray capabilities. This is complemented in the  $\gamma$ -rays by *Fermi*-LAT data (see Sect. 4.7.1). No instruments in the MeV energy range are currently sensitive enough for time resolved spectroscopy of blazars. Archival data are added to the broadband spectra using *Planck*, 2MASS, *WISE*, and *INTEGRAL* data.

In this Chapter, I introduce the telescopes, satellites, and instruments used in this thesis. I also explain the data reduction and extraction processes. In the following Chapter I explain how these data are used to compile broadband SEDs. Many of the methods used for data reduction and analysis have already been described in my Master's thesis (Krau, 2013). For completeness I discuss the important satellite specifications, methods of data reduction, and analysis again and use some of the parts in verbatim.

## X-ray astronomy

### Introduction

Earth's atmosphere is opaque to photons above ultraviolet wavelengths, due to photoabsorption by oxygen molecules (Longair, 2011). The US Naval Research Laboratory (NRL) began researching the ionosphere in the 1920s to explore the possibility of short wave communication (Butrica, 1997). In the 1940s, a V2 rocket was launched to measure solar X-rays using only a Geiger counter. Twenty years later Riccardo Giacconi and Bruno Rossi searched for fluorescent X-rays from the Moon. This failed, but instead they detected a very bright X-ray source in the constellation Scorpius, later renamed Scorpius X-1 (Giacconi et al., 1962, 1964). The first X-ray satellite *UHURU* was launched in 1970 and discovered many bright X-ray sources (Jagoda et al., 1972, Forman et al., 2012). Several satellite missions followed soon afterwards. The *ROSAT* satellite was launched in 1990 and performed a survey of the whole sky (Truemper, 1982). The ROSAT All Sky Survey (RASS) is a large source catalog with  $\sim 120000$  X-ray sources (Voges et al., 1999). Only the very recent source catalog by *XMM-Newton* includes a larger number of sources (Watson et al., 2008). Currently there are several X-ray and  $\gamma$ -ray missions, including *Swift*, the *X-ray Multi-Mirror Mission-Newton* (*XMM-Newton*), *Suzaku* (Mitsuda et al., 2007), the *Chandra X-ray observatory* (Weisskopf et al., 2000), the *International Gamma-Ray Laboratory* (*INTEGRAL*), *AGILE* (Tavani et al., 2009), and *Fermi*.

In the following Section I give a brief description of the instruments of X-ray astronomy that I used, the optics and detectors following Bradt (2004), Aschenbach (1985), Janesick (2001) and Lutz (2001).

### Wolter telescopes

Current optical telescopes usually consist of two parabolic mirrors, the primary and the secondary mirror, which reflect the incoming light to a focal point. Snell's law describes the angles of incident in relation to the refractive index of two media (Aschenbach, 1985, Wolf & Krotzsch, 1995, Rashed, 1990),

$$\frac{\sin \alpha_1}{\sin \alpha_2} = \frac{n_2}{n_1} = n. \quad (4.1)$$

For total reflection ( $\alpha_2 = 90^\circ$ ) the refractive index  $n$  has to be greater than one. The index of

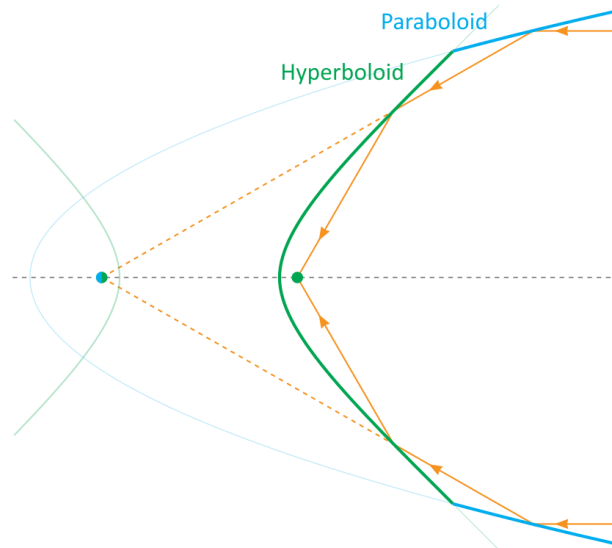


Figure 4.2.: Wolter type I schematic, showing the decrease in focal lengths by adding a hyperboloid to the paraboloid (after <https://lp.uni-goettingen.de/get/text/7272>).

refraction is given by the dielectricity constant,  $\epsilon$  and the permeability of the material,  $\mu \sim 1$ ,

$$n = \sqrt{\epsilon\mu}. \quad (4.2)$$

With the dielectricity constant for free electrons (Jackson, 1981) the critical angle for X-ray reflection is

$$\Theta_c = 5.6' \left( \frac{\rho}{1 \text{ g cm}^{-3}} \right)^{1/2} \cdot \frac{\lambda}{1 \text{ nm}}. \quad (4.3)$$

For X-ray wavelengths ( $\lambda \sim 1 \text{ nm}$ ) the critical reflection angle is  $\Theta_c \sim 1^\circ$ . The dielectricity constant is dependent on the atomic number  $Z$  and can be increased by using materials with a high density. Typically, gold and iridium are the materials of choice (e.g., iridium was used for the *Chandra* mirrors and gold for the *XMM-Newton* mirrors). This type of mirror is known as a “grazing incidence telescope”, due to the reflection of photons at small angles.

Paraboloids focus X-rays very well, but the focal lengths are not easily manageable due to limited rocket length. In a Wolter telescope, paraboloids are combined with hyperboloids to shorten the focal lengths to below  $\sim 10 \text{ m}$ . X-ray photons are thus reflected twice (Fig. 4.2). This mirror configuration is named after Hans Wolter, who invented the first Wolter mirror (Wolter, 1952a,b). To increase the effective area of the mirrors, several mirror shells are nested (Fig. 4.3).

Another possibility is the use of an extendable satellite. The Nuclear Spectroscopic Telescope Array (NuSTAR) launched in 2012 with a stowed mast, which successfully extended to its full length (10 m) after reaching its orbit (Harrison et al., 2013).

The X-ray photons focused by the mirror module can be detected by a charge-coupled device (CCD). X-ray CCDs are described in the following Section.

### X-ray charge-coupled devices (CCD)

X-ray CCDs are in principal the same as optical CCDs, however, they require a larger detector volume, due to the higher energies and subsequently larger penetration depths of the photons.

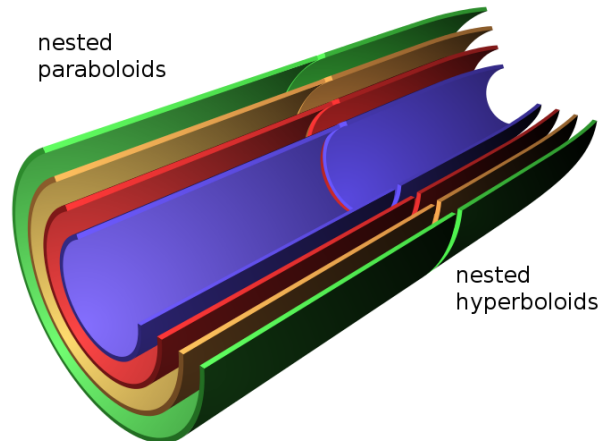


Figure 4.3.: Wolter type I schematic, showing the increase in area by nesting several mirrors (after <https://lp.uni-goettingen.de/get/text/7272>).

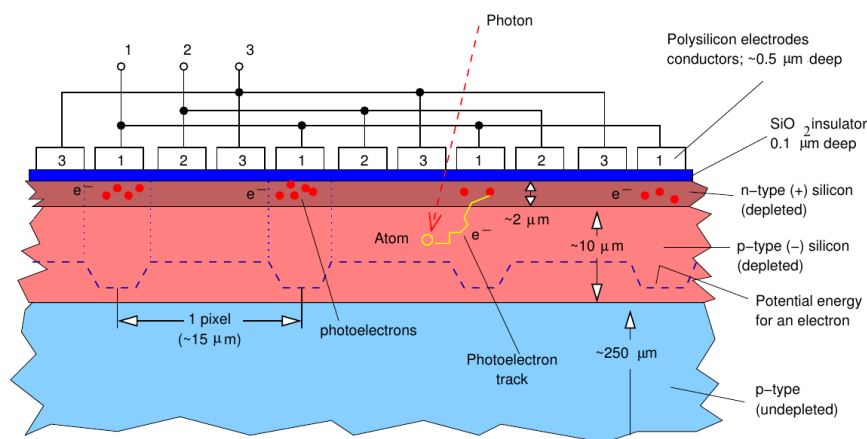


Figure 4.4.: Structure of a X-ray CCD during exposure, an incident X-ray photon (red) excites electrons, which are accumulated in potential wells and read out with three phased  $\phi$  pulses (Wilms after Bradt, 2004).

The structure of a X-ray CCD is shown in Fig. 4.4. CCDs are solid state devices and consist of a fully depleted pn-junction on a non-depleted p-type layer. The base material is usually silicon doped with phosphorus or boron (Lutz, 2001). Incident X-ray photons excite several thousand electron-hole pairs in the silicon. Contrary to optical CCDs ‘full well’ (a completely filled potential well; pixel) is reached much faster and X-ray CCDs are read out continuously. This enables us to identify individual photons and their corresponding energy. A full readout cycle is of the order of 2 seconds. For sources with count rates higher than 1 photon/2 seconds/pixel pile-up occurs. More than 1 photon hits a potential well (pixel) and the combined energies are read out. Many instruments have different read out mechanisms for brighter sources such as “small window mode” for the EPIC-pn CCD on board *XMM-Newton* or the “windowed timing mode” on board *Swift* to avoid the occurrence of pile-up. In this mode only a small part of the CCD is read out, decreasing the read out time.

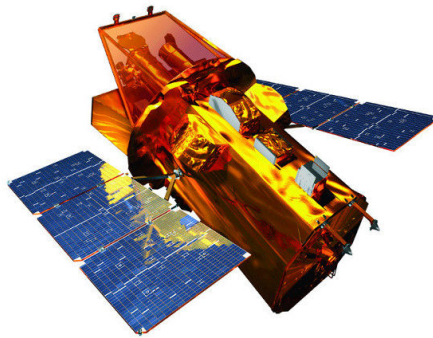


Figure 4.5.: The *Swift* satellite (NASA E/PO, Sonoma State University, Aurore Simonnet).

### *Swift Gamma-Ray Burst mission*

The *Swift* Gamma-Ray Burst mission was launched on 2004, November 20 into a low Earth orbit (see Fig. 4.5). It is managed by the NASA Goddard Space Flight Center. *Swift*'s main mission is to detect and observe gamma-ray bursts (GRBs) and perform follow-up observations at optical, ultraviolet and X-ray wavelengths (Gehrels et al., 2004). The name originates from its fast slewing capabilities that are required for observing the faint X-ray and optical afterglow of GRBs. *Swift*'s main goals are to determine the origin of  $\gamma$ -ray bursts and to thus study the evolution of the early universe.

With  $\sim 90$  GRBs/year<sup>2</sup>, the majority of time is spent observing non-GRB sources. *Swift* has a Guest Investigator Program, a Target of Opportunity (ToO) program as well as a Fill-In program. The Target of Opportunity program has a limited amount of time for the observation of non-GRB events. This includes transient events such as supernovas, pulsar outbursts and blazar flares. The Fill-In program allows us to request time for a large number of sources, which are used to fill gaps between observations or between large slewing angles. TANAMI sources are observed with *Swift* as a part of the Fill-In program. *Swift*'s three instrument are the Ultraviolet and Optical Telescope (UVOT), the X-ray Telescope (XRT) and the Burst Alert Telescope (BAT).

### The X-Ray Telescope, reduction and analysis

The X-Ray Telescope (XRT) on board *Swift* was designed and built to measure light curves, spectra, and fluxes of the X-ray afterglow of GRBs. *Swift*'s X-Ray Telescope consists of a grazing incidence Wolter type-I mirror module with 12 concentric gold-coated mirrors and a EEV CCD-22 in the focal plane.

The CCD was originally designed for the *XMM-Newton*/MOS instruments (see Sect. 4.5). It is a front illuminated three-phase frame-transfer device, which uses high-resistivity silicon and an open-electrode structure (Holland et al., 1996). Further details about construction, calibration, and performance of the X-ray telescope can be found in Burrows et al. (2000), Hill et al. (2000), Burrows et al. (2004), Hill et al. (2004), Burrows et al. (2005), Short et al. (2003), Osborne et al. (2005), Moretti et al. (2005), Romano et al. (2005), Pagani et al. (2007), Godet et al. (2009), and Cusumano & XRT Calibration Team (2006). A short summary of the performance, including typical calibration problems such as stray light, bright Earth, pile up, optical loading, and damage due to micrometeoroids is discussed by Krauß (2013).

---

<sup>2</sup>[http://swift.gsfc.nasa.gov/archive/grb\\_table/](http://swift.gsfc.nasa.gov/archive/grb_table/)

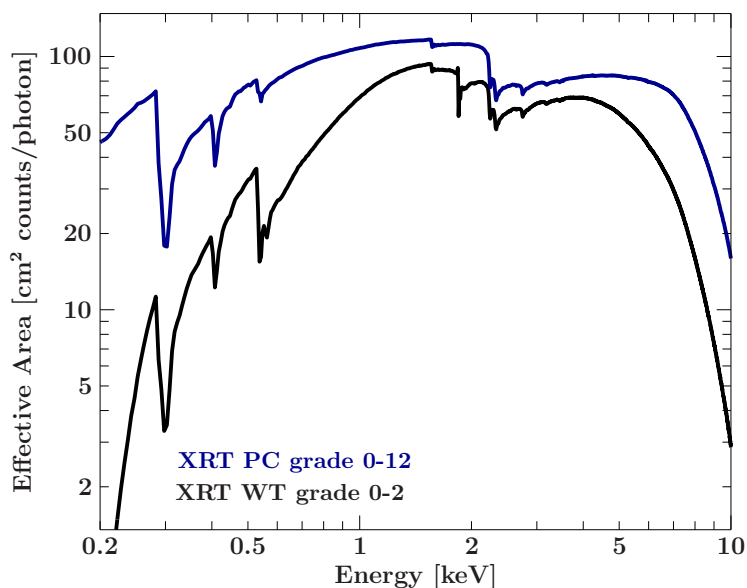


Figure 4.6.: Ancillary response function (ARF, effective area) of the XRT, for photon counting and windowed timing mode for the observation ID 00030795028.

Reduction of *Swift*/XRT data was done using scripts that were written by Laura Barragán and Jörn Wilms. The steps of the extraction pipeline are described in detail in the *Swift* User's guide<sup>3</sup> and summarized in Krauß (2013). After applying the newest calibration to the data, the source and background counts are extracted from a circle and annulus around the source coordinates. The source region was usually 80'' in radius, and the background region an annulus around the source with radii of 110'' and 165''. Source counts from these regions are stored in event files. Then `xrtmkarf` is run to generate the ancillary response function, sometimes called the effective area, for the source position and extraction region. The black line in Figure 4.6 shows the ARF of the grade 0-2 selection of the windowed timing mode and the blue line for the grade 0-12 selection in the photon counting mode. For *Swift*/XRT the effective area consists of the mirror area, the quantum efficiency of the CCD and the filter transmission. The QE is included in the RMF, while the ARF consists of the other two (Romano et al., 2005).

The effective area is not constant over the whole energy range. At high energies ( $> 10$  keV) the reflectivity of the mirror decreases. At low energies ( $< 0.5$  keV) it is limited by the quantum efficiency of the CCD. Additional features in the area, such as 0.54 keV edge are due to transitions of the materials used for the mirrors or the CCD. The 0.54 keV feature is an oxygen transition in the surface of the detector. A silicon K-edge is visible at 1.84 keV. The prominent edges at 2.2-3.425 keV are due to a change in the reflectivity at the Au M-edge of the mirrors (Fraser et al., 1994, Owens et al., 1996, 1997).

Figure 4.7 represents the Redistribution Matrix Function (RMF) of the XRT for the photon counting as well as the windowed timing mode. The RMF is a matrix that maps the channels, which are numbered and in units of Pulse Height Analysis (PHA) or Pulse Invariant (PI) to the corresponding energy. It also distributes (in an ideal case) the detected photons to the energies that they had before arriving at the detector. Figure 4.7 shows that the highest probability of input energy is at the detected energy. However, there is also clear 'escape peak' at 2 keV below

<sup>3</sup>[http://swift.gsfc.nasa.gov/analysis/xrt\\_swguide\\_v1\\_2.pdf](http://swift.gsfc.nasa.gov/analysis/xrt_swguide_v1_2.pdf)

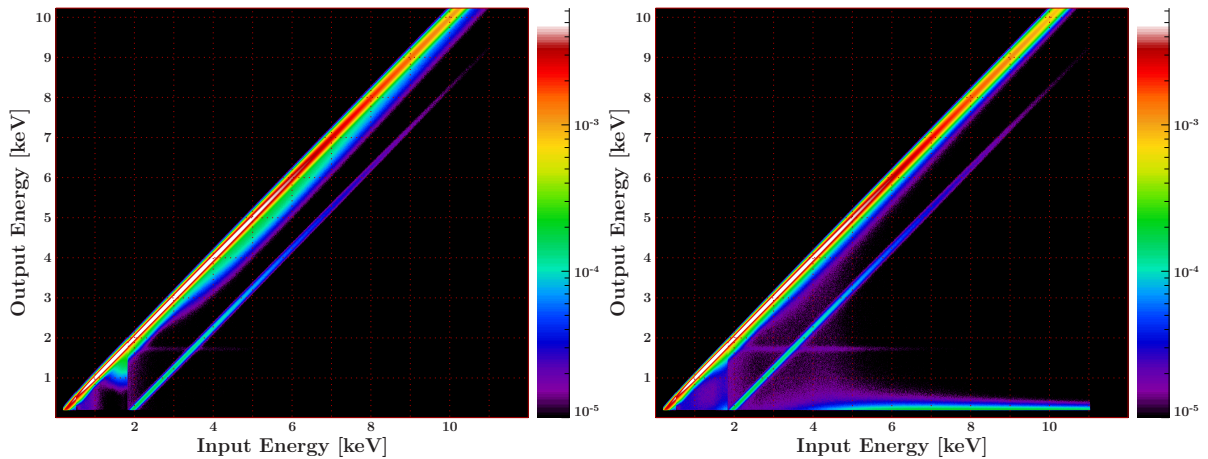


Figure 4.7.: Redistribution Matrix Function (RMF) of the XRT for the photon counting (left) and the windowed timing mode (right) showing the probability of the true energy of the photon energy dependent on the detected energy.

the original photon energy. This is due to the escape of a fluorescence photon from a K-shell transition. A Compton shoulder is also visible at energies below 2 keV and it is stronger in the windowed timing mode.

For the further analysis of the data, the information from the source and background counts, the RMF and the ARF are used in combination. In order to understand the intrinsic source spectrum – not the detected source spectrum – it is crucial to understand the detector; the calibration has to be extremely good to measure source properties such as the spectral shape, absorption, or fluxes. Instead of correcting for the calibration as a first step, the fit model is folded through the detector response and fit to the data. This allows us to see strange features in the spectrum and identify whether they are related to the source or the calibration. It is also obvious that this way of accounting for the detector calibration is independent of the source that is observed. For more details on the methods see Sect. 5.1.

### The Burst Alert Telescope

The Burst Alert Telescope (BAT) on board *Swift* is monitoring a third of the sky in order to detect and localize a GRB (with an accuracy of 1-4 arcminutes). The detection of a transient event triggers an autonomous slew of the spacecraft to the burst for follow-up observations of all *Swift* instruments, occasionally disrupting other observations. The BAT is a coded mask detector with 52,000 pieces of lead in the coded mask, as well as 32,768 pieces of CdZnTe in the detector plane. In between triggers due to Gamma-ray bursts, the Burst Alert Telescope is performing an all-sky hard X-ray survey (in the 14-195 keV band) with a sensitivity of  $\sim 2$  mCrab which allows quick follow-up observations and studies of transient sources (Barthelmy et al., 2005). In this thesis BAT data from the 104-month catalog (Baumgartner et al., 2014) were used. A short summary can also be found in Krauß (2013).

### The X-ray Multi-Mirror Mission

The X-ray Multi-Mirror Mission (XMM-Newton) was launched 1999, December 10 (Jansen et al., 2001). It consists of 3 imaging detectors on the European Photon Imaging Camera (EPIC), the

pn, and 2 MOS (Metal-Oxide-Semiconductor) cameras. Additionally, there are two gratings instruments, the Reflection Grating Spectrometer (RGS) with two cameras. The *XMM-Newton* also has includes an optical CCD (optical monitor; OM). For a more detailed description see Jansen et al. (2001), Kreikenbohm (2013), and Leiter (2013).

## INTEGRAL

The *INTErnational Gamma-Ray Astrophysics Laboratory (INTEGRAL)* was launched on 17 October, 2002 and has 4 instruments (Winkler et al., 2003). The IBIS imager consists of the ISGRI (energy range between 15 keV and 1 MeV), and the PICsIT (energy range up to 10 MeV; Ubertini et al., 2003, Lebrun et al., 2003, Labanti et al., 1996). The second instrument is the SPI, the spectrometer that observes between 20 keV and 8 MeV (Vedrenne et al., 2003). The JEM-X instruments provides lower energy coverage at 3 to 25 keV (Lund et al., 2003). INTEGRAL also has an optical monitor (OMC), in the 500 to 580 nm wavelength range (Mas-Hesse et al., 2003). A summary of the instrument and the analysis can be found in Grinberg (2013).

## Gamma-ray astronomy

In this Section I will introduce the instruments and methods of  $\gamma$ -ray astronomy used in this thesis, in particular the *Fermi* satellite. More details can be found in Atwood et al. (2009), Meegan et al. (2009), Böck (2012). Some parts have been taken in verbatim from Krauß (2013).

### *The Fermi Gamma-ray Space Telescope*

The *Fermi Gamma-ray Space Telescope* satellite was launched on 2008, June 11 on board a Delta-II rocket from Cape Canaveral. In 2008 August the name of the satellite was changed from *Gamma-ray Large Area Telescope (GLAST)* to *Fermi Gamma-ray Space Telescope*, honoring the work of Enrico Fermi. The instruments on board *Fermi* are the Large Area Telescope (LAT) and the Gamma-ray Burst Monitor (GBM). The aims of *Fermi* are to explore the most extreme environments, to search for the composition of dark matter, to explain how black holes accelerate jets, to study gamma-ray bursts, and to answer long-standing questions about various objects such as pulsars, cosmic rays and solar flares.

The Gamma-ray Burst Monitor (GBM) is designed to detect and study  $\gamma$ -ray bursts and transient sources. Most observations of GRBs before *Fermi* have been performed at energies below 1 MeV. The goal of the GBM is to study GRBs at higher energies (Meegan et al., 2009).

### Large Area Telescope (LAT)

*Fermi's* primary instrument is the Large Area Telescope (LAT). It is a wide field-of-view high energy  $\gamma$ -ray pair production telescope (Atwood et al., 2009). It is able to cover the whole sky in 3 hours and is thus ideal for monitoring sources. A preliminary analysis of the brightest sources is available online<sup>4</sup>.

The *Fermi*/LAT is a pair conversion telescope, converting a high-energy photon into an electron-positron pair. It is necessary to distinguish between  $\gamma$ -rays and cosmic rays – consisting mainly of protons – because the flux of the latter is 5 orders of magnitude larger. Charged particles are vetoed in the first layer, an anticoincidence shield. However, showers caused by  $\gamma$ -ray events can cause a signal in the anticoincidence shield.

<sup>4</sup>[http://fermi.gsfc.nasa.gov/ssc/data/access/lat/msl\\_lc/](http://fermi.gsfc.nasa.gov/ssc/data/access/lat/msl_lc/)



Figure 4.8.: The *Fermi* Gamma-ray Space Telescope shortly before launch with the Large Area Telescope at the top, and the Gamma-ray Burst Monitor at the left bottom side of the instrument. The solar panels are folded at the side. (NASA, DOE)

After the first layer, incident photons (and protons) pass through thin layers of materials with a high atomic number, called conversion foils. The trajectories of the newly generated electron-positron pair is traced in a tracker and calorimeter. A typical  $\gamma$ -ray signature has no signal in the anti-coincidence shield, more than one trajectory in the tracker and an electromagnetic shower in the calorimeter. The tracking detector consists of 18 layers of silicon strip detectors and the calorimeter consists of eight layers of 12 CsI bars in each tower, read out by photodiodes. The CsI crystals are oriented perpendicular to the crystals in the following layer. Due to the segmentation in the calorimeter it is possible to reconstruct the direction of the incident photon, as well as image the profile of the shower, which enables the rejection of background events (Atwood et al., 2009). Figure 4.9 shows the Hammer projection of the *Fermi*/LAT 5-year sky map in galactic coordinates. The Galactic plane is visible, as well as many extragalactic sources. Many bright blazars are marked and labeled.

### *Fermi*/LAT data extraction

The *Fermi*/LAT team provides the *Fermi*/LAT Science tools and calibration. The software is available online<sup>5</sup>. The reduction of the data requires an event file, a spacecraft file, and a

<sup>5</sup><http://fermi.gsfc.nasa.gov/ssc/data/analysis>

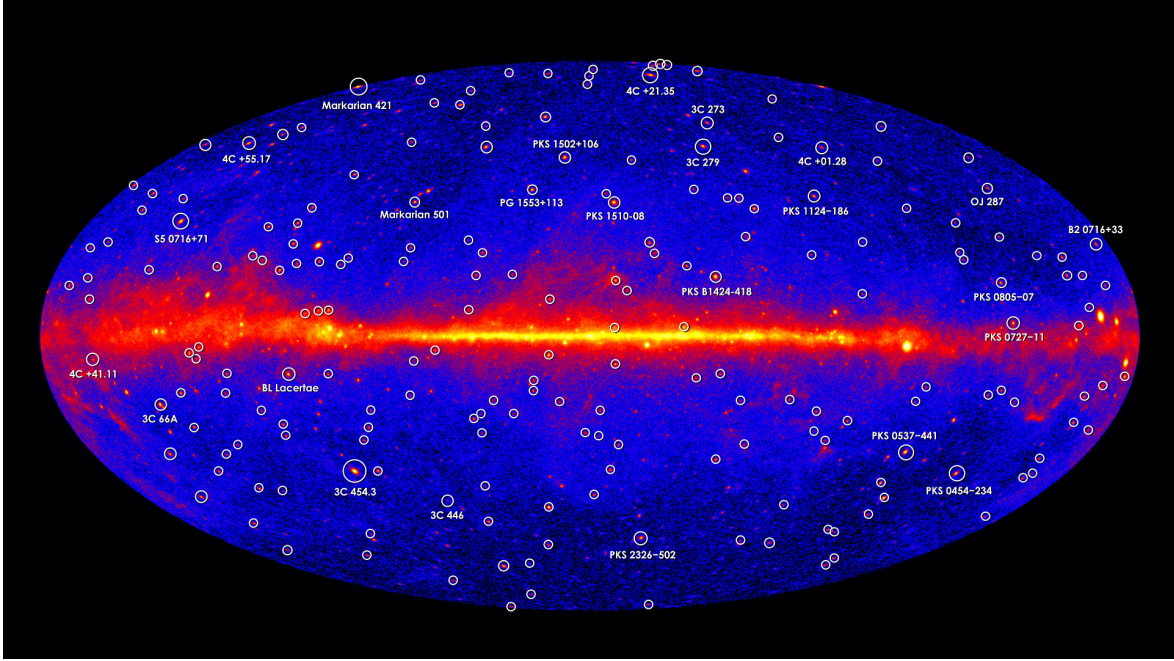


Figure 4.9.: Hammer projection of the *Fermi*/LAT 5 year sky map (NASA/DOE/*Fermi* LAT Collaboration)

background model. *Fermi*/LAT data are fitted by applying a Maximum Likelihood method. First the events are selected and filtered in a given time range and a region of interest. This region of interest has to be large enough to include neighboring sources for background rejection but small enough to limit the computing time to a reasonable value. The resulting file is filtered for good time intervals (GTI), an exposure map and a livetime cube is also computed. A source model, taken from the third *Fermi* source catalog (3FGL; Acero et al., 2015), or previously the second *Fermi* source catalog (2FGL; Nolan et al., 2012), is compared to the data. Diffuse background components are the extragalactic and the Galactic diffuse emission, and extended sources (e.g., the lobes of Centaurus A; Abdo et al., 2010e).

The maximum likelihood method is used to calculate the probability of obtaining a data set under the assumption that the input model is correct. The likelihood method produces a model (based on the input model from the 3FGL or 2FG catalog) that describes the data accurately, including the model parameters we wish to estimate. It also calculates the probability for the data for the given model and then maximizes the likelihood with respect to the parameters. The value that is used in the *Fermi*/LAT data extraction to estimate the significance of a source is the test statistic (TS) value, which is given by

$$TS = -2 \ln \left( \frac{\mathcal{L}_{\max,0}}{\mathcal{L}_{\max}} \right), \quad (4.4)$$

where  $\mathcal{L}_{\max,0}$  is the maximum likelihood of the null hypothesis (the model without the source), and  $\mathcal{L}_{\max}$  the model including the source. This TS value expresses a significance in the detection of the source.  $\sqrt{TS}$  roughly corresponds to a  $\sigma$  significance. The scripts that were used for the light curve analysis of *Fermi* data have been written by W. McConville, C. Müller and A. Schooley. The scripts for the extraction of *Fermi* spectral data have been written by T. Johnson and are

available online<sup>6</sup>. The extraction of *Fermi*/LAT data are described in detail by Müller (2014), Böck (2012), and a short summary is also given by Krauß (2013).

Since the analysis is based on maximum likelihood, the output includes source fluxes that have been corrected for the instrumental effects, e.g., background and varying exposures. In this thesis I have used the reprocessed Pass 7 data (event class 2) with Science Tools v9r32p5 and the P7REP\_SOURCE\_V15 instrumental response functions (IRF; Ackermann et al., 2012) and a region of interest (ROI) of 10°.

## Optical astronomy

### The UltraViolet and Optical Telescope (UVOT) and the Optical Monitor (OM)

The UltraViolet and Optical Telescope (UVOT) on board *Swift* is co-aligned with the XRT. It provides simultaneous coverage at optical and ultraviolet wavelengths (Gehrels et al., 2004, Roming et al., 2005). It consists of a filter wheel, allowing observations in the U, B, V, UVW1, UVM2, UVW2, white, and in grism mode. Only observations with the 6 filters in a narrow bandwidth were used, excluding the white filter and grism. The *Swift*/UVOT optics are flight spares from the *XMM-Newton* Optical Monitor (OM). Image artifacts in the UVOT and OM telescopes include internal reflections within the detector window (ghost image ‘smoke ring’) and reflections of off-axis starlight and background light. For more details on images artifacts in the OM see Litzinger (2011) and the *XMM-Newton* User’s Handbook<sup>7</sup>. The UVOT data reduction works in a similar way as the XRT data reduction. The calibration is applied to the data and then the source counts from within a source and background region are extracted, creating the necessary files, including a response function for the individual filters. For the OM detector it is not possible to generate event files and response function. The standard pipeline omichain (for the image mode) prepares the data (combining all exposure), then processes the image (applying corrections, e.g., bad pixels, fixed pattern, flat-fielding), and then finds all detected sources and stores the photometry and astrometry information in FITS files. The output file includes the sources and their respective fluxes and instrumental magnitudes. We use the flux densities, as they can be handled in broadband spectra since magnitudes are only defined in the optical waveband.

## Radio astronomy

This Section is based on the books by Thompson et al. (2001), and Burke & Graham-Smith (2002). Astronomy at long wavelengths (millimeters to centimeters) is performed with large radio telescopes (dish diameters between 5 and 100 m). Unlike other wavelengths, individual photons are not counted. The wave-particle duality is explored, often detecting the radio waves with dipole antennae. The angular resolution of a radio telescope is given by the Rayleigh criterion

$$\sin(\alpha) \approx 1.22 \frac{\lambda}{d}, \quad (4.5)$$

with an angular resolution,  $\alpha$  in radians, the wavelength,  $\lambda$ , and the diameter of the telescope,  $d$ . At a certain telescope size they become hard to maneuver and unstable in construction. The largest fully steerable radio telescope is the Robert C. Byrd Green Bank Telescope (GBT) in West Virginia in the USA with a 102 m dish<sup>8</sup>, closely followed by the Effelsberg Telescope with a

---

<sup>6</sup><http://fermi.gsfc.nasa.gov/ssc/data/analysis/user/>

<sup>7</sup>[http://xmm.esac.esa.int/external/xmm\\_user\\_support/documentation/uhb\\_2.1/node77.html](http://xmm.esac.esa.int/external/xmm_user_support/documentation/uhb_2.1/node77.html)

<sup>8</sup><https://science.nrao.edu/facilities/gbt/>

100 m dish<sup>9</sup>. The largest single-aperture telescope is the Arecibo radio telescope in Puerto Rico<sup>10</sup>. The main dish was built into a depression, and the receiver is moved to point the telescope at various directions<sup>11</sup>. Significantly larger resolutions ( $\sim 5$  orders of magnitude) can be achieved through interferometry. In interferometry several telescopes are synchronized. In Equation 4.5,  $d$ , then expresses the largest distance between two telescopes, called the baseline. Very large baseline interferometry (VLBI) uses large distances across continents to achieve very high resolutions. Using several telescope has the advantage of allowing image reconstruction if the phase and amplitude information of at least three telescopes is available. Interferometry is based on measuring the coherent wavefront arriving with a geometrical time delay (with respect to a reference antenna) at different telescopes (depending on the angle to the source with respect to the surface normal). The goal is to obtain an interference pattern ('fringe') in the correlator. This requires an extremely good time resolution, which is generally provided by an atomic clock, called maser. Each pair of telescopes used in the array provides a measurement in the Fourier space (spatial frequency domain). Due to Earth's rotation the time delay changes, providing additional visibility functions in the  $(u,v)$  plane, called Earth-rotation synthesis. Using Fourier techniques allows us to reconstruct images with milliarcsecond resolution. The TANAMI program uses the Australian Long Baseline Array (LBA)<sup>12</sup> in combination with additional dishes. On the northern hemisphere the largest baselines are achieved by the EVN<sup>13</sup>, and the VLBA<sup>14</sup>. On 2011 July 18, the Russian satellite RadioAstron was launched, carrying a 10 m radio dish. It was placed in a highly elliptical orbit, achieving baselines of up to 350,000 km (Alexandrov et al., 2012, Kardashev et al., 2012).

## Very Large Baseline Interferometry (VLBI)

Figure 4.10 shows a map of the southern hemisphere, centered on Australia, with the locations of the antennae of the TANAMI VLBI array. We use the Australian Long Baseline Array (LBA) in combination with an antenna at Hartebeesthoek, South Africa, two telescopes of the NASA Deep Space Network (DSN) in Tidbinbilla, two German antennas, GARS at O'Higgins, Antarctica and TIGO (was at Concepción, Chile, but is now in La Plata, Argentina). Recently two Australian dishes of AuScope in Yarragadee, Western Australia, and Katherine, Northern Territory, and a telescope in Warkworth, New Zealand, and one ASKAP antenna also in Western Australia were added.

The following paragraph has been taken in large parts in verbatim from Krauß (2013). The data taken by these antennae have to be cross-correlated and calibrated. The DiFX correlator at Curtin University in Perth, Western Australia (Deller et al., 2007, 2011) was used to correlate the data. Subsequent calibration, hybrid imaging, and image analysis is done following Ojha et al. (2010). The calibration is done in AIPS (van Moorsel et al., 1996). The first step is the a-priori amplitude calibration, which corrects for instrumental and atmospheric effects. The second step is the a-priori phase calibration, which corrects for time delays and changes in the visibility phases. Remaining effects are corrected for using fringe fitting, which allows to search for fringes and correct for remaining time delays. Calibration of TANAMI data is done by R. Ojha. TANAMI data are then read into the program DIFMAP for imaging and model fitting (Shepherd et al., 1994).

<sup>9</sup><http://www.mpifr-bonn.mpg.de/en/effelsberg>

<sup>10</sup><https://www.naic.edu/>

<sup>11</sup>[http://www.naic.edu/science/userguide\\_set.htm](http://www.naic.edu/science/userguide_set.htm)

<sup>12</sup><http://www.atnf.csiro.au/vlbi/>

<sup>13</sup><http://www.evlbi.org/>

<sup>14</sup><https://science.nrao.edu/facilities/vlba>

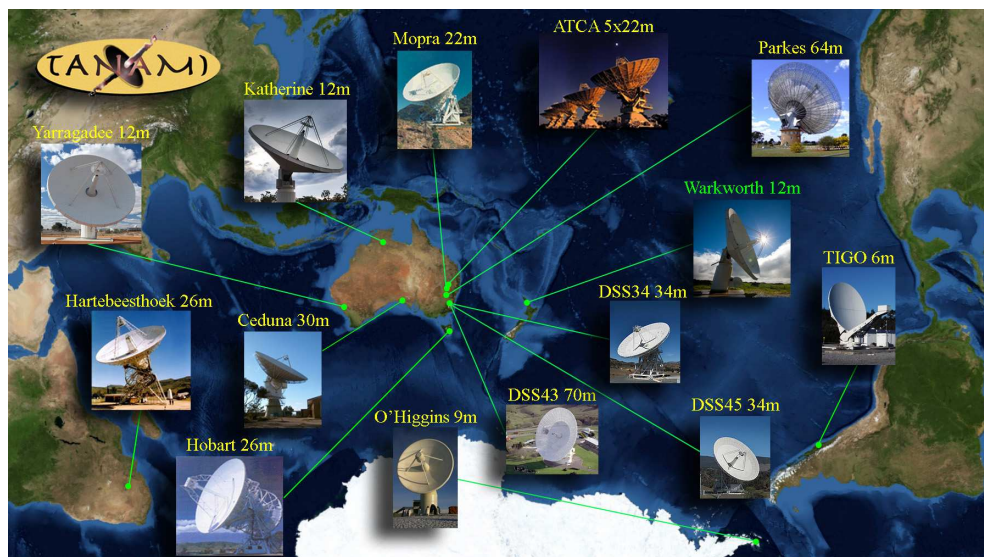


Figure 4.10.: Map of the Southern Hemisphere showing the locations of the radio telescopes, which are contributing to the TANAMI project. (J. Wilms, M. Kadler).

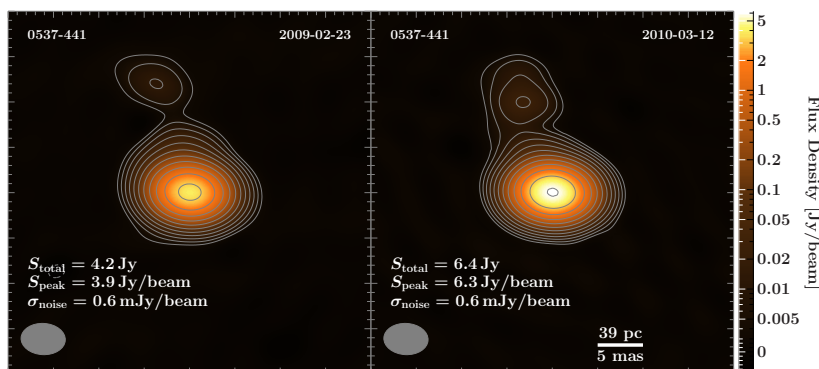


Figure 4.11.: 8.4 GHz parsec-scale VLBI image of the BL Lac object PKS 0537–441 at two epochs. The color scale indicates the flux density distribution, showing an increase in core flux in the later observation (Kadler et al., in prep.).

Details of radio interferometry theory and data analysis have been described by Ojha et al. (2010), Schulz (2012), Trüstedt (2013), Müller (2014), Müller, C. et al. (2016).

Figure 4.11 shows an example of a TANAMI contour plot. At 8.4 GHz (X-Band) a higher resolution is achieved due to the longer baselines of O’Higgins and TIGO, which are not operating at 22.3 GHz (K-Band). The contours in the image represent the significance of the fitted model and are in logarithmic order. The outermost contour corresponds to  $3\sigma$ . The colors give the flux density in mJy/beam of the model. Both images show a central bright component of the jet, defined as the “VLBI core”, as well as a bend in the jet. VLBI images such as these allow us to differentiate between the core flux of the source and the total flux which includes extended emission and the jet. The core flux is used in the broadband spectra.

TANAMI radio observations are supported by flux-density measurements with the Australia Telescope Compact Array (ATCA) (Stevens et al., 2012) and the Ceduna 30 m telescope (McCulloch et al., 2005).

## Additional data

This Section describes the additional quasi-simultaneous and archival data that was used in this thesis.

### *Fermi*/LAT 3FGL

In addition to the spectra calculated simultaneous to the observations at other wavelengths, we add the spectra from the 3FGL catalog. These were calculated over the first four years of *Fermi*, averaging over different source states (Acero et al., 2015). The 3FGL averaged spectra can therefore easily be compared to the spectra at different source states.

### SMARTS

SMARTS is monitoring *Fermi*/LAT detected blazars on the southern hemisphere daily with the SMARTS 1.3 m telescope, and ANDICAM located at Cerro Tololo Inter-American Observatory (CTIO). The observations are carried out with an optical CCD and an IR imager, obtaining data in the 0.4 to 2.2 microns wavelength range. Every two-to-four weeks spectroscopic measurements of the blazars are performed in order to search for emission lines and possible variations in line strength (Bonning et al., 2012, Buxton et al., 2012). The resulting magnitudes are publicly available online<sup>15</sup>.

### REM

The Rapid Eye Mount (REM) is a 60 cm telescope located in the ESO observatory in La Silla, Chile (Covino et al., 2002, Chincarini et al., 2003). In the framework of the TANAMI program, REM monitoring of 7 TANAMI blazars was obtained between January 2010 and January 2012; monitoring of 5 blazars was obtained between February 2011 and May 2015. The first monitoring campaign has been published (Nesci et al., 2013). Data from both campaigns are used for the broadband spectra.

### WISE

NASA's *Wide-field Infrared Survey Explorer* (WISE) is a satellite observing in the infrared waveband between 2.5 and 22 microns (Wright et al., 2010). Initial observations were performed between December 2009 and February 2011. The data are available online<sup>16</sup>. We include non-simultaneous data from the ALLWISE release.

### 2MASS

The Two Micron All-Sky Survey (2MASS) was a survey of the full sky in three bands, J (1.25 microns), H (1.65 microns), and K<sub>s</sub> (2.17 microns; Cutri et al., 2003, Skrutskie et al., 2006). The ALLWISE catalog has been cross-matched with the 2MASS catalog, using the better astrometric accuracy of 2MASS for positional reconstruction<sup>17</sup>.

<sup>15</sup><http://www.astro.yale.edu/smarts/glast/home.php>

<sup>16</sup><http://irsa.ipac.caltech.edu/frontpage/>

<sup>17</sup><http://wise2.ipac.caltech.edu/docs/release/allsky/>

### *Planck*

*Planck* was an ESA satellite that operated between 2009 and 2013 with the goal of mapping the anisotropies in the cosmic microwave background. It observed the full sky at wavelengths between 27 GHz and 1 THz (The Planck Collaboration, 2006, Planck Collaboration et al., 2014a). Detection of other sources have been added to various Planck catalogs. We have used data from the Planck Catalogue of Compact Sources (PCCS; Planck Collaboration et al., 2014b).

# Constructing a broadband spectrum

In this Chapter, I show how observations give us the broadband picture, and how we combine a multitude of instruments using different detector techniques to study the source properties. I use the *Interactive Spectral Interpretation System* (ISIS; Houck & Denicola, 2000, Houck, 2002, Noble & Nowak, 2008) for all of the steps mentioned, unless noted otherwise. ISIS is similar to XSPEC (Arnaud, 1996), but has additional features due to its programmability, e.g., timing tools.

## Calculating fluxes

Instruments and detection techniques are very different in the various wavebands (see Chapter 4). In order to study source properties it is necessary to study fluxes, intensities, or source intrinsic luminosities. Calculating the source flux (and subsequently intensities or luminosities) is still tricky. In the following I explain how the counts detected by an X-ray CCD can be converted to an astrophysical flux. Then I discuss fluxes for other wavebands.

Each X-ray CCD has its own response to incident photons and the optics vary with each instrument. Good calibration and knowledge of the instrument is crucial for a reliable flux measurement. X-ray CCDs ideally detect individual photons. The count spectrum shows the effects of the energy dependence of the optics and the detector. To study the source it is necessary to obtain the source spectrum, the unfolded spectrum. The intrinsic source spectrum  $s(E)$  relates to the observed counts spectrum  $C(h)$  as

$$C(h) = (N \tau) \int dE R(h, E) A(E) s(E) + B(h), \quad (5.1)$$

with the pulse-height channel  $h$ , the effective exposure time  $N \tau$ , the effective area  $A(E)$ , and the redistribution matrix  $R(h, E)$  (Davis, 2001b,a, Gorenstein et al., 1968). The term  $B(h)$  describes the additional instrumental and physical background, which includes X-ray photons, soft protons, and thermal contributions. This is a discrete matrix equation, as we measure the energy of counts in discrete energy channels given by

$$R_{h,E}^i = \frac{\int_{E_{j-1}}^{E_j} R(i, E') dE'}{(E_j - E_{j-1})}. \quad (5.2)$$

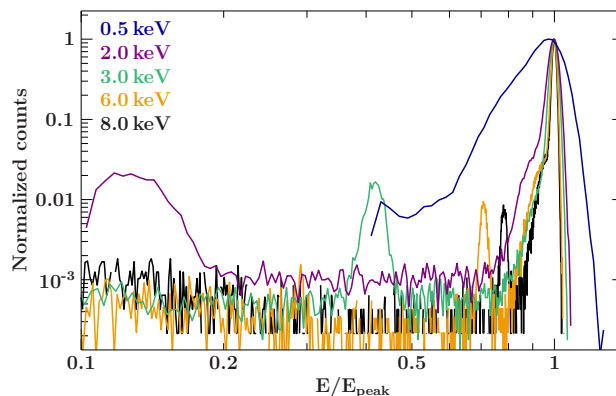


Figure 5.1.: Response of the *Swift*/XRT to photons of a single energy. The counts are normalized to the peak counts.

Inverting Eq. 5.2 is unstable, as there is cross talk among the energies (Fig. 5.1; see also Section 4.4.1). The alternative is a forward-folding approach. In this method we assume a spectral model (e.g., a power law) with a set of parameter values. This fit function is convolved with the redistribution matrix and ancillary response function. In ISIS the background is not subtracted from the counts spectrum but added to the fit function at this point. The resulting function is compared to the observed data, and a goodness-of-fit is determined. To find the best fit, the parameter values of the fit function (e.g., the photon index) are changed and the goodness of fits compared to the previous ones.

The typical goodness-of-fit used is the chi-squared test, where  $\chi^2$  is minimized (Gorenstein et al., 1968). In ISIS it is defined as

$$\chi^2 = \sum_i \frac{(d_i - m_i)^2}{\sigma_i^2}, \quad (5.3)$$

with the observed data points  $d_i \pm \sigma_i$  and the fit model  $m_i$ . The application of  $\chi^2$  requires Gaussian distributed data points. This is not the case for individual counts, which must be grouped to  $\sim 20$  counts. If this rebinning of the data yields only a small amount of bins, it is necessary to use Cash statistics, which is applicable to Poisson statistics data (Cash, 1979). The goodness-of-fit is then defined as

$$C = 2 \sum_{i=1}^n (t \cdot m_i) - d_i + d_i \ln(d_i/(t \cdot m_i)), \quad (5.4)$$

with the exposure time  $t$ . It has the advantage that no information is lost in the rebinning process.

In the forward-folding method ideally the spectrum is only unfolded after a good model has been found, assuring that the calibration is accurate. Forward-folding is not ‘unique’, since different physical models can yield similar goodness-of-fits. Unfolding in ISIS yields the source flux

$$F = \frac{C(h) - B(h)}{(\int R(h, E) A(E) dE) / dh / T} \quad (5.5)$$

(Nowak et al., 2005). The model flux, however, is given by

$$F_m = \frac{\int dE S(E)}{dE}, \quad (5.6)$$

such that the data only matches the model for small bin sizes. ISIS uses bin-integrated values to find the best fit. In order to calculate the flux, a bin-differential value, we have to integrate over the bin width. ISIS assumes that the flux is constant in a bin. For steep spectra this leads to a disagreement between flux data points and residuals.

The following paragraph has been taken in verbatim from Krauß et al. (2016). Broadband fitting is generally performed on energy flux spectra in the  $\nu F_\nu$ -representation. This approach is very problematic however, especially in the X-ray and gamma-ray regime, as the low spectral resolution of the instruments used in these bands makes it mathematically impossible to recover the source spectral shape and flux in an unambiguous way by “unfolding” (e.g., Lampton et al., 1976a, Broos et al., 2010, Getman et al., 2010). These “unfolded” flux densities are in general biased by the shape of the spectral model that was used in obtaining them (Nowak et al., 2005). For very broad energy bands and strongly energy-dependent spectra, which are present in blazar spectra, the unfolded flux densities can be in error by a factor of a few. To avoid these problems, we use ISIS and treat all data sets in detector space. ISIS allows us to use data with an assigned response function (e.g. *Swift*/XRT and *Swift*/UVOT data) in combination with data that are only available as flux or flux density such as the radio data, some of the optical data sets, or *Fermi*/LAT data from the *Fermi* catalog (see Sect. 4.7.1). A diagonal matrix is assigned to these latter data sets. All data modeling is performed in detector space, we use unfolded data only for display purposes. For the unfolding we use the model-independent approach discussed by Nowak et al. (2005).

*Fermi*-LAT data can be fitted in parallel to the X-ray data without unfolding the X-ray data before fitting. However, during unfolding of the spectra (for display purposes) ISIS calculates the bin-differential fluxes from the bin-integrated values, which introduces an error, as the *Fermi*-LAT fluxes are model-dependent, not constant. This offset in flux is corrected by introducing a correction factor that calculates the offset between a constant spectrum and a power law spectrum fitted to the *Fermi*-LAT data.

At infrared, optical, and ultraviolet wavelength the detection principle is similar to the X-ray method. Photons are reflected off of mirrors and focused onto a CCD. In the case of optical photons the information about the energy of the photon does not come from the charge detected by the CCD. Due to high count rates arriving at the instrument, the read-out time necessary for distinguishing between individual photons is impossible to achieve currently. Instead, optical astronomers use filters that only allow photons of a certain wavelengths (with a certain bandwidth) to pass through, similar to the response of an X-ray CCD. It would therefore be possible, in theory, to apply the same methods. For *Swift*/UVOT each filter has an assigned response and the data can be treated equivalent to the X-ray data. For historical reasons, many optical catalogs convert photon fluxes into magnitudes. Magnitudes are based on the system developed by the ancient Greek Hipparchus, who used numbers from 1 through 6 to classify a star’s brightness. In today’s observations a star’s magnitude is derived by comparing the source brightness to a reference star with known magnitude, therefore assuming a certain spectral shape. We calculate optical fluxes using the provided zero points of the instruments. The zero points give the flux values (typically in Jansky) for a star of 0 magnitude. This method potentially introduces systematic uncertainties, depending on the source spectrum. Only the ALLWISE catalog (see Sect. 4.11.4) gives a correction factor for different source spectra (Wright et al., 2010). We introduce the correction for a  $F_\nu \propto \nu^{-1}$  spectrum. This is not true for all sources, as there are deviations from this general trend. In a few sources, especially FSRQs, we see a big blue bump, an optical component similar to a blackbody, which could originate from the accretion disk.

## Systematic uncertainties

Systematic uncertainty is a non-random error that arises, e.g., due to calibration that is not well understood or imperfect methods such as wrong spectral models. In this Section I briefly mention the instruments and the systematic uncertainties that have been added to the statistical errors. Non-simultaneous data have not been used in the broadband fit, these are *Swift*/BAT, *Planck*, *WISE*, and 2MASS data.

**Fermi/LAT:** I added an uncertainty of 5%. The origin of the systematics are approximations in the instrumental response function (IRFs), such as neglecting the energy dispersion in the fit, binning, and interpolation. Further uncertainties originate from the shape of the PSF and the effective area <sup>1</sup>.

**Swift/XRT:** For the windowed timing/photon counting mode a systematic uncertainty of 5%/10% has been found by (Romano et al., 2005). The uncertainty is due to problems with the ancillary response, which was calibrated using the Crab nebula (for windowed timing mode) and the pulsar PSR B0540–69 and its pulsar wind nebula (for photon counting mode; Romano et al., 2005).

**XMM-Newton/pn and MOS:** *XMM-Newton* observed the isolated neutron star RXJ 1856.6–3754 twice per year in the Routine Calibration Plan. Deviations from the spectra are at the 2% uncertainty. Uncertainties in the absolute flux calibration are up to 5%, which we use as a the systematic uncertainty for the pn and the MOS cameras<sup>2</sup>.

**Swift/UVOT:** The systematic uncertainty for the *Swift*/UVOT detector is 2%. Contributions to the uncertainty include the change in filter sensitivity, i.e., the effective area. The uncertainty due to coincidence loss is less than 0.01 mag (less than 1%; Breeveld et al., 2005, Poole et al., 2008, Breeveld et al., 2010, 2011).

**XMM-Newton/OM:** The systematic uncertainty of the *XMM-Newton*/OM as been found to be  $\sim 0.1$  mag. This does not include the uncertainty in the zero points. We therefore use 3% as an estimate of the combined systematics <sup>3</sup>.

**SMARTS:** The photometric systematic uncertainty for the SMARTS program is  $\sim 0.05$  mag, with deviations up to 0.1 mag. We therefore use 0.07 mag for the systematic uncertainty. This does not include the uncertainty in the zero points.

**REM:** Based on photometry, the systematic uncertainty is 0.05 mag (R. Nesci, priv. comm.). This does not include the uncertainty of the zero points.

**VLBI:** The errors of VLBI flux measurements are currently not well determined. We add a conservative 20% flux uncertainty that covers statistical as well as systematic errors.

**Swift/BAT:** No calibration uncertainty for the flux values are given for the *Swift*/BAT instrument. We add an uncertainty of 0.75% to the *Swift*/BAT data, as this is the value listed for the uncertainty in the light curve (Baumgartner et al., 2013).

---

<sup>1</sup>[http://fermi.gsfc.nasa.gov/ssc/data/analysis/LAT\\_caveats\\_p7rep.html](http://fermi.gsfc.nasa.gov/ssc/data/analysis/LAT_caveats_p7rep.html)

<sup>2</sup><http://xmm2.esac.esa.int/docs/documents/CAL-SRN-0321-1-2.pdf>

<sup>3</sup>[http://xmm2.esac.esa.int/external/xmm\\_sw\\_cal/calib/rel\\_notes/index.shtml](http://xmm2.esac.esa.int/external/xmm_sw_cal/calib/rel_notes/index.shtml)

**Planck:** We include the aperture photometry values from the Planck Catalogue of Compact Sources. Above 100 GHz, sources above the Galactic plane have a contamination from CO of up to 6%. The photometric calibration uncertainty is  $< 1\%$   $< 217$  GHz and  $< 10\%$  at  $< 900$  GHz (Planck Collaboration et al., 2014b). We add an uncertainty of 10% to the Planck data to account for the contamination of CO and the photometric calibration uncertainty.

**WISE:** Contributions to the photometric uncertainty include: source confusion (negligible above the Galactic plane), uncertainty in zero points and in background estimation, and the photometric calibration ( $\sim 7\%$ <sup>4</sup>; Wright et al., 2010). The uncertainty of the zero points depends strongly on the filter, and lie between 4 and 20% (for W4)<sup>5</sup> We use an average uncertainty of 14.5%, as the data are not included in the fit.

**2MASS:** The 2MASS point source catalog (PSC) photometric uncertainty is hard to determine, as the data were taken over many months, with varying weather, seeing, atmospheric transparency, background, and moonlight contamination. The average uncertainty is 0.02 mag for bright sources above a Galactic latitude of  $75^\circ$ <sup>6</sup>. To account for other latitudes we use a systematic uncertainty of 0.05 mag. This does not include systematic uncertainties of the zero points.

**Additional systematics:** For optical instruments with no estimate of the zero points uncertainty, I have added an additional 5% uncertainty.

## Absorption and extinction

X-rays have a relatively long mean free path, but a part of the photons are absorbed (via photoelectric absorption) on their way to the Earth through Interstellar Medium (ISM), and Intergalactic Medium (IGM). Photons at optical wavelengths are extinguished by the dust in the ISM. The Galactic plane covers only a fraction of the sky. Since Earth is located in the Galactic plane we are surrounded by the ISM, but the density is much higher in the plane as there is a higher amount of material along these line of sights. The Milky Way has a higher density of gas, and dust than the surrounding intergalactic medium. Sources that lie in our Galaxy, or ‘behind’ the Galaxy are strongly affected by absorption. We can learn about the ISM (and subsequently the absorption and extinction) across the sky by measuring the neutral hydrogen line at 21 cm wavelength, which has been predicted in 1944 by van de Hulst (1951), and detected since the 1950s (Ewen & Purcell, 1951, Muller & Oort, 1951, van de Hulst, 1951). The 21 cm emission originates in the hyperfine structure, in the spin flip of neutral hydrogen. The spin flip occurs due to magnetic dipole radiation or absorption. Since the interstellar medium in our Galaxy consists mainly of hydrogen, it is possible to calculate the expected absorption of X-rays. Many partial surveys of the HI emission were conducted (e.g., Dickey et al., 1983, Hartmann & Burton, 1997, Barnes et al., 2001). The newest and most complete survey of the sky is the Leiden/Argentine/Bonn (LAB; Kalberla et al., 2005a, 2010). Efforts have also been undertaken to study the HI emission line in nearby galaxies (Stanimirovic et al., 1999, Walter et al., 2008). Contributing to the photoelectric absorption at X-ray energies are gas, molecules, and dust grains. The observed X-ray intensity of a source  $I_o$  is given by

$$I_o = e^{-\sigma_{\text{ISM}}(E)N_{\text{H}}} \cdot I_{\text{source}}(E), \quad (5.7)$$

<sup>4</sup>[http://wise2.ipac.caltech.edu/docs/release/allsky/expsup/sec6\\_3b.html](http://wise2.ipac.caltech.edu/docs/release/allsky/expsup/sec6_3b.html)

<sup>5</sup>[http://wise2.ipac.caltech.edu/docs/release/allsky/expsup/sec4\\_4h.html](http://wise2.ipac.caltech.edu/docs/release/allsky/expsup/sec4_4h.html)

<sup>6</sup>[http://www.ipac.caltech.edu/2mass/releases/allsky/doc/sec2\\_2.html](http://www.ipac.caltech.edu/2mass/releases/allsky/doc/sec2_2.html)

where the cross-section of the ISM  $\sigma_{\text{ISM}}$  is normalized to the total hydrogen number density  $N_{\text{H}}$  (Wilms et al., 2000). A good understanding of these cross-sections is necessary to study the intrinsic spectrum. In this thesis I use the photoionization cross-sections `vern` (Verner et al., 1996) and the `wilm` abundances (Wilms et al., 2000), unless noted otherwise. The absorption model `tbabs` (Wilms et al., 2000), has been updated to `tbnew` and is available online<sup>7</sup>. The left panel of Fig. 5.2 compares various cross-sections and abundances. The input model was a power law with a photon index of 1.8 (black). The absorption model is `tbnew`. The `vern` cross-sections and `wilm` abundances (blue) are compared to the previous cross-sections `bcmc` (Balucinska-Church & McCammon, 1992) and abundances `angr` (Anders & Grevesse, 1989), and to the newer cross-sections `vern` and abundances `aspl` (Asplund et al., 2009). There is a large difference between the old cross-sections and abundances, but both newer models seem to agree. X-ray spectra of blazars can typically be described by absorbed power laws (Donato et al., 2001). Ideally, the best fit to the data describes the absorption along the line of sight to the source.

Apart from uncertainties in the photoionization cross-sections and the abundances there is a degeneracy in the fit parameters. The photon index  $\Gamma$  ( $F = C \cdot E^{-\Gamma}$ ) is directly correlated with the absorbing column  $N_{\text{H}}$ . The right panel of 5.2 shows that a similar goodness-of-fit can be obtained with a slightly higher photon index and a higher absorption. This correlation is of mathematical, not of physical origin. The contour plot also shows that the errors on the photon index are smaller than for the absorbing column. I have performed simulations for various absorbed power law in order to estimate the source counts necessary for constraining the photon index and absorbing column to a certain percentage. Figure 5.3 shows the parameter errors at 90% confidence level for an absorbed power law with varying exposures (and therefore varying total number of source counts). It is obvious that for an extragalactic source with a low absorbing column ( $N_{\text{H}} \sim 1 \times 10^{21}$ ) a large number of source counts ( $\sim 20000$ ) are necessary to constrain the absorbing column to better than 10%. Only  $\sim 1000$  counts are necessary to constrain the photon index to better than 10%.

<sup>7</sup><http://pulsar.sternwarte.uni-erlangen.de/wilms/research/tbabs/>

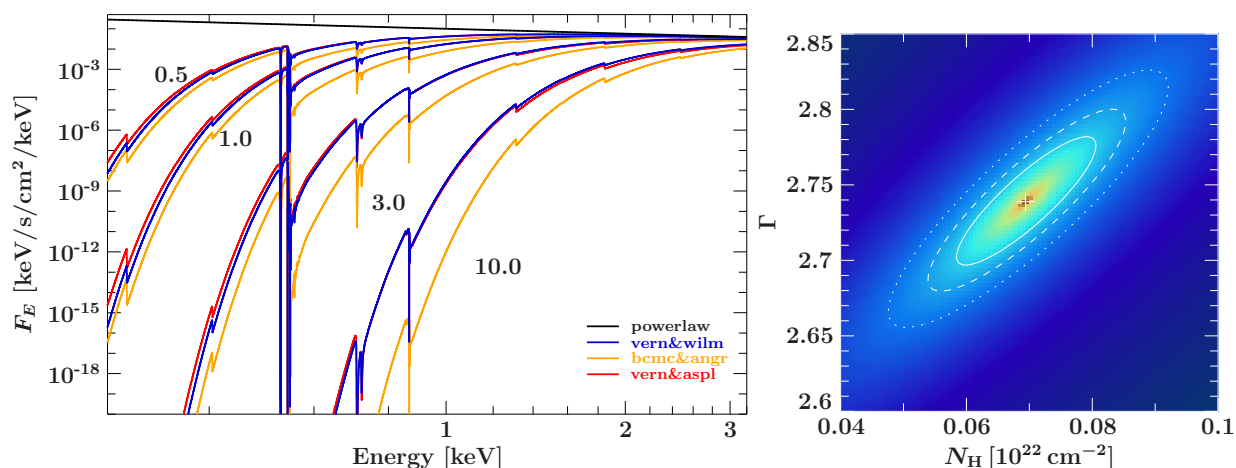


Figure 5.2.: *Left*: Absorption for 4 different absorbing columns using a power law as input model and various cross-sections and abundances. The  $N_{\text{H}}$  values are given in black in units of  $10^{22} \text{ cm}^{-2}$ . *Right*: Contour plot for an absorbed power law fit to observation 00030795057 of the BL Lac object PKS 2155–304. It shows a strong correlation between the photon index and the absorbing column. The contour lines are given at the 68%, 90%, and 99% confidence level and the best fit is marked with a cross.

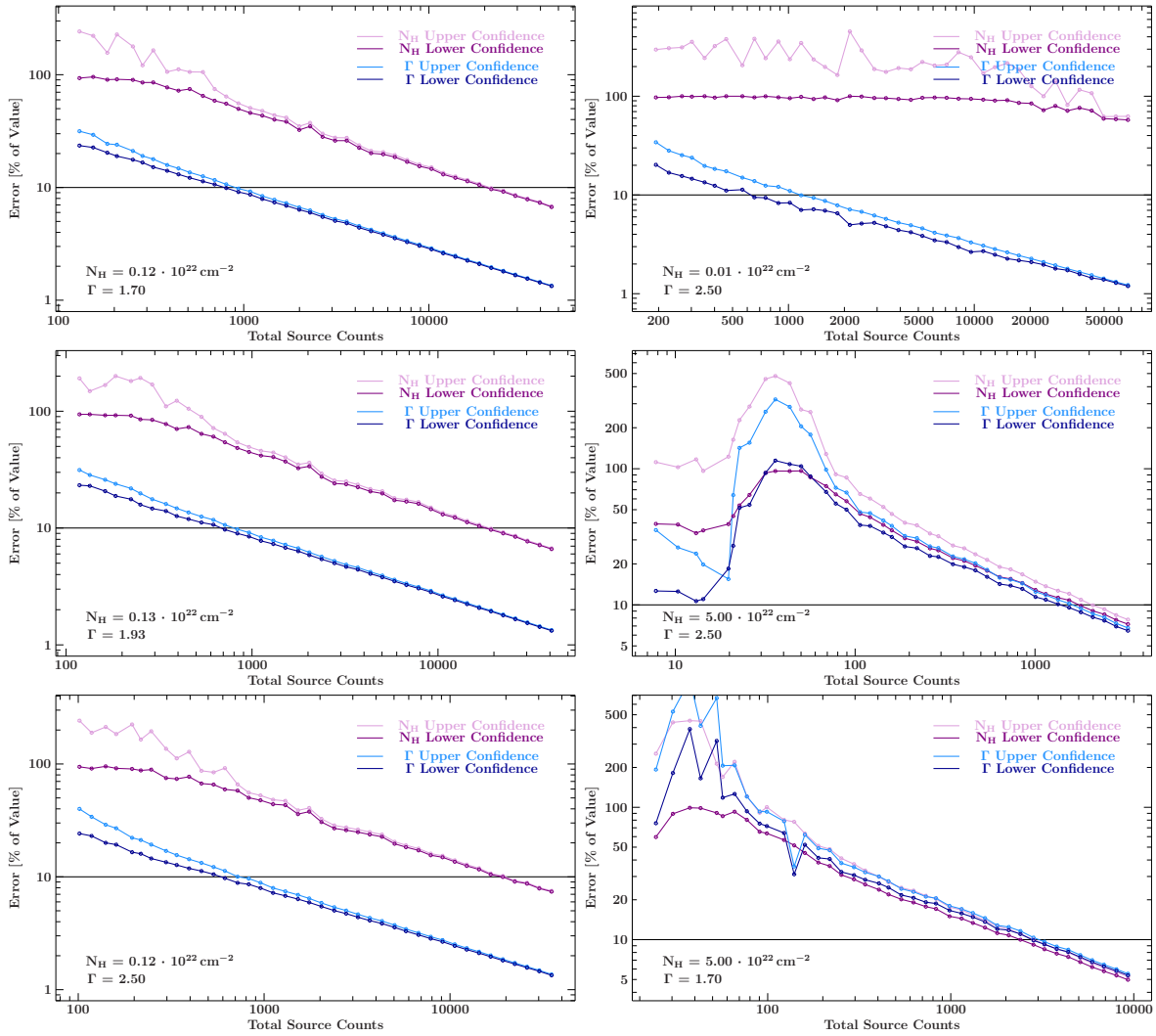


Figure 5.3.: Uncertainties in photon index and absorbing column for simulated power law spectra at varying exposures (and varying number of total counts). Each data point has been calculated from 20 simulated spectra and the parameters have been averaged and their errors propagated.

For high column densities ( $\sim 10^{22}$ ), only  $\sim 1000$  counts are necessary to constrain the absorbing column and the photon index to better than 10%.

### Unabsorbed fluxes

In order to study the source intrinsic spectrum, the absorption has to be taken into account. The easiest way to obtain an integrated unabsorbed flux is to fit a model to the data, and when the best fit has been found, the model flux is integrated. This integration can be done over the complete model or over only some of its components (e.g., integrating only the power law gives the unabsorbed power law flux). This has the advantage that the model can be evaluated on a very fine grid. In order to unabsorb the individual data points for a broadband SED a different approach is necessary. After the best fit model has been found the  $N_{\text{H}}$  is evaluated across the fit range, yielding the model output, which describes the factor by which the flux of the given data point is reduced (e.g., 0.5). For plotting purposes only, I use these factors and divide the

given data point by the value. This unabsorbed spectrum is only an estimate of the intrinsic spectrum and is not used for any fitting purposes. In all fit models the absorption (and extinction) is part of the model, with the parameter  $N_{\text{H}}$ . We use the absorbed and reddened data for fitting, which allows us to use the same absorbing column for dereddening and deabsorbing, and testing different values on the fly, while the fit model is adjusted.

## VLBI, small arrays and single dish

The various radio telescopes (depending on the array size) have a different beam size. Small arrays (such as ATCA) and single dish telescopes reach resolutions of arcseconds, while long baselines reach resolutions of milliarcseconds, which is a difference of  $\sim 10^3$ . This does not matter for compact sources that are unresolved in VLBI observations. For large jet structures the VLBI observations see only the innermost region of the jet. Due to this I often see a systematic offset between the TANAMI and the ATCA or Ceduna observations, which sometimes necessitates using only one instrument for the broadband fit. This is one of the current problems in describing broadband spectra. If the emission at other wavelengths (which cannot be resolved to milliarcsecond resolution) is originating close to the core, only the core emission should be modeled with the multiwavelength data. However, in many cases we do not know how much substructure remains unresolved in the VLBI images. On the other hand, if the multiwavelength emission is not only originating in the core, but in the jet or the lobes, the VLBI data would be insufficient.

## The big blue bump

The ‘big blue bump’ (BBB) is an excess at optical to ultraviolet wavelengths. It was first seen in 3C 273 (Shields, 1978). It should not be confused with the excess due to host galaxy emission in sources such as IC 310 (Glawion et al., in prep.). In some sources (e.g., Seyferts) with weak continuum emission, the emission of the host galaxy is not outshone by the continuum (e.g., NGC 4051, Maitra et al., 2011). This feature is very similar to the BBB, which is an excess at slightly higher energies. It is believed to originate from the accretion disk, a hot torus, or a combination of both. Details of the big blue bump can be found in Sect. 3.4.3. Typically this feature is visible in FSRQs (Jolley et al., 2009, and references therein). This is counter intuitive at first, since they are more luminous than BL Lac objects, and should therefore outshine most other emission. However, this seems to hint at a connection between the accretion and the luminosity of the source. The emission from the big blue bump can be described by a blackbody or a diskpnp model, since we only have fluxes in some wavebands.

## Fitting the broadband spectrum

In order to study the jet we combined the fluxes in various wavebands and fit a model to the data. The fit model include two logarithmic parabolas, which is an empirical model that describes the data surprisingly well. Physical models often have the problem of a large number of unknown parameters (e.g., black hole mass, Lorentz factor, jet opening angle; Böttcher et al., 2013) that cannot be fit due to the scarce data and correlation of the individual parameters ( $\sim 40$  data points from radio to  $\gamma$  rays). We therefore describe the data with the empirical logpar model,

$$F(E) = K \cdot \left( \frac{E}{E_1} \right)^{-(a+b \log(E/E_1))}, \quad (5.8)$$

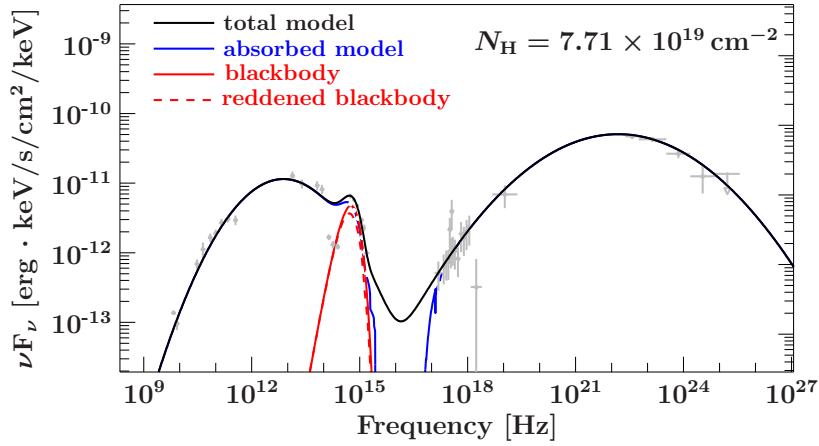


Figure 5.4.: Broadband spectral model of PKS 0402–362, including two absorbed logarithmic parabolas (blue), a blackbody (red), a reddened blackbody (red dashed), and the total unabsorbed model (black).

where  $a$  is the photon index at the energy  $E_1$ , and  $b$  the curvature. The energy  $E_1$  is frozen to a certain value, it has been found that a value close to the lower energy end of the parabola yields good results<sup>8</sup>. Deriving this equations yields the peak energy and flux

$$E_p = E_1 10^{(2-a)/(2-b)}, \quad (5.9)$$

and

$$\nu_p F(\nu_p) = C \cdot K E_1^2 10^{(2-a)^2/(4b)} \quad (5.10)$$

(Massaro et al., 2004). With the information of the peak frequency and flux it is possible to derive and study source properties, such as the blazar sequence, or the Compton dominance (see Chapter 3).

Two parabolas are necessary to describe the low and high-energy hump. I add the absorption and extinction models, as well as a blackbody component if necessary. The final model is `(logpar(1)+logpar(2)+blackbody(1))*tbnew_simple(1)*reddden(1)`.

Figure 5.4 shows an example of the complete model, including a big blue bump. The source shows the model of the flat spectrum radio quasar PKS 0402–362, which is discussed in Chapter 6. The black line shows the total source intrinsic model (unabsorbed and dereddened), the blue dashed line shows only the parabolas (also unabsorbed and dereddened), while the solid blue line shows the parabolas with absorption and reddening. Additionally the blackbody model is shown (reddened and dereddened), but no large difference is visible due to a very low absorbing column along the line of sight to this source.

The fit model is then used to find the best fit to the data. Occasionally, the lack of data necessitates that some parameters are frozen to a value in order to find a good fit. This is especially true for high-peaked BL Lac sources, where the peak of the high-energy hump lies above *Fermi* energies, i.e., is not covered by our data. It is not possible in these cases to constrain the curvature of the parabola from the data, and this parameter is then frozen to a reasonable value.

<sup>8</sup><https://heasarc.gsfc.nasa.gov/xanadu/xspec/models/logpar.html>

## Caveats

Several problems arise for this method, which are discussed here.

**Fluxes:** The methods to obtain the fluxes in the different energy band are not identical (see Sect. 5.1). The *Fermi*/LAT fluxes, and most of the optical data points are model dependent, while the X-ray, and *Swift*/UVOT, and *XMM-Newton*/OM fluxes are model independent.

**Absorption and extinction:** Most blazars show no absorption in excess of the Galactic absorption. In many studies the absorption is frozen to the Galactic value without a separate fit to the X-ray data. I fit the X-ray data separately with an absorbed power law, leaving the absorption free in order to determine the best fit value. In case of low statistics or a bad fit, the Galactic value is used, otherwise the absorption model includes the best fit value. In the broadband SEDs I first fit the  $N_{\text{H}}$  of the best fit (if it differs), and then refit with the Galactic value in order to compare the goodness-of-fit. The remaining problem is the uncertainty in the fit to the X-ray data, with error bars that are often large (see right panel of Fig. 5.2). The Galactic value from the LAB survey has a remaining error of  $\sim 30\%$  to the data. Uncertainties include stray radiation, unresolved structures, assumption of optical transparency (Kalberla et al., 2005a). Additional problems lie in the absorption models, e.g., in the cross-sections and abundance.

**Empirical model:** The model is not motivated by any physical processes, but the results (peak energy and flux) are used to infer physical properties of the source. Due to scarce data around the peak frequencies (typically in the sub-mm, and the MeV range) it is not clear what the exact shapes are. Some models predict steep bends or additional components (see Chapter 3). An averaged spectrum of 3C 273 (Türler et al., 1999) has shown a shape that is remarkably parabola like. In a few cases, e.g., PKS 0537–441 the parabola shape does not describe the data well.

**$\chi^2$  approach:** We use a  $\chi^2$  approach to determine the goodness-of-fit. This is not statistically sound, as it would require data with  $1\sigma$  statistical errors that have not been background subtracted. This is not true for the VLBI data, where the error is an estimate and covers the statistical, as well as the systematic uncertainties. It is also not true for the *Fermi*/LAT data, that has been background subtracted and treated with a maximum likelihood approach. In relative terms the (reduced)  $\chi^2$  values still give a good estimate of the goodness-of-fit, but are not indicative of an absolute goodness-of-fit, i.e., in the probability of the model.

**Redshifts:** For some sources the redshift is unknown. Therefore I have not applied a k-correction to the broadband spectra. In order to get the spectrum in the rest frame it is necessary to shift the frequencies of the arriving photons by  $(1+z)$ , where  $z$  is the redshift of the source.

## A southern hemisphere blazar catalog

You take your time, and you can do good work. You rush into things, and you might destroy a whole universe. What a pity that would be.

---

Alan Lightman, *Mr g: A novel about the creation*, May 2012, Vintage

In this Chapter I compile quasi-simultaneous broadband spectra for 22 of the TANAMI sources. Quasi-simultaneous means observations that were not performed exactly at the same time, but so close in time that the source has likely not changed what is usually called its ‘state’. Some blazars stay at a similar level of flux for many years (‘quiescence’), some show several outbursts (higher level of flux ‘flare’) in a year. In order to assure that a source has not changed its flux level I perform a light curve analysis to determine the optimal time ranges for these quasi-simultaneous spectra. The results from the spectral fitting can be used to evaluate a statistical sample and test for e.g., Compton dominance, and the blazar sequence. This Chapter has been taken in large parts from Krauß et al. (2016).

### *Fermi*/LAT light curve analysis

#### The sample

TANAMI is a flux-limited sample, covering all southern flat spectrum sources with catalogued flux densities above 1 Jy at 5 GHz, as well as all *Fermi* detected  $\gamma$ -ray loud blazars in the region of interest. These sources are monitored by TANAMI with Very Long Baseline Interferometry (VLBI) at 8.4 GHz and at 22 GHz (X-band and K-band, respectively). In addition to the VLBI monitoring, single dish observations are performed at further frequencies with the ATCA and Ceduna. These radio observations are complemented with multiwavelength observations, primarily with *Swift* and *XMM-Newton* in the X-rays, and the Rapid Eye Mount (REM) telescope at La Silla in the optical. The TANAMI sample is regularly extended by adding bright sources detected by *Fermi*-LAT (Böck et al., 2016).

Due to the good coverage in wavelength and time, the TANAMI sample is therefore ideal for a study of the multiwavelength behavior of blazar SEDs. Previous studies include detailed studies of the blazars 2142–758 (Dutka et al., 2013), and 0208–512 (Blanchard, 2013). Here, I study the multiwavelength evolution of the 22  $\gamma$ -ray brightest TANAMI sources according to the 3FGL catalog (Acero et al., 2015). Our results are therefore representative of a  $\gamma$ -ray flux-limited sample. The 22 sources are listed in Table 6.1. I include the IAU B1950 name, the 3FGL association,

Table 6.1.: Sources used in this chapter

No	Source	Catalog	3FGL	Class.	$z$	$\alpha$ [J2000]	$\delta$ [J2000]	$N_{\text{H}}$ [ $10^{20} \text{ cm}^{-2}$ ]	# SEDs
1	0208–512	PKS 0208–512	J0210.7–5101	BCU <sup>▲</sup>	0.99 <sup>♦</sup>	32.69 <sup>•</sup>	–51.02 <sup>•</sup>	1.84	8
2	0244–470	PKS 0244–470	J0245.9–4651	FSRQ <sup>■</sup>	1.39 <sup>†</sup>	41.50 <sup>■</sup>	–46.85 <sup>■</sup>	1.89	2
3	0332–376	PMNJ0334–3725	J0334.3–3726	BL Lac <sup>■</sup>	?	53.56 <sup>▲</sup>	–37.43 <sup>▲</sup>	1.54	2
4	0332–403	PKS 0332–403	J0334.3–4008	BL Lac <sup>■</sup>	?	53.56 <sup>•</sup>	–40.14 <sup>•</sup>	1.48	4
5	0402–362	PKS 0402–362	J0403.9–3604	FSRQ <sup>■</sup>	1.42 <sup>*</sup>	60.97 <sup>•</sup>	–36.08 <sup>•</sup>	0.60	2
6	0426–380	PKS 0426–380	J0428.6–3756	BL Lac <sup>■</sup>	1.11 <sup>*</sup>	67.17 <sup>•</sup>	–37.94 <sup>•</sup>	2.09	5
7	0447–439	PKS 0447–439	J0449.4–4350	BL Lac <sup>≈</sup>	0.11 <sup>℄</sup>	72.35 <sup>▲</sup>	–43.84 <sup>▲</sup>	1.24	3
8	0506–612	PKS 0506–61	J0507.1–6102	FSRQ <sup>≈</sup>	1.09 <sup>♦</sup>	76.68 <sup>•</sup>	–61.16 <sup>•</sup>	1.95	4
9	0521–365	PKS 0521–36	J0522.9–3628	BCU	0.06 <sup>*</sup>	80.74 <sup>•</sup>	–36.46 <sup>•</sup>	3.58	6
10	0537–441	PKS 0537–441	J0538.8–4405	BL Lac <sup>■</sup>	0.89 <sup>●</sup>	84.71 <sup>‡</sup>	–44.09 <sup>‡</sup>	3.14	6
11	0637–752	PKS 0637–75	J0635.7–7517	FSRQ <sup>■</sup>	0.65 <sup>○</sup>	98.94 <sup>•</sup>	–75.27 <sup>•</sup>	7.82	4
12	1057–797	PKS 1057–79	J1058.5–8003	BL Lac <sup>■</sup>	0.58 <sup>□</sup>	164.68 <sup>•</sup>	–80.07 <sup>•</sup>	6.34	2
13	1424–418	PKS B1424–418	J1427.9–4206	FSRQ <sup>■</sup>	1.52 <sup>♣</sup>	216.98 <sup>•</sup>	–42.11 <sup>•</sup>	7.71	7
14	1440–389	PKS 1440–389	J1444.0–3907	BL Lac <sup>■</sup>	0.07 <sup>⊗</sup>	220.99 <sup>■</sup>	–39.14 <sup>■</sup>	7.83	3
15	1454–354	PKS 1454–354	J1457.4–3539	FSRQ <sup>■</sup>	1.42 <sup>♣</sup>	224.36 <sup>⊗</sup>	–35.65 <sup>⊗</sup>	6.60	3
16	1610–771	PKS 1610–77	J1617.7–7717	FSRQ <sup>■</sup>	1.71 <sup>♠</sup>	244.46 <sup>•</sup>	–77.29 <sup>•</sup>	6.76	2
17	1954–388	PKS 1954–388	J1958.0–3847	FSRQ <sup>■</sup>	0.63 <sup>♮</sup>	299.50 <sup>⊗</sup>	–38.75 <sup>⊗</sup>	6.43	2
18	2005–489	PKS 2005–489	J2009.3–4849	BL Lac <sup>■</sup>	0.07 <sup>⊗</sup>	302.36 <sup>•</sup>	–48.83 <sup>•</sup>	3.93	2
19	2052–474	PKS 2052–47	J2056.2–4714	FSRQ <sup>■</sup>	1.49 <sup>♠</sup>	314.07 <sup>•</sup>	–47.25 <sup>•</sup>	2.89	2
20	2142–758	PKS 2142–75	J2147.3–7536	FSRQ <sup>■</sup>	1.14 <sup>♠</sup>	326.80 <sup>•</sup>	–75.60 <sup>•</sup>	7.70	2
21	2149–306	PKS 2149–306	J2151.8–3025	FSRQ <sup>≈</sup>	2.35 <sup>♦</sup>	327.98 <sup>•</sup>	–30.46 <sup>•</sup>	1.63	4
22	2155–304	PKS 2155–304	J2158.8–3013	BL Lac <sup>■</sup>	0.12 <sup>♯</sup>	329.72 <sup>⊗</sup>	–30.23 <sup>⊗</sup>	1.48	6

**Notes.** Columns: (1) source number (2) IAU B1950 name, (3) 3FGL association, (4) 3FGL catalog name (Acero et al., 2015), (5) classification, (6) redshift, (7) right ascension, (8) declination, (9) absorbing column (Kalberla et al., 2005a, Bajaja et al., 2005), (10) number of SEDs

<sup>♮</sup> Browne et al. (1975), <sup>●</sup> Peterson et al. (1976), <sup>○</sup> Hunstead et al. (1978), <sup>♦</sup> Hewitt & Burbidge (1987), <sup>♠</sup> Hunstead & Murdoch (1980) <sup>♠</sup> Jauncey et al. (1984), <sup>⊗</sup> Falomo et al. (1987), <sup>♣</sup> White et al. (1988), <sup>♯</sup> Falomo et al. (1993), <sup>•</sup> Johnston et al. (1995), <sup>℄</sup> Craig & Fruscione (1997), <sup>⊗</sup> Ma et al. (1998), <sup>♠</sup> Wisotzki et al. (2000), <sup>‡</sup> Beasley et al. (2002), <sup>♣</sup> Jackson et al. (2002), <sup>▲</sup> Skrutskie et al. (2006), <sup>\*</sup> Heidt et al. (2004), <sup>⊗</sup> Jones et al. (2004), <sup>⊗</sup> Fey et al. (2004), <sup>≈</sup> Véron-Cetty & Véron (2006), <sup>⊗</sup> Fey et al. (2006) <sup>■</sup> Healey et al. (2007), <sup>\*</sup> Jones et al. (2009), <sup>□</sup> Sbarufatti et al. (2009), <sup>†</sup> Shaw et al. (2012)

the 3FGL catalog name, the source classification that I used, the redshift, right ascension and declination, the Galactic absorbing column in the direction of the source, and finally the number of SEDs that I were able to construct for each of the sources. Our sample includes 9 BL Lac type objects, 11 FSRQs, and 3 blazars of unknown type. The source brightness enables us to extract *Fermi*/LAT light curves with 14-day binning. For some of these sources I present the first broadband SEDs. While a classification of many sources is relatively easy, some sources have contradicting classifications in different AGN catalogs. These are labeled as blazar candidates of unknown type (BCU). One example is 0208–512. In the CGRaBS (Healey et al., 2008a) the source was listed as a BL Lac type object, in agreement with the optical classification from the 12th catalog of quasars and active nuclei (Véron-Cetty & Véron, 2006). The CRATES catalog (Healey et al., 2007), however, lists the source as an FSRQ. The 5th Roma BZCAT lists the source as a BCU, and describes it as a transition object, but list it in the FSRQ (Massaro et al., 2009a). Note that possible misclassifications do not change any of our results, as I generally do not treat the two populations differently and find many of the results are not dependent on the source classification. For 0332–403 a redshift of 1.45 is often used (Hewitt & Burbidge, 1987), but Shen et al. (1998) point out that the origin of this value is unknown.

## Bayesian Blocks

*One can envision our quest for the optimal segmentation as nothing more than finding the best step function, or piecewise constant model, fit to the data – defined by maximizing a specific fitness measure [...]*

— Scargle et al. (2013)

The first step in compiling quasi-simultaneous SEDs is to define the time ranges in a uniform way. The only instrument continuously monitoring the sky is the *Fermi* satellite. Its continuous light curves are ideal for identifying flux states and applying a criterion to separate the data into time ranges. One such method is the Bayesian Blocks algorithm. It determines *change points*, where the flux is not consistent with being constant. This section is based on Scargle (1998), and Scargle et al. (2013). In the Bayesian statistics a prior probability distribution is used. This prior is an uncertain quantity but belief or knowledge enter the assumption before the data are taken into account to calculate the posterior probability. The Bayesian Block method is nonparametric, the data are not described by a model and evaluated, instead local (non-periodic) variability in the light curve is found by only taking the data into account using a maximum likelihood approach. It segments the light curve, finding the global optimum. At the point where the flux is no longer consistent with being constant, a change point is introduced, a discontinuous change at a discrete time. In reality sources rarely change discontinuously, however, this statistical approach allows to derive the necessary quantities. A geometric prior distribution is defined with a steepness parameter  $\gamma$  with the goal to assign smaller probability to larger number of blocks

$$P(N_{\text{blocks}}) = \begin{cases} P_0 \gamma^{N_{\text{blocks}}}, & \text{if } 0 \leq N_{\text{blocks}} \leq N \\ 0, & \text{otherwise} \end{cases}. \quad (6.1)$$

Then the normalization constant  $P_0$  can be obtained

$$\sum_0^N P(N_{\text{Blocks}}) = \sum_{i=0}^N P_0 \gamma^i \stackrel{!}{=} 1 \quad (6.2)$$

yielding,

$$P_0 = \frac{1 - \gamma}{1 - \gamma^{N+1}}, \quad (6.3)$$

where  $N$  is the total number of data points. The expected number of blocks is

$$\langle N_{\text{blocks}} \rangle = P_0 \sum_{N_{\text{Blocks}}=0}^N N_{\text{Blocks}} \gamma^{N_{\text{Blocks}}} = \frac{N \gamma^{N+1} + 1}{\gamma^{N+1} - 1} + \frac{1}{1 - \gamma} \quad (6.4)$$

While this assumption of states of constant flux is in reality not correct, as sources will rarely vary in a discontinuous way, this approach is still very powerful in identifying time ranges of source “states” where the flux is at least statistically constant. Here we adapt a significance of the change points at the 95% confidence level. Such a relatively low value was chosen as we want to keep the number of positive-falses (where real changes in flux are missed) low. Introducing a low number of false-positive, where constant flux is seen as a change point, however, does not harm our analysis. It only segments the data more than necessary, which in the worst case could lead to two missed broadband spectra (if the data in one energy band are only available in on of the time ranges). Figure 6.1 shows the changes in the resulting change points when the

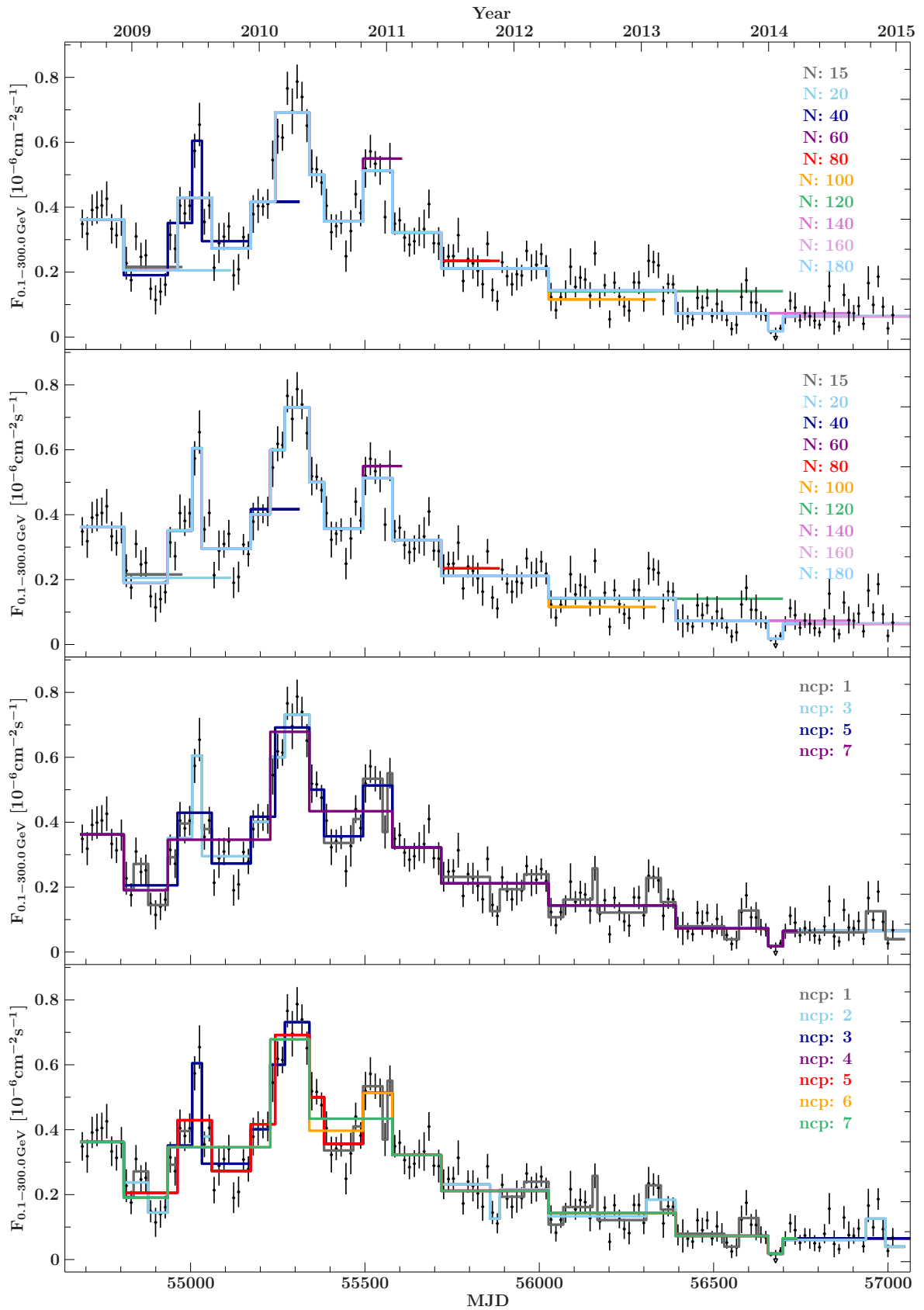


Figure 6.1.: First and second panel (top):  $\text{ncp\_prior} = 3$ , taking into account various light curve lengths (between 15 and 180 data bins), and bottom two panels with a variable  $\text{ncp\_prior}$  and varying light curve lengths

length of the light curve changes, i.e. the effect of lack of data at the end of the light curve in the top panels for a constant `ncp_prior`, and with a changing `ncp_prior` in the bottom panels. The *Fermi*/LAT light curves with the Bayesian Blocks algorithm are shown in Appendix A.1. The *Fermi*/LAT data points are shown in black, while the segmentation by the Bayesian blocks is shown in dark gray. The average flux across the whole light curve is shown in light gray. We additionally show available multiwavelength data above the light curve at the corresponding times of the observations. Blocks with a sufficient amount of multiwavelength data are marked in color and are labeled with Greek letters.

We therefore ensure that the flux at  $\gamma$ -ray energies is statistically constant, but no such criterion can be applied to other wavelengths due to a lack of monitoring observations. It is possible that variability in the X-ray, optical, or radio band is missed in *Fermi*/LAT and averaged over or completely absent. This effect might contribute to the problems of broadband fitting. Typically, blazar monitoring shows that often the largest and fastest relative changes in flux occur at high and very high energy  $\gamma$ -rays. Variability in the radio occurs on much longer time scales, consistent with the outward traveling of material from the base of the jet and becoming optically thin at different positions.

### Quasi-simultaneous time periods

Due to the large uncertainty of individual flux measurements in fainter AGN, the Bayesian blocks analysis can yield segments of longer than a year during which the  $\gamma$ -ray flux is found to be statistically constant. This behavior can hide true variations in flux. We therefore subdivide Bayesian blocks if they are longer than 1 year into a new size, depending on its *Fermi*/LAT flux in the time range. The new blocks have a size of at least 2, 5, 10, 25, or  $42 \times 14$  d bins, if the *Fermi*/LAT flux in the time range is greater than  $1 \times 10^{-6}$ ,  $0.5 \times 10^{-6}$ ,  $1 \times 10^{-7}$ , or  $1 \times 10^{-8}$   $\text{phs}^{-1} \text{cm}^{-2}$ . This selection of fluxes accounts for longer integration time needed for source with low flux in order to obtain a *Fermi*/LAT spectrum of good quality. For a time bin of 370 d duration with a flux of  $2 \times 10^{-7}$   $\text{phs}^{-1} \text{cm}^{-2}$ , for example, the new time range would be  $10 \cdot 14 \text{ d} = 140 \text{ d}$ . For this new block size we obtain  $370 \text{ d} / 140 \text{ d} = 2.64$  new bins, which means that we subdivide the original interval into  $\lceil 2.64 \rceil = 3$  bins with a length of 185 days each.

Time periods that include  $\gamma$ -ray, X-ray, optical, and VLBI observations are then used for quasi-simultaneous SEDs. Earlier works show that the radio flux varies on longer time scales than the  $\gamma$ -rays (e.g., Soldi et al., 2008). We therefore also include time periods that have  $\gamma$ -ray, X-ray, and optical data in the same block, as well as VLBI observations inside the block, or close to the block start or end. Close to the block is defined as within a time range  $t_{\text{start}}^* = t_{\text{block\_start}} - c$  and  $t_{\text{stop}}^* = t_{\text{block\_stop}} + c$  where  $c = \max\{0.6\Delta t, 50 \text{ d}\}$  and where  $\Delta t$  is the length of the block. The smaller value, 50 d was chosen, as the radio emission varies on much longer time scales, so even for a very short block of e.g., 14 days, using radio data 50 days prior to the start of the block is acceptable. For longer time periods of quiescence it is acceptable to use VLBI data that is offset to the start or stop of the block by 60% of the block length. In the case of the previous example,  $\Delta t = 185 \text{ d}$  and therefore  $c = 111 \text{ d}$ , such that radio data from an interval of  $111 \text{ d} + 185 \text{ d} + 111 \text{ d} = 407 \text{ d}$  length would be considered. It is only a small number of sources where the considered time range is this large. In sources with large error bars considerable time averaging in order to obtain a good quality *Fermi*/LAT spectrum has to be performed, which is why the original sample was limited to ensure that time-averaging is only necessary in a few cases. The time interval exceeds 365 days in 24 of the 81 SEDs due to low flux.

Blocks can be divided according to their average flux ranges into three categories: high, intermediate, and low flux states. We compared the flux in a block with the average flux across the

whole light curve in order to determine its flux “state”. Blocks with a flux between 0.8 and 1.5 of the average flux are labeled as intermediate states. The number of SEDs with the source being in the low state is relatively small. On the other hand, we expect sources to be close to their average flux for most of the time. In the high state, the large number of triggers on such flaring blazars and the higher overall source flux allow for better statistics.

## Fitting strategy

The broadband spectra are fitted with log parabolas. For details see chapter 5.

### Correlation of parameters

In order to produce the results, the fit parameters of the logarithmic parabolas are used. It is necessary to understand the parameters and their uncertainties, as well as their correlations. Figure 6.2 shows the error contours of the three free parameters of the log parabola, as well as the corresponding  $\chi^2$  landscape of the parameter space. Error contours are given at the 68%, 90% and 99% confidence level (solid, dashed and dotted), and the best fit is marked with a white cross. The parameters of the synchrotron parabola are shown in the top right three panels, marked with P1, and the parameters of the high energy parabola are marked with P2. A circular contour shows parameters that are uncorrelated, or only weakly correlated (e.g., the normalization and the curvature  $b$ , or the normalization and the slope  $a$  for P2). This is expected, as a different slope cannot be accounted for by adjusting the normalization. In the synchrotron parabola the normalization seems to be correlated with the slope, possibly indicating a lack of data and therefore a badly constrained parabola. The slope and the curvature of the parabolas are strongly correlated, making it more difficult to find the best fit. This calculation does not include the correlation of both parabolas to the absorbing column  $N_{\text{H}}$ . Curvature in the X-ray spectrum can be misinterpreted as a high absorbing column and vice versa. In cases of low number statistics in the X-rays, the Galactic absorbing column is used. If a good quality X-ray spectrum is available and if the best fit absorbing column exceeds the Galactic value, both are tested in the broadband fit as fixed quantities. This allows to minimize errors due to correlation of absorption and extinction with the parabola parameters. Freezing the absorbing column and the extinction to the same  $N_{\text{H}}$  assumes a Galactic gas-to-dust ratio. No sources were found where the fit to the broadband spectra necessitated using separated values.

Based on the methods outlined above, we fitted all 81 spectra with the spectral model of Eq. (5.8). The fit results are listed in Table A.1. The table shows that even though the logarithmic parabolas are not a physical model, they can describe the broadband behavior very well, reaching low  $\chi^2$  values. We note that FSRQs tend to have an index which is too soft to describe the *Swift*/XRT and the *Fermi*/LAT spectrum perfectly. In some sources the LAT spectrum constrains the curvature of the parabola well, for which the X-ray spectral indices are too soft (see e.g., 1424–418). The reason for this behavior might be due to a spectral break in the MeV energy range. Other possibilities include an accretion disk component in the soft X-rays, or a pion decay signature at MeV energies. We find one source, 2005–489, with a peculiar excess in the hard X-rays above 5 keV, which can be described with a thermal blackbody, but likely only due to a lack of data above 10 keV. It might be possible to explain this with a hadronic proton-synchrotron signature, but the origin is as yet unclear (see Sect. 6.7). In the following sections we describe the behavior of individual parameters in greater detail. For some sources the redshift is unknown. While all broadband SEDs are modeled without k-corrections, the analysis, e.g., of source fluxes or peak positions often

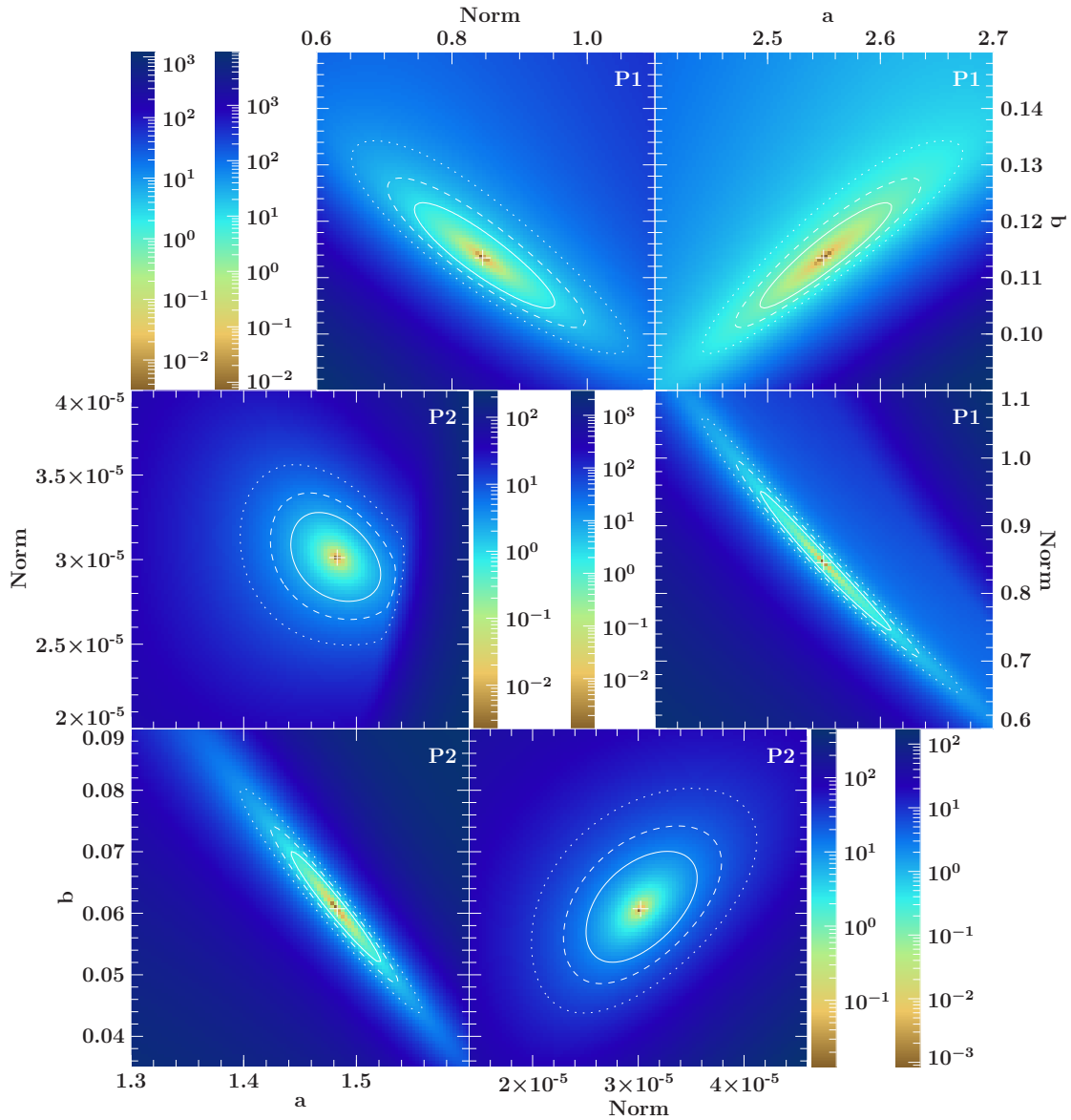


Figure 6.2.: Error contours for the  $\alpha$  time period of 0537–441, six free fit parameters for the case of both parabolas, assuming they both parabolas independent of each other. Colors give the  $\chi^2$  values of the parameter space. The contours are given at the 68%, 90% and 99% confidence level (solid, dashed and dotted), and the best fit is marked with a white cross.

requires knowledge of the redshift. Sources without redshifts are therefore not included in the results, unless noted otherwise.

## The peak positions

### Blazar sequence

The blazar sequence posits that more luminous blazars have lower peak frequencies (Fossati et al., 1998, Ghisellini et al., 1998). While it is heavily debated (e.g., Giommi et al., 2012a,b), it is

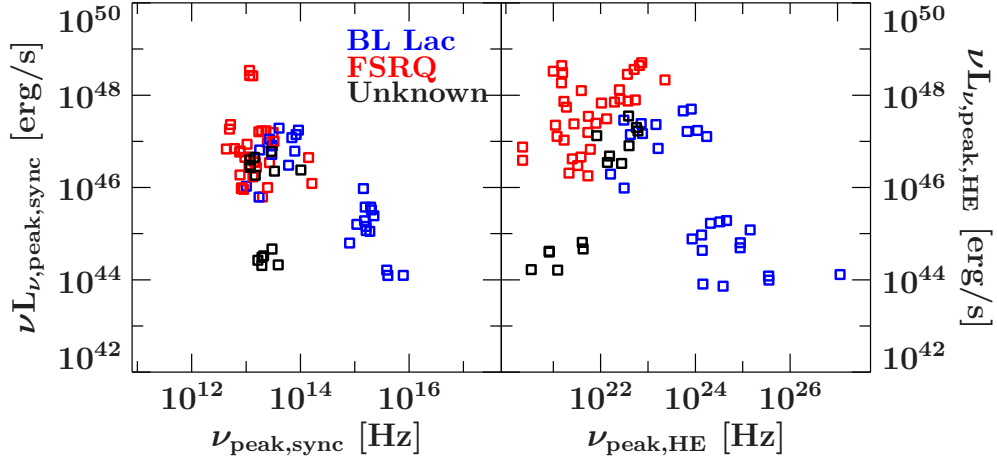


Figure 6.3.: Peak frequency (k-corrected) and peak luminosity for the synchrotron peak (left) and the high energy peak (right).

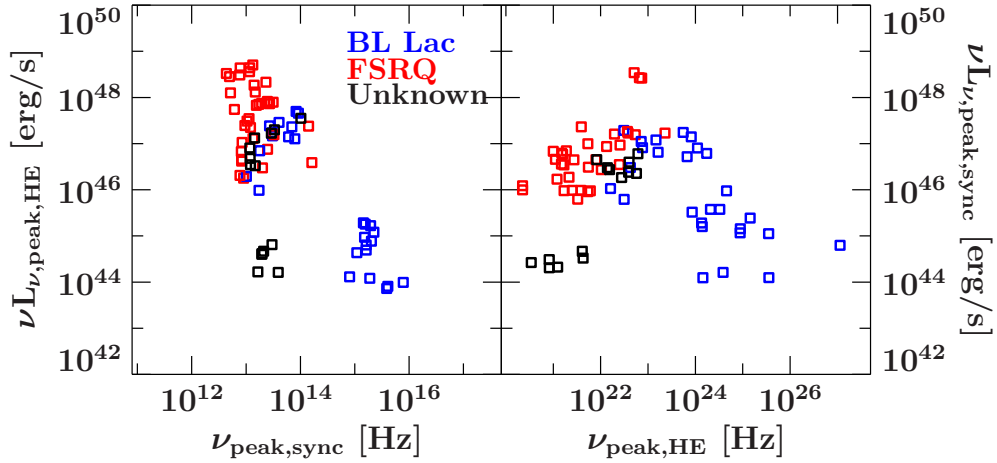


Figure 6.4.: “Inverted blazar sequence”: HE peak luminosity (left) vs. peak synchrotron frequency (k-corrected) and vice versa (right).

generally observed for most sources with known redshift, although sources with low luminosities at low peak frequencies have been found (Nieppola et al., 2006, Meyer et al., 2011, Giommi et al., 2012a). Sources at high luminosities at high peak frequencies are still missing, however. Meyer et al. (2011) propose a modified blazar sequence, where more luminous blazars are more efficient at accretion. Sources with lower peak luminosities and higher peak frequencies than expected are interpreted as being misaligned, leading to a shift in the peak.

Figure 6.3 shows the k-corrected peak frequencies and peak luminosities for all 21 sources in our sample for which a redshift measurement is available. The synchrotron peak results are consistent with the blazar sequence, with a gap between  $10^{14}$  and  $10^{15}$  Hz. This gap has also been seen in the 3LAC (Ackermann et al., 2015d) and has been named the *Fermi* blazars’ divide (Ghisellini et al., 2009). See Sect. 6.4 for a further discussion of this feature. We also find one source, 0521–365 with a lower peak frequency and peak luminosity than expected from the blazar sequence. It is interesting to note, but likely a coincidence, that the peak of this source is perpendicular to the blazar sequence at the location of the gap. While the positions of the high energy peak seem to generally follow the blazar sequence, the spread is much wider, consistent

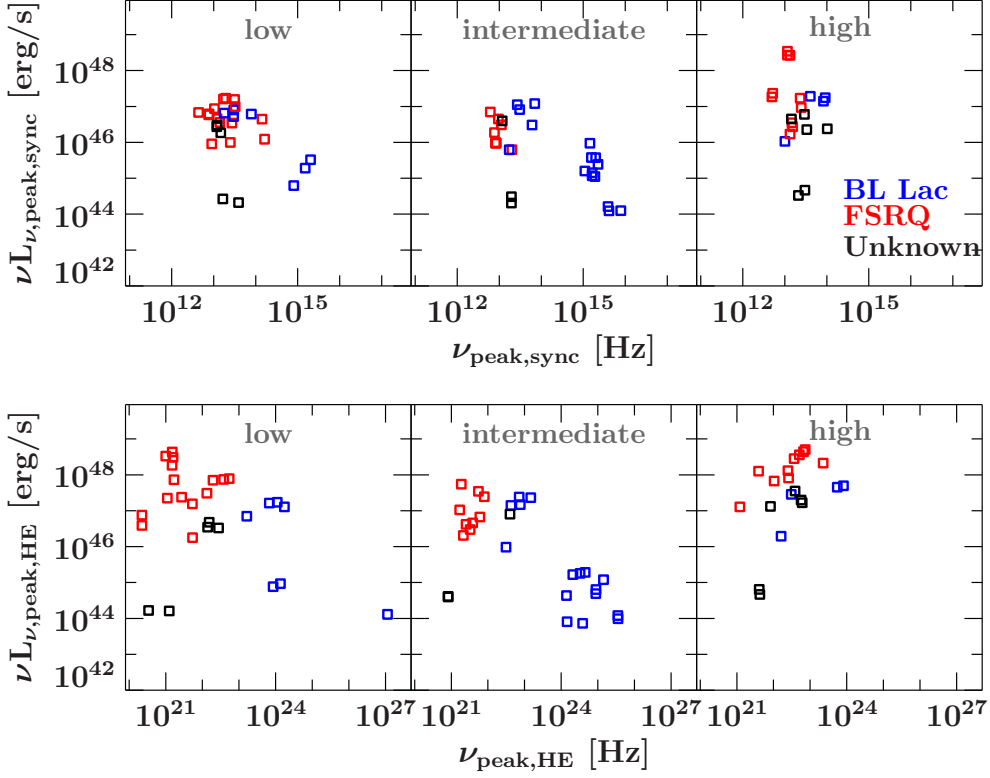


Figure 6.5.: Peak frequencies and peak luminosities, separated into low, intermediate, and high states for the synchrotron peak (top row) and high energy peak (bottom row). While the low and intermediate states follow the blazar sequence for both peaks, the high energy peak in both states show a peculiar, almost inverted behavior, although the number of sources (especially BL Lacertae objects) is too low for any conclusive evidence.

with expectations from a SSC model. We note that when “inverting” the blazar sequence, by looking at the synchrotron peak frequency versus the HE peak luminosity, it still follows the blazar sequence (see Fig. 6.4). The opposite is not true. The HE peak frequency vs the synchrotron luminosity shows a rising and a falling slope (or a V-shape flipped on the horizontal axis), which, when going back to the regular blazar sequence, might also be observed there.

Figure 6.5 shows the blazar sequence separated by the activity of the source at the given time. The upper panel shows the location of the synchrotron peak, the lower panel shows the position of the high energy peak. Both panels are separated into low, intermediate, and high states. We find that in the intermediate state (and possibly in the low state), the sources follow the blazar sequence (Fig. 6.3). In the high state the synchrotron peak results are inconclusive, and seem to scatter. We find what has been seen previously, high-peaked BL Lac objects show a much lower occurrence of large outbursts, and our sample includes no high-peaked SED (above  $10^{14.5}$  Hz) in a high state. And even when we take this lack of data into account, the blazar sequence slope of the high-energy peak in the high state is drastically different from the intermediate state, possibly showing an increase in peak frequency with peak luminosity.

To see whether this behavior is a statistical fluke, we have also looked at the individual behavior. We find that in the intermediate state the high energy peak tends to move towards lower frequencies, but it moves towards higher frequencies in high states. This behavior is discernible for the

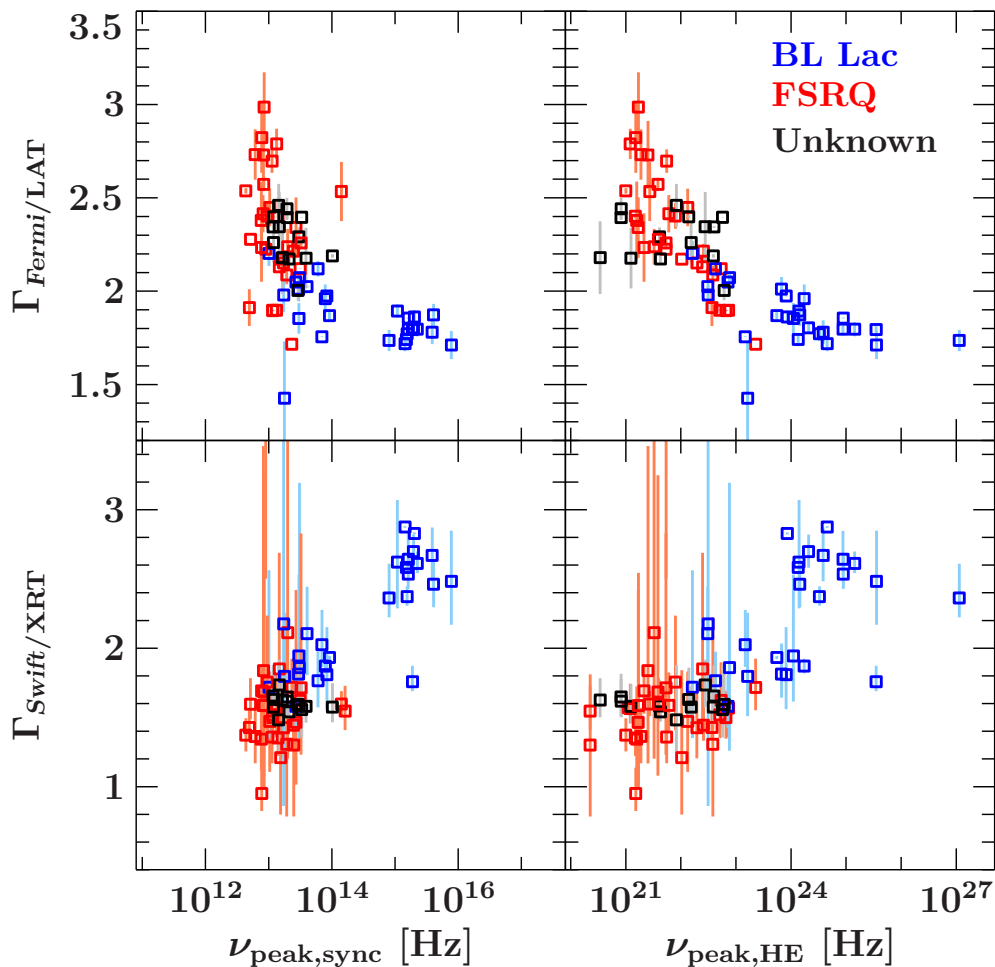


Figure 6.6.: Behavior of the synchrotron (left) and HE (right) peak frequency as a function of the photon index seen in the *Fermi*/LAT (top) and the *Swift*/XRT (bottom).

sources 0521–365, 0537–441, and 1454–354. For 0208–512, 0332–376, 0426–380, and 0402–362 only one of the effects is visible, likely due to a lack of data (see Fig. A.2). For the other sources no disagreeing trends have been found, but some SEDs lack information from all states, e.g., 0402–362 only has two high state SEDs, so no information about the peak shift is available. While this behavior has not been documented for a large sample, a “harder-when-brighter” trend is often seen in the X-ray spectra of flaring blazars and other AGN consistent with a peak shift to higher frequencies (Zamorani et al., 1981, Avni & Tananbaum, 1982, Pian et al., 1998, Vignali et al., 2003, Emmanoulopoulos et al., 2012). For a number of flaring *Fermi*/LAT sources a hardening of the spectral index has also been observed (Abdo et al., 2010c,d), which might be useful in future discrimination between intermediate and flaring states, but no physical explanation is available.

### Spectral index and peak position

The correlations between the spectral indices seen in *Fermi*/LAT and *Swift*/XRT and the synchrotron peak frequency are well documented by the 3FGL catalog (Acero et al., 2015). Correlations with the high-energy peak are less studied. All spectral indices are shown in Fig. 6.6. In Fig. 6.7 they are separated into the low, intermediate, and high state. The top panel of the figure shows the synchrotron peak frequency versus the XRT and LAT indices, while the lower panel

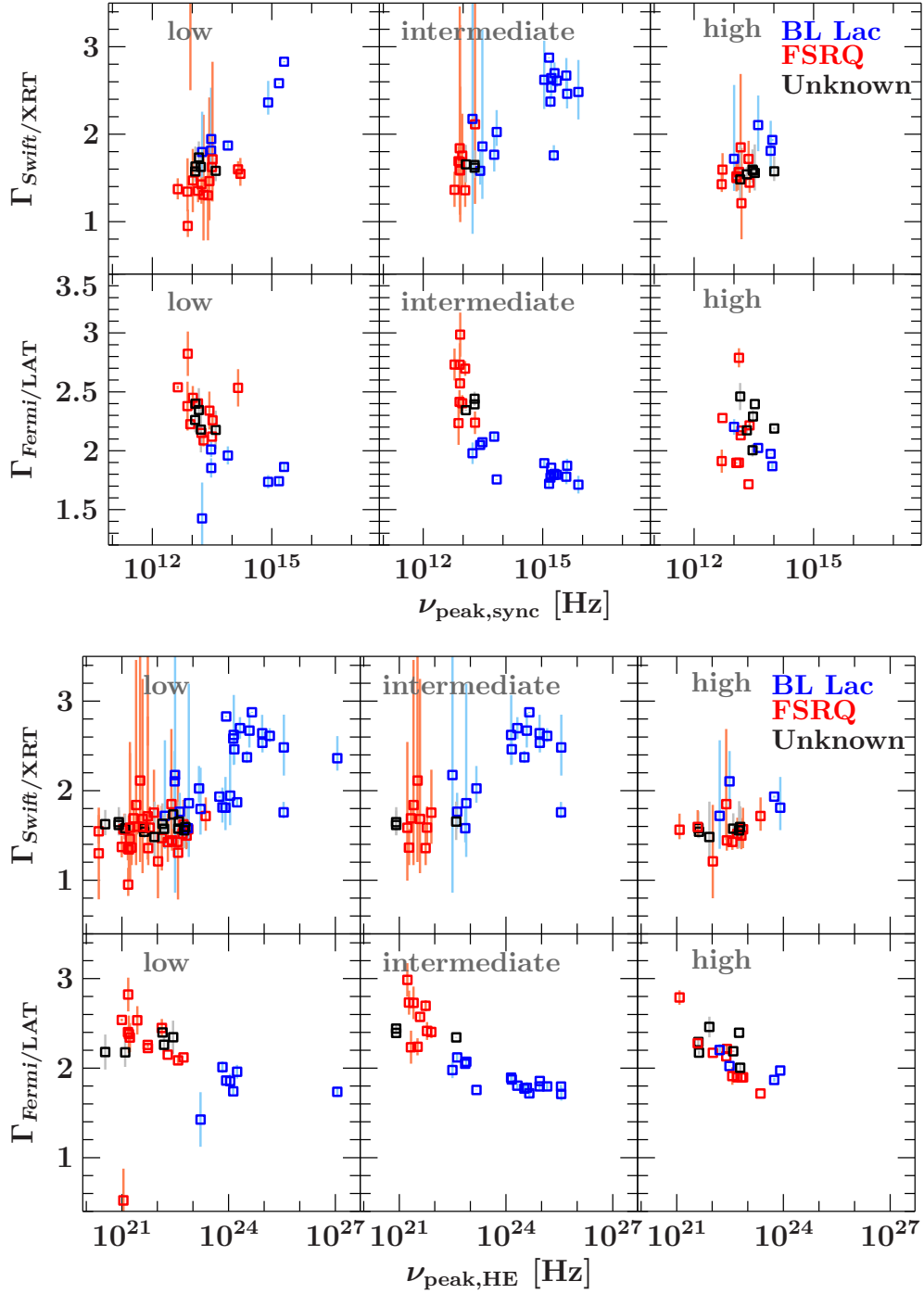


Figure 6.7.: Synchrotron (top) and HE (bottom) peak frequency versus the photon index seen by *Swift*/XRT (top) and *Fermi*/LAT (bottom) separated by low, intermediate, and high state.

shows the high-energy peak frequency versus the XRT and LAT indices. It is interesting to note that the LAT index shows varying behavior in the bottom panel of the top plot (synchrotron peak frequency) in Fig. 6.7 depending on source state, but not in the bottom panel of the bottom plot (HE peak frequency). This change in the high state is consistent with a difference in synchrotron and high-energy peak behavior of the sources. In the low and intermediate state the LAT index

shows a correlation with the synchrotron peak frequency, indicative of correlated processes. The data seems more scattered for SEDs in the high state. This change is indicative of a change in the jet during a high state, such as an acceleration of the jet flow (Marscher et al., 2010).

### Compton dominance and the blazar sequence

Giommi et al. (2012b) suggest that the blazar sequence is due to the selection bias of the observed samples. The sources missing in the blazar sequence are expected to peak in the optical/UV. These sources should be the brightest among the optical-selected blazars. Giommi et al. (2012b) argue that these sources are dominated by jet emission in the optical, making it nearly impossible to determine their redshift spectroscopically. The argument is therefore that these sources exist, and are known, but no luminosities are available. Therefore, Finke (2013) uses the Compton dominance  $F_{\text{peak,HE}}/F_{\text{peak,sync}}$ , a redshift independent quantity to verify the existence of the blazar sequence, and also finds a lack of sources at high peak frequencies and luminosities.

While we might miss low luminosity sources in the TANAMI sample, we would expect to have found sources with high luminosities at high peak frequencies if they exist. These are expected to be bright and have hard spectral indices in *Fermi*/LAT. As our sample is representative of a  $\gamma$ -ray flux-limited sample it is possible that we miss bright sources peaking in the optical if their Compton dominance is low, i.e., if their high-energy peak is faint, possibly even fainter than the synchrotron peak.

Consistent with earlier findings (Giommi et al., 2012b, Finke, 2013), Fig. 6.8 shows that there is a redshift-independent correlation between the ratio of the peak fluxes and the peak frequency. The sequence can be explained physically by increasing power leading to larger external radiation fields and a larger Compton dominance. Higher Compton scattering leads to faster cooling and a lower cut-off of high-energy photons, possibly explaining the observed blazar sequence.

Looking at the state separated behavior (Fig. 6.8, bottom), while the number of SEDs in the high state is low, the behavior during high states is different from the low, and intermediate states. As for the blazar sequence, the low and intermediate states are consistent with expectations from the blazar sequence and FSRQs at higher Compton dominances. In the high states, the Compton dominance shows a large scatter. We further generate the Compton dominance for the bolometric fluxes, instead of the peak flux. The bolometric fluxes are calculated by integrating over each of the two best-fit parabola functions separately (Fig. 6.9). The patterns in Fig. 6.8 and Fig. 6.9 are very similar. While the scatter is lower when using bolometric fluxes, it shows that the peak position is a reliable tracer of the bolometric flux.

### The *Fermi* blazar's divide

In the blazar sequence and Compton dominance a large gap is visible, which seems to separate flat spectrum radio quasars and BL Lacertae objects between  $10^{14}$  and  $10^{15}$  Hz. This gap has also been seen in the 3LAC (Ackermann et al., 2015d), and is now named the *Fermi* blazars' divide as first discussed by Ghisellini et al. (2009). These authors propose a physical difference in these objects with a separation of objects into low and high efficiency accretion flows. It is interesting to note, however, that in our  $\gamma$ -ray flux limited sample this separation is much stronger than in the 3LAC, suggesting a contribution of selection effects. These selection effects can contribute in the same way as to the blazar sequence, i.e., we would expect a lack of redshifts in objects peaking in the optical range ( $10^{14}$ – $10^{15}$  Hz), which would show a featureless spectrum due to a dominant jet component. Further, the extinction in the UV and far-UV, as well as the photoelectric absorption of soft X-rays in our Galaxy, hamper the detection of blazars peaking in this energy range, exactly

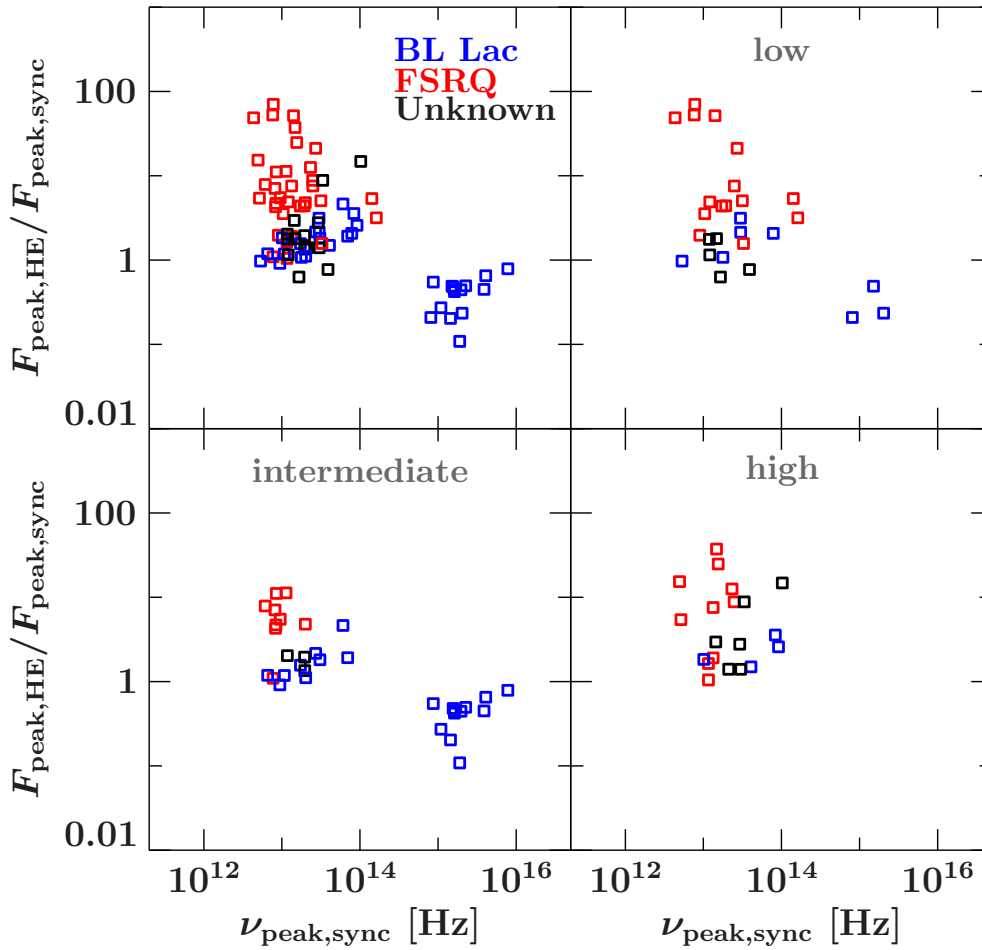


Figure 6.8.: Top left: Compton dominance for all SEDs for all sources (no k-correction). It is interesting to note that the blazar divide is particularly strong; only few sources are found between  $10^{14}$  and  $10^{15}$  Hz. Top right – bottom: Same as above, but SEDs are separated into low, intermediate, and high states.

those peak frequencies missing in the blazar’s divide. We expect that this can fully explain the *Fermi* blazar’s divide and is also consistent with observations of black hole binaries, which do not show a gap between accretion states.

Selection effects are able to explain the blazar’s divide, while the argument is less clear for the blazar sequence, which is found even in the Compton dominance, which is redshift-independent. While selection effects can explain many of the observed features, it is peculiar that no source has been found at high peak frequencies and luminosities so far.

## The big blue bump

It is generally believed that the thermal excess seen in many FSRQ objects and in a small number of BL Lac objects is the thermal emission from the accretion disk (Shields, 1978, Malkan & Sargent, 1982). An alternative model explains the BBB with free-free emission from the hot corona of the supermassive black hole (Barvainis, 1993). While no conclusive evidence for either theory has been presented, several problems with the accretion disk have been noted, namely the temperature problem, the ionization problem, the time-scale problem and the co-ordination problem. The

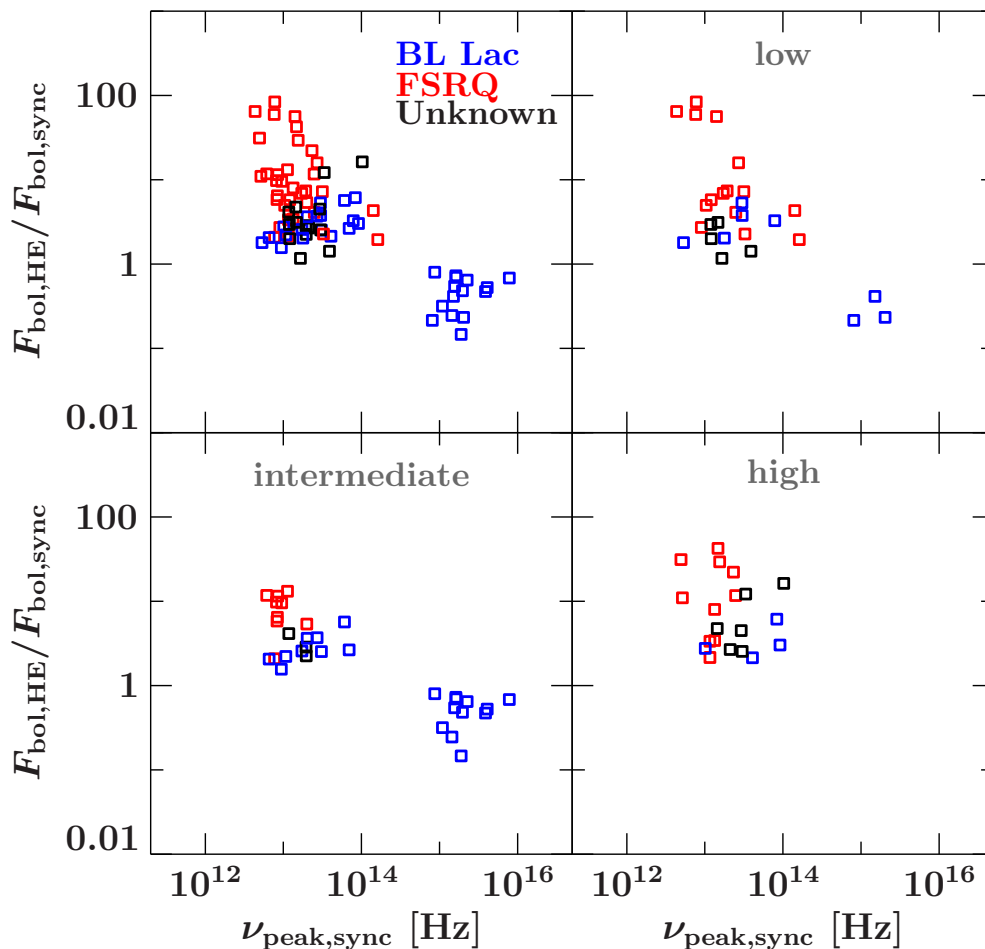


Figure 6.9.: Top left: Compton dominance for all SEDs for all sources (no k-correction). In comparison to Fig. 6.8, the bolometric fluxes were used. It is interesting to note that the blazar divide is particularly strong. Top right, bottom: Same as above, but SEDs are separated into low, intermediate, and high states.

temperature problem states that the observed temperatures at  $\sim 30000$  K are too low for what would be expected ( $\sim 76000$  K). Lawrence (2012) proposes a reprocessing of the accretion disk emission by clouds in the BLR and is able to explain all four problems.

Concerning the temperature, our results are consistent with what has been found previously (Zheng et al., 1997, Telfer et al., 2002, Scott et al., 2004, Binette et al., 2005, Shang et al., 2005).

For all sources the temperature remains below  $\sim 32000$  K. Some BL Lac objects exhibit temperatures of  $\sim 6000$  K (see Fig. 6.10, marked by a gray vertical line). Such cold black bodies are very likely emission from the host galaxy, which would support the theory of a weak disk and inefficient accretion in BL Lac objects<sup>1</sup>.

In general, the spectral shape of the thermal excess is also inconsistent with an accretion disk origin. For all SEDs the thermal excess can be well described by a single temperature black body. For an accretion disk extending from a few to several hundreds or thousands of gravitational radii a large range in temperature would be expected due to the  $r^{-3/4}$  temperature profile of accretion

<sup>1</sup>Note that gravitational redshifting decreases the observed temperature, but even taking this effect into account would only slightly increase the temperatures by  $\sim 3000$  K, still nowhere near the expected temperature for an accretion disk.

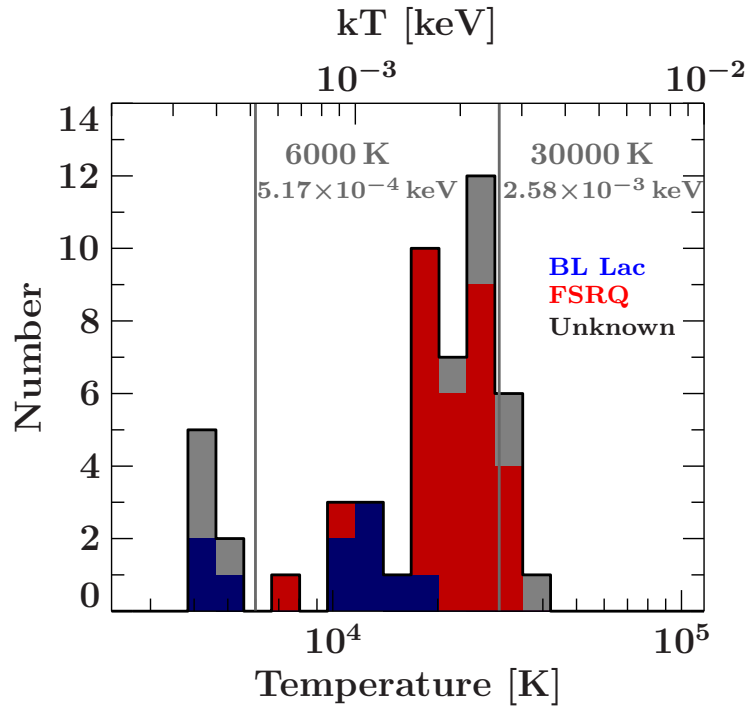


Figure 6.10.: Histogram of observed blackbody temperatures for all SEDs. Blackbody temperatures at  $\sim 6000$  K (marked in gray with a vertical line) very likely represent a detection of the host galaxy. A temperature of 30000 K is marked with another vertical gray line.

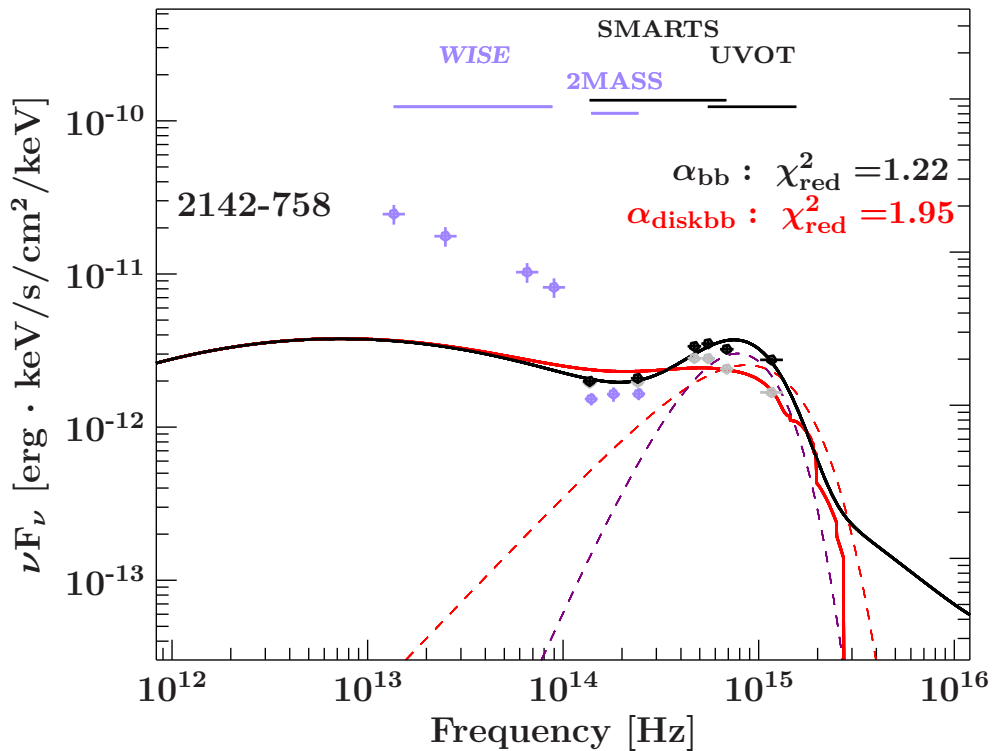


Figure 6.11.: SED of the  $\alpha$  state of 2142–758, with the best fit single temperature black body (purple) and best fit multi temperature accretion disk spectrum (red).

Table 6.2.: Parameters of the fundamental plane of black hole

Reference	$d$	$e$	$f$	$\nu_{\text{radio}}$ [GHz]	source population
Merloni et al. (2003)	$1.28 \pm 0.15$	$0.77 \pm 0.17$	9.40	5.0	Quasars, LINERs, Seyferts
Körding et al. (2006)	$1.28 \pm 0.30$	$0.73 \pm 0.20$	10.49	5.0	Quasars, LINERs, Seyferts
Gültekin et al. (2009)	$0.48 \pm 0.17$	$0.24 \pm 0.16$	0.83	5.0	Seyferts, Transition Objects, Unclassified Objects
Bonchi et al. (2013)	1.47	$0.57 \pm 0.07$	24.43	1.4	Type 1 & Type 2
Nisbet & Best (2016)	$1.45 \pm 0.22$	$0.94 \pm 0.18$	8.01	1.4	LINERs

disks, with further slight stretching of the spectrum by gravitational redshifting. Figure 6.11 shows that the shape is reasonably constrained by *Swift*/UVOT. The red curve shows the spectrum expected from a simple multi-temperature accretion disk. This diskbb model is not able to describe the narrow shape as well as a single temperature black body (purple line in Fig. 6.11). While this evidence is not conclusive due to the low spectral resolution of the UVOT, it nevertheless is indicative of a more complex disk structure, which might be puffed up and warped or truncated, leading to changes in the thermal emission. Further theoretical and observational studies are necessary to determine the origin and shape of the big blue bump.

## The black hole mass, $M_{\text{BH}}$

We study how the properties of the SED depend on the black hole mass. The fundamental plane of black holes (Merloni et al., 2003, Gallo et al., 2003, Falcke et al., 2004, Körding et al., 2006, Gültekin et al., 2009, Plotkin et al., 2012, Bonchi et al., 2013, Gültekin et al., 2014, Saikia et al., 2015, Nisbet & Best, 2016, and references therein) relates the radio and X-ray luminosity to the black hole mass,

$$\log\left(\frac{M_{\text{BH}}}{M_{\odot}}\right) = d \log\left(\frac{L_{\text{radio}}}{\text{erg s}^{-1}}\right) - e \log\left(\frac{L_{\text{X-ray}}}{\text{erg s}^{-1}}\right) - f \quad (6.5)$$

The parameters  $d$ ,  $e$ , and  $f$  depend on the source populations. Table 6.2 lists typical recent values for AGN. Here  $L_{\text{radio}}$  is the radio flux density measured at the frequency  $\nu_{\text{radio}}$  listed in Table 6.2, while  $L_{\text{X-ray}}$  is the X-ray flux in the 2–10 keV band. We caution that the radio luminosities listed are not “real” luminosities, as the differential flux at the given radio frequency is simply multiplied by  $4\pi d_L^2$ , instead of using an integrated flux in a waveband.

Black hole mass measurements, based on measurements of the BBB (for FSRQs), and variability arguments (BL Lacs), only exist for 8 of the 20 sources in our sample and are taken from Ghisellini et al. (2010). We note that for some sources very different black hole mass measurement exists (e.g., 0208–512; Stacy et al., 2003), which vary by an order of magnitude. We therefore use the fundamental plane to estimate the black hole mass and compare the estimates with measurements, where available. We use the distance corrected radio flux density from the best-fit parabola model at the same frequency as used in each of the studies. The X-ray 2–10 keV luminosity is taken from the separate fit to the X-ray data. We use all SEDs from this work and the corresponding X-ray and radio luminosities (where a redshift measurement is available, see Tab.6.1) and calculated estimated black hole masses following Merloni et al. (2003), Körding et al. (2006), and Nisbet & Best (2016). Our results are presented in Table 6.3. For the results from Gültekin et al. (2009) we use Eq. 4, with the parameters listed in Eq. 6, where a linear regression was performed in order to find an equation for an estimate of the black hole mass. For sources with more than one SED, the

Table 6.3.: Black hole masses as measured and as estimated from the fundamental plane of black holes

Source	$M_{\text{BH}}$ [ $M_{\odot}$ ]	$M_{\text{BH,Merloni}}$ [ $M_{\odot}$ ]	$M_{\text{BH,Koerding}}$ [ $M_{\odot}$ ]	$M_{\text{BH,Gültekin}}$ [ $M_{\odot}$ ]	$M_{\text{BH,Bonchi}}$ [ $M_{\odot}$ ]	$M_{\text{BH,Nisbet}}$ [ $M_{\odot}$ ]	$L_{\text{edd}}$ $10^{46}$ [ $\text{erg s}^{-1}$ ]
0208-512	$7 \times 10^8$	$(5.3^{+2.1}_{-648.0}) \times 10^5$	$(5.5^{+1266.2}_{-2.5}) \times 10^6$	$(2.8^{+1.0}_{-10.8}) \times 10^7$	$(7.3^{+3.0}_{-12289.4}) \times 10^8$	$(1.52^{+0.07}_{-0.08}) \times 10^4$	9.1
0244-470		$(1.4^{+1.5}_{-551.7}) \times 10^5$	$(1.5^{+607.2}_{-1.5}) \times 10^6$	$(1.8^{+1.8}_{-23.2}) \times 10^7$	$(6^{+7}_{-27579}) \times 10^7$	$(1.2^{+0.6}_{-0.9}) \times 10^3$	
0402-362		$(1.5^{+1.6}_{-733.1}) \times 10^5$	$(1.8^{+727.2}_{-1.8}) \times 10^6$	$(2.1^{+2.0}_{-31.2}) \times 10^7$	$(1.0^{+1.1}_{-5252.4}) \times 10^8$	$(7^{+4}_{-8}) \times 10^2$	
0426-380	$4 \times 10^8$	$(1.2^{+0.7}_{-186.9}) \times 10^6$	$(1.3^{+492.5}_{-0.7}) \times 10^7$	$(3.8^{+1.8}_{-17.7}) \times 10^7$	$(1.6^{+0.9}_{-3595.7}) \times 10^9$	$(3.91 \pm 0.13) \times 10^4$	5.2
0447-439	$6 \times 10^8$	$(3.0^{+2.2}_{-1210.0}) \times 10^2$	$(2.7^{+197.8}_{-1.9}) \times 10^3$	$(1.4^{+1.0}_{-23.5}) \times 10^6$	$(1.9^{+1.4}_{-4215.4}) \times 10^4$	$2.0^{+1.1}_{-3.9}$	7.8
0506-612		$(4.6^{+2.7}_{-856.8}) \times 10^5$	$(4.7^{+1488.7}_{-2.8}) \times 10^6$	$(2.7^{+1.5}_{-16.4}) \times 10^7$	$(6^{+4}_{-14094}) \times 10^8$	$(1.39^{+0.12}_{-0.14}) \times 10^4$	
0521-365		$(4.6^{+2.3}_{-884.7}) \times 10^3$	$(4.0^{+410.5}_{-2.0}) \times 10^4$	$(3.9^{+1.7}_{-2.8}) \times 10^6$	$(5.1^{+2.7}_{-8532.1}) \times 10^5$	$57^{+16}_{-35}$	
0537-441	$2 \times 10^9$	$(3.0^{+1.5}_{-378.9}) \times 10^6$	$(3.0^{+1402.4}_{-1.6}) \times 10^7$	$(5.3^{+2.2}_{-20.2}) \times 10^7$	$(7^{+4}_{-14066}) \times 10^9$	$(1.41^{+0.23}_{-0.18}) \times 10^5$	26.0
0637-752		$(5.1^{+3.0}_{-994.8}) \times 10^5$	$(5^{+1728}_{-1.1}) \times 10^6$	$(2.9^{+1.6}_{-18.2}) \times 10^7$	$(1.5^{+0.9}_{-3692.5}) \times 10^9$	$(2.70^{+0.13}_{-0.13}) \times 10^4$	
1057-797	$6 \times 10^8$	$(7^{+2}_{-1810}) \times 10^5$	$(6^{+3789}_{-7}) \times 10^6$	$(2.8^{+2.6}_{-26.7}) \times 10^7$	$(5^{+5}_{-17053}) \times 10^8$	$(1.85^{+0.13}_{-0.14}) \times 10^4$	7.8
1424-418		$(1.3^{+0.7}_{-201.6}) \times 10^6$	$(1.5^{+495.9}_{-0.7}) \times 10^7$	$(4.2^{+1.7}_{-18.5}) \times 10^7$	$(1.2^{+0.7}_{-2817.0}) \times 10^9$	$(1.30^{+0.09}_{-0.12}) \times 10^4$	
1440-389		$(9^{+7}_{-3840}) \times 10^1$	$(7^{+448}_{-6}) \times 10^2$	$(9^{+6}_{-155}) \times 10^5$	$(6^{+5}_{-14397}) \times 10^3$	$0.9^{+0.6}_{-2.2}$	
1454-354	$2 \times 10^9$	$(1.0^{+0.8}_{-210.7}) \times 10^6$	$(1.0^{+483.5}_{-0.8}) \times 10^7$	$(3.6^{+2.3}_{-24.3}) \times 10^7$	$(1.6^{+1.2}_{-4673.4}) \times 10^9$	$(3.71 \pm 0.07) \times 10^4$	26.0
1610-771		$(7^{+8}_{-2625}) \times 10^5$	$(8^{+4694}_{-8}) \times 10^6$	$(4^{+6}_{-41}) \times 10^7$	$(2.2^{+2.3}_{-10480.7}) \times 10^9$	$(2.2^{+0.4}_{-0.5}) \times 10^4$	
1954-388		$(6^{+6}_{-1619}) \times 10^5$	$(5^{+3137}_{-6}) \times 10^6$	$(2.7^{+2.5}_{-26.8}) \times 10^7$	$(7^{+8}_{-28345}) \times 10^8$	$(2.56 \pm 0.10) \times 10^4$	
2005-489	$5 \times 10^8$	$(1.2^{+1.2}_{-150.2}) \times 10^3$	$(1.0^{+150.1}_{-1.1}) \times 10^4$	$(2.3^{+2.3}_{-43.4}) \times 10^6$	$(1.1^{+1.1}_{-327.9}) \times 10^5$	$14^{+9}_{-25}$	6.5
2052-474		$(1.2^{+1.2}_{-377.9}) \times 10^6$	$(1.3^{+853.3}_{-1.3}) \times 10^7$	$(4^{+4}_{-41}) \times 10^7$	$(1.6^{+1.1}_{-7128.6}) \times 10^9$	$(2.46^{+0.27}_{-0.31}) \times 10^4$	
2142-758		$(3^{+4}_{-1164}) \times 10^5$	$(3^{+1664}_{-4}) \times 10^6$	$(2.5^{+2.3}_{-29.3}) \times 10^7$	$(5^{+5}_{-19771}) \times 10^8$	$(7.1^{+1.9}_{-2.3}) \times 10^3$	
2149-306		$(2.0^{+1.3}_{-605.2}) \times 10^5$	$(2.4^{+659.2}_{-1.5}) \times 10^6$	$(2.4^{+1.4}_{-21.4}) \times 10^7$	$(1.2^{+0.8}_{-4398.7}) \times 10^9$	$(5.1^{+1.7}_{-1.7}) \times 10^3$	

**Notes.** Columns: (1) IAU B1950 name, (2)  $M_{\text{BH}}$  from Ghisellini et al. (2009),  $M_{\text{BH}}$  estimated after (3) Merloni et al. (2003), (4) KÖrding et al. (2006), (5) Gültekin et al. (2009), (6) Bonchi et al. (2013), (7) Nisbet & Best (2016), (8) Eddington luminosity for the measure black hole mass, assuming isotropic emission Note. The black hole mass estimates include the uncertainties from the parameters, not the uncertainties in luminosities, as these are much smaller.

black hole mass estimates are averaged. The masses before averaging scatter depending on source state with a maximum factor of 5 between the lowest and the highest estimate.

All estimates except those using the parameters from Bonchi et al. (2013) are lower than the measured values, with the largest offset being that from the Merloni et al. (2003) parameters. Applying the relation by Bonchi et al. (2013) gives a very good agreement (less than a factor of 3) with the measurement values for several sources such as 0208–512, 0537–441, 1057–797, and 1454–354. The largest difference is seen between the measurement and the estimate for 0447–439, with four order of magnitude between the estimate using the Bonchi et al. (2013) parameters, and 6 orders of magnitude using the Merloni et al. (2003) parameters.

While a large scatter is observed for the fundamental plane, it probably does not explain a difference of four or six orders of magnitude. A possibility is that the relativistic boosting affects the observed masses in supermassive black holes, but not the Galactic black holes. However, this would imply that the intrinsic black hole masses in some of the AGN are much lower than previously believed. We note that the uncertainties on the parameters of the fundamental plane are large, which is represented in the large uncertainties of the black hole mass estimates.

## The strange SED of 2005–489

In general, all SEDs are well described by two log parabolas and a blackbody to describe the excess. 2005–489, a well known VHE emitter (Aharonian et al., 2005), is the only source with a strong deviation from this model (see Fig. 6.12). VLBI data of the source has been presented by Piner & Edwards (2014). The multiwavelength SED has been studied several times (Kaufmann et al., 2009, H.E.S.S. Collaboration: et al., 2010), with the latter arguing about a hard, separate spectral component emerging in the X-ray observations in September 2005. This is in agreement

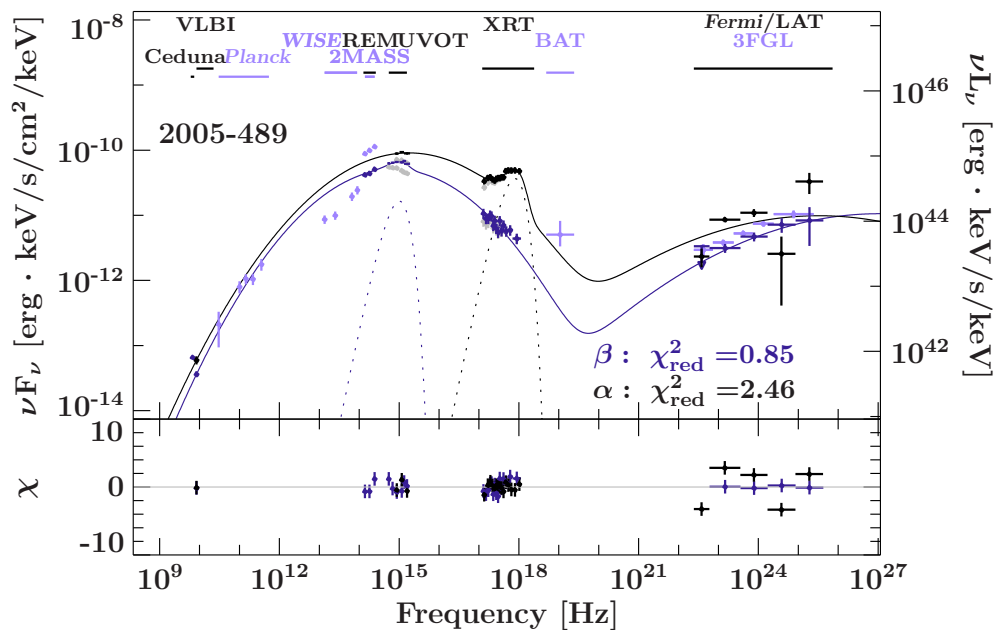


Figure 6.12.: SED of 2005–489 showing the additional component at hard X-rays, which is fitted with a blackbody model in the high state ( $\alpha$ ).

with our results of the source during a high state. While over most of the energy range it shows a non-thermal parabolic behavior, its X-ray behavior in the high state ( $\alpha$ ) seems to be inconsistent with a leptonic model. In the low state ( $\beta$ ), the photon index  $\Gamma = 2.28 \pm 0.12$  perfectly fits the parabolic shape, we note that the 104-month averaged BAT data point seems to indicate a small excess above a pure power law. While this is not conclusive, the photon index  $\Gamma = 1.70 \pm 0.04$  in the high state is inconsistent with the parabolic model (and a synchrotron model as well). The excess is reminiscent of hadronic proton-synchrotron signature in the spectrum, while the LAT data might also show a dip in the spectrum, possibly due to a hadronic pion decay signature. While this evidence is not conclusive it is the first source to show a clear deviation, with a large difference in the photon index within a time span of less than 2 years. A caveat of this SED is the long time range over which the data were averaged in LAT, but it does not explain the change in index and the inconsistency between the *Swift*/UVOT and *Swift*/XRT data.

# Chapter 7

## Neutrinos from blazar jets

Bert: Ernie! Get serious, will ya? We're supposed to be looking for Big Bird.  
Bert: See that yellow spot down there? It's Big Bird!

---

Judy Freudberg, *Sesame Street Presents: Follow that Bird*, 1985

This Chapter is based on the following publications and is taken in large parts in verbatim from them: Krauß et al. (2014) and Krauß et al. (2015). I lead these two publications. For the third publication I constructed the broadband spectra, fitted them and calculated the expected neutrino values, and also contributed to the text and discussion of the results (Kadler et al., 2015a). Since the text has been taken in verbatim from the publications, the text uses ‘we’, where appropriate.

One of the key questions of blazar studies is the physical mechanism responsible for the high-energy hump. The two main models (as discussed in Sect. 3.3.5) are leptonic and hadronic jets. Describing broadband SEDs with hadronic and leptonic models as a way to distinguish the mechanisms is difficult, due to large gaps in broadband coverage and a large number of unknown parameters (e.g., black hole mass, Lorentz factor, electron/proton injection rate). Currently, hadronic and leptonic model can describe the observed broadband spectra equally well (Böttcher et al., 2013). Unambiguous evidence of hadronic processes could be provided by neutrino observations, as neutrinos can only be explained by hadronic processes. It is worth noting that leptonic and hadronic processes are not exclusive and a leptonic contribution is generally expected. Neutrino emission has been theoretically predicted for extragalactic sources from the cores of active galactic nuclei (AGN, Stecker, 2013), AGN jets (Mannheim, 1995a), or gamma-ray bursts (Waxman & Bahcall, 1997). The detection of neutrinos at PeV energies in excess of the atmospheric background reported by the IceCube Collaboration (Aartsen et al., 2013, IceCube Collaboration, 2013) has therefore prompted a quest to identify their extraterrestrial sources. I show in this Chapter that blazars are energetically able to explain the observed neutrino flux. Furthermore, we study the probability that the observed neutrinos originate in blazars.

### Broadband transmission of Ernie and Bert

In 988 days of IceCube data (~3 years), three events above energies of 1 PeV have been detected (IC 20, dubbed ‘Ernie’, IC14, ‘Bert’ and IC 35, ‘Big Bird’), between May 2010 and May 2013 (Aartsen et al., 2014). A third event at 2 PeV (IC 35; dubbed ‘BigBird’) was recorded in the third year of IceCube data on 2012, Dec 4 (Aartsen et al., 2014). The IceCube analysis concentrated on very-high-energy events with interaction signatures that were fully contained within the detector (High Energy Starting Events; HESE). In combination with an equal-neutrino-flavor flux at Earth (Aartsen et al., 2015), this resulted in the majority of the detected events being cascade-like with

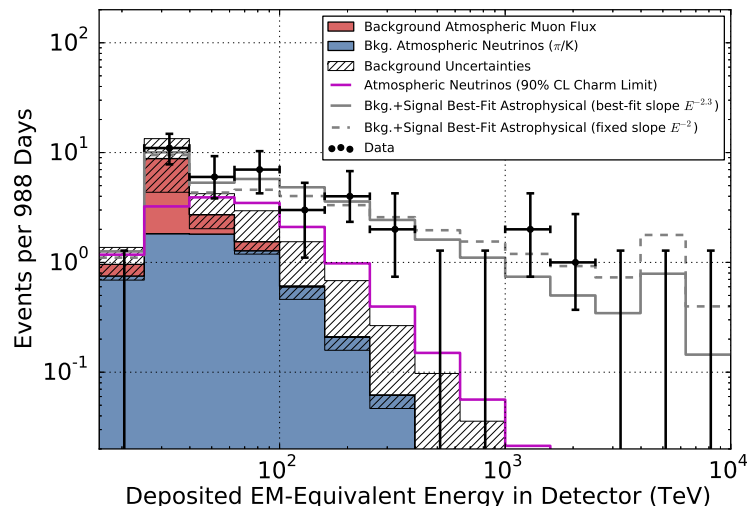


Figure 7.1.: Number of IceCube events in logarithmic energy bins in three years of IceCube data (black). The atmospheric background from neutrinos and muons is shown in blue and red and the corresponding uncertainty is shown shaded. The data at PeV energies clearly exceeds the models. (Aartsen et al., 2014)

relatively large median positional uncertainties ( $R_{50}$ ) of typically  $10^\circ$  to  $20^\circ$ . While a number of different source classes have been discussed as a possible origin of a diffuse neutrino flux (Krauß et al., 2014, Mannheim & Biermann, 1992, Mannheim, 1995a, Stecker, 2013, Fox et al., 2013, Taylor et al., 2014, Padovani & Resconi, 2014, Murase et al., 2014, Becker Tjus et al., 2014), no individual astrophysical object has been identified so far from which a neutrino flux with a substantial Poisson probability for a detection by IceCube is expected.

In this Section I discuss the first two events, detected in the first two year of IceCube. The third event will be discussed in the next Section. IC 20 and IC 14 have angular uncertainties of  $10.7^\circ$  and  $13.2^\circ$ , respectively (Aartsen et al., 2013), which impedes a direct association to an individual source or source class.

The total signal by IceCube in three years of data exceeds a purely atmospheric background at the  $5.7\sigma$  confidence level (see Fig. 7.1, Aartsen et al., 2014). The atmospheric background is expected to be steeply falling and the events at PeV energies are therefore of extraterrestrial origin. Furthermore, a fraction of the sub-PeV events detected are also expected to be extraterrestrial. Several of the detected neutrinos lie in the Galactic plane, towards the Galactic center. The Galactic center has been considered as origin of these neutrinos (Razzaque, 2013), but a single source has been excluded by Adrián-Martínez et al. (2014a). Pevatrons in the Galactic center region, such as young supernova remnants, produce neutrinos at well below 1 PeV (Aharonian & Atoyan, 1996). The overall distribution of all 37 IceCube events is consistent with an isotropic source population, and therefore extragalactic sources (AGN and GRBs) are the prime suspects.

Prevailing models for gamma-ray bursts have recently been excluded as neutrino sources (Abbasi et al., 2012), and revised models predict much lower neutrino fluxes than the observed excess (Winter, 2013). Among the models for a diffuse, isotropic neutrino flux at PeV energies, only the predicted flux of  $\sim 10^{-8} \text{ GeV cm}^{-2} \text{ s}^{-1} \text{ sr}^{-1}$  from AGN jets matches the observed excess flux well (Learned & Mannheim, 2000), although it does not explain the absence of Glashow-resonance events and the possible gap between 400 GeV and 1 PeV.

Table 7.1.: TANAMI sources compatible with the two IceCube PeV events IC 14, and IC 20.

Source	R.A.[°]	De.c[°]	z	Class.	$\Theta$ [°]
0235–618	39.2218 <sup>△</sup>	–61.6043 <sup>△</sup>	0.47 <sup>◆</sup>	FSRQ <sup>◆</sup>	5.61
0302–623	45.9610 <sup>†</sup>	–62.1904 <sup>†</sup>	1.35 <sup>◆</sup>	FSRQ <sup>◆</sup>	5.98
0308–611	47.4838 <sup>†</sup>	–60.9775 <sup>†</sup>	1.48 <sup>◆</sup>	FSRQ <sup>◆</sup>	7.39
1653–329	254.0699 <sup>△</sup>	–33.0369 <sup>△</sup>	2.40 <sup>◊</sup>	FSRQ <sup>◊</sup>	11.18
1714–336	259.4001 <sup>★</sup>	–33.7024 <sup>★</sup>	?	BL Lac <sup>▲</sup>	7.87
1759–396	270.6778 <sup>●</sup>	–39.6689 <sup>●</sup>	1.32 <sup>■</sup>	FSRQ <sup>■</sup>	12.50

**Notes.** Columns: (1) IAU B1950 name, (2) right ascension, (3) declination, (4) redshift, (5) optical classification, (6) angular distance to IceCube event coordinates

◆ Healey et al. (2008b), △ Cutri et al. (2003), † Lambert & Gontier (2009), ★ Immer et al. (2011), ● Fomalont et al. (2003), ▲ Véron-Cetty & Véron (2006), ■ Massaro et al. (2009b), ◊ Masetti et al. (2008)

### TANAMI sources in the two PeV-neutrino fields

Six TANAMI sources are located in the median positional uncertainty region for the two PeV events (Table 7.1). The three blazars PKS B0235–618 (in the following referred to as 0235–618), PKS B0302–623 (0302–623), and PKS B0308–611 (0308–611) are located in the E20 field. In the E14 field we find the three blazars Swift J1656.3–3302 (1653–329), PMN J1717–3342 (1714–336) and PMN J1802–3940 (1759–396). Of the twelve brightest  $\gamma$ -ray sources (in the two fields) from the 2FGL catalog, only these six named sources have correlated VLBI flux densities at 8.4 GHz above 400 mJy. All other sources are considerably fainter with typically 30 mJy to 160 mJy at 1.4 GHz and on kpc scales (Condon et al., 1998). The source 0235–618 is formally also consistent with IceCube event 7 (34.3 TeV), while 1653–329 and 1714–336 are also within the error circles of events 2 (117 TeV) and 25 (33.5 TeV). The source 1759–396 further agrees with the positions of events 2 (117 TeV), 15 (57.5 TeV), and 25 (33.5 TeV).

### VLBI images

The TANAMI VLBI jets of 0235–618, 0308–611, and 1759–396 are one-sided, indicating relativistic boosting at small angles to the line of sight (see Fig. 7.2). The northwest direction of the 0308–611 jet does not agree with the position angle indicated by the VLBI Space Observatory Program (VSOP) image of Dodson et al. (2008), which might be due to jet curvature or the limited  $(u, v)$ -coverage of VSOP. The source 0302–623, which appeared point-like in Ojha et al. (2004), shows a highly peculiar morphology with a compact core and a strong halo-like emission region around the core. The east-west extension agrees with Dodson et al. (2008). We find a high brightness temperature, which was derived following Kovalev et al. (2005) from Gaussian model fits to the visibility data. The brightness temperatures are several times  $10^{11}$  K in four objects, which is typical of  $\gamma$ -ray-emitting blazars (Linford et al., 2012). We resolve the core components at least partially, but the values should be considered lower limits, as smaller emission regions may contribute to the total emission. We find that 1714–336 is substantially scatter broadened. The image of 1653–329 is from one single scan in 2008 February, outside the IceCube integration period and does not have the same quality as other TANAMI images. The data are consistent with a point source with a total flux density of 340 mJy at 8.4 GHz and a flat spectral index of  $\lesssim -0.2$ . The spectral index is defined as  $S_\nu \propto \nu^\alpha$ . At 22.3 GHz, the cores are not resolved because of shorter baselines.

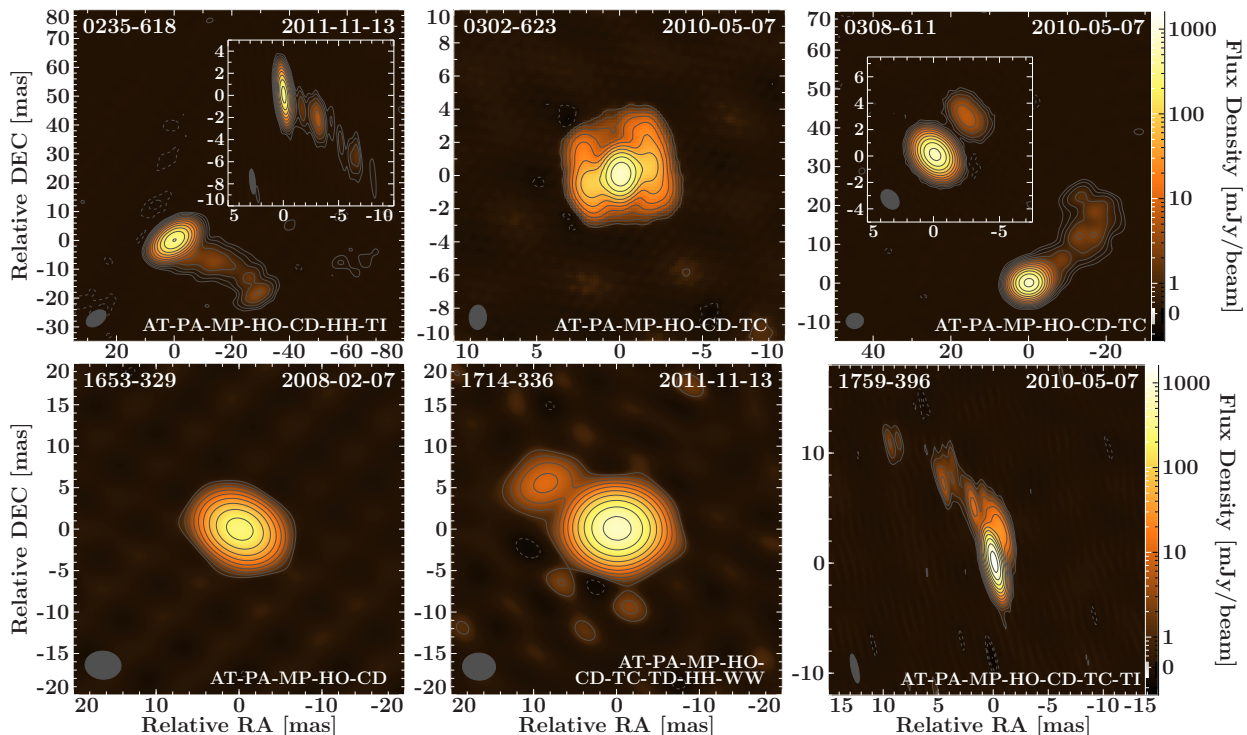


Figure 7.2.: VLBI images at 8.4 GHz (natural weighting for insets of 0235–618 and 0308–611 and all other images; tapered to 10% at  $100 M\lambda$  for main panels of 0235–618 and 0308–611). Restoring beams are shown in the bottom left corners. The color scale covers the range between the mean noise level and the maximum flux density (1759–396). The color scale covers the range between the mean  $\sigma_{\text{rms}}$  and the maximum  $S_{\text{peak}}$  (see Table 7.2 for image parameters). Contour lines start at  $3\sigma_{\text{rms}}$  and increase logarithmically by factors of 2. The array is given in the bottom right corner: PA: Parkes, AT: ATCA, MP: Mopra, HO: Hobart, CD: Ceduna, HH: Hartebeesthoek, TC: Tigo, TI: Tidbinbilla (70 m), TD: Tidbinbilla (34 m), WW:Warkworth

### Broadband spectra

For all six sources, we find characteristic double-humped blazar SEDs (Fig. 7.3). The source 1653–329 has an unusually dominant high-energy hump (see Fig. 7.4) and is bright at hard X-rays (Masetti et al., 2008, Baumgartner et al., 2013), while only upper limits are placed on the 14–195 keV flux by *Swift*/BAT for the other sources, based on the  $3\sigma$  level of background variations in the survey maps.

The high-energy humps of the three sources in the E14 field appear broader and less peaked than the SEDs of the sources in the E20 field. The high-energy peak frequencies lie between  $10^{20}$  Hz and  $10^{22}$  Hz. 1653–329 and 1714–336, and possibly 1759–396 show an additional component between  $10^{14}$  Hz and  $10^{15}$  Hz, which could be explained by a thermal accretion disk.

### Possible other AGN sources of the IceCube events

Other  $\gamma$ -ray-emitting AGN in the fields are fainter in the radio band (RBS 0300, PMN J0201–6638, PKS 0206–688, 2FGL J1656.9–2008, 2FGL J1745.1–1729, 2FGL J1823.6–3453, and 2FGL J1829.3–2419). The six TANAMI blazars are the brightest radio and  $\gamma$ -ray emitting AGN in the two IceCube

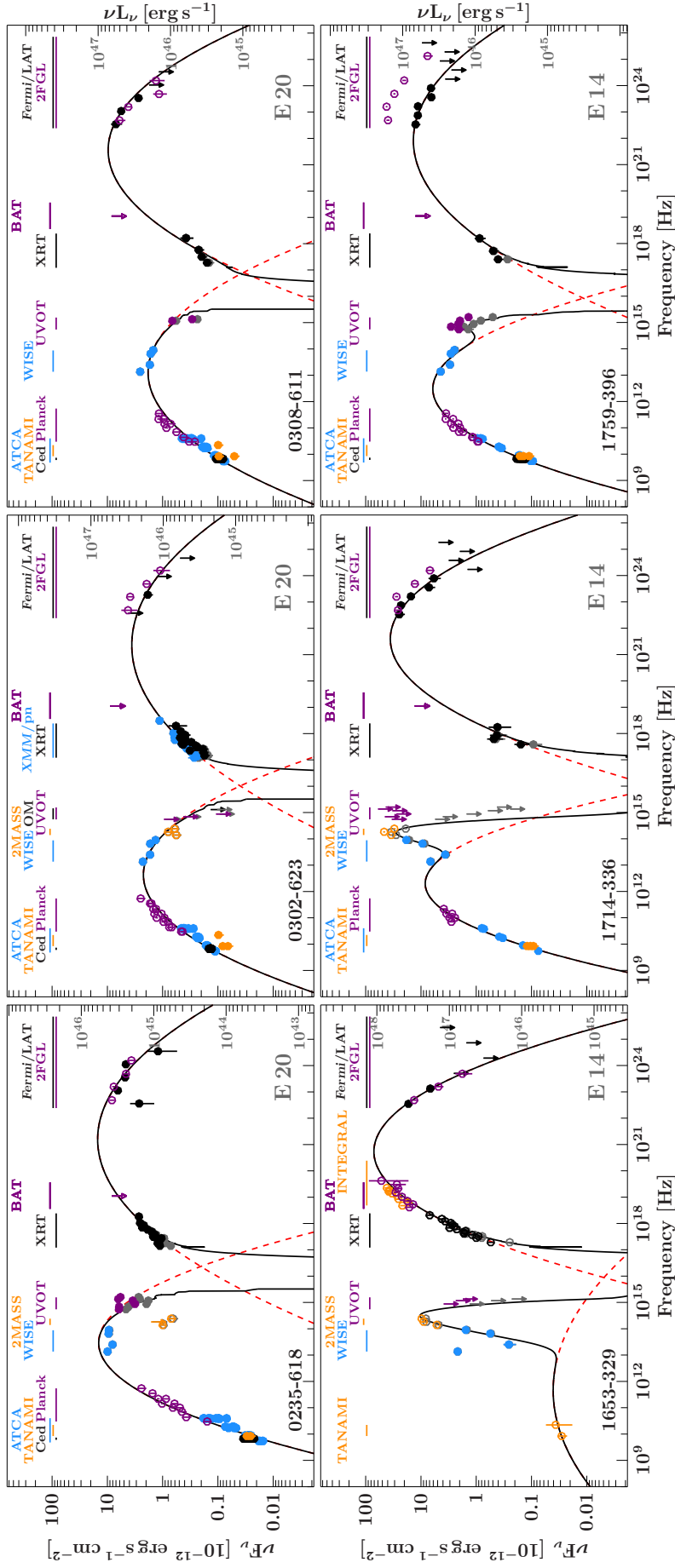


Figure 7.3.: Broadband SEDs for the six TANAMI blazars. Filled data points are from the IceCube integration period (2010 May–2012 May), open circles are archival data outside the time period. Gray shows the absorbed (X-ray) and reddened (optical/UV) spectra. The data have been parametrized with logarithmic parabolas (red dashed lines) modified by extinction and absorption, as well as by an additional blackbody component where necessary (black solid lines).

Table 7.2.: Details of interferometric observations and image parameters

Source	$\nu$	$S_{\text{peak}}^a$	$\sigma_{\text{rms}}^a$	$S_{\text{total}}^a$	$T_B$	Beam <sup>a</sup>
0235–618	8.4	0.32 (0.35)	0.08 (0.06)	0.38 (0.37)	1.6	$0.51 \times 2.28, 5.8$ $(4.85 \times 7.70, -54.9)$
0302–623	8.4	0.83	0.29	1.38	1.9	$1.05 \times 1.47, -2.8$
	22.3	0.45	0.12	0.69	1.2	$1.59 \times 2.28, 87.6$
0308–611	8.4	0.68 (0.73)	0.09 (0.05)	0.77 (0.77)	2.0	$1.20 \times 1.64, 38.8$ $(3.89 \times 4.49, -80.9)$
	22.3	0.50	0.13	0.54	0.3	$1.53 \times 1.82, -75.9$
1653–329	8.4	0.28	0.26	0.34	0.1	$3.38 \times 4.33, 86.8$
	22.3	– <sup>b</sup>	– <sup>b</sup>	0.17 <sup>b</sup>		– <sup>b</sup>
1714–336	8.4	0.74	0.36	1.27	0.02 <sup>c</sup>	$3.26 \times 3.98, 87.8$
1759–396	8.4	1.63	0.18	2.01	3.1	$0.64 \times 2.70, 12.2$
	22.3	1.12	0.18	1.19	0.2	$1.47 \times 4.32, 78.4$

**Notes.** Columns: (1) IAU B1950 source name, (2) observing frequency in GHz, (3) peak flux density in Jy/beam, (4) image noise level in mJy/beam, (5) total flux density in Jy (uncertainties are  $\leq 10\%$  and  $\leq 20\%$  at 8.4 GHz and 22.3 GHz), (6) minimum core brightness temperature in  $10^{11}$  K and (7) restoring beam (size, position angle) in  $\text{mas}^2$  and degree. <sup>(a)</sup> Values in brackets denote the application of a Gaussian taper to the visibility data of 10% at a baseline length of  $100M\lambda$ . <sup>(b)</sup> One baseline experiment, flux density only accurate to  $\sim 50\%$ . <sup>(c)</sup>  $z = 0$  assumed, affected by interstellar scattering broadening.

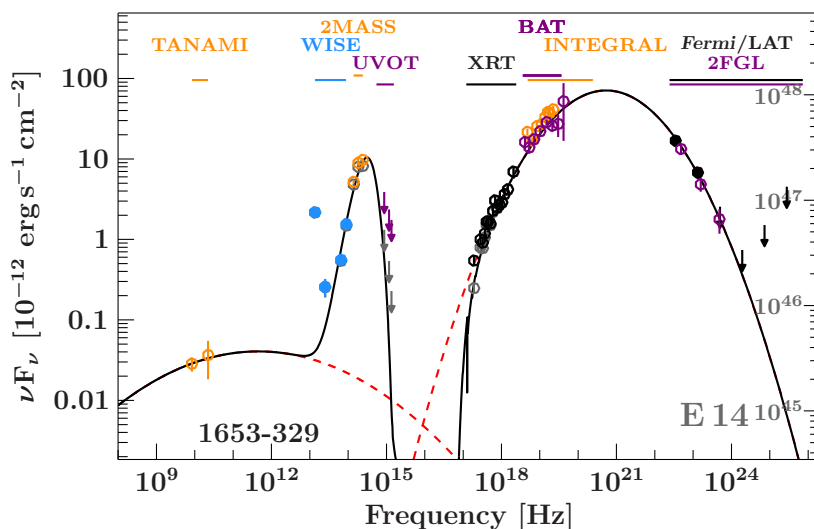


Figure 7.4.: Broadband SED of 1653–329.

PeV event fields. The two moderately bright extragalactic radio sources PKS 1657–261 and PKS 1741–312 (270 mJy and 470 mJy compact flux density at 8.4 GHz and 8.6 GHz, respectively) with compact jets (Ojha et al., 2004, Petrov et al., 2005, Condon et al., 1998) have not shown substantial  $\gamma$ -ray emission in the 2FGL period. The same is true of several hard X-ray detected blazars and radio galaxies (Baumgartner et al., 2013). Four blazars are slightly outside the uncertainty region of E14: NRAO 530, PKS 1622–29, PKS 1622–253, and PKS 1830–211 at  $15^\circ 0$ ,  $16^\circ 8$ ,  $17^\circ 3$ , and  $13^\circ 5$  distance to the coordinates at  $13^\circ 2$  error radius. The first three sources have been monitored by the MOJAVE program (Lister et al., 2009). We expect additional contributions from these sources to the neutrino fluence.

Table 7.3.: Integrated electromagnetic energy flux from 1 keV to 5 GeV and expected electron neutrino events at 1 PeV in 662 days of IceCube data for the six candidate blazars. Errors are statistical only.

Source	$F_\gamma [\text{erg cm}^{-2} \text{s}^{-1}]$	events
0235–618	$(1.0^{+0.5}_{-0.5}) \times 10^{-10}$	$0.19^{+0.04}_{-0.04}$
0302–623	$(3.4^{+0.7}_{-0.7}) \times 10^{-11}$	$0.06^{+0.01}_{-0.01}$
0308–611	$(7.5^{+2.9}_{-2.9}) \times 10^{-11}$	$0.14^{+0.05}_{-0.05}$
1653–329	$(4.5^{+0.5}_{-0.5}) \times 10^{-10}$	$0.86^{+0.10}_{-0.10}$
1714–336	$(2.4^{+0.5}_{-0.6}) \times 10^{-10}$	$0.46^{+0.10}_{-0.12}$
1759–396	$(1.2^{+0.3}_{-0.2}) \times 10^{-10}$	$0.23^{+0.50}_{-0.40}$
Total		$1.9 \pm 0.4$

### Expected neutrino rate from pion photoproduction

Proton acceleration occurs in blazar jets moving with bulk Lorentz factor  $\Gamma$ , thus avoiding pair attenuation above 511 keV. Pion production in the low-density jets is dominated by interactions of accelerated protons with low-energy photons rather than with ambient matter (Mannheim & Biermann, 1989). In pion photoproduction the neutrino flux is related to the bolometric high-energy electromagnetic flux. I calculate the expected amount of neutrinos as described in Sect. 3.3.5. Electromagnetic cascades emerge at X-ray and  $\gamma$ -ray energies, and we approximate the non-thermal bolometric photon flux  $F_\gamma$  by the integrated flux between 1 keV and 5 GeV. The broadband spectra were fit with two logarithmic parabolas (Massaro et al., 2004), as well as a blackbody component, X-ray absorption and optical extinction. This fit was then integrated in the given energy range. All but one of the blazars in our sample belong to the FSRQ class, showing strong emission lines due to photo-ionizing UV light from an accretion disk that could provide target photons. The exception is 1714–336, which has been classified as a BL Lac object (Véron-Cetty & Véron, 2006) but shows a particularly strong big blue bump in the UV and is possibly a misclassified quasar.

IceCube would have measured the following number of electron neutrino events  $N_{\nu_e}(E_\nu) \simeq A_{\text{eff}}(E_\nu)(S_{\nu_e}/E_\nu)\Delta t$ . Adopting  $E_\nu = 1$  PeV as the neutrino-production peak energy, an exposure time of  $\Delta t = 662$  days, and an effective area of  $A_{\text{eff}} = 10^5 \text{ cm}^2$  for contained PeV events, we obtain the values listed in Table 7.3. The numbers would be lower for a realistic spectrum of the emitted neutrinos or if some fraction of the emission were of a leptonic, proton-synchrotron, or Bethe-Heitler origin. The steepness of the blazar  $\gamma$ -ray luminosity function (Singal et al., 2012), implies that in a large field, the neutrino fluence will have significant contributions from the brightest sources in the field, as well as from fainter, unresolved sources.

The six candidate sources from the TANAMI sample are the radio-brightest blazars in the neutrino error fields. Assuming that the high-energy emission stems from pion photoproduction due to accelerated protons, the maximum expected number of electron neutrino events from the six blazars in 662 days is  $1.9 \pm 0.4$ . This is surprisingly close to the actual number of observed events, given the additional neutrinos expected from a large number of remote, faint blazars not included in the TANAMI sample. The most promising candidate sources are the three TANAMI blazars

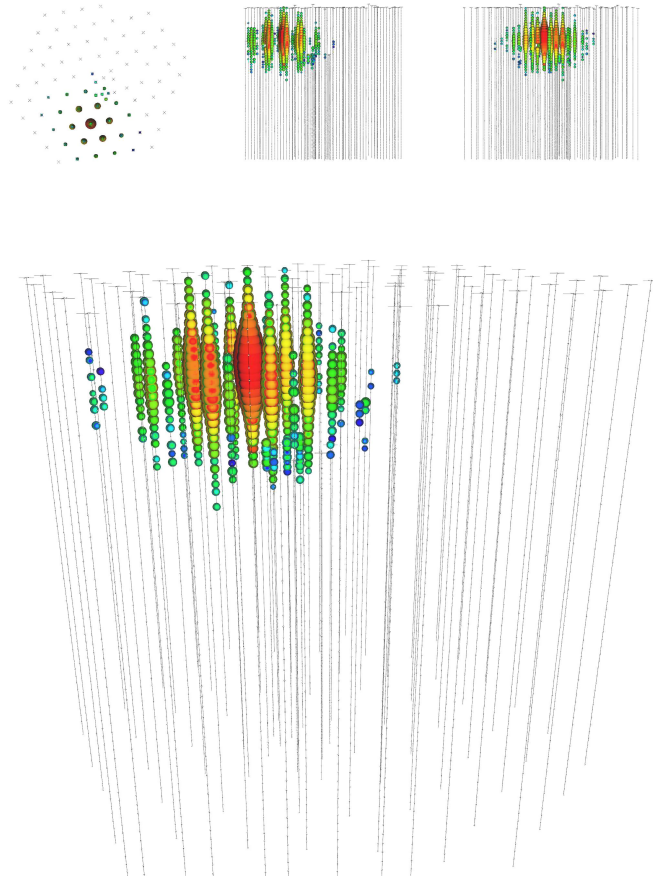


Figure 7.5.: IceCube data of IC 35. The IceCube ‘strings’ are show in gray. Colors correspond to arrival times of detected photons, red shows earliest arrival times, blue show the latest data (at 3 ms). The deposited energy is shown with the size of the spheres. (Aartsen et al., 2014).

in the E14 field, with the highest predicted neutrino rates and the prevalence of blue bumps. The detection statistics of neutrinos at these low fluxes is expected to be Poisson-distributed. For  $N=1$ , the  $1\sigma$  single-sided lower and upper limits are 0.173 and 3.300, respectively. With a predicted neutrino fluence of 0.39/1.55 events for the E20/E14 field, we are well inside the Poisson uncertainty ranges. The six TANAMI sources alone are already capable of producing the observed PeV neutrino flux.

## The story of Big Bird

### Introduction

The third PeV neutrino (IC 35) detected by the IceCube collaboration had an energy of  $2004_{-262}^{+236}$  TeV and a median positional uncertainty of  $R_{50} = 15.9^\circ$  centered around the coordinates  $RA = 208.4^\circ$ ,  $dec = -55.8^\circ$ . Figure 7.5 shows the IceCube detection of IC 35. Following our strategy from the previous section, we searched this field for positional coincidences with  $\gamma$ -ray emitting AGN. In the second catalog of AGN detected by the LAT (2LAC, Ackermann et al., 2011), which was based on observations between 2008 August and 2010 September, a total of 20  $\gamma$ -ray-bright AGN

Table 7.4.: **Maximum-possible number of PeV neutrino events in 988 days of IceCube data for the 17 2LAC  $\gamma$ -ray blazars in the field of the 2 PeV IceCube event based on 2LAC catalog  $\gamma$ -ray spectra and contemporaneous X-ray data.**

2FGL Name	Common Name	$F_\gamma$ (erg cm $^{-2}$ s $^{-1}$ )	$N_{\nu, \text{PeV}}^{\text{max}}$
2FGL J1230.2–5258	PMN J1229–5303	$(2.4^{+1.5}_{-1.5}) \times 10^{-11}$	0.14
2FGL J1234.0–5733	PMN J1234–5736	$(1.1^{+0.4}_{-0.4}) \times 10^{-11}$	0.06
2FGL J1303.5–4622	PMN J1303–4621	$(1.9^{+0.6}_{-0.6}) \times 10^{-11}$	0.11
2FGL J1303.8–5537	PMN J1303–5540	$(1.04^{+0.11}_{-0.11}) \times 10^{-10}$	0.38
2FGL J1304.3–4353	1RXS 130421.2–435308	$(2.11^{+0.25}_{-0.25}) \times 10^{-11}$	0.12
2FGL J1307.5–4300	1RXS 130737.8–425940	$(8.4^{+1.7}_{-1.7}) \times 10^{-12}$	0.05
2FGL J1307.6–6704	PKS B 1304–668	$(1.54^{+0.15}_{-0.15}) \times 10^{-10}$	0.89
2FGL J1314.5–5330	PMN J1315–5334	$(8.1^{+0.9}_{-0.9}) \times 10^{-11}$	0.47
2FGL J1326.7–5254	PMN J1326–5256	$(1.04^{+0.21}_{-0.18}) \times 10^{-10}$	0.59
2FGL J1329.2–5608	PMN J1329–5608	$(1.38^{+0.36}_{-0.29}) \times 10^{-10}$	0.93
2FGL J1330.1–7002	PKS B 1326–697	$(1.53^{+0.11}_{-0.11}) \times 10^{-10}$	0.89
2FGL J1352.6–4413	PKS B 1349–439	$(5.4^{+1.0}_{-1.0}) \times 10^{-11}$	0.32
2FGL J1400.6–5601	PMN J1400–5605	$(6.9^{+0.8}_{-0.8}) \times 10^{-11}$	0.40
2FGL J1407.5–4257	CGRaBS J1407–4302	$(1.6^{+0.5}_{-0.5}) \times 10^{-11}$	0.09
2FGL J1428.0–4206	PKS B1424–418	$(2.04^{+0.17}_{-0.16}) \times 10^{-10}$	1.57
2FGL J1508.5–4957	PMN J1508–4953	$(7.6^{+3.0}_{-2.3}) \times 10^{-11}$	0.55
2FGL J1514.6–4751	PMN J1514–4748	$(5.6^{+0.6}_{-0.6}) \times 10^{-11}$	0.32
Sum (2LAC)			7.9

were found in the median positional uncertainty ( $R_{50}$ ) field of IC 35. Seventeen of these AGN are blazars, two are radio galaxies (Centaurus A and Centaurus B), and one is a starburst galaxy (NGC 4945). The radio galaxy Cen A is the closest AGN and the brightest radio source in the field. However, most of the radio emission is emitted from the kpc-scale lobes of this FR I-type radio galaxy, and Padovani & Resconi (2014) discard Cen A as a possible source of the IceCube event, as the extrapolated SED at PeV energies is too low. Here, we do not consider non-blazar contributors and calculate the neutrino output from blazars in the field.

### 2LAC blazars in the error field of IC 35

In the following, we first calculate the maximum possible number of neutrinos from the blazars in the IC 35 field over the  $\Delta t=3$  year IceCube period assuming a flavor-uniform neutrino flux that peaks in the PeV range. Then, we compare this prediction to the observed all-sky rate of PeV neutrinos and determine an empirical scaling factor  $f$ : Using the effective area at the geometric mean of the three events' of the IceCube HESE analysis (IceCube Collaboration, 2013)  $A(E_\nu)_{\text{eff}, \nu_e} = 2.2 \cdot 10^5 \text{ cm}^2$  for charged-current (CC) interactions of electron neutrinos, we derive the possible number of neutrinos, as described in Sect. 3.3.5. Note that the assumption of the neutrino spectra peaking at  $\sim 2$  PeV increases the predicted neutrino counts compared to our previous estimates for IC 14 and IC 20 due to the increased effective area of IceCube towards higher energies. The integrated emission from all 17 blazars in the field predicts a maximum of  $\sim 7.9$  neutrino PeV events for 988 days of IceCube integration (see Table 7.4), confirming our previous result that blazars as a population are energetically capable of explaining the observed flux of PeV neutrinos.

It is not surprising that only one event has been detected, for the following reasons:

- I) Not all detected IceCube events are due to electron neutrino interactions.
- II) Photopion production at PeV energies is expected to be dominant only in the class of FSRQs, which harbor dense UV photon fields due to the emission of their optically thick accretion disks.
- III) The neutrino spectrum might not peak sharply at PeV energies.
- IV) Accounting for the large number of faint unresolved blazars that are seen in the diffuse  $\gamma$ -ray background has an opposing effect.

We introduce the scaling factor  $f$  to empirically match the maximum possible neutrino number  $N_{\nu,\text{max,PeV}}$  with the observed number of neutrinos at PeV energies  $S_{\nu,\text{obs,PeV}}$  within the solid angle  $\Omega_{\text{IC35}}$  (the  $R_{50}$  region of IC 35) in the southern sky

$$N_{\nu,\text{obs,PeV}}(\Omega_{\text{IC35}}) = f \cdot N_{\nu,\text{max,PeV}}(\Omega_{\text{IC35}}) \quad (\text{at 1 PeV}). \quad (7.1)$$

### Contribution from unresolved blazars

The integrated emission from the 17 2LAC blazars in the field predicts a maximum of  $\sim 7.9$  neutrino PeV events for 988 days of IceCube integration, but we also need to consider the contribution of fainter unresolved blazars. In total, blazars make up  $\sim 50\%$  of the extragalactic  $\gamma$ -ray background (EGB; Ackermann et al., 2015b, Ajello et al., 2015), but the integrated flux for all 2LAC blazars inside  $\Omega_{\text{IC35}}$  is only  $F_{100\text{MeV}-820\text{GeV}} = 8.5 \cdot 10^{-7} \text{ ph cm}^{-2} \text{ s}^{-1}$ . Distributed over  $\Omega_{\text{IC35}}$ , this corresponds to  $3.5 \cdot 10^{-6} \text{ ph cm}^{-2} \text{ s}^{-1} \text{ sr}^{-1}$ , which accounts for only about 30% of the EGB<sup>1</sup>. Thus, we may expect about  $\frac{0.2}{0.3} \cdot 7.9 \sim 5.3$  additional neutrinos at PeV energies from faint unresolved blazars within  $\Omega_{\text{IC35}}$  (taking their EGB contribution as a proxy for their integrated keV-to-GeV output). Thus, the maximum possible number of neutrinos predicted by this model from blazars in the IC 35 field is

$$N_{\nu,\text{PeV}}^{\text{max}}(\Omega_{\text{IC35}}) \sim 13 \quad , \quad (7.2)$$

which includes maximum-possible PeV neutrino counts from all  $\gamma$ -ray blazars from the 2LAC catalog plus a maximum-possible contribution of the large population of faint unresolved blazars.

### The empirical and theoretical scaling factor

By extrapolating from the representative field  $\Omega_{\text{IC35}}$ , we estimate the maximum number of PeV neutrino events from all blazars (both resolved and unresolved) over three years from the full southern sky to be

$$N_{\nu,\text{PeV}}^{\text{max}}(2\pi) = 13 \cdot \frac{2\pi}{\Omega_{\text{IC35}}} \sim 336 \quad . \quad (7.3)$$

This number of events would be expected if only electron neutrinos would be produced, all blazars harbor dense UV photon fields as typical for FSRQS, if the neutrino spectrum peaks sharply at PeV energies, and if the high-energy emission is purely of hadronic origin. All four conditions are clearly not fulfilled as only 3 events have been detected, leading to an empirical scaling factor of

$$f_{\text{emp}} = \frac{N_{\nu,\text{PeV}}^{\text{obs}}(2\pi)}{N_{\nu,\text{PeV}}^{\text{max}}(2\pi)} \sim \frac{3}{336} \sim 0.009 \quad . \quad (7.4)$$

<sup>1</sup>Given the rather shallow slope of the  $\log N \log S$  distribution (Ackermann et al., 2015d), future *Fermi*/LAT catalogs will mitigate this effect only slowly.

This can be compared to a theoretical value  $f_{\text{th}}$ , which accounts for physically motivated realistic deviations from the three ideal conditions. The theoretical scaling factor allows us to predict the number of detectable PeV events  $N_{\nu}^{\text{pred}}$  as

$$N_{\nu, \text{PeV}}^{\text{pred}}(\Omega_{\text{IC35}}) = f_{\text{th}} \cdot N_{\nu, \text{PeV}}^{\text{max}}(\Omega_{\text{IC35}}) \quad . \quad (7.5)$$

The scaling factor is factorized into a flavor factor  $f_{\text{I}}$ , a factor accounting for the different classes of blazars  $f_{\text{II}}$ , and a spectrum factor  $f_{\text{III}}$ :

$$f_{\text{th}} = f_{\text{I}} \cdot f_{\text{II}} \cdot f_{\text{III}} \quad . \quad (7.6)$$

The IceCube data indicate an equal flavor ratio (Aartsen et al., 2015) so that the flavor factor would be 1/3 if only electron neutrinos are accounted for when computing the maximum event numbers. When adding the two other flavors, it has to be considered that the number of detected cascade events due to muon and tau neutrinos is lower than for electron neutrinos because of the energy-dependent cross sections and inelasticities for neutral-current (NC) and charged-current interactions. Assuming an underlying neutrino power law with slope  $-2.3$ , as observed by IceCube Collaboration (2013), we estimate a fraction of  $f_{\text{I}} \sim 0.5$  for cascade events at  $(1 - 2)$  PeV in IceCube. The deepest available *Fermi*/LAT point source catalogs contain a fraction of FSRQs of about  $f_{\text{II}} \sim 0.5$  (and about the same numbers of BL Lac objects; Ackermann et al., 2011). For our basic model of a sharply peaked neutrino spectrum due to photopion production from monoenergetic UV photons,  $f_{\text{III}}$  would be equal to unity. In a more realistic scenario, a range of Doppler shifts (depending on the location of the seed-photon sources with respect to the relativistic jet base as discussed in our earlier work; Krauß et al., 2014) causes broader spectra extending to lower neutrino energies. Considering also broadening due to the different redshifts of sources, an output range of  $\sim 30$  TeV to  $\sim 10$  PeV can be expected. In addition, models which consider proton-proton collisions or assume accretion tori with virial temperatures of  $\sim 10^9$  K rather than optically thick accretion disks (Mannheim, 1993, 1995a,b) also predict softer spectra. Using a spectral index of  $-2.3$  as measured by (Aartsen et al., 2014) and the (30 TeV to 10 PeV) bandwidth of the spectrum reduces the number of PeV output neutrinos by  $f_{\text{III}} = 0.05$ , so that we estimate

$$f_{\text{th}} = 0.5 \cdot 0.5 \cdot 0.05 \sim 0.0125 \quad (7.7)$$

(see Eq. 7.4). Our model thus predicts  $0.0125 \cdot 336 \sim 4$  events at PeV energies from the full southern sky, which is remarkably close to the observed three PeV events. We conclude that the measured  $\gamma$ -ray emission of the blazars in the IC 35 field allows us to reproduce both the measured all-sky flux of PeV neutrinos and the measured spectral slope of the IceCube signal assuming a simple photo-hadronic emission model of FSRQs.

If  $\Omega$  becomes small, containing only one individual FSRQ, we can set  $f_{\text{II}} = 1$ . The predicted number of PeV neutrinos for an individual FSRQ is then

$$N_{\nu, \text{PeV}}^{\text{pred}}(\text{FSRQ}) = 0.025 \cdot N_{\nu, \text{PeV}}^{\text{max}}(\text{FSRQ}) \quad , \quad (7.8)$$

from which Poisson probabilities for detections of neutrinos from individual sources can be calculated. For the 2LAC sources in the IC 35 field, we find relatively low maximum-possible neutrino values ( $N_{\nu, \text{PeV}}^{\text{max}} \sim 0.04 - 0.9$ ) in 16 of the 17 cases, from which small predicted neutrino counts are predicted ( $N_{\nu, \text{PeV}}^{\text{pred}} \sim 0.001 - 0.023$ ), corresponding to small individual Poisson probabilities for any neutrino detections during the 3-year IceCube integration of ( $P \lesssim 0.1\% - 2.2\%$ ).

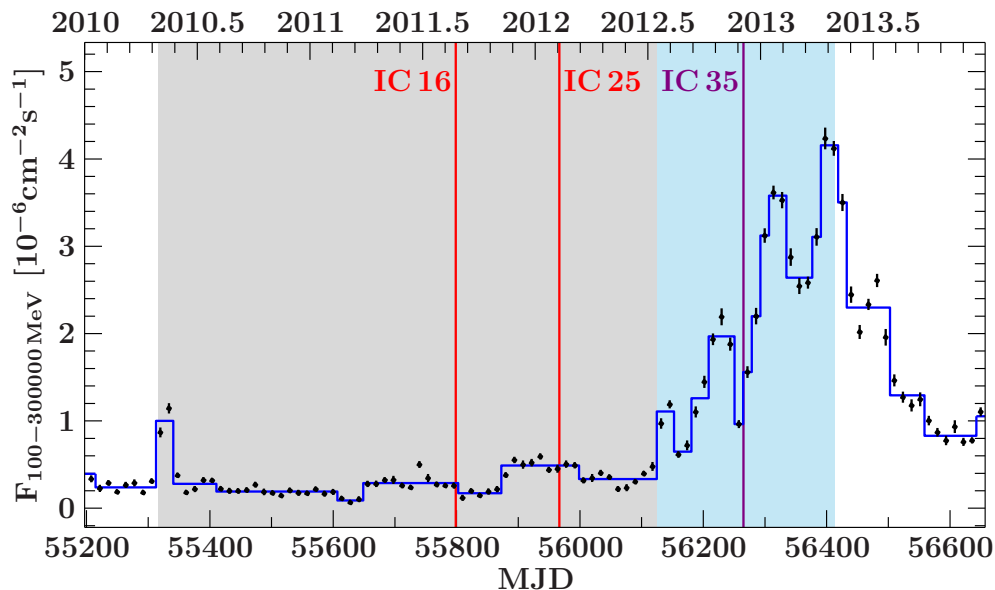


Figure 7.6.: *Fermi*/LAT  $\gamma$ -ray light curve of PKS B1424–418 with two-week binned photon fluxes between 100 MeV and 300 GeV (black), IC 35 time stamp (red line) with the Bayesian blocks light curve (blue). The first three years of IceCube integration (2010 May through 2013 May) and the included outburst time range are highlighted in color. Additionally, events at sub-PeV energies that are consistent with PKS 1424–418 are also shown.

### PKS B1424–418 in outburst

The dominant blazar in the field is PKS B1424–418 at redshift  $z = 1.522$  (White et al., 1988) and classified as an FSRQ. The source showed two  $\gamma$ -ray flares in 2009–2011 (Buson et al., 2014) and is listed as a bright  $\gamma$ -ray source in all subsequent *Fermi*/LAT catalogs. Still, Padovani & Resconi (2014) discarded it from their list of most-probable counterparts for the 2 PeV IceCube neutrino due to its relatively low  $\gamma$ -ray emission in the 2008–2011 period. In summer 2012, PKS B1424–418 commenced a dramatic rise in  $\gamma$ -ray brightness (Ojha & Dutka, 2012). In contrast to previous flares, this increase marked the beginning of a long-lasting high-fluence outburst over more than a year with  $\gamma$ -ray fluxes exceeding 15 to 30 times the flux reported in the *Fermi* 2LAC (see Fig. 7.6) and which coincides with the PeV neutrino event IC 35 both in position and in time. With a  $\gamma$ -ray photon fluence of  $(30.5 \pm 0.3) \text{ cm}^{-2}$ , PKS B1424–418 showed the highest 100 MeV to 300 GeV  $\gamma$ -ray fluence of all extragalactic sources in the 2012 July 16 through 2013 April 30 period, which coincides with the arrival of IC 35. Along with the very high  $\gamma$ -ray emission, an increase in X-ray, optical, and radio emission from PKS B1424–418 has also been reported (Ciprini & Cutini, 2013, Hasan et al., 2013, Nemenashi et al., 2013). The TANAMI VLBI data show that the sharp increase in radio flux density from  $\sim 1.5 \text{ Jy}$  to  $\sim 6 \text{ Jy}$  took place inside the VLBI core, i.e., on projected scales smaller than  $\sim 3 \text{ pc}$ . The September 2012 image is the first VLBI epoch within the GeV high-fluence phase and also the first to show a substantial increase in the core flux density. This high-amplitude radio outburst is unparalleled in the TANAMI sample since the beginning of the program in 2007.

In Fig. 7.7, we show the average broadband SED of PKS B1424–418 for the 2LAC period, the 3 yr IceCube integration period, the 2010 short flare around MJD 55327 (see Fig. 7.6), and the major outburst phase between 2012 July 16 and the end of the IceCube period in April 2013. With

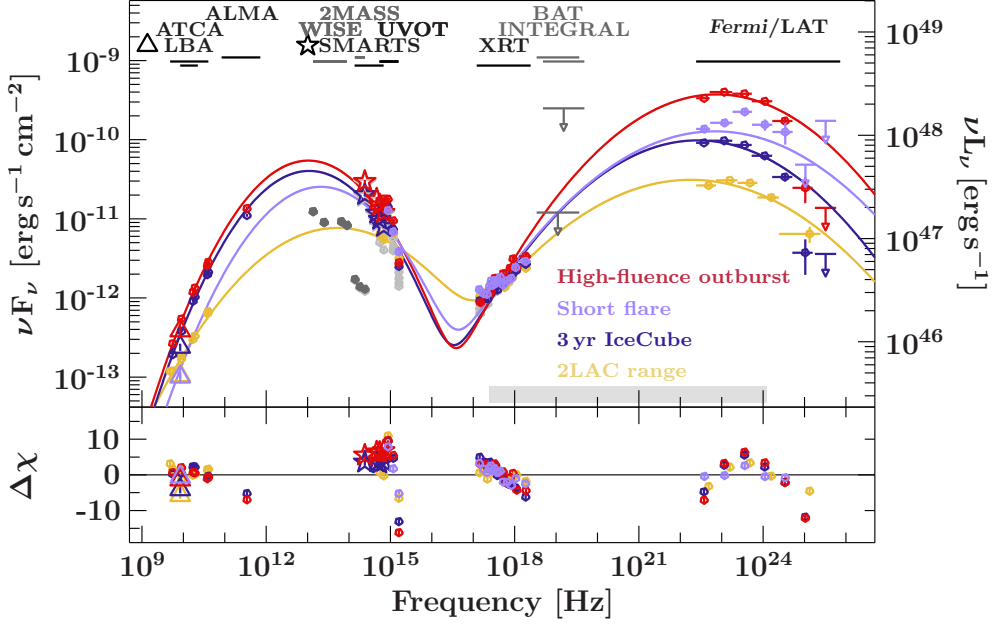


Figure 7.7.: Multi-epoch spectral energy distribution of PKS 1424–418 with fitted log parabolas for the 2LAC period (yellow), the first three years of IceCube integration (dark blue), the short 2010 flare around MJD 55327 (red), and the major outburst between MJD 56125 and MJD 56413 (light purple). The gray shaded area shows the keV to GeV integration range for the neutrino fluence calculation. Note that upper limits (downward arrows) are neglected in the fits (Kadler et al., 2015a).

the peak in the GeV range for all periods considered, and the X-ray spectrum changing mostly in photon index, we see that the *Fermi*/LAT flux values shown in the light curve are good proxies for the integrated high-energy output. In spite of the relatively high fluxes during the 2010 flare, the short duration yields only a small fluence, resulting in a low maximum-possible neutrino value of  $N_{\nu, \text{max, PeV}} \sim 0.2$ . Substantially higher values are derived for the 2LAC period ( $N_{\nu, \text{PeV}}^{\text{max}} \sim 1.6$ ,  $N_{\nu, \text{PeV}}^{\text{pred}} \sim 0.04$ ) and the three year IceCube period ( $N_{\nu, \text{PeV}}^{\text{max}} \sim 4.5$ ,  $N_{\nu, \text{PeV}}^{\text{pred}} \sim 0.11$ ).

The latter is dominated by the 9-months period between the start of the outburst (2012 July 16) and the end of the 3 yr IceCube period (2013 April 30). During these 9 months, the source increased its predicted neutrino-production rate by more than an order of magnitude so that the Poisson probability to detect a neutrino associated with the 9-month high-fluence outburst of PKS B1424–418 is at a considerable level of about 11 %, which is three times higher than the corresponding probability to detect an event from the integrated emission of all other known  $\gamma$ -ray blazars in the field during this 9-month period. Our model thus allows us to associate an individual blazar during a rare major outburst with the highest-energy extraterrestrial neutrino detected by IceCube to date. A  $\sim 5\%$  probability for a chance coincidence remains. It also cannot be excluded that the observed PeV neutrino could be associated with an historical (or future) outburst of the source.

### The non-detection of other outbursts

If our model is correct, it also has to explain the non-detection of PeV neutrinos in positional agreement with other high-fluence blazars and with the detection statistics of sub-PeV neutrino

events. We note that the positional uncertainties  $R_{50}$  given by the IceCube team are median values, which means that only half of all events originate inside their measured  $R_{50}$  regions while the other half are coming from larger offset angles. Above, we have calculated the maximum number of neutrino events that can be explained by individual astrophysical sources within  $R_{50}$  for a high-confidence event. When asking for the maximum number of IceCube events that might be associated with a given astrophysical source, a larger radius has to be considered. For example, within  $2 \times R_{50}$ , PKS B1424–418 is in positional agreement with the sub-PeV events IC 16 ( $30.6^{+3.6}_{-3.5}$  TeV at an offset of  $1.5R_{50}$ ) and IC 25 ( $33.5^{+4.9}_{-5.0}$  TeV,  $1.4R_{50}$ ) so that the data are not in disagreement with a rather broad and steep neutrino spectrum. A point source search with ANTARES, following the strategy applied to the candidate blazars in the IC 14 and IC 20 fields (ANTARES Collaboration: et al., 2015), will be able to exclude the doublet/triplet hypothesis in case of a non-detection of any events. A preliminary analysis of the ANTARES collaboration (Kadler, 2016) finds no excess signal at the position of PKS B1424–418, excluding the possibility of a very steep neutrino spectrum associated with the blazar outburst.

We have used the *Fermi*/LAT monitored source list light curves<sup>2</sup> to identify candidate sources for high keV-to-GeV fluence, compiled the average SEDs over the three years of IceCube integration for the top-ten candidate sources from the whole sky and derived their expected neutrino counts. Only three other sources reach a predicted neutrino output comparable to PKS B1424–418. The two FSRQs PKS B1510–089 and 3C 454.3 both have a maximum PeV-neutrino output on the order of 8 in three years of IceCube integration but do not coincide with any of the three observed PeV events. Applying the source scaling factor of 0.025 for the  $\gamma$ -ray blazars, the Poisson probability for detecting zero PeV events from a source of this fluence is  $\sim 80\%$ . On the other hand, the model predicts a  $\sim 50\%$  probability to detect at least one neutrino from one of the four top-ranked high-fluence blazars and the detection of more than one PeV event remains at a realistic probability of about 16%. The occurrence of multiple events is expected if a sparse population such as FSRQs produce a considerable fraction of the total IceCube intensity (Waxman, 2015). In this context, it is intriguing that also the gravitationally-lensed blazar PKS B1830–211, which is the highest-ranked source in the top-10 blazar-fluence list, is located only marginally outside the  $R_{50}$  region of the PeV event IC 14, which was detected by IceCube on 2011 August 9, coinciding with a high-fluence outburst phase of this blazar<sup>3</sup>.

Recently, a theoretical limit of  $(v - c)/c \leq (0.5 - 1.0) \times 10^{-20}$  for superluminal neutrinos has been derived from constraints on vacuum pair emission and neutrino splitting (Stecker et al., 2015). Assuming a physical association between the outburst activity of PKS B1424–418 and the IC 35 PeV neutrino, an observational constraint on the neutrino velocity is implied: the maximum possible time-travel delay between the beginning of the outburst and the arrival of the neutrino  $\sim 160$  days, constraining the relative velocity difference to  $(v - c)/c \lesssim \mathcal{O}(10^{-11})$  (for a light travel time of 9.12 billion years). This is about two orders of magnitude more constraining than the neutrino-velocity limit derived from SN 1987A (Longo, 1987).

Tentative associations of high-energy neutrinos with flaring blazars have been suggested before (Halzen & Hooper, 2005, Adrián-Martínez et al., 2012), but it remained questionable whether a high-enough neutrino flux could be produced in the candidate flares (Reimer et al., 2005). Here, we have identified for the first time a single source that has emitted a sufficiently high fluence during a major outburst to explain an observed coinciding PeV neutrino event. There is a remarkable coincidence with the IceCube-detected PeV neutrino event IC 35 with a probability of only  $\sim 5\%$  for a chance coincidence. In addition, the temporal coincidence of the major outburst

<sup>2</sup>[http://fermi.gsfc.nasa.gov/ssc/data/access/lat/msl\\_lc/](http://fermi.gsfc.nasa.gov/ssc/data/access/lat/msl_lc/)

<sup>3</sup>[http://fermi.gsfc.nasa.gov/FTP/glast/data/lat/catalogs/asp/current/lightcurves/PKS1830-211\\_604800.png](http://fermi.gsfc.nasa.gov/FTP/glast/data/lat/catalogs/asp/current/lightcurves/PKS1830-211_604800.png)

of PKS 1830–211 with the IceCube PeV event IC 14 is remarkable although the blazar is located marginally outside the  $R_{50}$  field of the neutrino event. A comparison of model predictions for monoenergetic neutrino spectra with the observed all-sky PeV neutrino flux, allows us to estimate a scaling factor of 0.028 for FSRQs, accounting for the distribution of neutrino events across the bandwidth expected for photohadronic neutrino production.

## Summary

We have shown that the first two neutrinos events at PeV energies detected by IceCube (IC 14 and IC 20) can be explained by the energetic output of blazars. The six candidate sources from the TANAMI sample are the radio-brightest blazars in these neutrino error fields. Assuming that the high-energy emission stems from pion photoproduction due to accelerated protons, the maximum expected number of electron neutrino events from the six blazars in 662 days is  $1.9 \pm 0.4$ . This is surprisingly close to the actual number of observed events, given the additional neutrinos expected from a large number of remote, faint blazars not included in the TANAMI sample.

For the third event (IC 35) we have shown that the long-term average measured  $\gamma$ -ray emission of the blazars in the IC 35 field is in agreement with both the measured all-sky flux of PeV neutrinos and the measured spectrum of the IceCube signal assuming a simple photopion-production emission model. We find that a major outburst of a single blazar dominated the predicted integrated neutrino flux of the field during the months around the time of the neutrino event. The energy output of the blazar PKS 1424–418 during this outburst alone was high enough to explain the PeV neutrino event, indicative of their physical association.

Even if contributions to the overall  $\gamma$ -ray emission of blazars in the IC 35 field other than photopion production and/or neutrino spectra which are not sharply peaked might reduce the neutrino output during the PKS B1424–418 outburst by two orders of magnitude, a significant Poisson probability for a detection of this single source with IceCube remains. A substantial increase of the significance of putative future coincidences between PeV neutrino events and high-fluence blazars could be achieved considering track events at smaller median angular errors or the observation of doublet events associated with the same blazar. However, it has to be kept in mind that only a small fraction of the total  $\gamma$ -ray emission of all blazars is associated with the brightest individual objects. In fact, only  $\sim 70\%$  of the blazar  $\gamma$ -ray emission has been resolved into point sources so far (Ackermann et al., 2015b) by *Fermi*/LAT. For any individual PeV neutrino event, there will thus always remain a large probability of being associated with the population of faint remote sources, which are not contained in the bright-source  $\gamma$ -ray catalogs. We thus expect one out of three future PeV neutrinos to be not associated with any known  $\gamma$ -ray blazar. Within the next years of IceCube observations, the combination of improved number statistics and continuous multiwavelength monitoring of high-fluence blazars is the key to develop a consistent scenario of hadronic processes in AGN jets and their long-suspected association with extragalactic cosmic rays (Hillas, 1984).



# Chapter 8

## Conclusion and Outlook

Keep your eyes on the stars, but remember to keep your feet on the ground.

---

Theodore Roosevelt, Address at the prize day exercises at Groton school, 1904<sup>1</sup>

In the first chapter I studied the explosion channels of supernovae type Ia. The current models suggest that a white dwarf either merges with another white dwarf or accretes material from a massive companion. In both cases the Chandrasekhar limit is reached and the white dwarf undergoes a thermonuclear runaway. Determining the explosion channel is crucial, as a merger scenario would not allow supernovae to be used in the distance ladder. Due to the different masses of white dwarfs the total mass differs from supernova to supernova, leading to different luminosities. We have studied the emission from  $^{55}\text{Fe}$ , as a method to distinguish between the channels, as the line flux is different for both models. I have used active and planned X-ray missions to simulate whether it is possible to observe this line flux. I found that with current instruments the emission line flux can only be significantly detected within  $\sim 3$  Mpc, within the Local Group of galaxies. SN2014J was the closest supernova type Ia in four decades and a promising target for an iron line flux measurement. Unfortunately it could not be observed by either *XMM-Newton* or *Chandra*.

The second part and the focus of my thesis was studying the emission observed from blazars. Observing relativistic jets requires multiwavelength observations, including temporal monitoring. These observations can be complemented by multimessenger observations. An association of neutrinos with an astrophysical source gives us a better insight into particle acceleration and production and would show that jets are indeed hadronic. In this thesis, I have studied AGN jets of the southern hemisphere, using multiwavelength observations from the TANAMI program. Continuous monitoring by *Fermi*/LAT is essential for quasi-simultaneous SEDs. In detail, I have studied the spectral evolution of the 22  $\gamma$ -ray brightest TANAMI sources. The multiwavelength data were fitted with log parabolic models. This allows me to study the peak position of these objects. I found that they reproduce the blazar sequence well. I then separated low, intermediate, and high activity SEDs, based on their  $\gamma$ -ray flux. I found that the SEDs in the high state do not follow the blazar sequence – indicative of a change in the jet. Furthermore, no high-peaked BL Lac object was found in a high state, consistent with previous results. However, we lack monitoring in the X-rays and in the VHE regime, where we might miss high states. I investigated the Compton dominance, and found it is in agreement with work in the literature, and consistent with the blazar sequence. This is indicative of a physical origin of the blazar sequence, possibly related

---

<sup>1</sup><http://www.theodore-roosevelt.com/images/research/txtspeeches/101.txt>

to the accretion efficiency and the angle to the line of sight. The Fermi’s blazar divide is most likely only a selection effect, due to extinction and photoelectric absorption in the optical/UV – soft X-ray band. I studied the fundamental plane of black holes and found that my estimate of the black hole mass using the parameters found by Bonchi et al. (2013) are close to the observed black hole masses. Two sources have estimates significantly lower than what has been observed, possibly due to boosting effects.

AGN have long been expected to be the source of high-energy and ultra-high energy cosmic rays. The relativistic outflows of AGN, called jets, may be able to accelerate protons to ultra-high energies. In the second part of the thesis I studied the jet composition. It is still unclear whether blazar jets include hadronic cascades, as correlations are present for a large number of parameters in physical models. Recent detections of neutrinos at PeV energies by IceCube are promising for determining the jet composition. The atmospheric background is steeply falling with increasing energy – the neutrinos at PeV energies are likely extraterrestrial. However, the neutrino-matter interaction products (muons, electrons/positrons, and taus) are detected in showers, which leads to high angular uncertainties of  $\sim 13^\circ$ . I study the TANAMI blazars and 3LAC blazars in positional agreement with the 3 PeV events detected by IceCube. For IC 14, and IC 20, I find that the TANAMI blazars are energetically capable of producing the observed neutrinos with a maximum number of neutrinos of  $1.9 \pm 0.4$ . This does not take faint, unresolved blazars into account, but assumes that the high-energy peak of the SED is produced solely in hadronic interactions. For the third PeV neutrino IC 35, I find one southern blazar in outburst at the time of arrival of the neutrino. This is indicative of a physical association, but a chance coincide of 5% remains. From the study of all 3LAC blazars in the field it is possible to estimate the factor by which the amount of neutrinos is reduced, due to astrophysical and particle physics arguments. It is further possible to estimate that we only expect to associate  $\sim 30\%$  of the observed neutrino events, if they stem from blazars, as they might be produced by faint, unresolved sources.

My studies can be improved by using monitoring at several wavebands, ideally all, or at least at optical, X-ray, and  $\gamma$ -ray wavelengths, to study correlations between the bands, which might be used to construct “source-simultaneous” SEDs, which take delays between the wavebands into account. The future *eROSITA* satellite might provide such monitoring in the X-ray band (Merloni et al., 2012). The spectroscopic resolution of *Hitomi* (*Astro-H*; Takahashi et al., 2012), *Athena* (Nandra et al., 2013), and the hard X-ray coverage of *Hitomi* and *NuSTAR* (Harrison et al., 2013) will improve knowledge about the X-ray spectra, including better constraints on photoelectric absorption and the spectral shape above 10 keV.

Spectral data in the optical/UV range can be used to further study the Big Blue Bump, which yields information about the environment and accretion of the supermassive black holes. The big blue bump, often observed in flat spectrum radio quasars is usually interpreted as thermal emission from the accretion disk surrounding the black hole. However, several problems arise from this association. The observed thermal emission is too cold for an accretion disk. While disk temperatures at  $\sim 76000$  K are expected (Lawrence, 2012), peculiarly most BBB are found at  $\sim 30000$  K, with little variation (Zheng et al., 1997, Binette et al., 2005). Further problems include the ionization and the time-scale (Lawrence, 2012). I have also found that for a sample of blazars the BBB can be described by a single blackbody (Krauß et al., 2016). AGN can have large accretion disks extending from  $\sim 5$  to 1000 gravitational radii, so a large range in temperatures is expected. Possible explanations for these problems include a reprocessing of the inner disk emission from the EUV range to the optical/UV range by dense clouds close to the black hole (Lawrence, 2012). This would explain the low temperature, ionization and time scale problem, but not the single-temperature blackbody model. Another explanation is optically-thin emission, i.e.,

---

free-free emission in the corona or surrounding clouds (Barvainis, 1993). Using existing optical data it is possible to study the shape of the big blue bump for a large sample ( $\sim 100$  bright FSRQs) in order to determine whether the data are better described by a multi-temperature blackbody, or a more complex disk model (e.g., a warped disk), or thermal Bremsstrahlung.

Using broadband observations of blazars, I am able to study the relativistic beaming pattern of neutrinos, which will improve current predictions of the expected neutrino flux. Neutrinos are expected to be relativistically boosted, but it is not clear if the boosting pattern is identical (Dermer, 1995). Cohen et al. (2007) have shown that the radio luminosity of the jet is closely related to the apparent jet speed. Calculating the bolometric high-energy luminosities for the MOJAVE sample in relation to their jet speeds/Lorentz factors yields the required beaming information. The neutrino beaming pattern can be investigated using radio jet speeds and neutrino luminosities. Then the correlation of the neutrino beaming pattern with the electromagnetic beaming pattern can be determined. By altering the assumed beaming pattern, it is possible to investigate if the correlation can be improved.

Further, I would like to pursue a direct association of a neutrino event with an individual blazar. The most promising approach for a direct association with an individual source – and therefore to study the origin of the high-energy cosmic rays – are the upward going muon tracks seen from the northern hemisphere. Their low angular uncertainty makes them ideal to search for counterparts. We have previously utilized the TANAMI sample, as it monitors southern blazars for the association of blazars with the downwards-going events at PeV energies. The MOJAVE sample contains northern blazars, and is thus ideal to find and study the possible counterparts of the upward going neutrinos. For these sources the neutrino flux estimates, as well as flare information from the *Fermi*/LAT light curves are crucial to determine whether the blazar(s) found in positional coincidence are likely counterparts. Multiwavelength spectra and timing analysis will answer whether candidate blazars have produced the observed neutrinos and are at the origin of the observed cosmic rays.

In order to study a large number of neutrinos, and to possibly find clustering, a new and larger neutrino observatory will be necessary. The KM3Net neutrino observatory will be similar to the ANTARES observatory, but with a much larger volume (Adrián-Martínez et al., 2016). For future neutrino observations it is interesting to use new methods in order to increase sensitivity, energy range, and spatial resolution, such as a radio telescope using the Askaryan effect to observe neutrinos (Vieregg et al., 2016). Particles traveling through a dielectric (such as glacial ice) faster than the local speed of light emit a cone of radiation in the radio or microwave band, this is called the Askaryan effect (Askaryan, 1962).

The identification of blazars as sources of neutrinos would provide conclusive evidence that active galactic nuclei contribute to the flux of cosmic rays. Studying the mechanisms involved, such as the neutrino beaming pattern is crucial for a better understanding of jet physics, including particle acceleration and accretion mechanisms.



# Bibliography

- Aaboe A., 1992, Babylonian mathematics, astrology, and astronomy In: Boardman J., Edwards I.E.S., Sollberger E., Hammond N.G.L. (eds.) *The Cambridge Ancient History* Cambridge University Press, second edition, p.276 Cambridge Histories Online
- Aartsen M.G., Abbasi R., Abdou Y., et al., 2013, PRL 111, 021103
- Aartsen M.G., Ackermann M., Adams J., et al., 2014, PRL 113, 101101
- Aartsen M.G., Ackermann M., Adams J., et al., 2015, PRL 114, 171102
- Abbasi R., Abdou Y., Abu-Zayyad T., et al., 2012, Nature 484, 351
- Abbott B., Abbott R., Adhikari R., et al., 2004, Nuclear Instruments and Methods in Physics Research A 517, 154
- Abbott B.P., Abbott R., Abbott T.D., et al., 2016, PRL 116, 061102
- Abdo A.A., Ackermann M., Agudo I., et al., 2010a, ApJ 716, 30
- Abdo A.A., Ackermann M., Ajello M., et al., 2010b, ApJ 722, 520
- Abdo A.A., Ackermann M., Ajello M., et al., 2009, ApJS 183, 46
- Abdo A.A., Ackermann M., Ajello M., et al., 2010c, ApJ 710, 1271
- Abdo A.A., Ackermann M., Ajello M., et al., 2010d, ApJ 710, 810
- Abdo A.A., Ackermann M., Ajello M., et al., 2010e, Science 328, 725
- Abdo A.A., Ackermann M., Ajello M., et al., 2011, ApJ 736, 131
- Accadia T., Acernese F., Alshourbagy M., et al., 2012, Journal of Instrumentation 7, 3012
- Acero F., Ackermann M., Ajello M., et al., 2015, ApJS 218, 23
- Ackermann M., Ajello M., Albert A., et al., 2012, ApJS 203, 4
- Ackermann M., Ajello M., Albert A., et al., 2015a, ApJL 813, L41
- Ackermann M., Ajello M., Albert A., et al., 2015c, ApJ 799, 86
- Ackermann M., Ajello M., Albert A., et al., 2015b, ApJ 799, 86
- Ackermann M., Ajello M., Allafort A., et al., 2011, ApJ 743, 171
- Ackermann M., Ajello M., Atwood W.B., et al., 2015d, ApJ 810, 14
- Adrián-Martínez S., Ageron M., Aharonian F., et al., 2016, Letter of Intent for KM3NeT2.0, arXiv:1601.07459
- Adrián-Martínez S., Al Samarai I., Albert A., et al., 2012, Astropart. Phys. 36, 204
- Adrián-Martínez S., Albert A., André M., et al., 2014a, ApJL 786, L5
- Adrián-Martínez S., Albert A., André M., et al., 2014b, JCAP 11, 17
- Adrián-Martínez S., Albert A., Samarai I.A., et al., 2013, A&A 559, A9
- Ageron M., Aguilar J.A., Al Samarai I., et al., 2011, Nuclear Instruments and Methods in Physics Research A 656, 11
- Aharonian F., Akhperjanian A.G., Anton G., et al., 2009, ApJL 696, L150
- Aharonian F., Akhperjanian A.G., Aye K.M., et al., 2005, A&A 436, L17
- Aharonian F.A., Atoyan A.M., 1996, A&A 309, 917
- Ajello M., Gasparrini D., Sánchez-Conde M., et al., 2015, ApJL 800, L27
- Aleksić J., Ansoldi S., Antonelli L.A., et al., 2015, A&A 576, A126
- Aleksić J., Ansoldi S., Antonelli L.A., et al., 2014a, Science 346, 1080
- Aleksić J., Antonelli L.A., Antoranz P., et al., 2013, A&A 556, A67
- Aleksić J., Antonelli L.A., Antoranz P., et al., 2014b, A&A 563, A91
- Alexandrov Y.A., Andreyanov V.V., Babakin N.G., et al., 2012, Solar System Research 46, 458
- Alexeyev E.N., Alexeyeva L.N., Krivosheina I.V., Volchenko V.I., 1988, Physics Letters B 205, 209
- Alfvén H., Herlofson N., 1950, Physical Review 78, 616
- Alvarez M.A., Wise J.H., Abel T., 2009, ApJL 701, L133
- Amaro-Seoane P., Aoudia S., Babak S., et al., 2012, Classical and Quantum Gravity 29, 124016

- Anchordoqui L.A., Paul T.C., da Silva L.H.M., et al., 2014, *Phys. Rev. D* 89, 127304
- Anders E., Grevesse N., 1989, *Geochim. Cosmochim. Acta* 53, 197
- Anderson W., 1930, *Zeitschrift für Physik* 66, 280
- ANTARES Collaboration: Adrián-Martínez S., Albert A., et al., 2015, *A&A* 576, L8
- Anton G., ANTARES Collaboration 2012, *Nuclear Physics B Proceedings Supplements* 229, 274
- Antonucci R., 1993, *ARA&A* 31, 473
- Antonucci R., 2002, In: Trujillo-Bueno J., Moreno-Insertis F., Sánchez F. (eds.) *Astrophysical Spectropolarimetry. XII, Canary Islands Winter School of Astrophysics, Puerto de la Cruz, Tenerife, Spain*, p.151
- Arnaud K.A., 1996, In: Jacoby G.H., Barnes J. (eds.) *Astronomical Data Analysis Software and Systems V, Tucson, AZ, USA, ASPC* 101, p. 17
- Aschenbach B., 1985, *Reports on Progress in Physics* 48, 579
- Askaryan G.A., 1962, *Journal of the Physical Society of Japan Supplement* 17, 257
- Asplund M., Grevesse N., Sauval A.J., Scott P., 2009, *ARA&A* 47, 481
- Atoyan A., Dermer C.D., 2001, *PhRL* 87, 221102
- Atoyan A.M., Dermer C.D., 2003, *ApJ* 586, 79
- Atri D., Melott A.L., 2014, *Aph* 53, 186
- Atwood W.B., Abdo A.A., Ackermann M., et al., 2009, *ApJ* 697, 1071
- Auchettl K., Slane P., Castro D., 2014, *ApJ* 783, 32
- Avni Y., Tananbaum H., 1982, *ApJL* 262, L17
- Bajaja E., Arnal E.M., Larrarte J.J., et al., 2005, *A&A* 440, 767
- Baloković M., Paneque D., Madejski G., et al., 2015, *ApJ*, in press (arXiv:1512.02235)
- Balucinska-Church M., McCammon D., 1992, *ApJ* 400, 699
- Barnes D.G., Staveley-Smith L., de Blok W.J.G., et al., 2001, *MNRAS* 322, 486
- Barthelmy S.D., Barbier L.M., Cummings J.R., et al., 2005, *Space Sci. Rev.* 120, 143
- Bartoli B., Bernardini P., Bi X.J., et al., 2012, *ApJ* 758, 2
- Bartoli B., Bernardini P., Bi X.J., et al., 2016, *ApJS* 222, 6
- Barvainis R., 1993, *ApJ* 412, 513
- Baumgartner W.H., Markwardt C., Troja E., et al., 2014, In: AAS, HEAD meeting, Chicago, Illinois, USA, AAS/High Energy Astrophysics Division 14, p. 120.18
- Baumgartner W.H., Tueller J., Markwardt C.B., et al., 2013, *ApJS* 207, 19
- Beasley A.J., Gordon D., Peck A.B., et al., 2002, *ApJS* 141, 13
- Becker Tjus J., Eichmann B., Halzen F., et al., 2014, *Phys. Rev. D* 89, 123005
- Becquerel H., 1896, *Comptes Rendus* 122, 420
- Bednarek W., Protheroe R.J., 1999, *MNRAS* 302, 373
- Begelman M.C., Fabian A.C., Rees M.J., 2008, *MNRAS* 384, L19
- Beringer J., Arguin J.F., Barnett R.M., et al., 2012, *Phys. Rev. D* 86, 010001
- Beuchert T., Markowitz A.G., Krauß F., et al., 2015, *A&A* 584, A82
- Bignami G.F., Boella G., Burger J.J., et al., 1975, *Space Science Instrumentation* 1, 245
- Binette L., Magris C. G., Krongold Y., et al., 2005, *ApJ* 631, 661
- Binns W.R., Israel M.H., Klarmann J., et al., 1981, *Nucl. Instr. Meth.* 185, 415
- Blanchard J., 2013, *Southern Hemisphere Gamma-ray Blazars*, PhD thesis
- Blandford R.D., Königl A., 1979, *ApJ* 232, 34
- Blandford R.D., Payne D.G., 1982, *MNRAS* 199, 883
- Blandford R.D., Znajek R.L., 1977, *MNRAS* 179, 433
- Blasi P., 2014, *Comptes Rendus Physique* 15, 329
- Błażejowski M., Blaylock G., Bond I.H., et al., 2005, *ApJ* 630, 130
- Bloom J.S., Kasen D., Shen K.J., et al., 2012, *ApJL* 744, L17
- Bloom S.D., Marscher A.P., 1993, In: Friedlander M., Gehrels N., Macomb D.J. (eds.) *Compton Gamma-ray observatory, AIPC* 280, p.578
- Blumenthal G.R., Gould R.J., 1970, *Rev. Mod. Phys.* 42, 237
- Böck M., Kadler M., Müller C., et al., 2016, *Radio and Gamma-ray Properties of Extragalactic Jets from the TANAMI Sample*, in press, ArXiv:1601.05099
- Boettcher M., Harris D., Krawczynski H., 2012, *Relativistic Jets from Active Galactic Nuclei*, Wiley-VCH, Weinheim, Germany
- Bonchi A., La Franca F., Melini G., et al., 2013, *MNRAS* 429, 1970
- Bonning E., Urry C.M., Bailyn C., et al., 2012, *ApJ* 756, 13
- Böttcher M., 2007, *Ap&SS* 309, 95
- Böttcher M., Reimer A., Marscher A.P., 2009, *ApJ* 703, 1168
- Böttcher M., Reimer A., Sweeney K., Prakash A., 2013, *ApJ* 768, 54
- Bowen I.S., 1927, *Nature* 120, 473
- Bradt H., 2004, *Astronomy Methods: A Physical Approach to Astronomical Observations*, Cambridge University Press, UK
- Brahe T., 1573, *De nova et nullius aevi memoria*

- prius visa stella, Laurentius Benedictus
- Breeveld A.A., Curran P.A., Hoversten E.A., et al., 2010, *MNRAS* 406, 1687
- Breeveld A.A., Landsman W., Holland S.T., et al., 2011, In: McEnery J.E., Racusin J.L., Gehrels N. (eds.) *Gamma Ray Bursts 2010*, Annapolis, MD, USA, AIPC 1358, p.373
- Breeveld A.A., Poole T.S., James C.H., et al., 2005, In: Siegmund O.H.W. (ed.) *UV, X-Ray, and Gamma-Ray Space Instrumentation for Astronomy XIV*, San Diego, CA, USA, Proc. SPIE 5898, p.391
- Bromm V., Loeb A., 2003, *ApJ* 596, 34
- Broos P.S., Townsley L.K., Feigelson E.D., et al., 2010, *ApJ* 714, 1582
- Brown P.J., Dawson K.S., de Pasquale M., et al., 2012, *ApJ* 753, 22
- Browne I.W.A., Savage A., Bolton J.G., 1975, *MNRAS* 173, 87P
- Burbidge E.M., Burbidge G.R., Fowler W.A., Hoyle F., 1957, *Rev. Mod. Phys.* 29, 547
- Burke B.F., Graham-Smith F., 2002, *An Introduction to Radio Astronomy: Second Edition*, Cambridge University Press, UK
- Burrows A., Lattimer J.M., 1987, *ApJL* 318, L63
- Burrows A., The L.S., 1990, *ApJ* 360, 626
- Burrows D.N., Hill J.E., Nousek J.A., et al., 2005, *Space Sci. Rev.* 120, 165
- Burrows D.N., Hill J.E., Nousek J.A., et al., 2004, In: Flanagan K.A., Siegmund O.H.W. (eds.) *X-Ray and Gamma-Ray Instrumentation for Astronomy XIII*, San Diego, CA, USA, Proc. SPIE 5165, p.201
- Burrows D.N., Hill J.E., Nousek J.A., et al., 2000, In: Flanagan K.A., Siegmund O.H. (eds.) *X-Ray and Gamma-Ray Instrumentation for Astronomy XI*, San Diego, CA, USA, Proc. SPIE 4140, p.64
- Buson S., Longo F., Larsson S., et al., 2014, *A&A* 569, A40
- Butrica A.J., 1997, *Beyond the ionosphere: fifty years of satellite communication*, NASA History Office, Washington, D.C., USA
- Buxton M.M., Bailyn C.D., Capelo H.L., et al., 2012, *AJ* 143, 130
- Böck M., 2012, *Observations of Active Galactic Nuclei from Radio to Gamma-rays*, Dissertation, FAU Erlangen
- Cao Y., Kasliwal M.M., McKay A., Bradley A., 2014, *The Astronomer's Telegram* 5786
- Carnerero M.I., Raiteri C.M., Villata M., et al., 2015, *MNRAS* 450, 2677
- Cash W., 1979, *ApJ* 228, 939
- Cavallo G., Rees M.J., 1978, *MNRAS* 183, 359
- Celotti A., Padovani P., Ghisellini G., 1997, *MNRAS* 286, 415
- Chandrasekhar S., 1994, *Journal of Astrophysics and Astronomy* 15, 105
- Chincarini G., Zerbi F., Antonelli A., et al., 2003, *The Messenger* 113, 40
- Churazov E., Sunyaev R., Isern J., et al., 2014, *Nature* 512, 406
- Ciprini S., Cutini S., 2013, *The Astronomer's Telegram* 4770
- Clagett M., 1989, *Ancient Egyptian Science: Calendars, clocks, and astronomy*, Ancient Egyptian Science, American Philosophical Society, Philadelphia, USA
- Clark G.W., Bradt H.V., Lewin W.H.G., et al., 1973, *ApJ* 179, 263
- Clayton D.D., 1984, *Principles of stellar evolution and nucleosynthesis*, 2nd edition, The University of Chicago Press, Chicago, USA
- Clayton D.D., The L.S., 1991, *ApJ* 375, 221
- Cohen M.H., Lister M.L., Homan D.C., et al., 2007, *ApJ* 658, 232
- Condon J.J., Cotton W.D., Greisen E.W., et al., 1998, *AJ* 115, 1693
- Covino S., Zerbi F., Chincarini G., et al., 2002, In: Favata F., Drake J.J. (eds.) *Stellar Coronae in the Chandra and XMM-NEWTON Era*, Astronomical Society of the Pacific Conference Series 277, p. 449
- Cracco V., Ciroi S., di Mille F., et al., 2011, *MNRAS* 418, 2630
- Craig N., Fruscione A., 1997, *AJ* 114, 1356
- Curtis H.D., 1918, *Publications of Lick Observatory* 13, 9
- Cusumano G., XRT Calibration Team 2006, *Nuovo Cimento B Serie* 121, 1463
- Cutri R.M., Skrutskie M.F., van Dyk S., et al., 2003, *VizieR Online Data Catalog* 2246
- Czerny B., Hryniewicz K., 2011, *A&A* 525, L8
- D'Ammando F., Antolini E., Tosti G., et al., 2013, *MNRAS* 431, 2481
- Datlowe D.W., Elcan M.J., Hudson H.S., 1974, *Solar Phys.* 39, 155
- Davis J.E., 2001a, *ApJ* 562, 575
- Davis J.E., 2001b, *ApJ* 548, 1010
- Davis R., Harmer D.S., Hoffman K.C., 1968, *Physical Review Letters* 20, 1205
- de Gouveia Dal Pino E.M., Piovezan P.P., Kadowaki L.H.S., 2010, *A&A* 518, A5
- Deller A.T., Brisken W.F., Phillips C.J., et al., 2011, *PASP* 123, 275
- Deller A.T., Tingay S.J., Bailes M., West C., 2007, *PASP* 119, 318
- Dermer C.D., 1995, *ApJL* 446, L63
- Dermer C.D., 2007, In: *30th International Cosmic Ray Conference*

- Dermer C.D., Murase K., Inoue Y., 2014, *Journal of High Energy Astrophysics* 3, 29
- Dermer C.D., Schlickeiser R., 1993, *ApJ* 416, 458
- Dickey J.M., Kulkarni S.R., van Gorkom J.H., Heiles C.E., 1983, *ApJS* 53, 591
- Diehl R., Siebert T., Hillebrandt W., et al., 2014, *Science* 345, 1162
- Dilday B., Howell D.A., Cenko S.B., et al., 2012, *Science* 337, 942
- Dimitrakoudis S., Mastichiadis A., Protheroe R.J., Reimer A., 2012, *A&A* 546, A120
- Dimitrakoudis S., Petropoulou M., Mastichiadis A., 2014, *Aph* 54, 61
- Djorgovski S.G., Volonteri M., Springel V., et al., 2008, In: Kleinert H., Jantzen R.T., Ruffini R. (eds.) *The Eleventh Marcel Grossmann Meeting On Recent Developments in Theoretical and Experimental General Relativity, Gravitation and Relativistic Field Theories*, Berlin, Germany, p.340
- Dodson R., Fomalont E.B., Wiik K., et al., 2008, *ApJS* 175, 314
- Donato D., Ghisellini G., Tagliaferri G., Fossati G., 2001, *A&A* 375, 739
- Done C., Krolik J.H., 1996, *ApJ* 463, 144
- Donnarumma I., Vittorini V., Vercellone S., et al., 2009, *ApJL* 691, L13
- Dreyer J.L.E., 1888, *Mem. R. Astron. Soc.* 49, 1
- Duschl W.J., Strittmatter P.A., 2011, *MNRAS* 413, 1495
- Dutka M.S., Ojha R., Pottschmidt K., et al., 2013, *ApJ* 779, 174
- Eddington A.S., 1919a, *Nature* 104, 372
- Eddington A.S., 1919b, *The Observatory* 42, 119
- Edge D.O., Shakeshaft J.R., McAdam W.B., et al., 1959, *Mem. R. Astron. Soc.* 68, 37
- Einstein A., 1915a, *Sitzungsber. preuss. Akad. Wiss.* 47, 831
- Einstein A., 1915b, *Sitzungsber. preuss. Akad. Wiss.* 778–786
- Elvis M., Wilkes B.J., McDowell J.C., et al., 1994, *ApJS* 95, 1
- Emmanoulopoulos D., Papadakis I.E., McHardy I.M., et al., 2012, *MNRAS* 424, 1327
- Evans J., 1998, *The history and practice of ancient astronomy*, Oxford University Press, UK
- Ewen H.I., Purcell E.M., 1951, *Nature* 168, 356
- Falcke H., Biermann P.L., 1995, *A&A* 293
- Falcke H., Körding E., Markoff S., 2004, *A&A* 414, 895
- Falcke H., Melia F., Agol E., 2000, *ApJL* 528, L13
- Falomo R., Maraschi L., Treves A., Tanzi E.G., 1987, *ApJL* 318, L39
- Falomo R., Pesce J.E., Treves A., 1993, *ApJL* 411, L63
- Farrell S.A., Servillat M., Pforr J., et al., 2012, *ApJL* 747, L13
- Farrell S.A., Webb N.A., Barret D., et al., 2009, *Nature* 460, 73
- Fath E.A., 1909, *Lick Observatory Bulletin* 5, 71
- Feenberg E., Primakoff H., 1948, *Physical Review* 73, 449
- Fermi E., 1949, *Physical Review* 75, 1169
- Fey A.L., Ma C., Arias E.F., et al., 2004, *AJ* 127, 3587
- Fey A.L., Ojha R., Quick J.F.H., et al., 2006, *AJ* 132, 1944
- Fichtel C.E., Kniffen D.A., Hartman R.C., 1973, *ApJL* 186, L99
- Finke J.D., 2013, *ApJ* 763, 134
- Finke J.D., Dermer C.D., Böttcher M., 2008, *ApJ* 686, 181
- Fish V.L., Johnson M.D., Doeleman S.S., et al., 2016, *ApJ*, in press
- Fitzpatrick E.L., 1999, *PASP* 111, 63
- Fleishman G.D., Bietenholz M.F., 2007, *MNRAS* 376, 625
- Fomalont E.B., Petrov L., MacMillan D.S., et al., 2003, *AJ* 126, 2562
- Forman W., Jones C., Cominsky L., et al., 2012, *VizieR Online Data Catalog* 9004, 0
- Forrest D.J., Chupp E.L., Ryan J.M., et al., 1980, *Solar Phys.* 65, 15
- Fossati G., Maraschi L., Celotti A., et al., 1998, *MNRAS* 299, 433
- Fossey S.J., Cooke B., Pollack G., et al., 2014, *Central Bureau Electronic Telegrams* 3792, 1
- Fox D.B., Kashiyama K., Mészáros P., 2013, *ApJ* 774, 74
- Fraser G.W., Abbey A.F., Holland A., et al., 1994, *Nuclear Instruments and Methods in Physics Research A* 350, 368
- Fukuda S., Fukuda Y., Hayakawa T., et al., 2003, *Nuclear Instruments and Methods in Physics Research A* 501, 418
- Fukugita M., Suzuki A., 2013, *Physics and Astrophysics of Neutrinos*, Springer, Japan
- Furniss A., Noda K., Boggs S., et al., 2015, *ApJ* 812, 65
- Gaibler V., Krause M., Camenzind M., 2009, *MNRAS* 400, 1785
- Gallo E., Fender R.P., Pooley G.G., 2003, *MNRAS* 344, 60
- Gehrels N., Chincarini G., Giommi P., et al., 2004, *ApJ* 611, 1005
- Getman K.V., Feigelson E.D., Broos P.S., et al., 2010, *ApJ* 708, 1760
- Ghisellini G., 2013, In: *Jets 2013: The Innermost Regions of Relativistic Jets and Their Magnetic*

- Fields, Granada, Spain, EPJ Web of Conferences 61, p. 5001
- Ghisellini G., Celotti A., Fossati G., et al., 1998, MNRAS 301, 451
- Ghisellini G., Madau P., 1996, MNRAS 280, 67
- Ghisellini G., Maraschi L., Tavecchio F., 2009, MNRAS 396, L105
- Ghisellini G., Maraschi L., Treves A., 1985, A&A 146, 204
- Ghisellini G., Tavecchio F., 2010, MNRAS 409, L79
- Ghisellini G., Tavecchio F., Foschini L., et al., 2010, MNRAS 402, 497
- Giacconi R., 2003, Reviews of Modern Physics 75, 995
- Giacconi R., Branduardi G., Briel U., et al., 1979, ApJ 230, 540
- Giacconi R., Gursky H., Paolini F.R., Rossi B.B., 1962, Phys. Rev. Lett. 9, 439
- Giacconi R., Gursky H., Waters J.R., et al., 1964, Nature 204, 981
- Giannios D., 2010, MNRAS 408, L46
- Ginzburg V.L., Syrovatskii S.I., 1965, ARA&A 3, 297
- Giommi P., Ansari S.G., Micol A., 1995, A&AS 109, 267
- Giommi P., Blustin A.J., Capalbi M., et al., 2006, A&A 456, 911
- Giommi P., Capalbi M., Fiocchi M., et al., 2002, In: Giommi P., Massaro E., Palumbo G. (eds.) Blazar Astrophysics with BeppoSAX and Other Observatories, p. 63
- Giommi P., Padovani P., Polenta G., et al., 2012a, MNRAS 420, 2899
- Giommi P., Polenta G., Lähteenmäki A., et al., 2012b, A&A 541, A160
- Girardi L., Bressan A., Bertelli G., Chiosi C., 2000, A&AS 141, 371
- Godet O., Beardmore A.P., Abbey A.F., et al., 2009, A&A 494, 775
- Gorenstein P., Gursky H., Garmire G., 1968, ApJ 153, 885
- Grandi P., Urry C.M., Maraschi L., et al., 1996, ApJ 459, 73
- Grinberg V., 2013, Investigations of the long term variability of black hole binaries, Dissertation, FAU Erlangen
- Gültekin K., Cackett E.M., King A.L., et al., 2014, ApJ 788, L22
- Gültekin K., Cackett E.M., Miller J.M., et al., 2009, ApJ 706, 404
- Halzen F., 2006, European Physical Journal C 46, 669
- Halzen F., Hooper D., 2005, Astropart. Phys. 23, 537
- Harrison F.A., Craig W.W., Christensen F.E., et al., 2013, ApJ 770, 103
- Hartmann D., Burton W.B., 1997, Atlas of Galactic Neutral Hydrogen, Cambridge University Press, UK
- Hasan I., MacPherson E., Buxton M., et al., 2013, The Astronomer's Telegram 4775
- Hawking S.W., 1975, Communications in Mathematical Physics 43, 199
- Hayakawa S., 1952, Progress of Theoretical Physics 8, 571
- Hayashida M., Nalewajko K., Madejski G.M., et al., 2015, ApJ 807, 79
- Hazard C., 1961, Nature 191, 58
- Hazard C., 1962, MNRAS 124, 343
- Hazard C., Mackey M.B., Shimmins A.J., 1963, Nature 197, 1037
- Healey S.E., Romani R.W., Cotter G., et al., 2008a, ApJS 175, 97
- Healey S.E., Romani R.W., Cotter G., et al., 2008b, ApJS 175, 97
- Healey S.E., Romani R.W., Taylor G.B., et al., 2007, ApJS 171, 61
- Heidt J., Tröller M., Nilsson K., et al., 2004, A&A 418, 813
- Herschel W., 1786, Royal Society of London Philosophical Transactions Series I 76, 457
- Herschel W., 1800, Philosophical Transactions of the Royal Society of London 90, 284
- Hertz H., 1888, Annalen der Physik 270, 273
- Hertz H., 1889, Annalen der Physik 272, 769
- Hess V., 1912, Physikalische Zeitschrift 13, 1084
- H.E.S.S. Collaboration: Acero F., Aharonian F., et al., 2010, A&A 511, A52
- Hewitt A., Burbidge G., 1987, ApJS 63, 1
- Hill J., Burrows D., Nousek J., et al., 2004, In: APS Meeting, Denver Colorado, USA, APS Meeting Abstracts, p. 10005
- Hill J.E., Zuger M.E., Shoemaker J., et al., 2000, In: Flanagan K.A., Siegmund O.H. (eds.) X-Ray and Gamma-Ray Instrumentation for Astronomy XI, San Diego, CA, USA, Proc. SPIE 4140, p.87
- Hillas A.M., 1984, ARA&A 22, 425
- Hillebrandt W., Kromer M., Röpke F.K., Rüter A.J., 2013, Frontiers of Physics 8, 116
- Hillebrandt W., Niemeyer J.C., 2000, ARA&A 38, 191
- Hillebrandt W., Nomoto K., Wolff R.G., 1984, A&A 133, 175
- Hoffmeister C., 1929, Astronomische Nachrichten 236, 233
- Holland A.D., Turner M.J., Abbey A.F., Pool P.J., 1996, In: Siegmund O.H., Gummin M.A. (eds.) EUV, X-Ray, and Gamma-Ray Instrumentation for

- Astronomy VII, San Diego, CA, USA, Proc. SPIE 2808, p.414
- Hörandel J.R., 2013, In: Ormes J.F. (ed.) Centenary symposium 2012: Discovery of Cosmic Rays, AIPC Series 1516, p.52
- Houck J.C., 2002, In: Branduardi-Raymont G. (ed.) High Resolution X-ray Spectroscopy with XMM-Newton and Chandra, Holmbury St Mary, UK, p. 17
- Houck J.C., Denicola L.A., 2000, In: Manset N., Veillet C., Crabtree D. (eds.) Astronomical Data Analysis Software and Systems IX, Kona, Hawaii, ASPC 216, p. 591
- Hubble E.P., 1926, ApJ 64, 321
- Huggins M.L., 1898, ApJ 8, 54
- Huggins W., Miller W.A., 1864, Royal Society of London Philosophical Transactions Series I 154, 437
- Hunstead R.W., Murdoch H.S., 1980, MNRAS 192, 31P
- Hunstead R.W., Murdoch H.S., Shobbrook R.R., 1978, MNRAS 185, 149
- IceCube Collaboration 2013, Science 342, 6161, 1242856
- Immer K., Brunthaler A., Reid M.J., et al., 2011, ApJS 194, 25
- Inoue Y., Totani T., 2009, ApJ 702, 523
- Jackson C.A., Wall J.V., Shaver P.A., et al., 2002, A&A 386, 97
- Jagoda N., Austin G., Mickiewicz S., Goddard R., 1972, In: 18th Nuclear Science Symposium and 3rd Nuclear Power Systems Symposium, San Francisco, CA, USA, IEEE Transactions on Nuclear Science 19, p. 579
- Janesick J.R., 2001, Scientific charge-coupled devices, SPIE Optical Engineering Press
- Jansen F., Lumb D., Altieri B., et al., 2001, A&A 365, L1
- Jansky K., 1933, Proc. IRE 21, 1387
- Jansky K.G., 1932, Proc. IRE 20, 1920
- Jauncey D.L., Batty M.J., Wright A.E., et al., 1984, ApJ 286, 498
- Johnston K.J., Fey A.L., Zacharias N., et al., 1995, AJ 110, 880
- Jolley E.J.D., Kuncic Z., Bicknell G.V., Wagner S., 2009, MNRAS 400, 1521
- Jones D.H., Read M.A., Saunders W., et al., 2009, MNRAS 399, 683
- Jones D.H., Saunders W., Colless M., et al., 2004, MNRAS 355, 747
- Joye W.A., Mandel E., 2003, In: Payne H.E., Jędrzejewski R.I., Hook R.N. (eds.) Astronomical Data Analysis Software and Systems XII, Baltimore, MD, USA, ASPC 295, p. 489
- Junde H., 2008, Nuclear Data Sheets 109, 787
- Kadler M., 2016, Constraining the Possible Neutrino Spectra of High-Fluence Blazars with ANTARES, in press (2015)
- Kadler M., Krauß F., Mannheim K., 2015a, Coincidence of a high-fluence blazar outburst with a PeV-energy neutrino event, in press (arXiv:1602.02012)
- Kadler M., Ojha R., TANAMI Collaboration 2015b, Astron. Nachr. 336, 499
- Kalberla P.M.W., Burton W.B., Hartmann D., et al., 2005a, A&A 440, 775
- Kalberla P.M.W., Burton W.B., Hartmann D., et al., 2005b, A&A 440, 775
- Kalberla P.M.W., McClure-Griffiths N.M., Pisano D.J., et al., 2010, A&A 521, A17
- Kardashev N.S., Kovalev Y.Y., Kellermann K.I., 2012, The Radio Science Bulletin 343, 22
- Kasen D., 2010, ApJ 708, 1025
- Kataoka J., Mattox J.R., Quinn J., et al., 1999, ApJ 514, 138
- Katz U.F., Spiering C., 2012, Progress in Particle and Nuclear Physics 67, 651
- Kaufmann S., Hauser M., Kosack K., et al., 2009, In: 2009 Fermi Symposium, Washington D.C., USA, eConf Proceedings C091122
- Kelner S.R., Aharonian F.A., 2008, Phys. Rev. D 78, 034013
- Kembhavi A.K., Narlika J.V., 1999, Quasars and Active Galactic Nuclei, Cambridge University Press, UK
- King A., 2003, ApJL 596, L27
- Kobayashi C., Nomoto K., 2009, ApJ 707, 1466
- Koch-Westenholz U., 1995, Mesopotamian Astrology, Museum Tusulanum Press, Copenhagen, Denmark
- Körding E., Falcke H., Corbel S., 2006, A&A 456, 439
- Kormendy J., Richstone D., 1995, ARA&A 33, 581
- Kovalev Y.Y., Kellermann K.I., Lister M.L., et al., 2005, AJ 130, 2473
- Kraushaar W., Clark G.W., Garmire G., et al., 1965, ApJ 141, 845
- Kraushaar W.L., Clark G.W., Garmire G.P., et al., 1972, ApJ 177, 341
- Krauß F., 2013, Multiwavelength Observations of TANAMI Sources, Master's Thesis, FAU Erlangen
- Krauß F., Kadler M., Mannheim K., et al., 2014, A&A 566, L7
- Krauß F., Wang B., Baxter C., et al., 2015, In: 5th Fermi Symposium, Nagoya, Japan, arXiv:1502.02147
- Krauß F., Wilms J., Kadler M., 2016, The TANAMI Multiwavelength Program: Dynamic SEDs of

- Southern Blazars, in prep.
- Kreikenbohm A., 2013, An X-ray analysis of an XMM-Newton Sample of Compton-thick AGN, MSc Thesis, University Würzburg
- Krolik J.H., 1999, *Active Galactic Nuclei*, Princeton University Press, Princeton, New Jersey, USA
- Krolik J.H., Begelman M.C., 1988, *ApJ* 329, 702
- Kromer M., Sim S.A., Fink M., et al., 2010, *ApJ* 719, 1067
- Kunitzsch P., 1987, *The Messenger* 49, 42
- Labanti C., Di Cocco G., Malaguti G., et al., 1996, In: Ramsey B.D., Parnell T.A. (eds.) *Gamma-Ray and Cosmic-Ray Detectors, Techniques, and Missions*, Denver, Colorado, USA, Proc. SPIE 2806, p.269
- Lambert S.B., Gontier A.M., 2009, *A&A* 493, 317
- Lampton M., Margon B., Bowyer S., 1976a, *ApJ* 208, 177
- Lampton M., Margon B., Bowyer S., 1976b, *ApJ* 208, 177
- Laplace P.S., 1796, *Exposition du Système du Monde, A Paris, de l'imprimerie du Cercle-Social, rue du Théâtre-Français, n°4. L'An IV de la République française*
- Laughlin G., Bodenheimer P., Adams F.C., 1997, *ApJ* 482, 420
- Lawrence A., 1991, *MNRAS* 252, 586
- Lawrence A., 2012, *MNRAS* 423, 451
- Learned J.G., Mannheim K., 2000, *Annual Review of Nuclear and Particle Science* 50, 679
- Lebrun F., Leray J.P., Lavocat P., et al., 2003, *A&A* 411, L141
- Leising M.D., 2001, *ApJ* 563, 185
- Leising M.D., 2006, *ApJ* 651, 1019
- Leiter K., 2013, *Emissionseigenschaften von Mega-Masergalaxien im weichen Röntgenbereich*, Diploma thesis, University Würzburg
- Li T.P., Ma Y.Q., 1983, *ApJ* 272, 317
- Lichti G.G., Balonek T., Courvoisier T.J.L., et al., 1995, *A&A* 298, 711
- Linford J.D., Taylor G.B., Schinzel F.K., 2012, *ApJ* 757, 25
- Lister M.L., Aller M.F., Aller H.D., et al., 2013, *AJ* 146, 120
- Lister M.L., Cohen M.H., Homan D.C., et al., 2009, *AJ* 138, 1874
- Lister M.L., Homan D.C., 2005, *AJ* 130, 1389
- Litzinger E., 2011, *Observations of Compact Objects*, Diploma thesis, FAU Erlangen
- Liu Y., Zhang S.N., 2011, *ApJL* 728, L44
- Longair M.S., 2011, *High Energy Astrophysics*, Cambridge University Press, UK
- Longo M.J., 1987, *Phys. Rev. D* 36, 3276
- Lund N., Budtz-Jørgensen C., Westergaard N.J., et al., 2003, *A&A* 411, L231
- Lutz G., 2001, *Semiconductor Radiation Detectors: Device Physics*, Springer, Berlin, Heidelberg
- Lynden-Bell D., Rees M.J., 1971, *MNRAS* 152, 461
- Lyutikov M., Lister M., 2010, *ApJ* 722, 197
- Ma C., Arias E.F., Eubanks T.M., et al., 1998, *AJ* 116, 516
- Mackay C.D., 1986, *ARA&A* 24, 255
- Maeda K., Terada Y., Kasen D., et al., 2012, *ApJ* 760, 54
- Maitra D., Miller J.M., Markoff S., King A., 2011, *ApJ* 735, 107
- Makishima K., Maejima Y., Mitsuda K., et al., 1986, *ApJ* 308, 635
- Malkan M.A., Sargent W.L.W., 1982, *ApJ* 254, 22
- Mannheim K., 1993, *A&A* 269, 67
- Mannheim K., 1995a, *Astropart. Phys.* 3, 295
- Mannheim K., 1995b, *A&A* 297, 321
- Mannheim K., Biermann P.L., 1989, *A&A* 221, 211
- Mannheim K., Biermann P.L., 1992, *A&A* 253, L21
- Mannheim K., Schlickeiser R., 1994, *A&A* 286, 983
- Maraschi L., Ghisellini G., Celotti A., 1992, *ApJL* 397, L5
- Markert T.H., Canizares C.R., Clark G.W., et al., 1977, *ApJ* 218, 801
- Markowitz A.G., Krumpe M., Nikutta R., 2014, *MNRAS* 439, 1403
- Marscher A.P., Jorstad S.G., D'Arcangelo F.D., et al., 2008, *Nature* 452, 966
- Marscher A.P., Jorstad S.G., Larionov V.M., et al., 2010, *ApJL* 710, L126
- Mas-Hesse J.M., Giménez A., Culhane J.L., et al., 2003, *A&A* 411, L261
- Masetti N., Mason E., Landi R., et al., 2008, *A&A* 480, 715
- Massaro E., Giommi P., Leto C., et al., 2009a, *A&A* 495, 691
- Massaro E., Giommi P., Leto C., et al., 2009b, *A&A* 495, 691
- Massaro E., Perri M., Giommi P., Nesci R., 2004, *A&A* 413, 489
- Matteson J.L., 1978, In: *16th Aerospace Sciences Meeting*, Huntsville, Alabama, USA, p. 9
- Maxwell J.C., 1865, *Philosophical Transactions of the Royal Society of London* 155, 459
- Mayer L., Kazantzidis S., Escala A., Callegari S., 2010, *Nature* 466, 1082
- Mazzali P.A., Röpke F.K., Benetti S., Hillebrandt W., 2007, *Science* 315, 825
- McCulloch P.M., Ellingsen S.P., Jauncey D.L., et al., 2005, *AJ* 129, 2034
- McHardy I.M., 2010, In: Belloni T. (ed.) *From Microquasars to Quasars*, Lecture Notes in Physics

- McHardy I.M., Koerding E., Knigge C., et al., 2006, *Nature* 444, 730
- McK Mahille J., Schild R., Wendorf F., Brenner R., 2007, *African Skies* 11, 2
- McKinney J.C., Tchekhovskoy A., Blandford R.D., 2012, *MNRAS* 423, 3083
- Meegan C., Lichti G., Bhat P.N., et al., 2009, *ApJ* 702, 791
- Meier D.L., 2012, *Black Hole Astrophysics: The Engine Paradigm*, Springer, Berlin Heidelberg
- Meller H., Lipták J., Landesmuseum für Vorgeschichte (Halle S., et al., 2004, *Der geschmiedete Himmel: die weite Welt im Herzen Europas vor 3600 Jahren*, Theiss, Darmstadt, Germany
- Merloni A., Heinz S., di Matteo T., 2003, *MNRAS* 345, 1057
- Merloni A., Predehl P., Becker W., et al., 2012, *ArXiv:1209.3114*
- Messier C., 1781, *Catalogue des Nébuleuses & des amas d'Étoiles (Catalog of Nebulae and Star Clusters)*, *Connaissance des Temps*
- Meyer E.T., Fossati G., Georganopoulos M., Lister M.L., 2011, *ApJ* 740, 98
- Michell J., 1783, *Philosophical Transactions of the Royal Society of London* 74, 35
- Misner C.W., Thorne K.S., Wheeler J.A., 1973, *Gravitation*, W.H. Freeman and Co., San Francisco
- Mitsuda K., Bautz M., Inoue H., et al., 2007, *PASJ* 59, 1
- Mitsuda K., Inoue H., Koyama K., et al., 1984, *PASJ* 36, 741
- Moretti A., Campana S., Mineo T., et al., 2005, In: Siegmund O.H.W. (ed.) *UV, X-Ray, and Gamma-Ray Space Instrumentation for Astronomy XIV*, San Diego, CA, USA, *Proc. SPIE* 5898, p.360
- Morrison P., 1958, *Il Nuovo Cimento* 7, 858
- Mücke A., Protheroe R.J., 2001, *Aph* 15, 121
- Mücke A., Protheroe R.J., Engel R., et al., 2003, *Aph* 18, 593
- Mücke A., Rachen J.P., Engel R., et al., 2000, *Nuclear Physics B Proceedings Supplements* 80, C810
- Mukherjee R., Bertsch D.L., Bloom S.D., et al., 1997, *ApJ* 490, 116
- Müller C., Kadler M., Ojha R., et al., 2014a, *A&A* 562, A4
- Müller C., Kadler M., Ojha R., et al., 2014b, *A&A* 569, A115
- Müller C., Kadler M., Ojha R., et al., 2011, *A&A* 530, L11
- Müller C., Krauß F., Dauser T., et al., 2015, *A&A* 574, A117
- Muller C.A., Oort J.H., 1951, *Nature* 168, 357
- Murase K., Inoue Y., Dermer C.D., 2014, *Phys. Rev. D* 90, 023007
- Murdin P., Murdin L., 1985, *Supernovae*, Cambridge University Press, UK
- Müller C., 2014, *High-Resolution Observations of Active Galactic Nuclei in the Southern Hemisphere*, Dissertation, FAU Erlangen
- Müller, C. et al. 2016, *TANAMI: tracking active galactic nuclei with austral milliarcsecond interferometry. II. Additional Sources*, in prep.
- Nagai H., Haga T., Giovannini G., et al., 2014, *ApJ* 785, 53
- Nandra K., Barret D., Barcons X., et al., 2013, *ArXiv:1306.2307*
- Nemenashi P., Gaylard M., Ojha R., 2013, *The Astronomer's Telegram* 4819
- Nenkova M., Sirocky M.M., Nikutta R., et al., 2008, *ApJ* 685, 160
- Nesci R., Tosti G., Pursimo T., et al., 2013, *A&A* 555, A2
- Netzer H., 2015, *ARA&A* 53, 365
- Nieppola E., Tornikoski M., Valtaoja E., 2006, *A&A* 445, 441
- Nisbet D.M., Best P.N., 2016, *MNRAS* 455, 2551
- Noble M.S., Nowak M.A., 2008, *PASP* 120, 821
- Nolan P.L., Abdo A.A., Ackermann M., et al., 2012, *ApJS* 199, 31
- Nomoto K., Thielemann F.K., Yokoi K., 1984, *ApJ* 286, 644
- Norton A., 2000, *Dynamic Fields and Waves, The physical world*, Taylor & Francis, London, UK
- Nowak M.A., Neilsen J., Markoff S.B., et al., 2012, *ApJ* 759, 95
- Nowak M.A., Wilms J., Heinz S., et al., 2005, *ApJ* 626, 1006
- Oda M., Gorenstein P., Gursky H., et al., 1971, *ApJL* 166, L1
- Ojha R., Dutka M., 2012, *The Astronomer's Telegram* 4494
- Ojha R., Fey A.L., Johnston K.J., et al., 2004, *AJ* 127, 3609
- Ojha R., Kadler M., Böck M., et al., 2010, *A&A* 519, A45
- Oka T., Mizuno R., Miura K., Takekawa S., 2016, *ApJL* 816, L7
- Oppenheimer J.R., Snyder H., 1939, *Physical Review* 56, 455
- Osborne J.P., Beardmore A.P., Godet O., et al., 2005, In: Siegmund O.H.W. (ed.) *UV, X-Ray, and Gamma-Ray Space Instrumentation for Astronomy XIV*, San Diego, CA, USA, *Proc. SPIE* 5898, p.352

- Owens A., Bayliss S.C., Durham P.J., et al., 1996, *ApJ* 468, 451
- Owens A., Denby M., Wells A., et al., 1997, *ApJ* 476, 924
- Pacciani L., Vittorini V., Tavani M., et al., 2010, *ApJL* 716, L170
- Pacini D., 1912, *Nuovo Cimento VI/3*, 93 translated and commented by Alessandro De Angelis, arXiv: 1002.1810
- Padovani P., Giommi P., 1995, *ApJ* 444, 567
- Padovani P., Giommi P., Ábrahám P., et al., 2006, *A&A* 456, 131
- Padovani P., Resconi E., 2014, *MNRAS* 443, 474
- Pagani C., Morris D.C., Racusin J., et al., 2007, In: *UV, X-Ray, and Gamma-Ray Space Instrumentation for Astronomy XV*, San Diego, CA, USA, Proc. SPIE 6686, p. 9
- Pakmor R., Kromer M., Taubenberger S., et al., 2012, *ApJL* 747, L10
- Paliya V.S., Sahayanathan S., Stalin C.S., 2015, *ApJ* 803, 15
- Parker R.A., 1950, *The calendars of ancient egypt*, The University of Chicago Press, Chicago, USA
- Pasachoff N., 1997, *Marie Curie: And the Science of Radioactivity*, Oxford Portraits in Science, Oxford University Press, UK
- Patat F., Chandra P., Chevalier R., et al., 2007, *Science* 317, 924
- Penrose R., 1969, *Nuovo Cimento Rivista Serie 1*, 252
- Perlmutter S., Aldering G., Goldhaber G., et al., 1999, *ApJ* 517, 565
- Perucho M., 2013, In: *Jets 2013: The Innermost Regions of Relativistic Jets and Their Magnetic Fields*, Granada, Spain, EPJ Web of Conferences 61, p. 02002
- Peterson B.A., Jauncey D.L., Condon J.J., Wright A.E., 1976, *ApJL* 207, L5
- Peterson B.M., 1997, *An Introduction to Active Galactic Nuclei*, Cambridge University Press, UK
- Peterson B.M., Bentz M.C., Desroches L.B., et al., 2005, *ApJ* 632, 799
- Petropoulou M., Mastichiadis A., 2012, *MNRAS* 426, 462
- Petropoulou M., Mastichiadis A., 2015, *MNRAS* 447, 36
- Petrov L., Kovalev Y.Y., Fomalont E., Gordon D., 2005, *AJ* 129, 1163
- Petrov L., Phillips C., Bertarini A., et al., 2011, *MNRAS* 414, 2528
- Petschek A.G., (ed.) 1990, *Supernovae*, Springer Verlag, New York
- Pian E., Vacanti G., Tagliaferri G., et al., 1998, *ApJL* 492, L17
- Pickel J.C., Blandford, Jr. J.T., 1980, *IEEE* 27, 1006
- Piner B.G., Edwards P.G., 2014, *ApJ* 797, 25
- Planck Collaboration Ade P.A.R., Aghanim N., et al., 2014a, *A&A* 571, A1
- Planck Collaboration Ade P.A.R., Aghanim N., et al., 2014b, *A&A* 571, A28
- Plotkin R.M., Markoff S., Kelly B.C., et al., 2012, *MNRAS* 419, 267
- Poole T.S., Breeveld A.A., Page M.J., et al., 2008, *MNRAS* 383, 627
- Predehl P., Schmitt J.H.M.M., 1995, *A&A* 293, 889
- Rachen J.P., Mészáros P., 1998, *Phys. Rev. D* 58, 123005
- Rashed R., 1990, *Isis* 81, 464
- Razzaque S., 2013, *Phys. Rev. D* 88, 081302
- Reid M.J., Biretta J.A., Junor W., et al., 1989, *ApJ* 336, 112
- Reimer A., Böttcher M., Postnikov S., 2005, *ApJ* 630, 186
- Reynolds S.P., 1982, *ApJ* 256, 13
- Riess A.G., Filippenko A.V., Challis P., et al., 1998, *AJ* 116, 1009
- Ritter J.W., 1803, *Annalen der Physik* 12, 409
- Roland J., Sol H., Pelletier G., 1992, *Extragalactic radio sources - from beams to jets*. Proceedings., Cambridge University Press, UK
- Romano P., Cusumano G., Campana S., et al., 2005, In: *Siegmund O.H.W. (ed.) UV, X-Ray, and Gamma-Ray Space Instrumentation for Astronomy XIV*, San Diego, CA, USA, Proc. SPIE 5898, p.369
- Roming P.W.A., Kennedy T.E., Mason K.O., et al., 2005, *Space Sci. Rev.* 120, 95
- Röntgen W.C., 1898a, *Annalen der Physik* 300, 1
- Röntgen W.C., 1898b, *Annalen der Physik* 300, 18
- Röpke F.K., Kromer M., Seitenzahl I.R., et al., 2012, *ApJL* 750, L19
- Ruggles C.L.N., 2005, *Ancient astronomy : an encyclopedia of cosmologies and myth*, ABC-CLIO, Santa Barbara, CA, USA
- Ryan S.G., Norton A.J., 2010, *Stellar Evolution and Nucleosynthesis*, Cambridge University Press, UK
- Rybicki G.B., Lightman A.P., 1979, *Radiative processes in astrophysics*, Wiley-Interscience, New York
- Saba I., Tjus J.B., Halzen F., 2013, *Astropart. Phys.* 48, 30
- Saikia P., Körding E., Falcke H., 2015, *MNRAS* 450, 2317
- Salpeter E.E., 1964, *ApJ* 140, 796
- Sambruna R.M., Maraschi L., Urry C.M., 1996, *ApJ* 463, 444

- Sanders D.B., Phinney E.S., Neugebauer G., et al., 1989, *ApJ* 347, 29
- Sbarufatti B., Ciprini S., Kotilainen J., et al., 2009, *AJ* 137, 337
- Scannapieco C., Tissera P.B., White S.D.M., Springel V., 2008, *MNRAS* 389, 1137
- Scargle J.D., 1998, *ApJ* 504, 405
- Scargle J.D., Norris J.P., Jackson B., Chiang J., 2013, *ApJ* 764, 167
- Schmidt B.P., Suntzeff N.B., Phillips M.M., et al., 1998, *ApJ* 507, 46
- Schmidt M., 1963, *Nature* 197, 1040
- Schulz R., 2012, A Study of the Active Galaxy 3C111 with mm-VLBI, Master's Thesis, Universität Würzburg
- Schwarzschild K., 1916a 424–434
- Schwarzschild K., 1916b, *Sitzungsber. preuss. Akad. Wiss.* 189–196
- Schwinger J., 1949, *Physical Review* 75, 1912
- Scott J.E., Kriss G.A., Brotherton M., et al., 2004, *ApJ* 615, 135
- Seitzzahl I.R., Cescutti G., Röpke F.K., et al., 2013a, *A&A* 559, L5
- Seitzzahl I.R., Ciaraldi-Schoolmann F., Röpke F.K., et al., 2013b, *MNRAS* 429, 1156
- Seitzzahl I.R., Summa A., Krauß F., et al., 2015, *MNRAS* 447, 1484
- Seneca, Hine, H. M. 2010, *Natural Questions*, University Of Chicago Press, Chicago An english translation of Seneca's *Naturales quaestiones*
- Seyfert C.K., 1943, *ApJ* 97, 28
- Shakeshaft J.R., Ryle M., Baldwin J.E., et al., 1955, *Mem. R. Astron. Soc.* 67, 106
- Shang Z., Brotherton M.S., Green R.F., et al., 2005, *ApJ* 619, 41
- Shaw M.S., Romani R.W., Cotter G., et al., 2012, *ApJ* 748, 49
- Shen K.J., Kasen D., Weinberg N.N., et al., 2010, *ApJ* 715, 767
- Shen Z.Q., Wan T.S., Moran J.M., et al., 1998, *AJ* 115, 1357
- Shepherd M.C., Pearson T.J., Taylor G.B., 1994, *BAAS* 26
- Shields G.A., 1978, *Nature* 272, 706
- Short A.D., Ambrosi R.M., Hutchinson I.B., et al., 2003, In: Ricker G.R., Vanderspek R.K. (eds.) *Gamma-Ray Burst and Afterglow Astronomy 2001: A Workshop Celebrating the First Year of the HETE Mission*, Woods Hole, Massachusetts, USA, *AIPC* 662, p.511
- Shu F.H., 1991, *The physics of astrophysics. Volume 1: Radiation.*, University Science Books, Mill Valley, CA, USA
- Sikora M., Begelman M.C., Madejski G.M., Lasota J.P., 2005, *ApJ* 625, 72
- Sikora M., Begelman M.C., Rees M.J., 1994, *ApJ* 421, 153
- Sikora M., Stawarz Ł., Moderski R., et al., 2009, *ApJ* 704, 38
- Sim S.A., Mazzali P.A., 2008, *MNRAS* 385, 1681
- Sim S.A., Seitzzahl I.R., Kromer M., et al., 2013, *MNRAS* 436, 333
- Singal J., Petrosian V., Ajello M., 2012, *ApJ* 753, 45
- Sironi L., Petropoulou M., Giannios D., 2015, *MNRAS* 450, 183
- Sitko M.L., Junkkarinen V.T., 1985, *PASP* 97, 1158
- Skrutskie M.F., Cutri R.M., Stiening R., et al., 2006, *AJ* 131, 1163
- Sol H., Pelletier G., Asseo E., 1989, *MNRAS* 237, 411
- Soldi S., Türler M., Paltani S., et al., 2008, *A&A* 486, 411
- Spalinger A., 2002, *Journal of the American Research Center in Egypt* 39, 241
- Spiering C., 2012, *European Physical Journal H* 37, 515
- Stacy J.G., Vestrand W.T., Sreekumar P., 2003, *ApJ* 598, 216
- Stanev T., 2004, *High energy cosmic rays*, Springer, Chichester, UK
- Stanimirovic S., Staveley-Smith L., Dickey J.M., et al., 1999, *MNRAS* 302, 417
- Stecker F.W., 2013, *Phys. Rev. D* 88, 047301
- Stecker F.W., Scully S.T., Liberati S., Mattingly D., 2015, *Phys. Rev. D* 91, 045009
- Sternberg A., Gal-Yam A., Simon J.D., et al., 2011, *Science* 333, 856
- Stevens J., Edwards P.G., Ojha R., et al., 2012, In: *Fermi & Jansky Proceedings: Our Evolving Understanding of AGN*, St Michaels, MD, USA, *eConf C1111101*, arXiv:1205.2403
- Summa A., Ulyanov A., Kromer M., et al., 2013, *A&A* 554, A67
- Tagliaferri G., Foschini L., Ghisellini G., et al., 2008, *ApJ* 679, 1029
- Tagliaferri G., Ghisellini G., Perri M., et al., 2015, *ApJ* 807, 167
- Takahashi T., Mitsuda K., Kelley R., et al., 2012, In: *Space Telescopes and Instrumentation 2012: Ultraviolet to Gamma Ray*, Amsterdam, The Netherlands, *Proc. SPIE* 8443, p. 84431Z
- Tanaka Y.T., Stawarz Ł., Thompson D.J., et al., 2011, *ApJ* 733, 19
- Tavani M., Barbiellini G., Argan A., et al., 2009, *A&A* 502, 995
- Tavecchio F., Ghisellini G., 2008, *MNRAS* 385, L98
- Taylor A.M., Gabici S., Aharonian F., 2014, *Phys. Rev.*

- D 89, 103003
- Tchekhovskoy A., Narayan R., McKinney J.C., 2011, *MNRAS* 418, L79
- Telfer R.C., Zheng W., Kriss G.A., Davidsen A.F., 2002, *ApJ* 565, 773
- The L.S., Bridgman W.T., Clayton D.D., 1994, *ApJS* 93, 531
- The L.S., Burrows A., 2014, *ApJ* 786, 141
- The Planck Collaboration 2006, The Scientific Programme of Planck, arXiv:0604069
- Thompson A.R., Moran J.M., Swenson, Jr. G.W., 2001, *Interferometry and Synthesis in Radio Astronomy*, 2nd Edition, Wiley, New York
- Toomer G., 1984, *Ptolemy's Almagest*, Springer-Verlag
- Truemper J., 1982, *Advances in Space Research* 2, 241
- Trüstedt J., 2013, *Multiepoch VLBI Observations of TANAMI Jets*, Master's Thesis, Universität Würzburg
- Türler M., Paltani S., Courvoisier T.J.L., et al., 1999, *A&AS* 134, 89
- Turner M.J.L., Abbey A., Arnaud M., et al., 2001, *A&A* 365, L27
- Ubertini P., Lebrun F., Di Cocco G., et al., 2003, *A&A* 411, L131
- Ulmer M.P., Matz S.M., Grabelsky D.A., et al., 1995, *ApJ* 448, 356
- Urry C.M., Padovani P., 1995, *PASP* 107, 803
- Valtaoja E., Lähteenmäki A., Teräsanta H., Lainela M., 1999, *ApJS* 120, 95
- van de Hulst H.C., 1951, *AJ* 56, 144
- van Moorsel G., Kembell A., Greisen E., 1996, In: Jacoby G.H., Barnes J. (eds.) *Astronomical Data Analysis Software and Systems V*, Tucson, AZ, USA, ASPC 101, p. 37
- Vedrenne G., Roques J.P., Schönfelder V., et al., 2003, *A&A* 411, L63
- Vercellone S., Chen A.W., Vittorini V., et al., 2009, *ApJ* 690, 1018
- Vermeulen R.C., Ogle P.M., Tran H.D., et al., 1995, *ApJL* 452, L5
- Verner D.A., Ferland G.J., Korista K.T., Yakovlev D.G., 1996, *ApJ* 465, 487
- Véron-Cetty M.P., Véron P., 2006, *A&A* 455, 773
- Vierregg A.G., Bechtol K., Romero-Wolf A., 2016, *JCAP* 2, 005
- Vignali C., Brandt W.N., Schneider D.P., 2003, *AJ* 125, 433
- Voges W., Aschenbach B., Boller T., et al., 1999, *A&A* 349, 389
- von Montigny C., Aller H., Aller M., et al., 1997, *ApJ* 483, 161
- von Montigny C., Bertsch D.L., Chiang J., et al., 1995, *ApJ* 440, 525
- Vuillaume T., Henri G., Petrucci P.O., 2015, *A&A* 581, A18
- Walter F., Brinks E., de Blok W.J.G., et al., 2008, *AJ* 136, 2563
- Watson M.G., Schroder A.C., Fyfe D., et al., 2008, *VizieR Online Data Catalog* 349, 30339
- Waxman E., 2015, *The origin of IceCube's neutrinos: Cosmic ray accelerators embedded in star forming calorimeters*, Submitted
- Waxman E., Bahcall J., 1997, *PRL* 78, 2292
- Wehrle A.E., Pian E., Urry C.M., et al., 1998, *ApJ* 497, 178
- Weidemann V., 1990, *ARA&A* 28, 103
- Weidemann V., Koester D., 1983, *A&A* 121, 77
- Weidinger M., Spanier F., 2015, *A&A* 573, A7
- Weisskopf M.C., Tananbaum H.D., Van Speybroeck L.P., O'Dell S.L., 2000, In: Truemper J.E., Aschenbach B. (eds.) *X-Ray Optics, Instruments, and Missions III*, Munich, Germany, Proc. SPIE 4012, p.2
- Wendorf F., Malville J.M., 2001, *The Megalithic Alignments In: Wendorf F., Schild R., Nelson K. (eds.) Holocene Settlement of the Egyptian Sahara* Springer, New York, USA, Ch. 16, p.489
- White G.L., Jauncey D.L., Wright A.E., et al., 1988, *ApJ* 327, 561
- Wilms J., Allen A., McCray R., 2000, *ApJ* 542, 914
- Wilms J., Reynolds C.S., Begelman M.C., et al., 2001, *MNRAS* 328, L27
- Wilsing J., Scheiner J., 1896, *Annalen der Physik* 295, 782
- Winkler C., Courvoisier T.J.L., Di Cocco G., et al., 2003, *A&A* 411, L1
- Winter W., 2013, *Phys. Rev. D* 88, 083007
- Wisotzki L., Christlieb N., Bade N., et al., 2000, *A&A* 358, 77
- Wolf K.B., Krotzsch G., 1995, *European Journal of Physics* 16, 14
- Wolter H., 1952a, *Annalen der Physik* 445, 94
- Wolter H., 1952b, *Annalen der Physik* 445, 286
- Woltjer L., 1959, *ApJ* 130, 38
- Woosley S.E., Weaver T.A., 1994, *ApJ* 423, 371
- Wright E.L., Eisenhardt P.R.M., Mainzer A.K., et al., 2010, *AJ* 140, 1868
- Wulf T., 1909a, *Physikalische Zeitschrift* 8, 251
- Wulf T., 1909b, *Physikalische Zeitschrift* 10, 997
- Wulf T., 1910, *Physikalische Zeitschrift* 11, 811
- Xu Z., Pankenier W., Jiang Y., 2000, *East-Asian Archaeoastronomy: Historical Records of Astronomical Observations of China, Japan and Korea*, Earth Space Institute Book Series, Taylor & Fran-

- cis, Abingdon, UK
- Yajima H., Khochfar S., 2016, MNRAS 457, 2423
- Zamorani G., Henry J.P., Maccacaro T., et al., 1981, ApJ 245, 357
- Zel'dovich Y.B., 1964, Soviet Physics Doklady 9, 195
- Zenitani S., Hoshino M., 2001, ApJL 562, L63
- Zhao F.Y., Strom R.G., Jiang S.Y., 2006, Chinese Journal of Astronomy and Astrophysics 6, 635
- Zheng W., Kriss G.A., Telfer R.C., et al., 1997, ApJ 475, 469

## Fermi/LAT light curves

This section contains all the *Fermi*/LAT light curves used for determining the source epochs in the Bayesian Block analysis for the SED analysis (see Chap. 6).

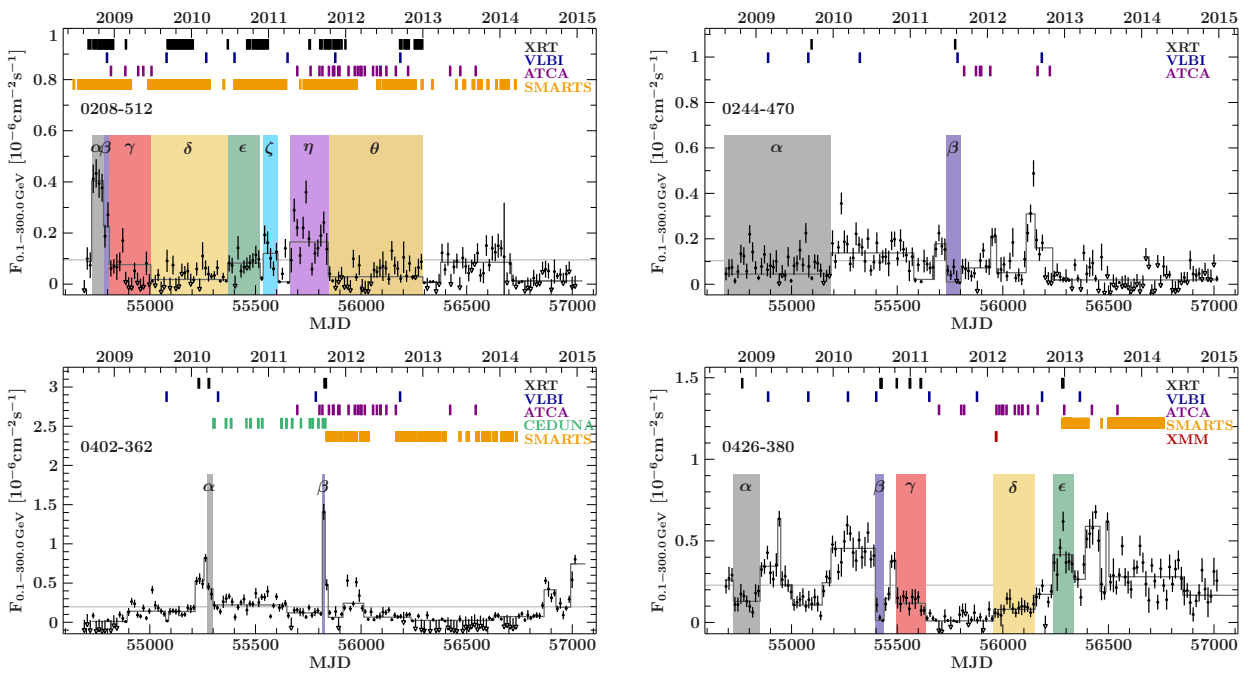


Figure A.1.: *Fermi*/LAT light curves for all sources with a known redshift, from August 2008 up to 2015 January 1. A Bayesian blocks analysis was performed on the data and is shown in dark gray. The horizontal light-gray line shows the average flux over the full light curve. Observations by *Swift*, *XMM-Newton*, REM, SMARTS, Ceduna, ATCA, or VLBI are marked with a line at the corresponding time. Blocks with sufficient data for a broadband SED are marked in color, and labeled with Greek letters. The colors correspond to the colors used in the broadband spectra.

APPENDIX A.

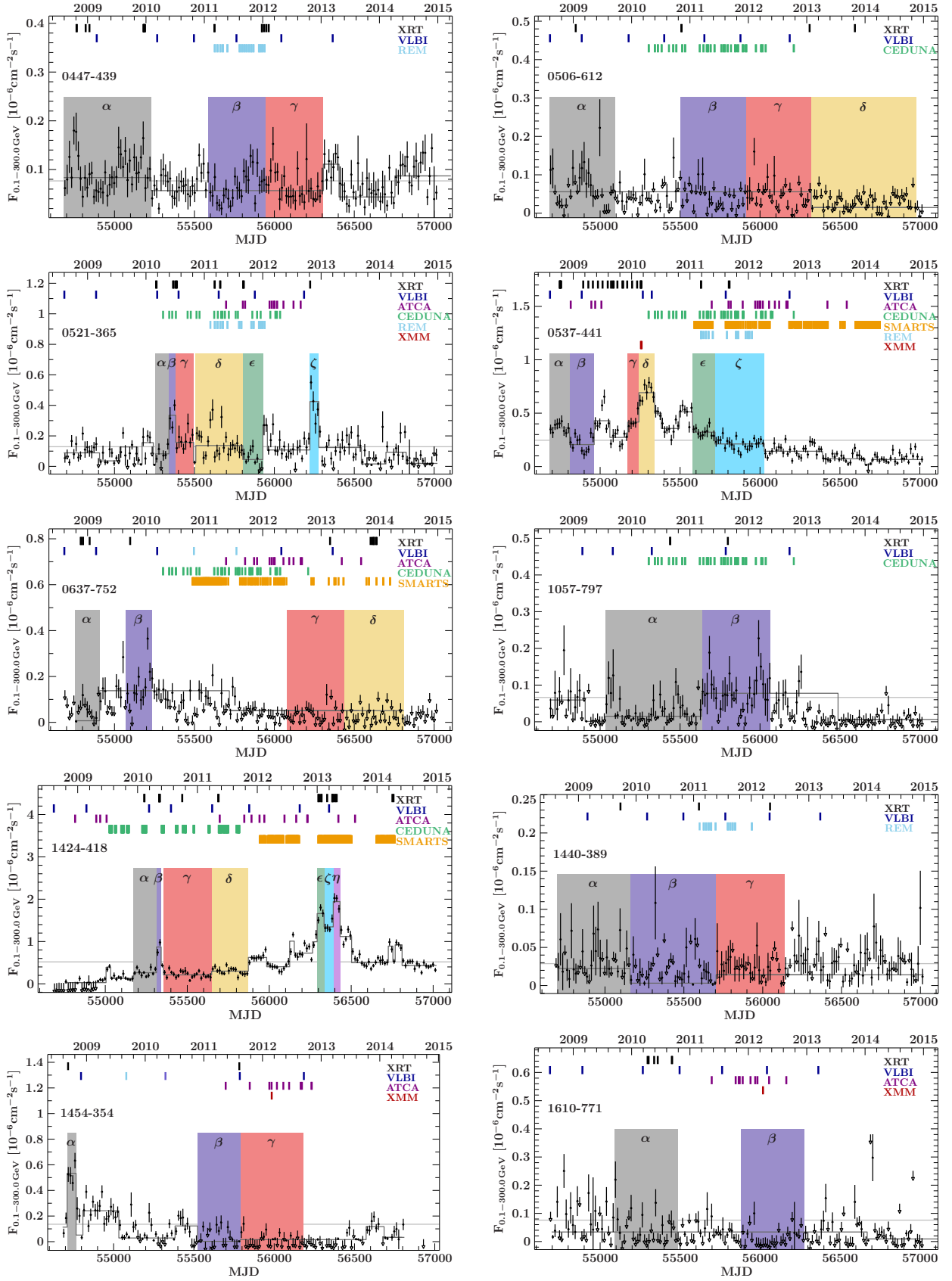


Figure A.1.: (contd.)

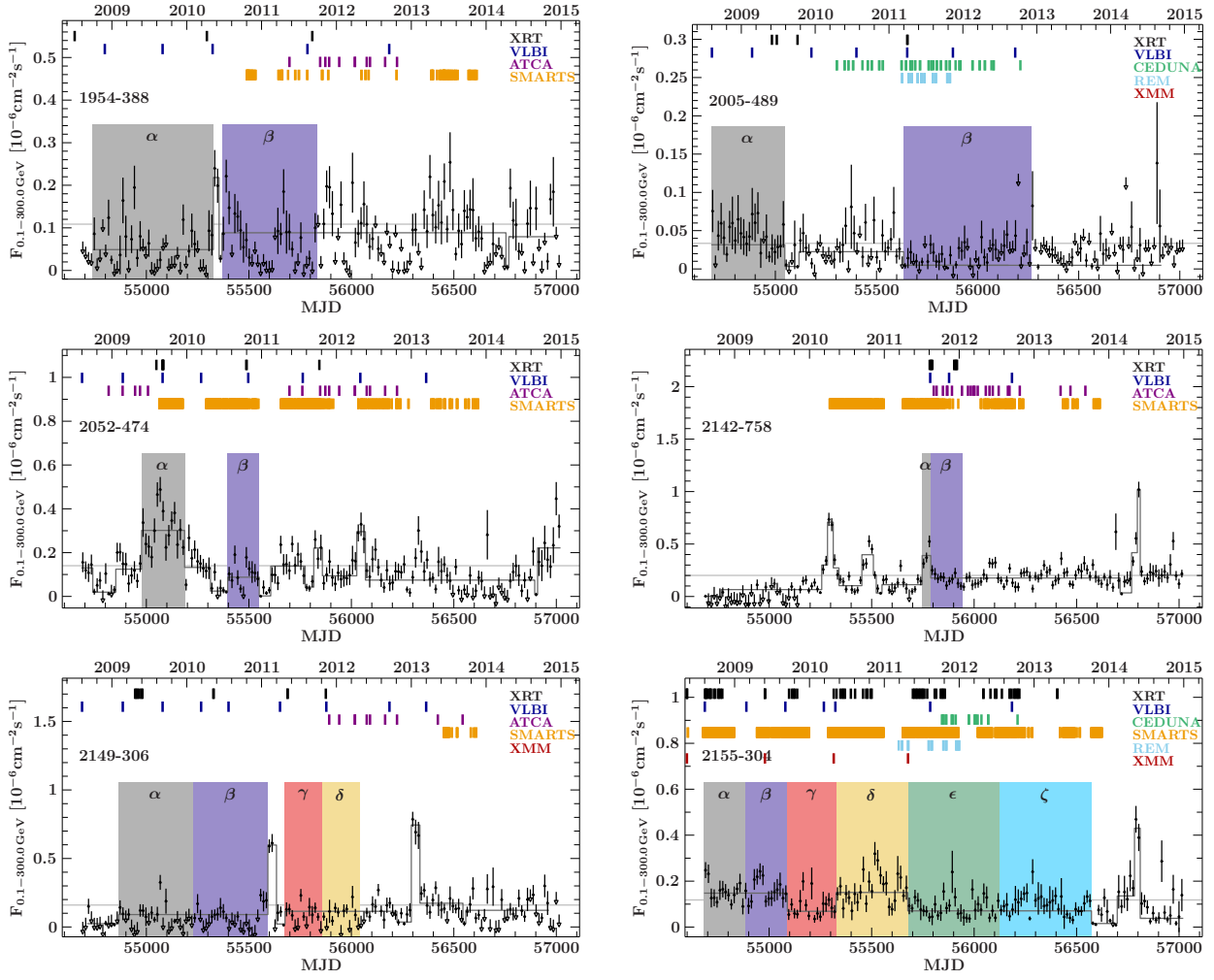


Figure A.1.: (contd.)

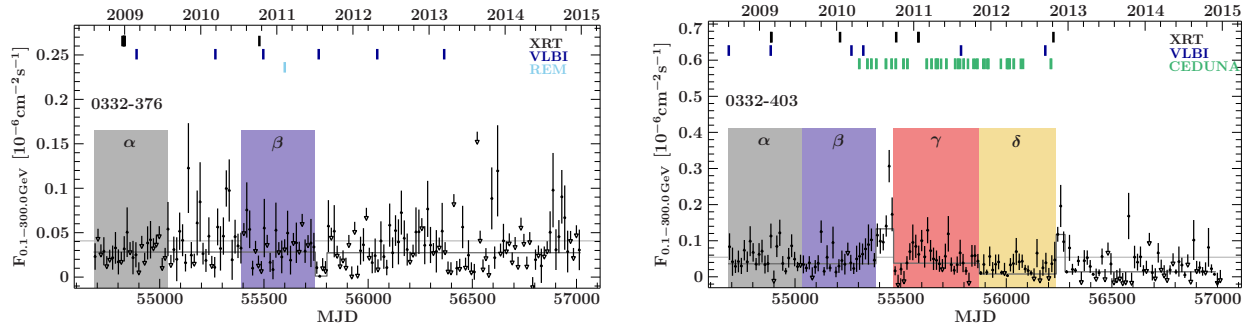


Figure A.2.: *Fermi*/LAT light curves for both sources without a known redshift, from August 2008 up to 2015 January 1. A Bayesian blocks analysis was performed on the data and is shown in dark gray. The horizontal light gray line shows the average flux over the full light curve. Observations by *Swift*, REM, Ceduna, and VLBI are marked with a line at the corresponding time. Blocks with sufficient data for a broadband SED are marked in color, and labeled with Greek letters. The colors correspond to the colors used in the broadband spectra.

## TANAMI Broadband spectra

This section contains all the broadband SEDs that were used in Chap. 6.

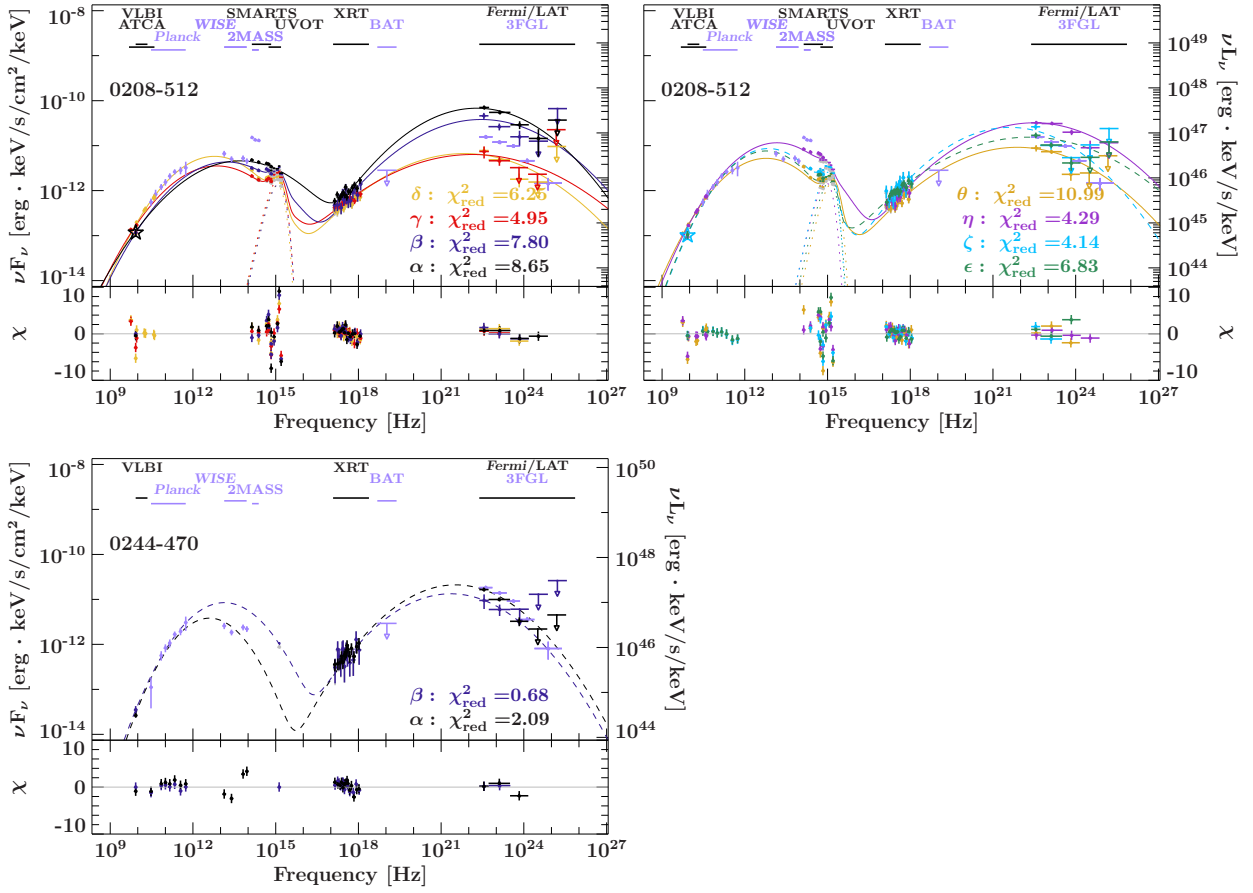


Figure A.3.: Broadband spectral energy distributions of all sources with a redshift in the loglog  $\nu F_\nu$  representation. For sources with more than 3 states with sufficient data, the plots were split into two parts, to ensure that the SEDs are easily visible. Spectra are shown in dashed if archival data had to be included in the fit. For sources with a thermal excess in the optical/UV, a blackbody was included (dotted). The instruments (including their spectral range) are shown above the spectrum. The colors correspond to the colors used in the light curve. The best fit reduced  $\chi^2$  value is shown at the bottom right for every state. Residuals are shown in the lower panel. The spectra have not been k-corrected.

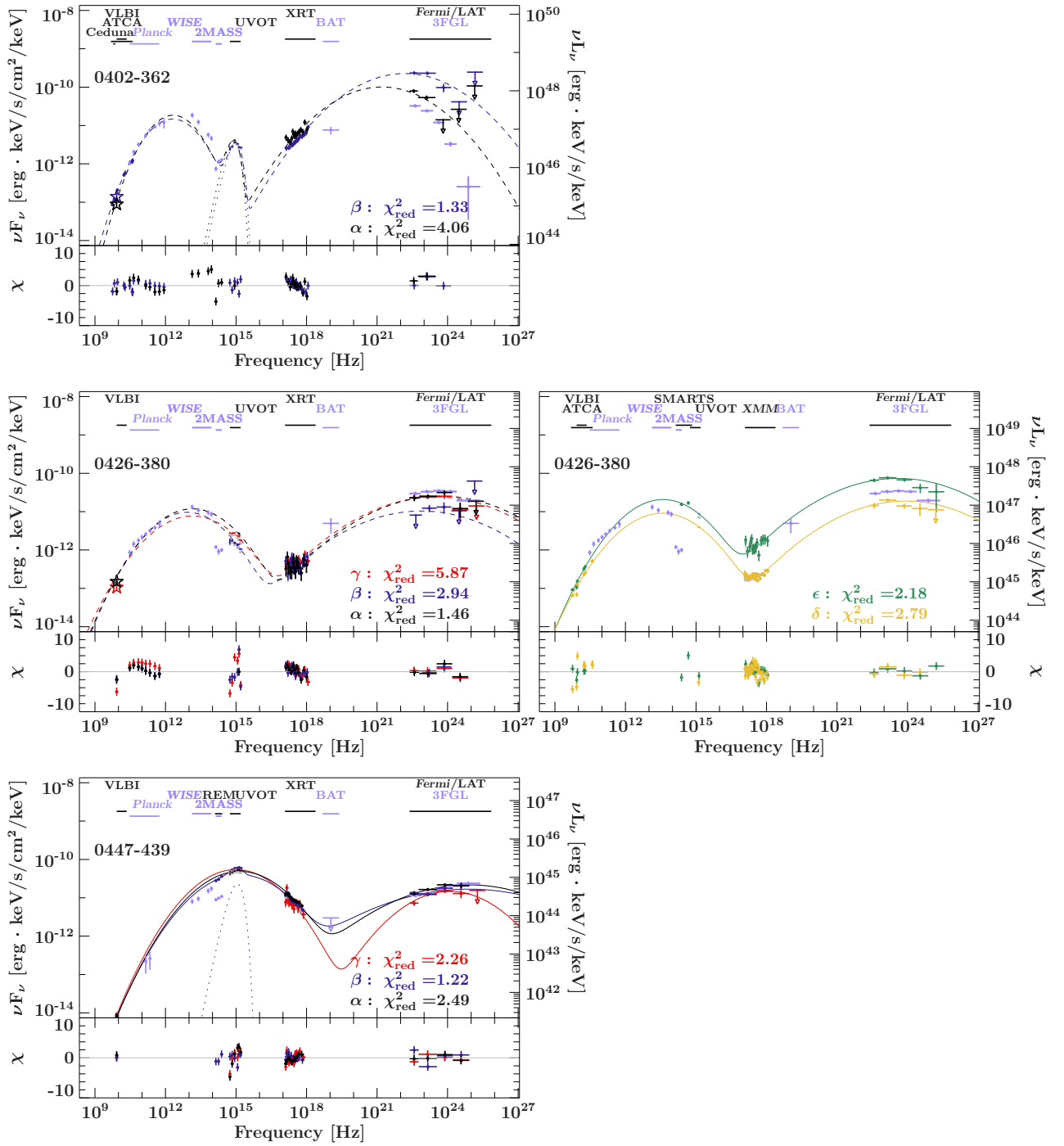


Figure A.3.: (contd.)

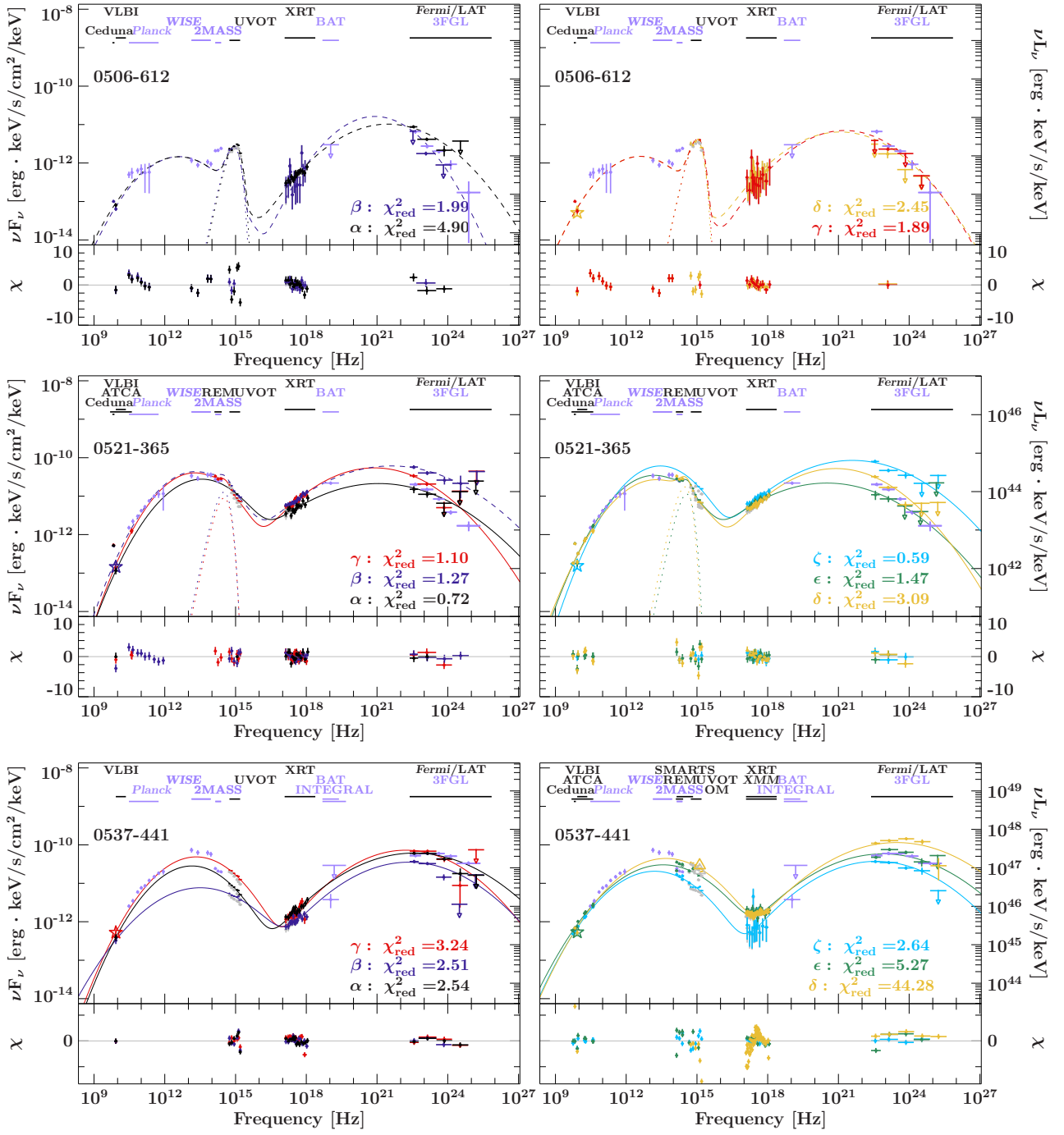


Figure A.3.: (contd.)

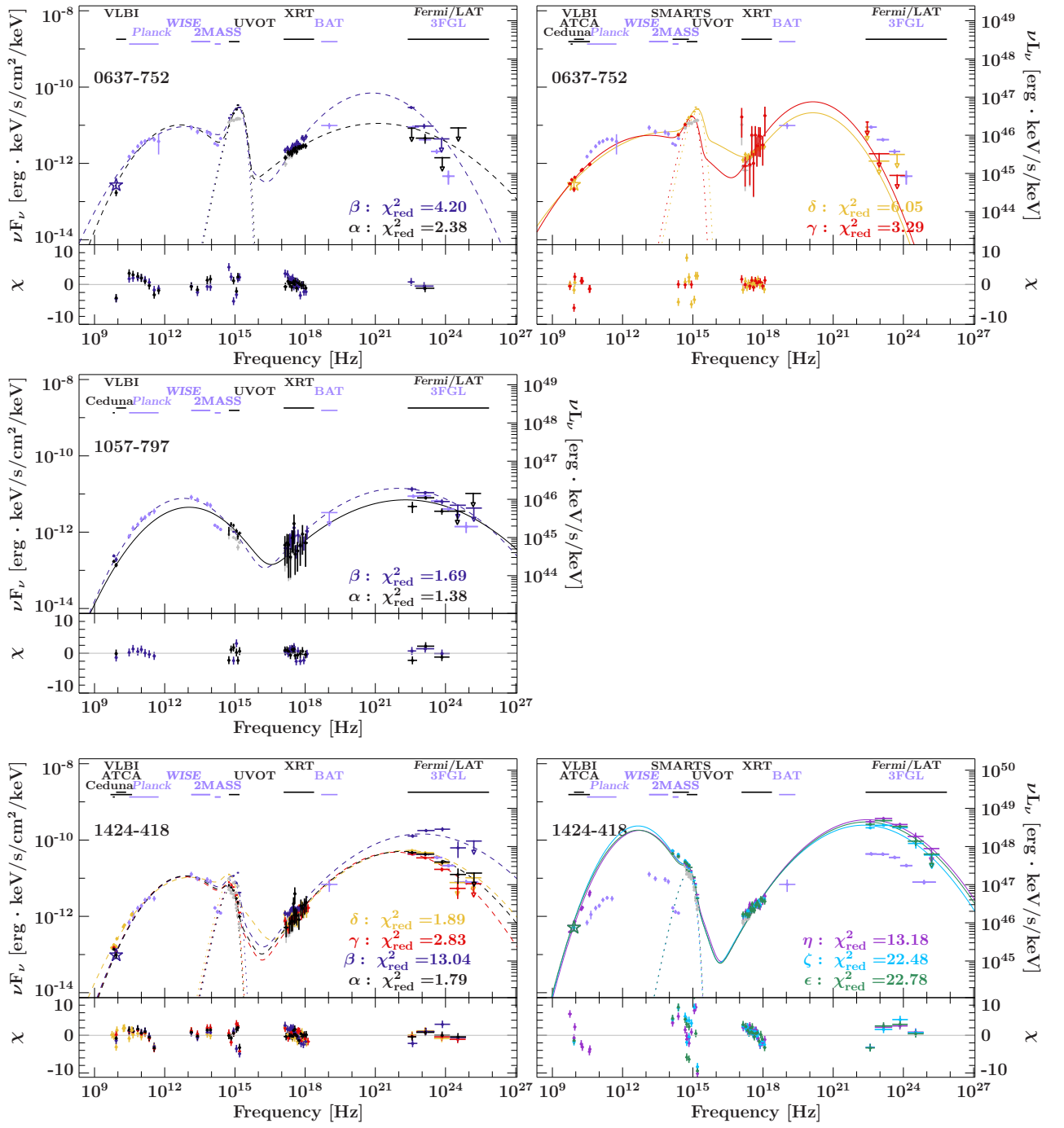


Figure A.3.: (contd.)

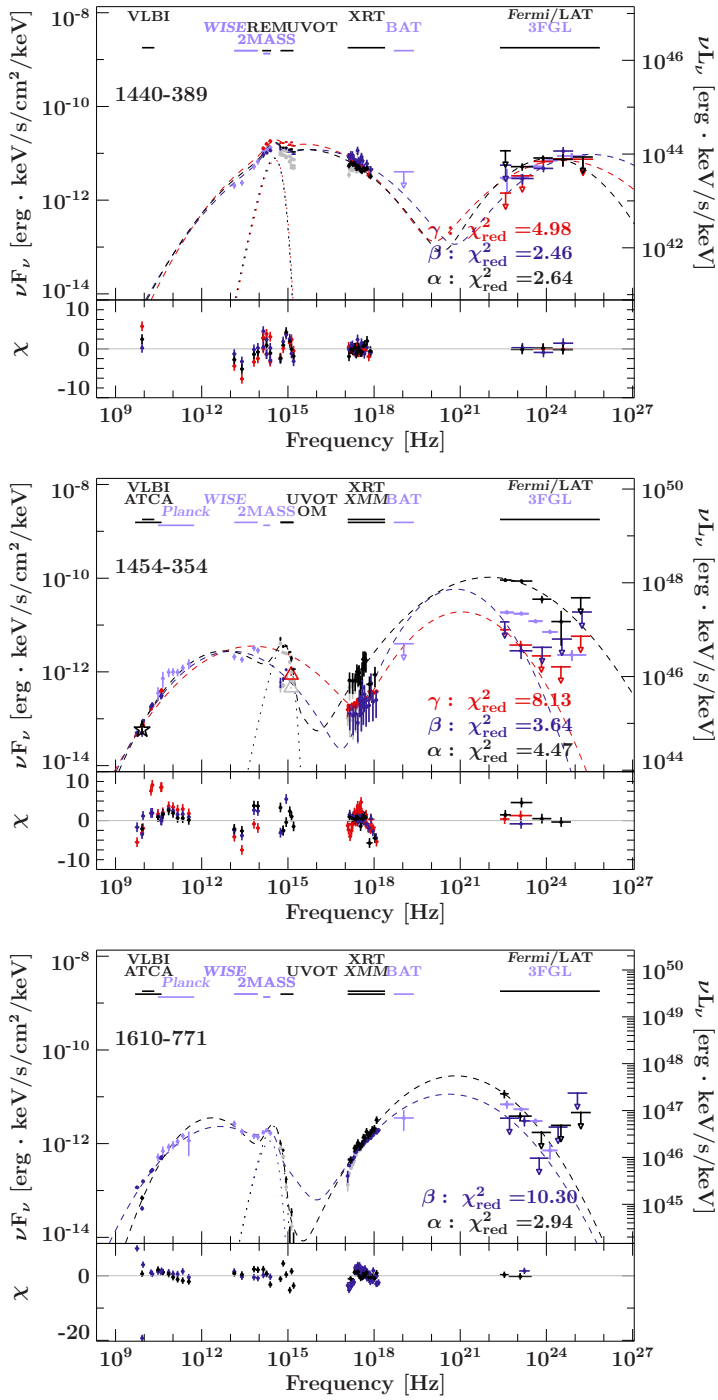


Figure A.3.: (contd.)

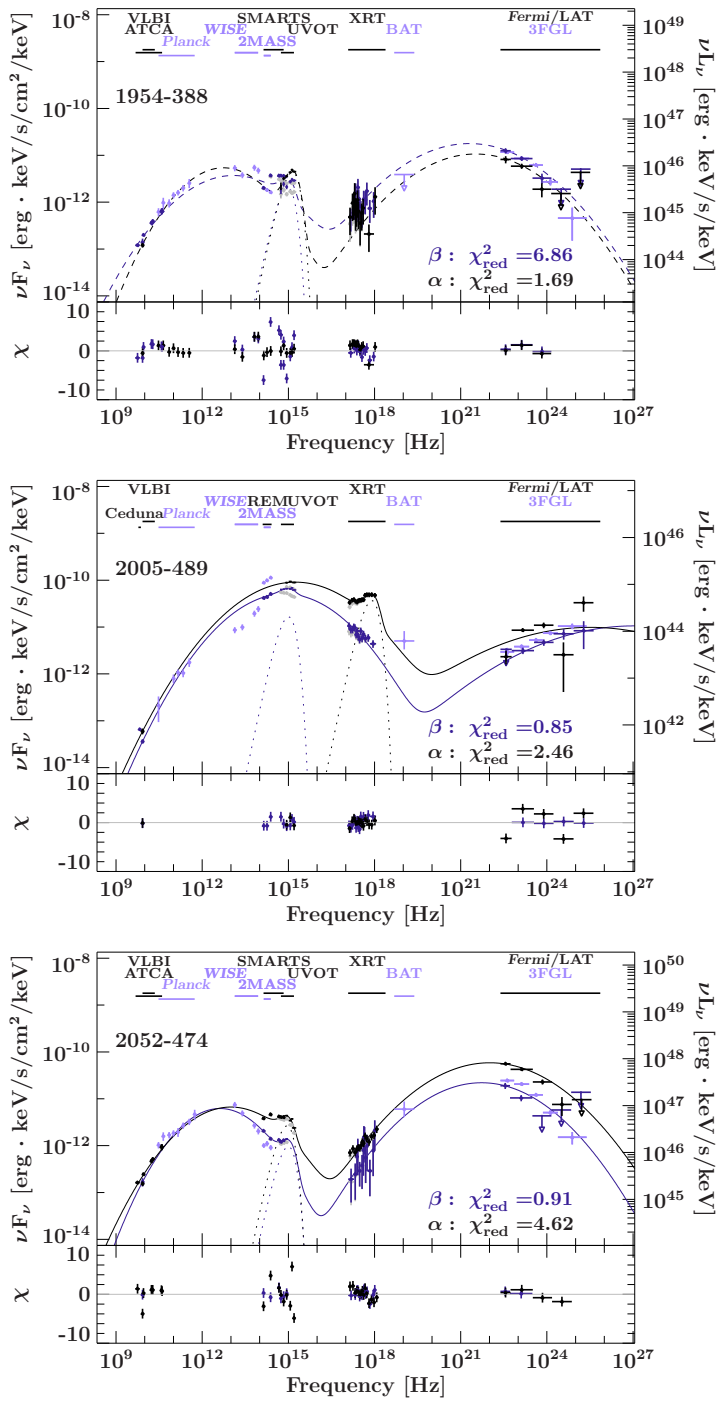


Figure A.3.: (contd.)

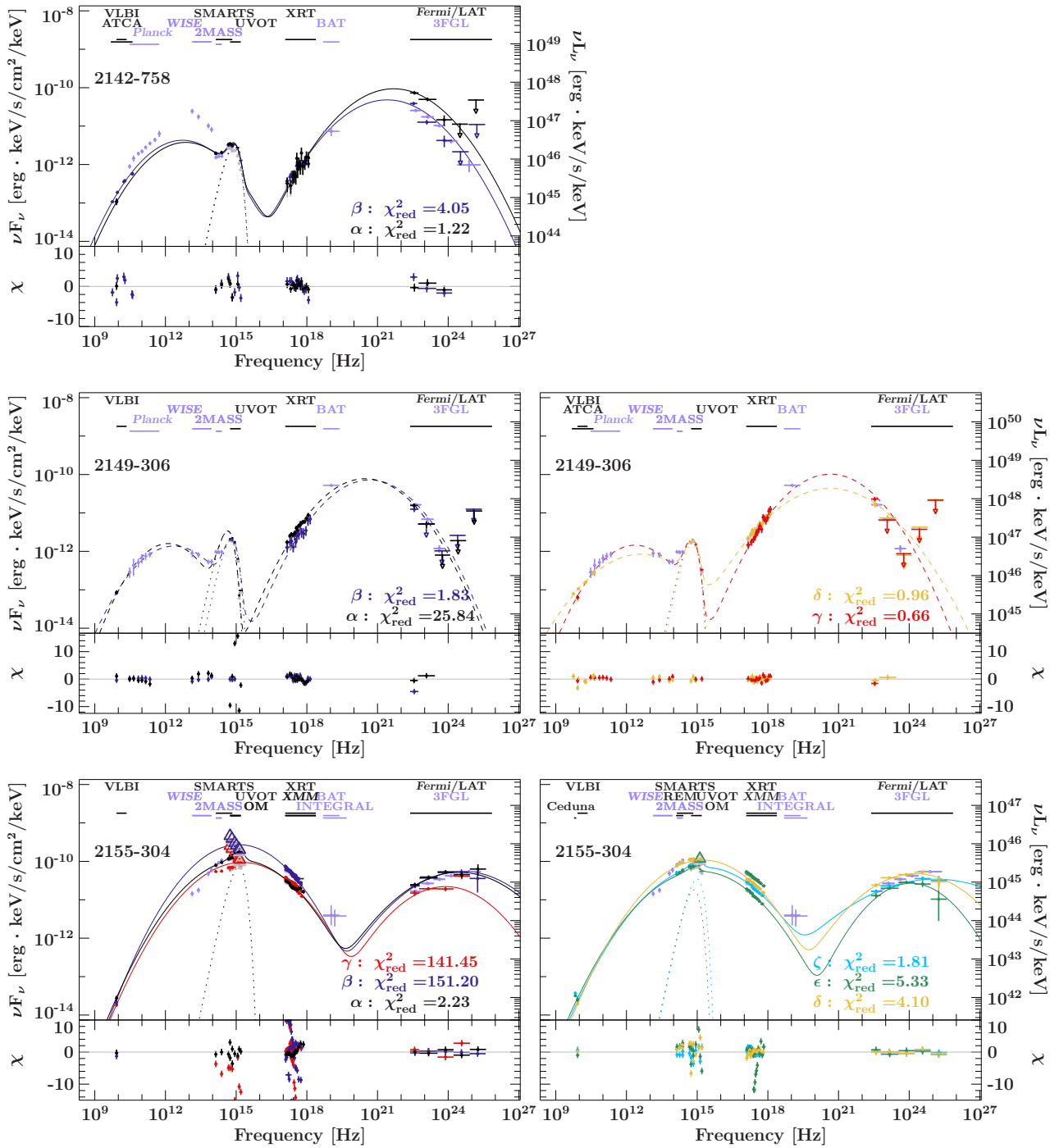


Figure A.3.: (contd.)

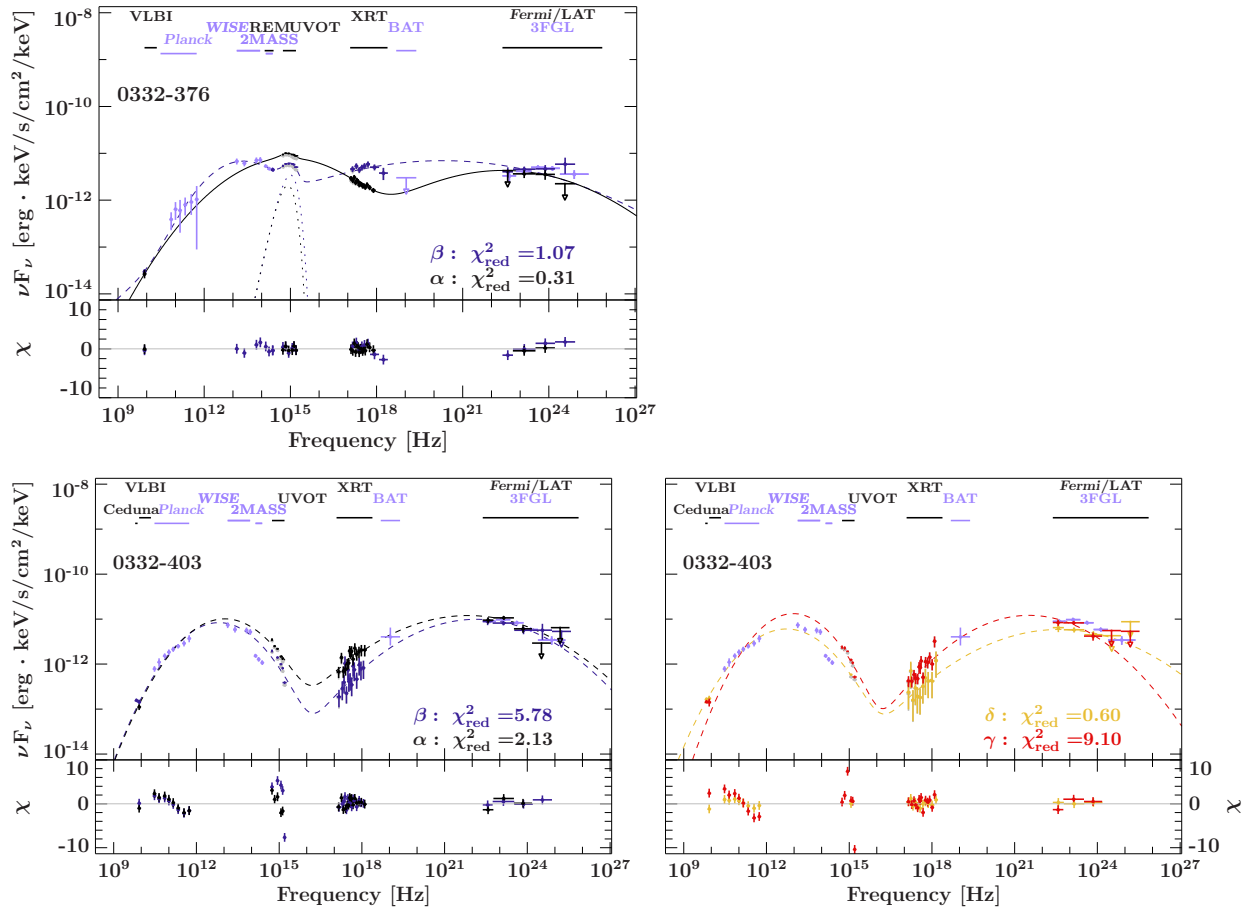


Figure A.4.: Broadband spectral energy distributions for both sources without a redshift in the  $\log \log \nu F_\nu$  representation. For sources with more than 3 states with sufficient data, the plots were split into two parts, to ensure that the SEDs are easily visible. Spectra are shown in dashed if archival data had to be included in the fit. For sources with a thermal excess in the optical/UV, a blackbody was included (dotted). The instruments (including their spectral range) are shown above the spectrum. The colors correspond to the colors used in the light curve. The best fit reduced  $\chi^2$  value is shown at the bottom right for every state. Residuals are shown in the lower panel. The spectra have not been k-corrected.

## Fit result of the Broadband SEDs

Table A.1.: Fit results for all individual SEDs, listed by source and state. In addition to the fit parameters, the time ranges, the degrees of freedom, the reduced  $\chi^2$  values, and the ratio of  $L_X/L_{\text{edd}}$  are given.

Source	SED	$t_{\text{min}}$ t-54000	$t_{\text{max}}$ t-54000	$N_{\text{sync}}$ [log <sub>10</sub> ]	$a_{\text{sync}}$	$b_{\text{sync}}$	$N_{\text{HE}}$ [log <sub>10</sub> ]	$q_{\text{HE}}$	$p_{\text{HE}}$	$N_{\text{blackbody}}$ [log <sub>10</sub> ]	$kT$ [log <sub>10</sub> +4]	$N_{\text{H}}$	dof	$\chi^2_{\text{red}}$	$L_X/L_{\text{edd}}$	$L_{\text{bol}}/L_{\text{edd}}$
0208-512	$\alpha$	724.66	780.66	-0.56±0.05	2.52±0.05	0.109±0.009	-6.12±0.10	1.49±0.04	0.088±0.016	-4.05±0.09	1.43±0.04	1.84	24	8.78	1.28e-01	3.92e+01
	$\beta$	808.66	808.66	-1.15±0.27	2.93±0.20	0.145±0.026	-6.33±0.18	1.54±0.06	0.075±0.053	-4.05±0.14	1.41±0.04	1.84	21	8.24	1.08e-02	2.25e+01
	$\gamma$	808.66	1004.66	-1.64±0.29	2.99±0.23	0.153±0.027	-6.78±0.07	1.72±0.034	0.050±0.065	-3.95±0.05	1.42±0.018	1.84	22	5.27	7.31e-02	6.30e+00
	$\delta$	1004.66	1368.66	-1.87±0.32	3.23±0.12	0.186±0.015	-6.75±0.15	1.70±0.026	0.062±0.029	-4.07±0.05	1.382±0.017	1.84	27	6.61	6.71e-02	6.42e+00
	$\epsilon$	1368.66	1522.66	-2.20±0.15	3.50±0.14	0.226±0.022	-6.47±0.20	1.690±0.021	0.053±0.024	-3.99±0.04	1.398±0.020	1.84	26	6.99	1.41e-01	1.29e+01
0244-470	$\alpha$	1662.66	1606.66	-1.97±0.20	3.43±0.14	0.222±0.020	-6.23±0.25	1.62±0.05	0.09±0.03	-3.77e±0.028	1.356±0.013	1.84	27	4.14	1.59e-01	1.47e+01
	$\gamma$	1662.66	1844.66	-1.06±0.08	3.04±0.08	0.178±0.010	-6.36±0.09	1.57±0.028	0.06±0.013	-4.01±0.13	1.275±0.021	1.84	45.3	9.70e-02	2.52e+01	
	$\theta$	1844.66	2292.66	-1.91±0.08	3.22±0.05	0.185±0.006	-6.65±0.12	1.67±0.04	0.065±0.018	-4.022±0.019	1.487±0.023	1.84	27	11.29	8.04e-02	8.54e+00
	$\alpha$	682.66	1186.66	-3.6±0.7	4.06±0.38	0.30±0.04	-6.35±0.11	1.56±0.04	0.103±0.017	-4.48±0.18	0.93±0.04	1.89	18	2.78		
	$\beta$	1732.66	1802.66	-1.69±0.13	3.36±0.14	0.231±0.024	-6.47±0.20	1.61±0.05	0.107±0.04	-4.48±0.18	1.07±0.04	1.89	8	0.73		
0332-376	$\alpha$	682.66	1037.32	0.16±0.04	2.22±0.06	0.098±0.010	-6.98±0.54	1.73±0.11	0.045±0.043	-4.48±0.18	0.93±0.04	1.54	16	0.27		
	$\beta$	1391.99	1746.66	-1.8±0.5	3.41±0.32	0.25±0.008	-6.38±0.04	1.958±0.015	0.0231±0.0021	-4.25±0.07	1.025±0.027	1.54	25	0.93		
	$\gamma$	1391.99	1746.66	-1.8±0.5	3.41±0.32	0.25±0.008	-6.38±0.04	1.958±0.015	0.0231±0.0021	-4.25±0.07	1.025±0.027	1.54	25	0.93		
0332-403	$\alpha$	682.66	1032.66	-1.43±0.08	3.20±0.09	0.197±0.014	-6.45±0.70	1.73±0.037	0.054±0.019	-3.41±0.029	1.31±0.07	1.48	20	2.44		
	$\beta$	1032.66	1382.66	-1.94±0.02	3.38±0.08	0.212±0.012	-6.71±0.13	1.64±0.05	0.065±0.010	-3.41±0.029	1.31±0.07	1.48	16	9.18		
	$\gamma$	1466.66	1872.66	-1.84±0.14	3.51±0.16	0.243±0.023	-6.49±0.14	1.66±0.04	0.080±0.032	-3.41±0.029	1.31±0.07	1.48	22	10.55		
	$\delta$	1872.66	2236.66	-1.95±0.10	3.27±0.09	0.189±0.014	-6.97±0.10	1.670±0.029	0.0510±0.0334	-3.41±0.029	1.31±0.07	1.48	9	0.66		
	$\alpha$	1270.66	1298.66	-4.74±0.26	4.88±0.15	0.384±0.019	-5.51±0.10	1.66±0.04	0.095±0.010	-3.41±0.029	1.31±0.07	0.60	26	4.09		
0402-362	$\beta$	1816.66	1830.66	-4.2±0.9	4.5±0.6	0.34±0.05	-5.50±0.06	1.538±0.023	0.083±0.007	-3.48±0.075	1.400±0.019	0.60	32	1.45		
	$\alpha$	724.66	850.66	-0.98±0.08	2.99±0.09	0.169±0.015	-6.74±0.07	1.566±0.021	0.050±0.010	-3.48±0.075	1.400±0.020	2.09	13	1.95		
	$\beta$	1396.66	1438.66	-1.49±0.07	3.18±0.08	0.187±0.013	-6.80±0.70	1.65±0.047	0.050±0.018	-3.48±0.075	1.400±0.020	2.09	25	2.96		
0426-380	$\beta$	1494.66	1634.66	-1.01±0.06	2.88±0.06	0.150±0.009	-6.67±0.02	1.589±0.013	0.050±0.009	-3.48±0.075	1.400±0.020	2.09	27	6.24		
	$\delta$	1956.66	2152.66	-0.559±0.023	2.78±0.024	0.145±0.004	-7.0±0.0	1.527±0.014	0.052±0.0041	-3.48±0.075	1.400±0.020	2.09	49	2.74		
	$\epsilon$	2236.66	2334.66	-0.28±0.08	2.80±0.023	0.160±0.011	-6.22±0.08	1.580±0.013	0.050±0.011	-3.48±0.075	1.400±0.020	2.09	14	2.55		
	$\alpha$	682.66	1228.66	0.969±0.011	2.25±0.018	0.1385±0.0021	-7.2±0.2	1.53±0.21	0.042±0.009	-3.48±0.075	1.400±0.020	1.24	20	2.53		
	$\beta$	1587.99	1947.32	0.886±0.033	2.246±0.023	0.135±0.005	-6.92±0.30	1.66±0.13	0.031±0.043	-3.48±0.075	1.400±0.020	1.24	20	1.21		
0447-439	$\gamma$	1947.32	2306.66	0.958±0.016	2.321±0.017	0.147±0.004	-8.40±0.70	1.07±0.5	0.106±0.010	-3.48±0.075	1.400±0.020	1.24	19	2.31		
	$\alpha$	682.66	1092.16	-2.5±0.6	3.18±0.33	0.17±0.04	-6.58±0.11	1.63±0.04	0.089±0.017	-3.70±0.021	1.336±0.011	1.95	26	5.06		
	$\beta$	1501.66	1911.16	-2.6±0.4	3.27±0.18	0.182±0.018	-6.98±0.09	1.717±0.028	0.05±0.017	-3.70±0.021	1.336±0.011	1.95	12	2.60		
	$\gamma$	1911.16	2320.66	-2.7±0.4	3.30±0.40	0.187±0.015	-6.71±0.15	1.624±0.034	0.10	-3.52	1.37±0.05	1.95	20	1.89		
	$\delta$	2320.66	2978.66	-2.7±0.4	3.30±0.40	0.187±0.015	-6.66±0.10	1.69±0.05	0.09	-3.569±0.024	1.342±0.019	1.95	15	3.82		
0506-612	$\alpha$	682.66	1340.66	-0.30±0.17	2.90±0.39	0.180±0.021	-6.03±0.13	1.822±0.016	0.0528±0.0180	-3.64±0.20	0.55±0.06	3.58	13	0.48		
	$\beta$	1340.66	1382.66	-0.52±0.07	3.12±0.08	0.201±0.012	-5.69±0.06	1.757±0.029	0.055±0.010	-3.64±0.15	0.56±0.05	3.58	26	1.32		
	$\gamma$	1382.66	1494.66	-0.69±0.10	3.20±0.10	0.214±0.015	-5.65±0.11	1.77±0.04	0.078±0.017	-3.64±0.15	0.56±0.05	3.58	21	1.19		
	$\delta$	1508.66	1802.66	-0.58±0.08	3.00±0.09	0.177±0.015	-5.67±0.09	1.751±0.027	0.083±0.014	-3.50±0.07	0.532±0.015	3.58	25	3.19		
	$\epsilon$	1802.66	1928.66	-0.68±0.08	3.12±0.08	0.194±0.006	-5.94±0.70	1.87±0.04	0.057±0.024	-3.69±0.08	0.611±0.023	3.58	24	1.64		
0521-365	$\zeta$	2222.66	2278.66	-0.26±0.19	3.10±0.04	0.21±0.02	-5.58±0.10	1.728±0.028	0.062±0.012	-3.69±0.08	0.611±0.023	3.58	19	0.39		
	$\alpha$	682.66	808.66	-0.68±0.07	3.04±0.07	0.178±0.012	-6.03±0.07	1.618±0.022	0.060±0.010	-3.69±0.08	0.611±0.023	3.14	15	2.64		
	$\beta$	808.66	962.66	-0.42±0.07	2.55±0.08	0.106±0.011	-6.27±0.10	1.59±0.04	0.070±0.017	-3.69±0.08	0.611±0.023	3.14	18	2.58		
	$\gamma$	1172.66	1242.66	4.07±0.04	2.39±0.06	0.169±0.015	-5.98±0.05	1.548±0.015	0.080±0.006	-3.69±0.08	0.611±0.023	3.14	19	2.70		
	$\delta$	1242.66	1340.66	0.318±0.005	2.606±0.005	0.11264±0.0019	-6.145±0.010	1.510±0.007	0.06000±0.00028	-3.69±0.08	0.611±0.023	3.14	66	10.70		
0537-441	$\epsilon$	1578.66	1718.66	0.14±0.06	2.59±0.05	0.117±0.007	-6.18±0.07	1.579±0.017	0.06±0.013	-3.69±0.08	0.611±0.023	3.14	28	5.56		
	$\zeta$	1718.66	2026.66	-0.42±0.05	2.78±0.04	0.136±0.005	-6.34±0.10	1.56±0.04	0.06±0.013	-3.69±0.08	0.611±0.023	3.14	21	3.31		
	$\alpha$	682.66	808.66	-0.68±0.07	3.04±0.07	0.178±0.012	-6.03±0.07	1.618±0.022	0.060±0.010	-3.69±0.08	0.611±0.023	3.14	15	2.64		
	$\beta$	808.66	962.66	-0.42±0.07	2.55±0.08	0.106±0.011	-6.27±0.10	1.59±0.04	0.070±0.017	-3.69±0.08	0.611±0.023	3.14	18	2.58		
	$\gamma$	1172.66	1242.66	4.07±0.04	2.39±0.06	0.169±0.015	-5.98±0.05	1.548±0.015	0.080±0.006	-3.69±0.08	0.611±0.023	3.14	19	2.70		
0637-752	$\alpha$	752.66	906.66	-2.0±3.6	3.41±0.17	0.206±0.020	-6.33±0.11	1.80±0.04	0.057±0.023	-2.888±0.032	1.41±0.04	7.82	24	2.40		
	$\beta$	1069.06	1231.46	-1.1±0.4	2.93±0.20	0.147±0.023	-5.64±0.024	1.616±0.011	0.13	-2.905±0.018	1.369±0.020	7.82	28	4.17		
	$\gamma$	2077.99	2437.32	-0.78±0.21	2.63±0.10	0.108±0.012	-5.70±0.15	1.70	0.20	-3.19±0.05	1.22±0.08	7.82	8	5.18		
	$\delta$	2437.32	2810.66	-0.12±0.06	2.32±0.04	0.077±0.005	-5.99±0.09	1.70	0.20	-3.014±0.016	1.425±0.019	7.82	20	6.45		

Table A.1.: contd.

Source	SED	$t_{\min}$	$t_{\max}$	$N_{\text{sync}}$	$\alpha_{\text{sync}}$	$b_{\text{sync}}$	$N_{\text{HE}}$	$\theta_{\text{HE}}$	$\theta_{\text{HE}}$	$N_{\text{blackbody}}$	$kT$	$N_{\text{H}}$	$\chi^2_{\text{red}}$	$L_X/L_{\text{edd}}$	$L_{\text{bol}}/L_{\text{edd}}$	
1057-797	$\alpha$	1032.66	1634.66	$-1.4^{+3.0}_{-0.4}$	$2.9^{+0.4}_{-0.5}$	$0.16^{+0.05}_{-0.07}$	$-6.85 \pm 0.19$	$1.66^{+0.05}_{-0.08}$	$0.058^{+0.026}_{-0.008}$	$0.070^{+0.022}_{-0.020}$	$1.182^{+0.028}_{-0.030}$	6.34	2.65	$6.05e-03$	$2.67e+00$	
	$\beta$	1634.66	2061.66	$-1.71 \pm 0.11$	$3.22^{+0.10}_{-0.11}$	$0.186^{+0.015}_{-0.016}$	$-6.54 \pm 0.15$	$1.63 \pm 0.05$	$0.070^{+0.022}_{-0.020}$	$0.080^{+0.028}_{-0.014}$	$1.319 \pm 0.017$	6.34	1.64	$1.82e-02$	$4.14e+00$	
1424-418	$\alpha$	1172.66	1312.66	$-1.90^{+0.22}_{-0.33}$	$3.47^{+0.13}_{-0.18}$	$0.230^{+0.017}_{-0.020}$	$-6.11 \pm 0.11$	$1.55 \pm 0.04$	$0.080^{+0.026}_{-0.011}$	$0.07$	$1.182^{+0.028}_{-0.030}$	7.71	18	2.50		
	$\beta$	1312.66	1340.66	$-1.62^{+0.30}_{-0.33}$	$3.33^{+0.19}_{-0.19}$	$0.214^{+0.025}_{-0.027}$	$-5.938 \pm 0.26$	$1.500 \pm 0.11$	$0.093 \pm 0.012$	$-3.01 \pm 0.04$	$1.319 \pm 0.017$	7.71	27	13.63		
$\gamma$	$\alpha$	1354.66	1648.66	$-2.01^{+0.25}_{-0.25}$	$3.51^{+0.17}_{-0.16}$	$0.232^{+0.018}_{-0.016}$	$-6.11 \pm 0.08$	$1.533^{+0.027}_{-0.030}$	$0.079 \pm 0.014$	$-3.20 \pm 0.04$	$1.200 \pm 0.016$	7.71	28	3.00		
	$\beta$	1648.66	1872.66	$-1.05^{+0.25}_{-0.40}$	$2.99^{+0.16}_{-0.12}$	$0.165^{+0.016}_{-0.012}$	$-6.16 \pm 0.09$	$1.537^{+0.030}_{-0.031}$	$0.079 \pm 0.014$	$-2.84^{+0.054}_{-0.054}$	$1.18^{+0.67}_{-0.26}$	7.71	29	1.76		
$\epsilon$	$\alpha$	2292.66	2334.66	$-2.07 \pm 0.06$	$4.182^{+0.020}_{-0.020}$	$-0.50$	$-5.650^{+0.025}_{-0.025}$	$1.393 \pm 0.009$	$0.10$	$-3.44^{+0.025}_{-0.025}$	$1.215 \pm 0.008$	7.71	24	22.83		
	$\zeta$	2334.66	2390.66	$-2.11^{+0.05}_{-0.05}$	$4.269^{+0.028}_{-0.020}$	$-0.48$	$-5.670^{+0.025}_{-0.025}$	$1.416 \pm 0.009$	$0.10$	$-2.881^{+0.054}_{-0.054}$	$1.193 \pm 0.007$	7.71	24	18.62		
$\eta$	$\alpha$	2390.66	2432.66	$-1.95^{+0.11}_{-0.12}$	$4.14 \pm 0.09$	$0.318 \pm 0.012$	$-5.620^{+0.028}_{-0.030}$	$1.384 \pm 0.010$	$0.10$	$-2.864^{+0.025}_{-0.026}$	$1.207 \pm 0.008$	7.71	29	13.66		
	$\beta$	2432.66	2432.66	$0.449 \pm 0.014$	$2.106^{+0.011}_{-0.011}$	$0.106^{+0.006}_{-0.004}$	$-10.0^{+0.07}_{-0.07}$	$0.45^{+0.10}_{-0.09}$	$0.16^{+0.03}_{-0.12}$	$-3.84^{+0.07}_{-0.07}$	$0.576^{+0.038}_{-0.038}$	7.83	23	2.66		
1440-389	$\alpha$	1158.66	1704.66	$0.473^{+0.018}_{-0.019}$	$2.041^{+0.019}_{-0.016}$	$0.095 \pm 0.004$	$-10.0^{+0.07}_{-0.07}$	$0.772^{+0.155}_{-0.155}$	$0.10$	$-3.84^{+0.06}_{-0.07}$	$0.576^{+0.038}_{-0.038}$	7.83	27	2.55		
	$\beta$	1704.66	2138.66	$0.559^{+0.018}_{-0.016}$	$2.122 \pm 0.010$	$0.117^{+0.009}_{-0.005}$	$-9.0^{+0.07}_{-0.07}$	$0.97^{+0.39}_{-0.23}$	$0.10$	$-3.88^{+0.07}_{-0.07}$	$0.60 \pm 0.04$	7.83	26	5.23		
1454-354	$\alpha$	710.66	766.66	$-2.2^{+0.30}_{-0.6}$	$3.26^{+0.27}_{-0.27}$	$0.19 \pm 0.04$	$-5.87^{+0.12}_{-0.12}$	$1.48 \pm 0.04$	$0.100^{+0.015}_{-0.015}$	$-3.47^{+0.05}_{-0.06}$	$1.251^{+0.021}_{-0.022}$	6.60	18	3.39	$5.99e-02$	$3.89e+01$
	$\beta$	1522.66	1788.66	$-1.62 \pm 0.12$	$2.96 \pm 0.08$	$0.158 \pm 0.010$	$-6.0^{+0.07}_{-0.07}$	$1.30^{+0.11}_{-0.11}$	$0.24^{+0.10}_{-0.10}$	$0.100^{+0.015}_{-0.015}$	$1.251^{+0.021}_{-0.022}$	6.60	21	4.23	$1.94e-02$	$1.64e+01$
$\gamma$	$\alpha$	1788.66	2180.66	$-0.673^{+0.024}_{-0.024}$	$2.536 \pm 0.015$	$0.11157^{+0.0026}_{-0.0026}$	$-6.425^{+0.024}_{-0.024}$	$1.40$	$0.18$	$-3.47^{+0.05}_{-0.06}$	$1.251^{+0.021}_{-0.022}$	6.60	51	8.13	$2.79e-02$	$6.39e+00$
	$\beta$	2180.66	2275.86	$-4.17^{+0.21}_{-0.24}$	$3.14^{+0.13}_{-0.12}$	$0.296^{+0.017}_{-0.017}$	$-6.04^{+0.13}_{-0.13}$	$1.61^{+0.04}_{-0.05}$	$0.134^{+0.024}_{-0.022}$	$-3.55 \pm 0.05$	$0.939^{+0.013}_{-0.014}$	6.76	29	2.98		
1610-771	$\alpha$	1091.46	1486.26	$-2.16 \pm 0.19$	$3.37 \pm 0.13$	$0.206 \pm 0.017$	$-6.61^{+0.22}_{-0.22}$	$1.59^{+0.08}_{-0.08}$	$0.10 \pm 0.04$	$-3.727^{+0.028}_{-0.028}$	$1.38^{+0.04}_{-0.04}$	6.43	20	1.94		
	$\beta$	1486.26	2275.86	$-2.20^{+0.26}_{-0.30}$	$3.14^{+0.13}_{-0.12}$	$0.167^{+0.014}_{-0.013}$	$-6.33 \pm 0.04$	$1.705 \pm 0.019$	$0.12$	$-4.05^{+0.08}_{-0.08}$	$1.21 \pm 0.05$	6.43	21	9.26		
1954-388	$\alpha$	738.66	1326.66	$1.44 \pm 0.13$	$2.53^{+0.14}_{-0.15}$	$0.132^{+0.022}_{-0.022}$	$-6.28^{+0.19}_{-0.19}$	$1.66 \pm 0.06$	$0.089^{+0.028}_{-0.025}$	$-3.17^{+0.08}_{-0.08}$	$3.96^{+0.08}_{-0.08}$	3.93	16	2.55	$1.55e-02$	$1.67e-01$
	$\beta$	1326.66	1830.66	$1.44 \pm 0.13$	$2.53^{+0.14}_{-0.15}$	$0.132^{+0.022}_{-0.022}$	$-6.28^{+0.19}_{-0.19}$	$1.66 \pm 0.06$	$0.089^{+0.028}_{-0.025}$	$-3.17^{+0.08}_{-0.08}$	$3.96^{+0.08}_{-0.08}$	3.93	16	2.55	$1.55e-02$	$1.67e-01$
2005-489	$\alpha$	682.66	1046.66	$1.277^{+0.021}_{-0.021}$	$2.188^{+0.024}_{-0.024}$	$0.112 \pm 0.005$	$-7.6^{+0.07}_{-0.07}$	$1.54 \pm 0.08$	$0.04$	$-3.51^{+0.08}_{-0.08}$	$1.06^{+0.06}_{-0.06}$	3.93	16	2.55	$1.55e-02$	$1.67e-01$
	$\beta$	1046.66	2264.66	$0.917^{+0.024}_{-0.023}$	$2.309^{+0.015}_{-0.014}$	$0.128 \pm 0.004$	$-8.4^{+0.07}_{-0.07}$	$1.43^{+0.14}_{-0.13}$	$0.04$	$-3.51^{+0.08}_{-0.08}$	$1.06^{+0.06}_{-0.06}$	3.93	21	0.76	$1.28e-03$	$1.01e-01$
2052-474	$\alpha$	976.66	1186.66	$-1.26^{+0.24}_{-0.24}$	$2.96^{+0.17}_{-0.18}$	$0.156^{+0.021}_{-0.020}$	$-6.05 \pm 0.07$	$1.533^{+0.023}_{-0.023}$	$0.089^{+0.011}_{-0.010}$	$-3.58^{+0.06}_{-0.06}$	$1.370^{+0.016}_{-0.016}$	2.89	26	4.74		
	$\beta$	1186.66	1550.66	$-2.4^{+0.24}_{-0.8}$	$3.49^{+0.18}_{-0.18}$	$0.22 \pm 0.07$	$-6.4^{+0.07}_{-0.07}$	$1.54^{+0.14}_{-0.11}$	$0.10^{+0.010}_{-0.005}$	$-4.02^{+0.13}_{-0.13}$	$1.42^{+0.09}_{-0.09}$	2.89	5	1.07		
2142-758	$\alpha$	1746.66	1788.66	$-1.90^{+0.10}_{-0.09}$	$3.16^{+0.04}_{-0.04}$	$-0.74$	$-5.97^{+0.15}_{-0.14}$	$1.41 \pm 0.05$	$0.123^{+0.025}_{-0.022}$	$-3.649^{+0.029}_{-0.031}$	$1.248 \pm 0.020$	6.55	17	1.22		
	$\beta$	1788.66	1942.66	$-2.01 \pm 0.13$	$3.21^{+0.03}_{-0.03}$	$0.180 \pm 0.009$	$-6.05 \pm 0.12$	$1.48 \pm 0.05$	$0.127^{+0.010}_{-0.010}$	$-3.672^{+0.024}_{-0.024}$	$1.254 \pm 0.013$	6.55	25	4.00		
2149-306	$\alpha$	864.66	1228.66	$-4.7 \pm 0.4$	$4.18^{+0.17}_{-0.18}$	$0.275^{+0.022}_{-0.021}$	$-5.50 \pm 0.08$	$1.655^{+0.023}_{-0.023}$	$0.158^{+0.014}_{-0.013}$	$-3.213 \pm 0.021$	$1.188 \pm 0.005$	1.63	25	26.76		
	$\beta$	1228.66	1592.66	$-3.3^{+4.9}_{-0.3}$	$3.51^{+0.25}_{-0.26}$	$0.203^{+0.029}_{-0.030}$	$-5.61^{+0.04}_{-0.05}$	$1.587^{+0.013}_{-0.014}$	$0.16$	$-3.45 \pm 0.05$	$1.34 \pm 0.05$	1.63	23	1.87		
$\gamma$	$\alpha$	1676.66	1858.66	$-3.5^{+0.5}_{-0.5}$	$3.65 \pm 0.26$	$0.22 \pm 0.04$	$-5.45^{+0.05}_{-0.05}$	$1.60 \pm 0.05$	$0.156 \pm 0.025$	$-3.44^{+0.08}_{-0.07}$	$1.321^{+0.028}_{-0.030}$	1.63	21	0.66		
	$\delta$	1858.66	2040.66	$-2.20 \pm 0.27$	$2.88 \pm 0.14$	$0.127^{+0.015}_{-0.016}$	$-5.74^{+0.14}_{-0.15}$	$1.73 \pm 0.04$	$0.108 \pm 0.024$	$-3.51 \pm 0.04$	$1.36 \pm 0.05$	1.63	22	1.09		
2155-304	$\alpha$	682.66	885.66	$1.315 \pm 0.019$	$2.246^{+0.011}_{-0.012}$	$0.131 \pm 0.004$	$-7.97^{+0.07}_{-0.07}$	$1.026^{+0.040}_{-0.040}$	$0.096^{+0.011}_{-0.008}$	$-2.84^{+0.04}_{-0.04}$	$1.19 \pm 0.04$	1.48	23	2.21	$7.08e-03$	$4.48e-01$
	$\beta$	885.66	1088.66	$1.698 \pm 0.022$	$2.2914 \pm 0.0017$	$-0.82$	$-8.08^{+0.08}_{-0.08}$	$1.00^{+0.026}_{-0.026}$	$0.096^{+0.008}_{-0.008}$	$-2.84^{+0.04}_{-0.04}$	$1.19 \pm 0.04$	1.48	53	153.85	$7.55e-03$	$7.81e-01$
$\gamma$	$\alpha$	1088.66	1326.66	$1.2821^{+0.0019}_{-0.0020}$	$2.2140 \pm 0.0015$	$-0.89$	$-8.5^{+0.5}_{-0.5}$	$0.82^{+0.23}_{-0.23}$	$0.13^{+0.007}_{-0.007}$	$-2.84^{+0.04}_{-0.04}$	$1.19 \pm 0.04$	1.48	54	143.83	$4.15e-03$	$2.83e-01$
	$\beta$	1326.66	1676.66	$1.337^{+0.007}_{-0.007}$	$2.222 \pm 0.006$	$0.132^{+0.0023}_{-0.0023}$	$-8.1^{+0.7}_{-0.7}$	$0.9^{+0.37}_{-0.37}$	$0.11^{+0.006}_{-0.006}$	$-3.44^{+0.07}_{-0.07}$	$1.321^{+0.028}_{-0.030}$	1.48	27	4.28	$5.83e-03$	$3.92e-01$
$\epsilon$	$\alpha$	1676.66	2124.66	$1.025 \pm 0.014$	$2.231^{+0.008}_{-0.009}$	$0.1215^{+0.0030}_{-0.0028}$	$-9.5^{+0.7}_{-0.8}$	$0.4^{+0.8}_{-0.8}$	$0.170^{+0.030}_{-0.028}$	$-3.44^{+0.07}_{-0.07}$	$0.934^{+0.023}_{-0.023}$	1.48	25	5.50	$9.24e-03$	$6.05e-01$
	$\zeta$	2124.66	2572.66	$1.168^{+0.020}_{-0.017}$	$2.188 \pm 0.008$	$0.121^{+0.005}_{-0.005}$	$-7.4^{+0.7}_{-0.7}$	$1.38^{+0.56}_{-0.56}$	$0.05^{+0.004}_{-0.004}$	$-3.15^{+0.06}_{-0.06}$	$1.063^{+0.019}_{-0.019}$	1.48	26	1.91	$4.75e-03$	$3.14e-01$



## Acknowledgments

First and foremost I want to thank my supervisors Jörn Wilms and Matthias Kadler. I am very thankful for their support, knowledge, encouragement, and advice. I'm also very grateful for the opportunity to attend international conferences where I presented my work.

Furthermore, I want to thank all of the Remeisen for the great working atmosphere at the Observatory. I want to thank Christina Gräfe, Katharina Leiter, Annika Kreikenbohm, Cornelia Müller, and Rosamunde Pare for their support and the discussions. I want to thank my office mates, Christina Gräfe, Michael Wille, and Marco Fink for interesting discussions. I greatly appreciate the help from the proof-readers of my thesis: Jonas Trüstedt, Robert Schulz, Cornelia Müller, Thomas Dauser, Tobias Beuchert, Dorit Glawion, Eugenia Litzinger, and Macarena Sagredo. I am grateful to Cornelia Müller for the very helpful discussions about radio astronomy, TANAMI data, *Fermi* data, and active galaxies. I also want to thank Thomas Dauser, Sebastian Falkner and Matthias Kühnel for much help throughout this work through discussions as well as with *ISIS*, *S-Lang* and *SLXfig*. I appreciate the help and discussions with Christian Schmid and Michael Wille about CCD detectors. I also want to thank Tobias Beuchert and Sebastian Falkner for the helpful discussions. I also want to thank Maria Hirsch, Mirjam Örtel, Matthias Kühnel, Victoria Grinberg, Nathalie Hell, Christina Gräfe, Alex Markowitz, and Peter Nemeth for the interesting meetings of the CCD lab group.

I want to thank the whole TANAMI collaboration for the great help, support and discussions. I especially thank Roopesh Ojha, Cornelia Müller, Bryce Carpenter, Mike Dutka, and Sara Buson. I also want to thank the Admins, Ingo Kreykenbohm, Thomas Dauser, Fritz Schwarm and Jörn Wilms of the Observatory for doing an amazing work at maintaining the computer system, software and local cluster. I want to thank the groups of M. Kadler and K. Mannheim for making me feel welcome at the University of Würzburg. I especially want to thank Annika Kreikenbohm, Daniela Dorner, Natalia Lewandowska, Till Steinbring, Rosamunde Pare, Dorit Glawion, Marcus Langejahn, Jonas Trüstedt, Katharina Leiter, and Robert Schulz. I want to thank Roopesh Ojha, Katja Pottschmidt and Jörn Wilms for the possibility to visit the GSFC twice. I want to thank them, and Mike Dutka and Bryce Carpenter for making the visits very enjoyable. I further thank Eduardo Ros for the possibility to visit the MPIfR and for being able to present my work. I further thank Roberto Angioni for the interesting discussions.

I want to thank the H.E.S.S. group at ECAP for welcoming me during their lunch breaks, especially Johannes Veh, Susanne Raab, Philipp Willmann, and Andre Wörnlein. I further thank the ANTARES group for the great TANAMI-ANTARES meetings, especially Clancy James and Alexander Kappes.

I am very grateful to Johannes Veh for the support and the helpful discussions about solid state physics and very high energy astrophysics. Finally, I also want to thank my parents and my sister Leticia very much for their support.

---

This work has made use of SAOImage DS9, developed by Smithsonian Astrophysical Observatory (Joye & Mandel, 2003). I acknowledge the use of the data obtained from the High Energy Astrophysics Science Archive Research Center (HEASARC), provided by NASA's Goddard Space Flight Center. Further, I have used the Astrophysics Data System by NASA (<http://adsabs.harvard.edu/>). This work has made use of the XRT Data Analysis Software (XRT-DAS) developed under the responsibility of the ASI Science Data Center (ASDC), Italy. This

research has made use of the SIMBAD database, operated at CDS, Strasbourg, France, as well as of the NASA/IPAC Extragalactic Database (NED) which is operated by the Jet Propulsion Laboratory, California Institute of Technology, under contract with the National Aeronautics and Space Administration. I thank J.E. Davis and T. Johnson for the development of the `s1xfig` module and the SED scripts that have been used to prepare the figures in this work. This research has made use of a collection of ISIS scripts provided by the Dr. Karl Remeis-Observatory, Bamberg, Germany at <http://www.sternwarte.uni-erlangen.de/isis/>. This thesis has made use of up-to-date SMARTS optical/near-infrared light curves that are available at [www.astro.yale.edu/smarts/glast/home.php](http://www.astro.yale.edu/smarts/glast/home.php). This thesis makes use of data products from the Two Micron All Sky Survey, which is a joint project of the University of Massachusetts and the Infrared Processing and Analysis Center/California Institute of Technology, funded by the National Aeronautics and Space Administration and the National Science Foundation.